Tuning Light-Matter Interaction Inside Organic Microcavities Using Semiconducting Polymer Chain Geometry



Florian Le Roux

Wolfson College

University of Oxford

A thesis submitted for the degree of

Doctor of Philosophy

Hilary 2020

À mon grand-père Jacques, qui m'a appris à toujours garder le sourire.

Acknowledgments

I would like to start by thanking Prof. Donal Bradley for giving me the chance to join his research group at the University of Oxford, and Prof. Robert Taylor, for offering his precious support, guidance and inspiring optimism during the second half of my doctoral studies. I also wish to acknowledge the financial support of Wolfson College and Dr Simon Harrison for their award of a Wolfson Harrison Scholarship, and the Engineering and Physical Sciences Research Council.

Je tiens à remercier mes parents, Alain et Mireille pour leur soutien indéfectible au cours de toutes mes études et leur amour inconditionnel. Bastien et Céleste, mon frère et ma soeur, vous êtes des personnes extraordinaires, merci d'avoir toujours cru en moi. Jean-Baptiste et Dominique, papi, mami, merci pour tous ces moments d'exception passés à Meudon avec vous. Théo, Sarah, c'est un vrai plaisir de vous avoir dans la famille, merci pour tout. Andrée, merci pour tous tes encouragements. Enfin Lily, merci d'apporter ta bonne humeur et tes sourires à nous tous, j'ai hâte de te voir grandir.

Bien sûr, merci aux potes: Kévin, Sébastien, Thomas, Martin, Tou-Geu, Marie, Hugues, Quentin, Adrien et tous les autres sans qui ma vie serait bien terne.

I also want to thank my friends in Oxford, in particular my flatmates Ravinda and Sam for all the wonderful scenes during my time here.

Last but not least, I would like to thank Madeleine for never losing patience when I wrote this thesis, you have been the best inspiration for this work.

Abstract

Strong light-matter interaction inside planar microcavities has been the object of intense scrutiny thanks to a wide variety of technological and theoretical achievements for which future applicability relies on understanding and controlling both photonic and excitonic environments. Recently, demonstrations of polariton lasing, non-equilibrium Bose Einstein Condensation (BEC) and superfluidity at room temperature have been reported thanks to the large oscillator strengths and exciton binding energies of Frenkel excitons in organic semiconductors.
Among this class of material, semiconducting conjugated polymers are promising thanks to their versatility, remarkable optical properties and tunability. In this thesis, we explore different methods to manipulate the intra- and inter-chain properties of a subgroup of semiconducting polymers, the polyfluorenes, to shape the interactions of their excitons with light.
We begin our work by examining the essential properties of semiconducting conjugated polymers, which we then embed inside microcavities to observe strong light-matter interactions. We present a brief overview of exciton-polaritons in organic microcavities, highlight recent developments in their understanding and introduce the measurement and fabrication techniques that we use throughout the thesis.
In our first experimental investigation, we perform conformational changes to a polymer's backbone inside metallic microcavities thereby inducing two sub-populations of excitons with a pre-determined fraction. We present the mode characteristics of these structures with ultrastrong coupling (USC) of the first disordered population of excitons and a splitting of the lower polariton branch induced via gradual introduction of the second population of excitons. We measure the photoluminescence (PL) only emanating from the lowermost polariton branch, which allows us to exert conformational control over the emission energy and its angular variation to create dispersion-free cavities with highly saturated blue-violet emission.
In our second experimental realization, we report an inter-chain tunability via the fabrication and optical characterization of organic microcavities containing liquid-crystalline conjugated polymers (LCCP)s aligned on top of a thin transparent Sulfuric Dye 1 (SD1) photoalignment layer. Transition dipole moment alignment enables a systematic increase in the interaction strength, with unprecedented solid-state Rabi splitting energies $\hbar\Omega_0$ of up to 1.80 eV, the first to reach energies comparable to those in the visible spectrum, accompanied by the highest-to-date organic microcavity coupling ratio, $\eta = 65\%$. We also demonstrate that the coupling strength is polarization-dependent with bright polariton PL for TE polarization parallel to the polymer chains and either no emission or weakly coupled emission from the corresponding TM polarization.
We finally examine the reflectivity and transmissivity of TE-polarized waves incident on microcavities containing excitons with in-plane uniaxially oriented transition dipole moments both theoretically and experimentally. We discuss the propagation of the electric field through the cavity and compare our results with previous reports. We confirm that in all cases, the reflected and transmitted electric fields derive from photons leaking parallel and perpendicular to the transition dipole moment orienta-

tion. We conclude our work by examining the opportunities that are enabled from our two experimental techniques for the future of polaritonics.

Publications

1. Conformational Control of Exciton-Polariton Physics in Metal-Poly(9,9-dioctylfluorene)-Metal Cavities - F. Le Roux, D. D. C. Bradley *Physical Review B*, **98**, 195306 (2018)

2. How β-Phase Content Moderates Chain Conjugation and Energy Transfer in Polyfluorene Films - H. Eggimann, F. Le Roux, L. M. Herz *Journal of Physical Chemistry Letters*, **10**, 8, 1729-1736 (2019)

3. Enhanced and Polarization-Dependent Coupling for Photoaligned Liquid Crystalline Conjugated Polymer Microcavities - F. Le Roux, R. A. Taylor, D. D. C. Bradley *ACS Photonics*, 7, 3, 746–758 (2020)

4. Transmissivity and Reflectivity of a TE-polarized Wave Incident on a Microcavity Containing Strongly Coupled Excitons with In-plane Uniaxially Oriented Transition Dipole Moments - F. Le Roux, R. A. Taylor, D. D. C. Bradley *Physica Status Solidi B*, doi: 10.1002/pssb.202000235 (2020)

Presentations

1. Strong Coupling of Exciton-Polaritons Mediated By Conformational Control of Poly(9-9,dioctylfluorene) in an All Metal Cavity - F. Le Roux, D. D. C. Bradley *Symposium on Recent Advances in Organic Electronics - Workshop, Hong Kong Baptist University* (2017)

2. Tuning Coincident Ultrastrong- and Strong-Coupling Interactions via Molecular Geometry Control in Polymer Microcavities - F. Le Roux, R. A. Taylor, D. D. C. Bradley *Nanophotonics and Micro/Nano Optics International Conference - Munich, Germany* (2019)

3. Tuning Coincident Ultrastrong- and Strong-Coupling Interactions via Molecular Geometry Control in Polymer Microcavities - F. Le Roux, R. A. Taylor, D. D. C. Bradley *Molecular Quantum Technology Workshop - Puerto Natales, Chile* (2019)

List of Symbols and Abbreviations

Abbreviations

LCCP	Liquid-Crystal Conjugated Polymer
BO	Born-Oppenheimer
LCAO	Linear Combination of Atomic Orbitals
HOMO	Highest Occupied Molecular Orbital
LUMO	Lowest Unoccupied Molecular Orbital
FRET	Förster resonant energy transfer
BEC	Bose Einstein Condensation
SC	Strong Coupling
LP	Lower Polariton
MP	Middle Polariton
UP	Upper Polariton
HA	Hopfield-Agranovich (model)
HTC	Holstein-Tavis-Cummings (model)
USC	Ultrastrong Coupling
PL	Photoluminescence
PDI	Polydispersity Index
PFO	Poly(9,9-dioctylfluorene)
F8BT	Poly(9,9-dioctylfluorene-co-benzothiadiazole)
F6T2	Poly(2,7-(9,9-dihexylfluorene)-co-bithiophene)
SD1	Sulfuric Dye 1
DBR	Distributed Bragg Reflector
COM	Coupled Oscillators Model
VASE	Variable Angle Spectroscopic Ellipsometry
LED	Light-Emitting Diode
FWHM	Full Width at Half Maximum
TMC	Transfer Matrix Calculations
MIM	Metal-Insulator-Metal
GS	Ground State
PI	Polyimide

TE	Transverse Electric
TM	Transverse Magnetic
R	Reflectivity
T	Transmissivity

Symbols

η	Normalized Coupling Ratio
E_g	Bandgap Energy
E_B	Exciton Binding Energy
$\hbar\Omega_0$	Rabi-Splitting Energy at Resonance
n_eff	Effective Refractive Index
Mw	Molecular Weight
Mp	Peak Molecular Weight
$\boldsymbol{\mu}$	Dipole Operator/Transition Dipole Moment
f	Oscillator Strength
ϵ	Dielectric Permittivity
ρ	Roundtrip Phase Change
κ	Cavity Mode Spectral Broadening
γ_cav	Cavity Mode Homogeneous Broadening
ω_cav	Cavity Mode Pulse Frequency
γ_ex	Exciton Homogeneous (Radiative) Broadening
ω_ex	Excitonic Transition Pulse Frequency
E_X	Exciton Energy
E_C	Cavity Mode Energy
ω_0	Resonance Pulse Frequency
Q	Q-Factor
Ta_2O_5	Tantalum Pentoxide
SiO_2	Silicon Dioxide
TiO_2	Titanium Dioxide
V_m	Mode Volume
$\tilde{n}$	Complex Refractive Index
n	Real Part of the Complex Refractive Index

k	Imaginary Part of the Complex Refractive Index
c	Speed of Light in Vacuum
$\mathbf{A}$	Magnetic Vector Potential
h	Planck Constant
$\hbar$	Reduced Planck Constant
N	Number of Participating Dipoles
θ	Polar Angle
ϕ	Azimuthal Angle
rpm	Revolutions Per Minute

Contents

Introduction **1**

1 Conjugated Semiconducting Polymers **4**

1.1 Introduction 5

1.2 The Origin of Semiconductivity in Conjugated Polymers 5

1.2.1 The Born-Oppenheimer Approximation 6

1.2.2 The Hartree-Fock Method 6

1.2.3 Linear Combination of Atomic Orbitals 7

1.3 The Concept of Bands in Organic Semiconductors 7

1.3.1 Filling The Orbitals 7

1.3.2 Hybridization of Carbon 8

1.3.3 Carbon Bonds 8

1.4 Excitation and Relaxation Processes in Conjugated Polymers 10

1.4.1 π-conjugation 10

1.4.2 Fundamental Excitations 11

1.4.3 The Role of Molecular Vibrations 13

1.4.4 Vibronic Transitions and Oscillator Strength 14

1.4.5 Excitation and Emission Processes 18

1.5 Structure/Photophysics Relationship 21

2 Exciton-Polaritons in Organic Microcavities **22**

2.1 Introduction 23

2.2 Planar Microcavities 23

2.2.1 Confining Photons in Planar Microcavities 23

2.2.2 Dielectric and Metallic Mirrors 24

2.3 Light-Matter Interaction from Linear Dispersion Theory 26

2.3.1 Weak and Strong Coupling Regimes 26

2.3.2 Time-Domain Perspective 30

2.4 Strong Light-Matter Interaction from a Quantum Perspective 31

2.4.1 Quantum Description of Polaritons as the Interaction of the Electromagnetic Field with a Polarization Field 31

2.4.2 Coupling of Excitons as a Quantized Set of Polarization Fields 32

2.4.3 Strong Light-Matter Coupling in the Rotating Wave Approximation 34

2.4.4 Ultrastrong Coupling, Beyond the Rotating Wave Approximation 36

2.4.5 Semi-classical Equivalent 39

2.4.6 Disorder and Inhomogeneous Broadening 41

2.4.7 Notes on the Normalized Coupling Ratio 42

2.5 Applicability of the Model to Microcavities Containing Conjugated Polymers 44

2.5.1 Organic Polariton Dynamics in the Linear Regime 44

2.5.2 The Importance of the Vibronic Structure, the Holstein-Tavis-Cummings Model 46

3 Sample Fabrication and Characterization **48**

3.1 Sample Fabrication 49

3.1.1 Materials 49

3.1.2 Thin Film Fabrication 50

3.1.3 The Glassy- and β-phase of PFO 50
3.1.4 Thermal Evaporation of Aluminium 51
3.1.5 Microcavity Fabrication 52
3.2 Optical Characterization: Experimental 53
3.2.1 UV-Visible Absorption 53
3.2.2 Variable Angle Spectroscopic Ellipsometry 54
3.2.3 Angle-Resolved Reflectivity and Photoluminescence 54
3.3 Optical Characterization: Simulation 57
3.3.1 Transfer Matrix Calculations 57
3.3.2 Fitting Model 57

4 Conformational Control for Strong Coupling 59

4.1 Introduction 60
4.2 PFO Thin Film Optical Properties 60
4.2.1 Absorption and Photoluminescence Spectra 60
4.2.2 Optical Constants 62
4.3 Exciton-Polariton Physics: Measurement and Simulation 65
4.3.1 Microcavity Fabrication 65
4.3.2 Angle-Resolved Reflectivity Spectra for Varying β-phase Fractions 65
4.3.3 Angle-Resolved Photoluminescence Emission 68
4.4 Theoretical Analysis 71
4.5 Discussion 77
4.5.1 Limitations of the Theoretical Model 77
4.5.2 Rabi Energies and their Dependence on the Oscillator Strengths of the X_{g} and X_{β} Populations 79
4.6 Conclusion 85

5 Enhanced and Polarization Dependent Coupling for Photoaligned Liquid Crystalline Conjugated Polymer Microcavities **87**

5.1 Introduction 88

5.2 LCCP Orientation 90

5.3 Thin Film Fabrication and Optical Properties 91

5.3.1 Oriented LCCP Thin Film Fabrication 91

5.3.2 Optical Properties of Oriented LCCP Thin Films 92

5.4 Microcavities Containing Oriented LCCP: Fabrication, Measurement and Analysis 97

5.4.1 Microcavity Fabrication 97

5.4.2 Angle-Resolved Reflectivity and Analysis 98

5.4.3 Angle-Resolved Photoluminescence 103

5.5 Conclusion 107

6 Transmissivity and Reflectivity of a TE-polarized Wave Incident on a Microcavity Containing Strongly Coupled Excitons with In-plane Uniaxially Oriented Transition Dipole Moments **108**

6.1 Introduction 109

6.2 TE-polarized Wave Propagation 110

6.3 Simulations 113

6.4 Experimental Comparison with a Microcavity Containing an Oriented LCCP 119

6.5 Conclusion 122

7 Summary And Outlook **123**

Appendices **126**

A Weak Coupling and the Purcell Effect **127**

B Supporting Information: Chapter 4 **129**

B.1 PFO Thin Film Optical Properties 130

B.1.1 Absorption and Photoluminescence Spectra 130

B.1.2 Optical Constants 131

B.2 Metal-PFO-Metal Exciton-Polariton Physics: Measurement and Simulation 132

B.2.1 Angle-resolved TE-polarized Reflectivity Maps 132

B.2.2 Angle-resolved TM-polarized Reflectivity Maps 133

B.2.3 Photoluminescence Spectral Characteristics 134

B.3 Photon-mode Dispersion 135

C Supporting Information: Chapter 5 **137**

C.1 Fabrication of Aligned PFO in its β-phase 138

C.2 Optical constants of non-aligned (NA) and aligned (A) LCCP films . 138

C.3 Angular variation of TE- and TM-polarized transmissivities at normal incidence for a thin film of aligned PFO 140

C.4 Experimental and Analytical Results for Non-aligned F8BT and PFO Microcavities 142

C.5 TMC Results 142

D Supporting Information: Chapter 6 **147**

D.1 TE-polarized Wave Propagation in an In-plane/Out-of-plane Anisotropic Medium 148

D.1.1 In-plane/Out-of-plane Anisotropy 149

D.1.2 Biaxial Anisotropy 150

D.2 Strong Coupling in a Microcavity Containing an In-plane/Out-of-plane Anisotropic Central Layer 151

D.3 Fitting of the Rabi-splitting Energies 153

D.4 Experimental Analysis 154

Bibliography **157**

List of Figures

1.1 Schematic representation of (a) the 2s, $2p_x$, $2p_y$ and $2p_z$ orbitals, (b) the sp^2 hybrid orbitals of carbon with the corresponding energy diagram (c), (d) the formation of π and σ bonds and the corresponding energy diagram (e) for the ethene (C_2H_4) molecule. Note that the energy difference is larger for the σ bond than for the π bond due to greater atomic orbitals overlap. 9

1.2 (a), (b) π-conjugation inside a benzene molecule thanks to alternating single and double carbon bonds which also enable semiconductivity inside conjugated polymers such as polyacetylene (c). (d) Formation of bands in conjugated polymers, where N is the number of participating carbon atoms. The conduction and valence bands, as well as the LUMO, HOMO and E_g are defined in the text. 11

1.3 Schematic representation of fundamental excitations inside semiconducting polymers. The different energy levels and processes are defined in the main text. An exciton is formed by Coulomb interaction between and electron and hole polarons. According to their spin states this leads to either a singlet or triplet exciton obeying specific photodynamics as illustrated on the right. 13

1.4 (a) Illustration of the Franck-Condon principle in absorption and emission between the ground electronic state S_0 and the first excited electronic state S_1 separated in nuclear coordinates by ΔQ. The maximum vibrational wavefunction overlap between the two electronic states in absorption (green arrow) and emission (red arrow) correspond to the strongest absorption and emission peaks in the corresponding vibronic structure (b). 19

1.5 Typical absorption (in green) and emission spectra (in red) observed for semiconducting polymers. The inhomogeneously broadened absorption is a result of the large degree of disorder. Conformational relaxation of the excited state followed by rapid migration of the excitations to lower energy sites before emission results in the well resolved vibronic progression in luminescence. 20

2.1 (a) Schematic representation of a planar microcavity containing a dielectric with constant refractive index n with two mirrors separated by a distance L. In red, green, and blue, the three first cavity modes characterized in reflectivity (b) by their energies $E_{\mathrm{cav}_{0,1,2}} = \hbar\omega_{\mathrm{cav}_{0,1,2}}$ defined in the text. 24

2.2 (a) Planar microcavity filled with a dielectric medium of permittivity $\epsilon(\omega)$ modelled using a Lorentzian susceptibility, resulting in the complex refractive index $\tilde{n} = n + ik$ shown in (b). (c) Roundtrip phase change ρ vs energy in the weak (orange solid line) and strong (red solid line) coupling regimes (dashed blue lines represent the empty cavity situation). In the SC regime, the two outermosts crossings for $\rho(E) \equiv 0\ (2\pi)$ correspond to the $E_{\mathrm{LP}_{\mathrm{res}}}$ and $E_{\mathrm{UP}_{\mathrm{res}}}$ while the crossing at $E = E_{\mathrm{ex}} = E_{\mathrm{cav}_0}$ is destroyed by absorption resulting in the LP and UP (solid red) in transmissivity (d) separated by $\hbar\Omega_0$. 30

2.3 Relaxation Pathways in strongly coupled organic microcavities under non-resonant (NR) excitation (represented by the purple band). The straight blue arrow shows relaxation inside the exciton reservoir, the green one represents vibronically assisted scattering in which a phonon is first emitted out of the exciton reservoir with the remaining excitation then populating the LP, the black lines show the different interactions between the UP and the reservoir with a thermal equilibrium in favour of the latter. The different vertical curved arrows represent radiative emission from the polaritons. All time scales are estimate and depend eventually on the characteristic of the system. 45

3.1 Chemical structure and molecular weights of the polymers: (a) PFO, (b) F6T2 and (c) F8BT. (d) Chemical structure of SD1 used as photoalignment layer. 49

3.2 The glassy- (a) and β-phase (b) conformations of PFO displayed together with their respective intermonomer torsion angle ϕ_{tor}. 51

3.3 Microcavity fabrication process: (1) The Al pellets contained in the tungsten boat are heated up to sublimation through resistive heating, the QCM located above the metal source allowing for evaporation rate and target thickness control for the deposited layers; (2) The samples are taken out of the chamber and the organic layers are spincoated; (3) The samples are brought back into the evaporation chamber where the top mirror is evaporated. 53

3.4 (a) Schematic representation of the optical setup built to measure angle-resolved reflectivity (specific parts in red) and PL (specific parts in blue) for different polar (θ) and azimuthal (ϕ) angles. The numbers in (a) match the real components shown in the picture (b) of the actual setup. 55

4.1 Absorption and PL spectra for spin-coated PFO films containing: (a) 0 (glassy-phase), (b) 3.7, (c) 12.3, and (d) 15.8% β-phase chain segments. Note the emergence of a shoulder (b) and then a resolved peak ((c) and (d)) on the red edge of the absorption with increasing β-phase fraction. A schematic glassy-phase chain segment (one conformer of many) is shown in panel (a) and the β-phase chain extended structure in panel (d). 63

4.2 Optical constants for spin-coated PFO thin films containing: (a) 0 % (glassy-phase), (b) 3.7, (c) 12.3, and (d) 15.8% β-phase chain segments. The black and blue lines are, respectively, the real (n) and imaginary (k) parts of the complex refractive index, $\tilde{n} = n + ik$. Solid lines give in-plane (n_{xy}, k_{xy}) and dashed lines out-of-plane (n_z, k_z) values. . . . 64

4.3 Experimental, angle-resolved, TE-polarized reflectivity maps for microcavities containing (a) 0, (b) 3.7, (c) 12.3, and (d) 15.8% β-phase chain segments. The inset to each panel shows the spectral dispersion of the polariton branches between 2.80 and 2.98 eV for incidence angles (bottom to top) 45, 60 and 75°. Note the splitting of the LP into two separate branches (LP and MP) for $\geqslant$ 3.7% β-phase fraction (panels (b), (c) and (d)), spaced either side of the X_β (0-0) vibronic peak at 2.87 eV (3.7%) and 2.86 eV (12.3%, 15.8%) (orange dashed vertical line). The corresponding normalized, in-plane, bare-film, colour-rendered extinction coefficient spectra taken from Figure. 4.2 are shown to the right of each map. Also shown, as overlaid white dashed lines, are the reflectivity minima dispersion curves obtained from TMC. . . 67

4.4 Angle-resolved PL spectral intensity maps for microcavities containing 0% ((a) and (c)) and 12.3% ((b) and (d)) β-phase chain segments, with TE ((a) and (b)) and TM ((c) and (d)) polarized spectra plotted separately. The colour-rendered spectra to the left of (a) and (c) and right of (b) and (d) present the PL emission obtained for the corresponding bare films (Figure 4.1 (a) and (c)). The overlaid blue dashed line is the LP angular dispersion obtained from TMC. 69

4.5 Experimental and calculated exciton, cavity, and polariton angular dispersions for the 0% ((a) and (c)) and 12.3% ((b) and (d)) cavities for both TE- ((a) and (b)) and TM-polarization ((c) and (d)). The background to each panel comprises the associated R-map obtained from TMC, on top of which are overlaid exciton oscillator energies (horizontal white dashed lines), experimental (black squares) polariton branch, and calculated coupling-free cavity photon mode (green dashed line) dispersions. The black squares data are LP PL maxima (Figure 4.4) for incidence angles between 15 and 45° and R-minima (Figure 4.3) between 45 and 75°, with $M_{\mathbf{q}}$ polariton eigenvalue fits shown by red dashed lines. The normalized in-plane extinction coefficients (Figure 4.2) for bare films with corresponding β-phase fractions are shown to the right of each panel. 74

4.6 TE-polarized Hopfield coefficients for 0% and 12.3% microcavities, obtained using the model presented in Section 4.4. Results are shown for: (a) LP, (b) MP, (c) UP, and (d) GS. Note the efficient mixing of excitons from populations 1 (solid light blue line) and 2 (solid green line) within the LP (a) and MP (b) of the 12.3% microcavity. 77

4.7 (a) Rabi splitting energy ($\hbar\Omega_{02_{\mathrm{TE}}}$, filled blue squares data) as a function of β-phase fraction. The solid blue line is the square-root fit ($\hbar\Omega_{02_{\mathrm{TE}}}$ =(43.4±0.9) $\sqrt{\%_\beta}$ meV) described in the text. (b) In-plane extinction coefficient, k_{X_β}(E), for the β-phase component of a 15.8 % film, extracted from Figure 4.2(d) following the procedure described in Section 4.5.2. The oscillator strength associated with the light-blue highlighted part of the de-convolved (0-0) vibronic transition (dashed blue line) is sufficient to explain the observed Rabi-splitting ($\hbar\Omega_{02_{\mathrm{TE}}}$) between LP and MP. The remainder of the (0-0) together with the (0-1) and (0-2) vibronic transitions can then contribute to the Rabi-splitting ($\hbar\Omega_{01_{\mathrm{TE}}}$) between MP and UP, compensating for the interchange in exciton populations between X_{g} and X_β. 83

5.1 (a) Optical components n_x n_y, n_z, k_x, k_y, k_z for a thin film of SD1 aligned along the y direction. (b),(c),(d) In green: In-plane n_{ord}, k_{ord} optical components for spincoated F8BT (b), PFO (c) and F6T2 (d). The in-plane optical components of the films following alignment are shown in blue for n_y, k_y (parallel to the alignment direction) and in red for n_x, k_x (perpendicular to the alignment direction) for SD1 (a), F8BT (b), PFO (c) and F6T2 (d). Dashed lines give the real component of the complex refractive index $\tilde{n} = n + ik$, solid lines the imaginary component. 94

5.2 PL spectra for non-aligned ((a), (c) and (e)) and aligned ((b), (d) and (f)) F8BT ((a) and (b)), PFO ((c) and (d)) and F6T2 ((e) and (f)) thin films. For a given polymer in a given alignment state, the parallel and perpendicular spectra were plotted on the same scaled intensity axis range to allow for their comparisons. Solid blue lines show the PL collected using a polarizer in the vertical direction and red lines in the horizontal direction. In panels (b), (d) and (f): $/\!/$ and $\perp$ indicate that the collection polarizer direction respectively matches or is perpendicular to the orientation direction of the polymer chains in the film. A fast Fourier transform algorithm was used for F6T2 ((e) and (f)) to reduce noise in the recorded signal. 96

5.3 Experimental, angle-resolved, TE-polarized reflectivity maps for microcavities containing: (a) non-aligned F6T2, (b) aligned PFO, (c) aligned F6T2 and (d) aligned F8BT. For (b), (c) and (d), the measurements were performed at $\Phi = 0°$ (see text and schematic experimental geometry shown above the maps). The overlaid solid white lines show the exciton E_{X} and cavity mode E_{C} dispersions and the black dashed lines the polariton branch dispersions derived from the analytical model. Note the Fano-like asymmetry around the LP for (a), (b) and (c) similar to that observed in a previous report and the reduced LP linewidth relative to the UP as a consequence of motional narrowing. 100

5.4 Experimental, angle-resolved, TM-polarized reflectivity maps for microcavities containing (a) non-aligned F6T2, (b) aligned PFO, (c) aligned F6T2 and (d) aligned F8BT. For (b), (c) and (d), the measurements were performed at $\Phi = 0°$ (see text for definition) and the overlaid solid white lines show the respective exciton energies, E_X. In (a) in addition to E_X, the second white line presents the cavity mode dispersion, E_C. The black dashed lines show the polariton branch dispersions derived from the analytical model. 101

5.5 Angle-resolved PL spectral intensity maps for microcavities containing non-aligned F8BT ((a) and (b)), PFO ((c) and (d)) and F6T2 ((e) and (f)), with TE ((a), (c), (e)) and TM ((b), (d), (f)) polarized spectra plotted separately. Overlaid dashed blue lines correspond to the lower polariton modes fitted previously using the analytical model. The excitation energy, Exc, is given for each measurement. Each polarization pair ((a) and (b)), ((c) and (d)), ((e) and (f)) was plotted on the same scaled intensity axis range. 105

5.6 Angle-resolved PL spectral intensity maps for microcavities containing aligned F8BT ((a) and (b)), PFO ((c) and (d)) and F6T2 ((e) and (f)), with TE ((a), (c), (e)) and TM ((b), (d), (f)) polarized spectra plotted separately. Overlaid dashed blue lines correspond to the lower polariton modes fitted previously using the analytical model. The measurements were performed at $\Phi = 0°$ (see text for definition) . Each polarization pair ((a) and (b)), ((c) and (d)), ((e) and (f)) was plotted on the same scaled intensity axis range. 106

6.1 Geometry and angles used in this chapter, θ is the polar angle formed between $\mathbf{k}$ and the z-axis, for a TE-polarized wave ϕ is the azimuthal angle formed between E and the y-axis, and $\mathbf{k}_{/\!/}$ is the in-plane component of the wavevector $\mathbf{k}$. In (a) $\phi \neq 0°$, in (b) $\phi = 0°$: E is parallel to the transition dipole moment $\boldsymbol{\mu}$ of the excitons and the wave propagates experiencing ϵ_y, a similar situation arises for $\phi = 90°$, where E becomes parallel to the x-axis and the wave experiences ϵ_x. 110

6.2 (a) In red and blue respectively (n_y, k_y) and (n_x, k_x) optical components for a simulated material M1 with susceptibility $\chi(\omega)$ using the physical parameters in the inset. Dashed lines give the real component of the complex refractive index $\tilde{n} = n + \mathrm{i}k$, solid lines the imaginary component. (b) Simulated TE-transmissivity at $\theta = 0°$ for $\phi = 0°, 18°, 36°, 54°, 72°, 90°$ of the microcavity displayed in the inset of (c), the black curves represents the total transmissivity which is a superposition of the transmissivities originating from the y direction (in dashed red) and x direction (in dashed blue). Peaks 1 and 2 (in dashed red) are the result of strong light matter coupling in the y direction, peak 3 is the photonic mode (in dashed blue) resulting from the uncoupled x direction. Note the increasing amplitude of peak 3 and decreasing amplitude of peaks 1 and 2 as ϕ is increased. (c) Dispersions of the TE-transmissivity maxima for ϕ varying by steps of 1°: the black crosses indicate the positions of the maxima for the two peaks in the main signal up until $\phi = 73°$, angle from which the two maxima are no longer resolved and replaced by a single maximum, in red the angle-independent positions of the two peaks induced by SC along the y-axis, in blue the angle-independent position of the photonic mode along the x-axis. Note that the maxima from the overall signal converge towards the photonic mode energy with increasing ϕ. 115

6.3 (a) In red and blue respectively (n_y, k_y) and (n_x, k_x) optical components for a simulated material M2 with susceptibility $\chi(\omega)$ using the physical parameters in the inset. Dashed lines give the real component of the complex refractive index $\tilde{n} = n + \mathrm{i}k$, solid lines the imaginary component. (b) Simulated TE-transmissivity at $\theta = 0°$ for $\phi = 0°, 18°, 36°, 54°, 72°, 90°$ of the microcavity displayed in the inset of (c), the black curves represents the total transmissivity which is a superposition of the transmissivities originating from the y direction (in dashed red) and x direction (in dashed blue). Peaks 1 and 2 (in dashed red) are the result of USC in the y direction, peak 3 is the photonic mode (in dashed blue) resulting from the uncoupled x direction. Note the increasing amplitude of peak 3 and decreasing amplitude of peaks 1 and 2 as ϕ is increased. (c) Dispersions of the TE-transmissivity maxima for ϕ varying by steps of 1°: the black crosses indicate the angle-independent positions of the maxima for the well resolved three peaks in the main signal up until $\phi = 70°$, angle from which the two maxima from the y direction are no longer visible, in red the angle-independent positions of the two peaks induced by SC along the y-axis, in blue the angle-independent position of the photonic mode along the x-axis. Note that the positions of the maxima in the main signal matches the positions of peak 1, 2 and 3. 117

6.4 Simulated TE-reflectivity at $\theta = 30°$ for $\phi = 0°, 18°, 36°, 54°, 72°, 90°$ of the microcavities displayed in the inset of Figure 6.2 (c) for (a) and Figure 6.3 (c) for (b) with a 99.5 nm material layer thickness. In both cases the simulated values at $\phi = 0°$ (in solid red) correspond to the reflectivity contributions from the LP and UP in the y direction, the simulated values at $\phi = 90°$ (in solid blue) correspond to the reflectivity contribution from the photonic mode in the x direction. For other values of ϕ, two main minima are visible in (a) and get closer in energy with increasing values of ϕ as the relative reflectivity contribution along the y-axis decreases and the one along the x-axis increases until only one peak corresponding to the photonic mode along the x-axis is visible. In (b) three main minima are visible but do not shift in energy with increasing values of ϕ as the relative reflectivity contribution along y decreases and the one along x increases. 118

6.5 (a) Schematic of the microcavity structure fabricated. The PFO chains were oriented (A) using the protocol presented in Chapter 5. The TE-reflectivity is measured at $\theta = 46°$. (b) Bottom view of the orientation of the PFO chains along the y-axis, the measurement is performed by rotating the sample relative to the electric field E (in green), forming the azimuthal angle ϕ. (c) Simulated TE-transmissivity at $\theta = 46°$ for $\phi = 0°, 18°, 36°, 54°, 72°, 90°$, the black curves represent the total transmissivity which is a superposition of the transmissivities originating from the y direction (in dashed red) and x direction (in dashed blue). Peaks 1, 2 and 3 (in dashed red) are the result of USC along y for the lowest lying energy cavity mode (1 and 3) and the second lowest lying energy cavity mode (2). Peak 4 and 5 are the result of a splitting of the photonic mode in the x direction due to remaining optical activity. Further explanations can be found in text. (d) Measured TE-reflectivity at $\theta = 46°$ for $\phi = 0°, 18°, 36°, 54°, 72°, 90°$, the numbered minima correspond to the ones simulated in transmissivity. (e) Simulated TE-Reflectivity at $\theta = 46°$ for $\phi = 0°, 18°, 36°, 54°, 72°, 90°$ confirming the experimental observations. 121

B.1 Absorption and PL spectra for spin-coated PFO films containing: (a) 1.1, (b) 1.5, (c) 10, and (d) 13.9% β-phase chain segments. 130

B.2 Optical constants for spin-coated PFO thin films containing: (a) 1.1, (b) 1.5, (c) 10, and (d) 13.9% β-phase chain segments. The black and blue lines are, respectively, the real (n) and imaginary (k) parts of the complex refractive index, $\tilde{n} = n + ik$. Solid lines give in-plane (n_{xy}, k_{xy}) and dashed lines out-of-plane (n_z, k_z) values. 131

B.3 Experimental, angle-resolved, TE-polarized reflectivity maps for microcavities containing (a) 1.1, (b) 1.5, (c) 10, and (d) 13.9% β-phase chain segments. The overlaid, white dashed lines are the reflectivity minima dispersion curves obtained from TMC. 132

B.4 Experimental, angle-resolved, TM-polarized reflectivity maps for microcavities containing (a) 0, (b) 1.1, (c) 1.5, (d) 3.7, (e) 10.0, (f) 12.3, (g) 13.9 and (h) 15.8% β-phase chain segments. The overlaid, white dashed lines are the reflectivity minima dispersion curves obtained from TMC. 133

B.5 Thin film PL spectra for (a) 0% and (d) 12.3% film samples, and TE-polarized lower polariton PL spectra for (b) and (c) 0% and (e) and (f) 12.3% cavities. The LP emission from cavities is shown for both 10° ((b) and (e)) and 60° ((c) and (f)) to illustrate the spectral dispersion as a function of angle, which is weak for the 0% cavity and absent for the 12.3% cavity. To the right of each spectrum is a CIE (x,y) plot with the corresponding coordinates marked by a cross. The numerical values are also reported together with the dominant wavelength (nm) and saturation (%). 134

B.6 Exact and approximated TE-polarized cavity mode fittings for the 0% microcavity. The fitted thickness obtained using the exact cavity mode (Equation B.1) is 84.5 ± 1 nm in good agreement with $\hbar\omega_{\mathrm{cav}}(0) = 3.32$ eV (corresponding to a thickness of 84 nm for $n_{\mathrm{eff}_{\mathrm{TE}}} = 1.7$ using TMC) for the approximated cavity mode. The fitted background permittivity is found to be $\epsilon_{\mathrm{d}} = 2.89$ using both exact and approximated cavity modes. The small differences between the two methods at higher angles (towards 70° for the UP and cavity modes is at most 0.02 eV and therefore not enough to explain the deviations (∼0.1 eV) between our experimental and analytical results. 136

C.1 In green and grey respectively in-plane (n_{ord}, k_{ord}) and out-of-plane (n_{ex}, k_{ex}) optical components for non-aligned PFO (a), F8BT (c), F6T2 (e) thin films. In blue, red and grey respectively in-plane in the aligned polymer chains direction (n_y, k_y), in-plane in the direction perpendicular to the chains (n_x, k_x) and out-of plane (n_z, k_z) optical components for aligned PFO (b), F6T2 (c), F8BT (d). Dashed lines give the real component of the complex refractive index $\tilde{n} = n + ik$, solid lines the imaginary component. 139

C.2 In-plane optical components of a PFO film following alignment and exposition to toluene vapour for 24 hours are shown in blue for n_y, k_y (parallel to the alignment direction) and in red for n_x, k_x (perpendicular to the alignment direction). Dashed lines give the real component of the complex refractive index $\tilde{n} = n + ik$, solid lines the imaginary component. Note the pronounced peak in absorption at ∼2.87 eV once the β-phase has been formed in the alignment direction. 140

C.3 R_T vs sample angle as defined in text. Two minimas are clearly observed at 0° and 90° while a maximum is observed at 45°. These three specific geometries correspond to the represented experiment schematics. 141

C.4 Experimental, angle-resolved, TE-polarized reflectivity maps for microcavities containing non-aligned F8BT (a,c) and PFO (b,d) for the TE (a,b) and TM (c,d) polarizations. Overlaid are the fitting curves obtained using the analytical model presented in Methods, the fitting values are shown in Table 1. Overlaid solid white lines are the Excitons E_{X_j} and cavity E_C modes, black dashed lines are the polaritons obtained from fitting using the analytical model. 142

C.5 On the left, Experimental, angle-resolved, TE-(a,e) and TM-(c,g) polarized reflectivity maps for microcavities containing non-aligned (a,c) and aligned (e,g) F8BT. On the right, TMC results showing angle-resolved, TE-(b,f) and TM-(d,h) polarized reflectivity maps for microcavities containing non-aligned (b,c) and aligned (e,g) F8BT. For the aligned cavities, the measurements and calculations were performed for $\Phi = 0°$. The thicknesses displayed in white correspond to the SD1 and polymer layer thicknesses used in the TMC. 144

C.6 On the left, Experimental, angle-resolved, TE-(a,e) and TM-(c,g) polarized reflectivity maps for microcavities containing non-aligned (a,c) and aligned (e,g) PFO. On the right, TMC results showing angle-resolved, TE-(b,f) and TM-(d,h) polarized reflectivity maps for microcavities containing non-aligned (b,c) and aligned (e,g) PFO. For the aligned cavities, the measurements and calculations were performed for $\Phi = 0°$. The thicknesses displayed in white correspond to the SD1 and polymer layer thicknesses used in the TMC. 145

C.7 On the left, Experimental, angle-resolved, TE-(a,e) and TM-(c,g) polarized reflectivity maps for microcavities containing non-aligned (a,c) and aligned (e,g) F6T2. On the right, TMC results showing angle-resolved, TE-(b,f) and TM-(d,h) polarized reflectivity maps for microcavities containing non-aligned (b,c) and aligned (e,g) F6T2. For the aligned cavities, the measurements and calculations were performed for $\Phi = 0°$. The thicknesses displayed in white correspond to the SD1 and polymer layer thicknesses used in the TMC. 146

D.1 Simulated, angle-resolved, TE-polarized reflectivity map for a microcavity containing the material M1 as described in the main text. Overlaid are the fitting curves obtained using the HA model. Overlaid solid white lines are the Excitons E_X and cavity E_C modes, black dashed lines are the polaritons (LP/UP) obtained from fitting using the analytical model. 154

D.2 Simulated, angle-resolved, TE-polarized reflectivity map for a microcavity containing the material M2 as described in the main text. Overlaid are the fitting curves obtained using the HA model. Overlaid solid white lines are the Excitons E_X and cavity E_C modes, black dashed lines are the polaritons (LP/UP) obtained from fitting using the analytical model. 155

D.3 Experimental, angle-resolved, TE-polarized reflectivity map for a microcavity containing aligned PFO as described in the main text. Overlaid are the fitting curves obtained using the HA model. Overlaid solid white lines are the Excitons E_X and cavity E_C modes, black dashed lines are the polaritons (LP/UP) obtained from fitting using the analytical model. 155

D.4 Simulated, angle-resolved, TE-polarized reflectivity map for a microcavity containing aligned PFO as described in the main text. Overlaid are the fitting curves obtained using the HA model. Overlaid solid white lines are the Excitons E_X and cavity E_C modes, black dashed lines are the polaritons (LP/UP) obtained from fitting using the analytical model. 156

List of Tables

4.1 Extracted and pre-set parameter values for microcavities containing various β-phase fractions, as modelled in the text. The values are shown for both TE- and TM-polarization. 75

5.1 Extracted and pre-set parameter values for microcavities containing non-aligned and aligned polymers, modelled using the HA Hamiltonian. Values are shown for both TE- and TM-polarization, at $\Phi = 0°$ (see definition in the text) for the aligned cavities. The initials A and NA respectively designate aligned and non-aligned polymer layers. . . 102

5.2 Peak positions and FWHM values at normal incidence ($\theta = 0°$) for the TE- and TM-polarized emissions displayed in Figures 5.5 and 5.6. The angular dispersion of the emission for both polarizations from $\theta = 0$ to 60° is also reported. The initials A and NA respectively designate aligned and non-aligned polymer layers. 107

Introduction

The strong coupling (SC) regime in semiconductor microcavities,[1] in which exciton and cavity photon states mix to yield new light-matter excitations (termed microcavity polaritons) has grown into a rich field of research with significant application potential.[2] Among semiconductor excitons, it has been shown that the Frenkel excitons of organic semiconductors have oscillator strengths sufficient to readily support giant Rabi splittings, $\hbar\Omega_0$, of many tens to hundreds of meV[3–10] and large enough binding energies ($E_{\mathrm{B}} \sim 0.5 \pm 0.25$ eV[11,12]) that SC can be observed at room temperature.[2–10]

Based on earlier experiments with inorganic III-V semiconductors there had been skepticism that organic semiconductor exciton linewidths would allow the observation of strong coupling and for a considerable time following the first demonstration[3] by Lidzey *et al.* (for porphyrin Soret-band states) the working hypothesis remained that narrow (for organic semiconductors) linewidths would be a necessary pre-requisite. As a consequence, all of the organic systems then studied were selected on that basis, including J-aggregated cyanine dyes, sigma-conjugated polysilanes, porphyrins and napthalene-tetracarboxylic-dianhydride.[4–10] Subsequent studies[13–16] on anthracene, ladder poly(p-phenylene)s and phenyl-substituted fluorene trimers showed, instead, that in the presence of such large Rabi splitting the existence of a vibronic progression and significant inhomogeneous broadening was not, in fact, problematic. Indeed, it was in these latter systems that room temperature polariton logic,[17] lasing,[14] non-equilibrium Bose-Einstein condensation (BEC)[15,16] were first observed and for which the study of condensate physics (e.g. superfluidity of light[18,19] and dynamical instability[20]) has been undertaken. This has opened up a much wider selection of materials for use in strongly-coupled microcavities, many of which have desirable electrical properties, suited to device application.

The specific use of two metal mirrors, that reduce the microcavity mode volume[21] and

provide broader stop bands than for two alternating dielectric layer distributed Bragg reflectors[1,13–15] (DBR)s or a combination of one dielectric and one metal mirror[3–10] has additionally led to the observation of Rabi-splitting energies, $\hbar\Omega_0$, in excess of 1 eV with operation then occurring in the USC regime.[22–24] USC physics, for which $\hbar\Omega_0$ exceeds a significant fraction ($\geq\sim 20\%$) of the coupled exciton transition energy, yields a number of important differences in spectral features compared to the more commonly observed SC regime[23,25–28] and has recently emerged as an interesting path towards novel light-emitting devices[22,24,29–31] and counter intuitive quantum applications, for example the emission of bunched-light from a single quantum emitter.[32] This interaction space has received great recent attention[33,34] with experimental realizations of increasingly higher coupling ratios reported for inorganic semiconductor based on intersubband polaritons,[35] and other physical systems, including superconducting circuits,[36] Landau polaritons[37] and plasmonic picocavities interacting with vibrational degrees of freedom of individual molecules.[38]

In organic microcavities, tuning the nature of the SC in order to explore the associated physics has, however, remained challenging. Reducing the interaction strength has been achieved by (i) varying the intra-cavity film thickness, (ii) varying the exciton oscillator strength via dispersion at different concentrations in an inert matrix,[3–5] (iii) varying the photon-exciton spatial overlap through normal-to-plane spacer layers,[5–7] and (iv) incorporating more than one chemical species[5,39] with more recent approaches including (v) spiropyran-to-merocyanine photoswitching,[40] (vi) adjusting the mirror-to-mirror distance in an open microcavity[41,42] and (vii) reducing dimensionality via the creation of mirror micro-defects.[42] Increasing the interaction strength has proven more difficult as direct increase of the number of coupled chromophores can be difficult. The use of metallic mirrors was a first step towards higher coupling strengths and in-plane anisotropy observed along the principal axes of organic crystals[13] or along oriented J-aggregates[43] was a milestone that enabled recent demon-

strations of even more intense interactions using transition dipole moment alignment in nanotubes (carbon[44] and tungsten disulfide[45]) and vibrational strong coupling of oriented liquid crystals (LC)s.[46]

In this thesis, we first review the fundamentals of semiconductivity in conjugated polymers in Chapter 1 and the main features of organic exciton-polaritons in Chapter 2. In Chapter 3 we introduce the experimental and simulation techniques which we use in the following chapters to enhance, tune and polarize light-matter interaction. In Chapter 4, acting on the intra-chain properties of a semiconducting polymer, we mediate light-matter coupling between two exciton populations which among other possibilities enable us to fabricate microcavities exhibiting narrow and dispersionless light-emission profiles. In Chapter 5, we orient LCCPs inside microcavities using a novel photoalignment technique, which through transition dipole moment orientation results in a systematic enhancement of $\hbar\Omega_0$ to previously unreached values and demonstrate polarization sensitive interaction. In Chapter 6, we examine the applicability of routine measurements (angle-resolved transmissivity and reflectivity) commonly performed in SC studies to microcavities containing excitons with uniaxially oriented transition dipole moments. We demonstate the existence of two specific measurement cases, explore the first one in light of a previous report[44] and the second one by performing our own measurement on a microcavity containing an oriented LCCP. We conclude in Chapter 7 by discussing the possibilities offered by our experimental techniques for new research alleys into exciton-polariton physics.

Chapter 1

Conjugated Semiconducting Polymers

1.1 Introduction

In this chapter, we examine the origin of semiconductivity in organic semiconductors, a group composed of small molecules as well as conjugated polymers. We first present the methods that allow us to derive a quatitatively satisfying electronic structure and describe π-conjugation along the backbone of conjugated polymers, which enables their semiconductivity. We also cover the photophysics essential to the understanding of the subsequent chapters with particular attention given to the different excitation and relaxation processes.

1.2 The Origin of Semiconductivity in Conjugated Polymers

Quantum chemistry offers a description of the structure as well as the quantum states of electrons and nuclei inside organic semiconductors.[47] This information is fully contained in the wavefunction Ψ which is solution of the Schrödinger equation:

$$\hat{H}\Psi(\mathbf{R},\mathbf{r}) = E\Psi(\mathbf{R},\mathbf{r}), \tag{1.1}$$

where $\hat{H}$ is given by:

$$\hat{H} = \hat{T}_{\mathrm{n}} + \hat{T}_{\mathrm{e}} + \hat{V}_{\mathrm{nn}} + \hat{V}_{\mathrm{ne}} + \hat{V}_{\mathrm{ee}}, \tag{1.2}$$

where $\hat{T}_{\mathrm{n,e}}$ are the kinetic energy operators respectively for the nuclei and electrons and $\hat{V}$ includes the different Coulombic interations between nucleus-nucleus (n-n), nucleus-electron (n-e) and electron electron (e-e). This equation quickly becomes impossible to solve analytically as soon as few electrons are involved[47] and the methods detailed in the subsequent sections are commonly used to derive qualitatively satisfying solutions.

1.2.1 The Born-Oppenheimer Approximation

The Born-Oppenheimer (BO) approximation[48] first recognized that the electrons, much lighter than their nuclei counterparts, react almost instantaneously to changes in nuclear configurations with the wavefunction being consequently separable into:

$$\Psi = \Psi_{\mathrm{e}}\Psi_{\mathrm{n}}. \tag{1.3}$$

Equation 1.1 can then be solved separately for the nuclei and electrons. For Ψ_e, Equation 1.1 is solved in a fixed nuclear framework where the nuclear coordinates become parameters and $\hat{V}_{\mathrm{nn}}$ is a constant. Ψ_{n} is then obtained by using the dependence of the electronic energy on the nuclear coordinates, with the final solution found by minimizing the global energy of the system.[47]

1.2.2 The Hartree-Fock Method

With the problem reduced to finding the electronic wave functions in a fixed nuclear framework Hartree first came up[49] with a solution which neglected the interactions between electrons and allowed him to develop a self-consistent field method to determine single-electron wave functions, called orbitals, and their corresponding energies. Since electrons are Fermions they must obey the Pauli exclusion principle and the total wavefunction (including the spin) must be anti-symmetric under exchange.[50] Hartree did not fulfill this condition and an accurate reformulation of the problem came in the following years[51,52] using a single Slater determinant on which the use of the variational principle allows for derivation of the atomic χ_i and molecular orbitals u_j.[47]

1.2.3 Linear Combination of Atomic Orbitals

For molecular systems, an efficient method to solve the the Hartree-Fock equation[47] is to use the linear combination of atomic orbitals (LCAO) to form the molecular orbitals u_j. The atomic orbitals χ_i used for the basis set can be those of the analytically derived hydrogen-like atoms or atomic orbitals pseudopotentials with resulting molecular orbitals only as faithful as the basis choice is relevant.

The combination itself relies on the assumption that the number of molecular orbitals formed is equal to the number of atomic orbitals included in the linear expansion which leads to the following expression for the j^{th} molecular orbital:

$$u_j = \sum_{i=1}^{n} c_{i,j}\chi_i, \tag{1.4}$$

where $c_{i,j}$ is the contribution of the i^{th} atomic orbital χ_i to the molecular orbital u_j.

1.3 The Concept of Bands in Organic Semiconductors

1.3.1 Filling The Orbitals

Once the orbitals have been determined, one fills them with the available electrons according to a set of rules. The lowest energy orbitals fill first with the filling pattern following 1s, 2s, 2p, 3s, 3p, 4s, 3d, etc... Since orbitals within a subshell are degenerate the entire subshell of a particular orbital type is filled before moving to the next subshell. In order to fill a subshell, the Pauli exclusion principle must be respected: only two electrons are permitted per orbital and they must have opposite spin: such two electrons with opposite spins in the same orbital are referred to as being paired. Finally, Hund's Rule[53] states that the most stable arrangement of

electrons in a subshell occurs when the maximum number of unpaired electrons exist: since electrons are repulsive to one another they only pair after all of the orbitals have been singly filled. Once the electronic structure has been addressed and the orbitals have been filled, the Highest Occupied Molecular Orbital (HOMO) and Lowest Unoccupied Molecular Orbital (LUMO) are determined.

1.3.2 Hybridization of Carbon

Carbon is prevalent in all organic semiconductors and the procedure presented up to now allows to derive its basic electronic structure: $(1s)^2(2s)^2(2p)^2$. Since the Hartree-Fock method neglects electron-electron interactions it is in reality possible for the orbitals to further combine with one another giving rise to hybrid orbitals. In carbon, this hybridization process is made possible since the energy difference between the (2p) and (2s) orbitals is small enough for the electrons from the (2s) shell to be promoted into the (2p) shell and will depend on the bonds that the atom form with its neighbours. One set of hybrids of particular interest is composed of the three sp^2 orbitals which consist of a combination of one s-orbital, one p_x and one p_y orbital. This result in a planar configuration with 120° angle between the three newly-created sp^2 orbitals, shown in Figure 1.1 (b), with the p_z orbital laying orthogonal to the plane formed by the sp^2 orbitals. These hybrids play a key role in semiconductivity as we will see in the following sections.

1.3.3 Carbon Bonds

A covalent bond between two atoms is formed when some of each atom's respective electrons are shared resulting in a stabilization of the molecular energy. For two carbons, the overlap of two sp^2 orbitals along the inter-atom axis creates a σ bond. The two neighbouring p_z orbitals also interact and form a π bond localized above and below the σ bond (the two bonds of interest are represented in Figure 1.1 (d)).

As stated in the LCAO method, the linear combination of two sp^2 orbitals or two p_z orbitals leads to the creation of an equal number of molecular orbitals. This results in the creation of two bonding (σ,π) and two antibonding (σ^* and π^*) orbitals as represented in Figure 1.1 (e).

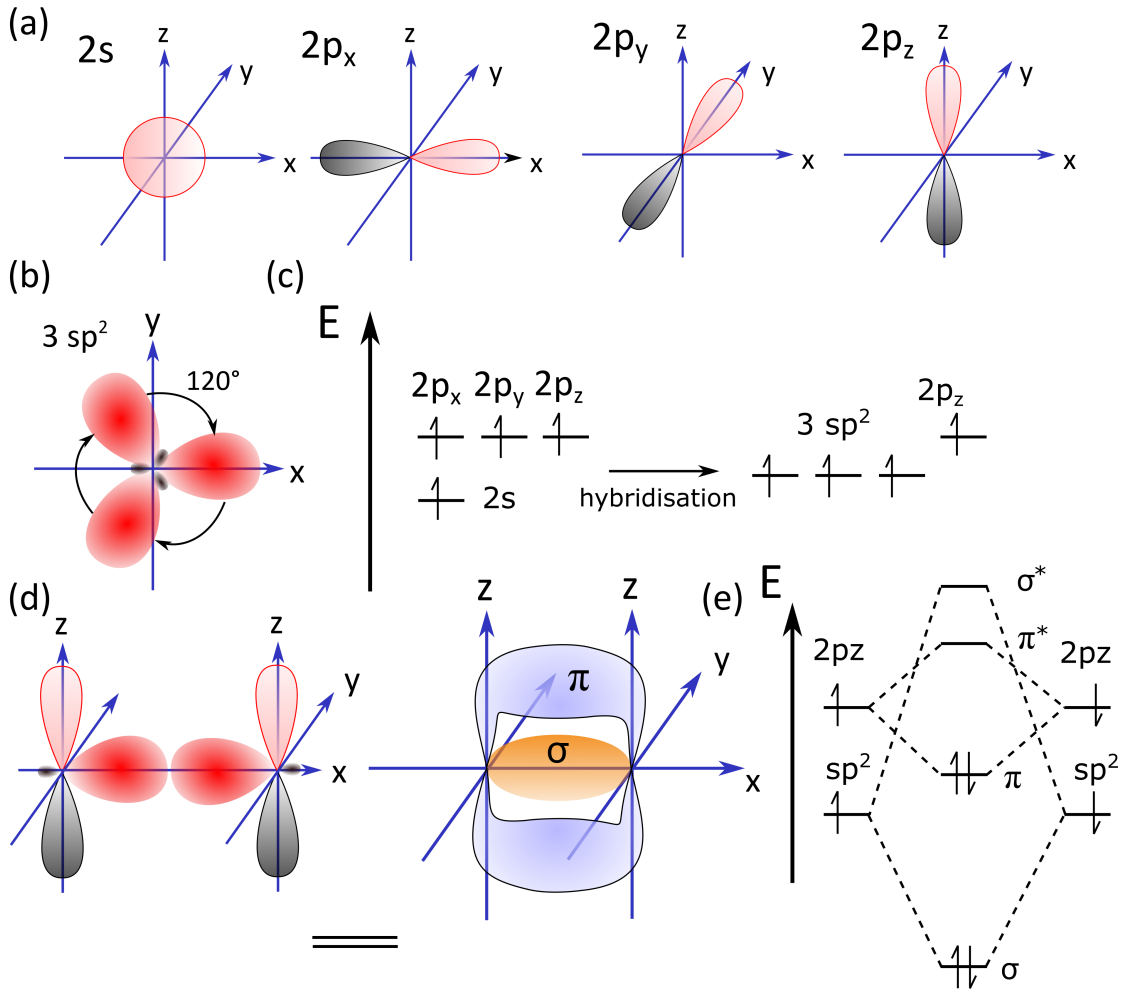


Figure 1.1: Schematic representation of (a) the 2s, $2p_x$, $2p_y$ and $2p_z$ orbitals, (b) the sp^2 hybrid orbitals of carbon with the corresponding energy diagram (c), (d) the formation of π and σ bonds and the corresponding energy diagram (e) for the ethene (C_2H_4) molecule. Note that the energy difference is larger for the σ bond than for the π bond due to greater atomic orbitals overlap.

1.4 Excitation and Relaxation Processes in Conjugated Polymers

1.4.1 π-conjugation

π-conjugation represents the overlap of one p_z orbital with another across an intervening σ bond resulting in the effective delocalization of the electron system over the scale of a few molecular units, the conjugation length.[54] Benzene offers an example of this phenomenom in which six carbons form a ring where the double bonds have an equal probability (Figure 1.2 (a)) to be located between each atom resulting in a π system evenly distributed above and below the ring (Figure 1.2 (b)). It is also this mechanism that allows semiconductivity in conjugated polymers, a fundamental example of this is polyacetylene, whose structure is represented in Figure 1.2 (c), which was historically the first polymer found to be conductive in presence of halogen vapours.[55] In conjugated polymers, π-conjugation lowers the overall energy of the system increasingly with the number of participating carbon atoms and the geometry of the polymer gives each newly formed molecular orbital a slightly dissimilar energy. This gives rise to two bands: the valence band made of the π bonding orbitals and whose maximum is the HOMO, and the conduction band made of the π^* antibonding orbitals whose minimum is the LUMO. These two bands are schematically represented in Figure 1.2 (d) with the energy difference between HOMO and LUMO called the bandgap (E_g).

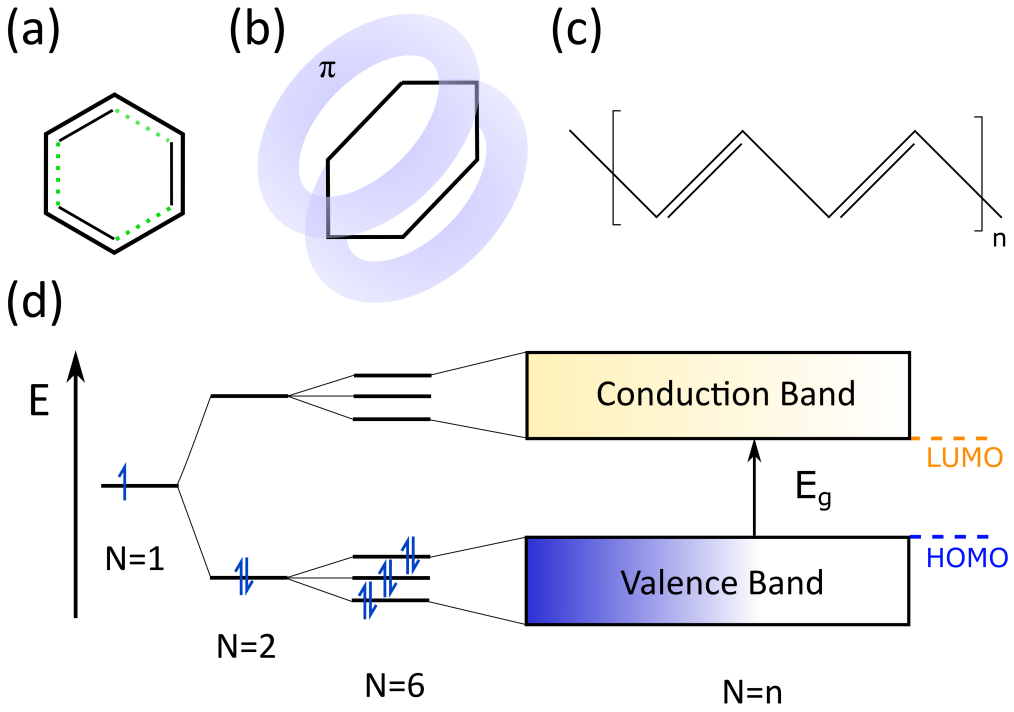


Figure 1.2: (a), (b) π-conjugation inside a benzene molecule thanks to alternating single and double carbon bonds which also enable semiconductivity inside conjugated polymers such as polyacetylene (c). (d) Formation of bands in conjugated polymers, where N is the number of participating carbon atoms. The conduction and valence bands, as well as the LUMO, HOMO and E_g are defined in the text.

1.4.2 Fundamental Excitations

The excitation of an electron from the HOMO to the LUMO is accompanied by the creation of a hole vacancy. Due to the inherent softness of conjugated polymers, the formation of either of those charge carriers is responsible for a local molecular distortion arising from strong electron-phonon coupling; the charge carrier together with its respective distortion then being called either an electron or hole polaron.

As the reconfiguration stabilizes the structure, the electron and hole polarons exist inside the bandgap of the material.[54] Once an electron polaron is created, it is bound to the hole polaron it left behind via Coulombic interaction forming an exciton. Their small radii ($\sim$ 1 nm) and large binding energies ($E_B \sim 0.5 \pm 0.25$ eV[11,12]), which allow for room-temperature observation, further classify them as Frenkel excitons. A fun-

damental difference between excitons found in conjugated polymers and in crystalline inorganic semiconductors is their strong localization: while inorganic excitons can be delocalized across large sections of the crystal, Frenkel excitons tend to be localized over a few molecular units and their mobility relies on hopping mechanisms between adjacent molecules.[56]

Frenkel excitons can be sorted into two sub-categories according to their total spin S: triplets (S=1) and singlets (S=0). This difference in total spin leads to specific photophysics; the singlet transition is dipole allowed enabling efficient optical excitation and radiative recombination through fluorescence at very short timescales (typically a few hundred ps[57]) while the triplet direct optical excitation is forbidden[57] and its recombination can only be measured at much longer timescales (ms to s), following intersystem crossing (ISC), via phosphorescence. The excited states can be written as:

$$|S=0\rangle = (\frac{1}{\sqrt{2}})(|\uparrow\downarrow\rangle - |\downarrow\uparrow\rangle) \tag{1.5}$$

$$|S=1\rangle = (\frac{1}{\sqrt{2}})(|\uparrow\downarrow\rangle + |\downarrow\uparrow\rangle) \tag{1.6}$$

$$|S=1\rangle = |\uparrow\uparrow\rangle \tag{1.7}$$

$$|S=1\rangle = |\downarrow\downarrow\rangle\,, \tag{1.8}$$

where the three triplet states that can be formed are identified by their spin projections ($m_\mathrm{s} = -1, 0, 1$) and the only singlet by its spin value (S=0). The triplet spin wavefunction is symmetric but the exciton wavefunction must be antisymmetric under exchange; this forces the triplet space wavefunction to be antisymmetric which reduces the spatial overlap between carriers therefore weakening the Coulomb interaction. The triplet energy (E_T) is consequently lower than its singlet counterpart (E_S) with a difference in energy called the exchange energy (E_exch). This energy can be relatively low and overcome (for example via spin-orbit coupling) leading to ISC in

which the spin of the excited electron of a singlet is flipped to form a triplet state.[47,56] Another way to form triplet states is through electrical injection, spin statistics dictate that upon meeting on a single molecule, uncorrelated oppositely charged carriers are three times more likely to form triplets compared with singlets.[58] In this thesis, only optical excitation is used and ISC is negligible, the corresponding discussion is therefore dedicated to the vast majority of singlets formed.

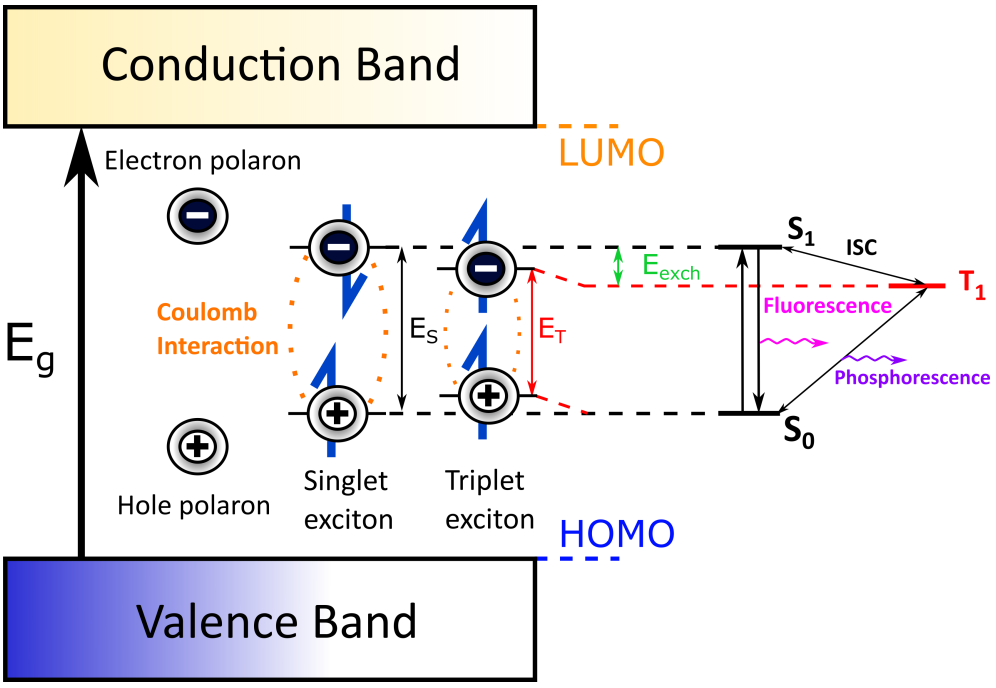


Figure 1.3: Schematic representation of fundamental excitations inside semiconducting polymers. The different energy levels and processes are defined in the main text. An exciton is formed by Coulomb interaction between and electron and hole polarons. According to their spin states this leads to either a singlet or triplet exciton obeying specific photodynamics as illustrated on the right.

1.4.3 The Role of Molecular Vibrations

We have so far examined the electronic structure in a fixed nuclear framework. For a given electronic configuration, molecular nuclei can move in a collective fashion or normal modes which in first approximation are well modelled by harmonic oscillators

with energies:

$$E_{\text{vib,n}} = \hbar \left(n + \frac{1}{2} \right) \omega_{\text{vib}}, \tag{1.9}$$

where ω_{vib} is the vibration pulse frequency typically located in the infrared.[47,59] A better approximation for the vibrational structure of the molecule accounting for bond breaking, anharmonicity corrections and the non-zero transition probability for overtones is the Morse potential:

$$E_p = E_{\text{Mo}} \left(1 - e^{a(R - R_{\text{eq}})} \right)^2, \tag{1.10}$$

where $|R - R_{\text{eq}}|$ is the inter-nuclei distance relative to the nuclei equilibrium positions, a is a constant and E_{Mo} is the depth of the potential which relates to the dissociation energy E_{D} via $E_{\text{Mo}} = E_{\text{D}} + \frac{1}{2}\hbar\omega_{\text{vib}}$. Contrary to the harmonic oscillator model where the energy levels are equally spaced, the level-spacing decreases as the energy approaches the dissociation energy. These potentials can be observed in Figure 1.4 for the electronic states S_0 and S_1.

1.4.4 Vibronic Transitions and Oscillator Strength

An electronic transition is accompanied by a modification in the equilibrium positions of the nuclei and available vibrational modes giving rise to an energy progression (the vibronic structure) observable in the absorption or emission spectra. By classical analogy, the dipole operator for an ensemble of α particles is defined as:

$$\boldsymbol{\mu} = \sum_{\alpha} q_\alpha \mathbf{r}_\alpha. \tag{1.11}$$

$\boldsymbol{\mu}$ acting on a given state ψ: $\langle\psi|\,\boldsymbol{\mu}\,|\psi\rangle$ allows us to determine if a dipole moment exists and if it does, evaluate its magnitude. Also, the transition dipole moment between an initial ψ_{i} and final state ψ_{f} is defined as the dipole operator acting on the transition

between those two states:

$$\langle \psi_{\mathrm{f}} | \, \boldsymbol{\mu} \, | \psi_{\mathrm{i}} \rangle \, . \tag{1.12}$$

This operation corresponds to the probability amplitude that exists for the transition between those two states.

In a molecular system, the transition probability from the lowest vibrational state of the ground electronic level ψ_{e_0,v_0} to a given vibrational state of the first excited electronic level ψ_{e_1,v'_j} (a similar reasoning can be applied for a transition to the n^{th} excited electronic level) is:

$$P_{(e_0,v_0),(e_1,v'_j)} \propto | \left\langle \psi_{e_1,v'_j} \right| \boldsymbol{\mu} \, | \psi_{e_0,v_0} \rangle \, |^2. \tag{1.13}$$

The dipole operator can be written as the sum of the respective contributions from the nuclei and electrons: $\boldsymbol{\mu} = \boldsymbol{\mu_n} + \boldsymbol{\mu_e}$. In the BO approximation, the wavefunctions can be separated into their spatial (electronic, vibrational, rotational) and spin components. We can ignore the rotational component since the difference in energy between two rotational levels is small[56] and leave the spin contribution aside as it is not affected by the electric field (spin considerations lead to the spin selection rules). We have $\psi_{e_0,v_0} = \psi_{e_0}\psi_{v_0}$ and $\psi_{e_1,v'_j} = \psi_{e_1}\psi_{v'_j}$, which gives:

$$\begin{aligned}
\left\langle \psi_{e_1,v'_j} \right| \boldsymbol{\mu} \, | \psi_{e_0,v_0} \rangle &= \left\langle \psi_{e_1}\psi_{v'_j} \right| \boldsymbol{\mu} \, | \psi_{e_0}\psi_{v_0} \rangle \\
&= \int \psi^*_{e_1}\psi^*_{v'_j}(\boldsymbol{\mu_n} + \boldsymbol{\mu_e})\psi_{e_0}\psi_{v_0}\mathrm{d}\tau \\
&\approx \int \psi^*_{e_1}\boldsymbol{\mu_e}\psi_{e_0}\mathrm{d}\tau_e \int \psi^*_{v'_j}\psi_{v_0}\mathrm{d}\tau_n + \int \psi^*_{e_1}\psi_{e_0}\mathrm{d}\tau_e \int \psi^*_{v'_j}\boldsymbol{\mu_n}\psi_{v_0}\mathrm{d}\tau_n \\
&\approx \int \psi^*_{e_1}\boldsymbol{\mu_e}\psi_{e_0}\mathrm{d}\tau_e \int \psi^*_{v'_j}\psi_{v_0}\mathrm{d}\tau_n
\end{aligned} \tag{1.14}$$

In Equation 1.14, the separation of integrals going from the second to the third line relies on the Condon approximation which recognizes that while the electron coordi-

nates depend parametrically on the nuclear ones (in the BO approximation), resulting variations are smooth and can therefore be neglected.[56,60] Going from the third to the fourth line, $\int \psi_{e_1}^* \psi_{e_0} \mathrm{d}\tau_e$ is null since different electronic states are orthogonal to one another.

In the last expression, $\int \psi_{v_j'}^* \psi_{v_0} \mathrm{d}\tau_n$ is the Franck-Condon overlap integral $F_{(e_0,v_0),(e_1,v_j')}$ associated with the transition from the initial vibrational state of the ground electronic level to the j^{th} vibrational state of the first excited electronic level and $\int \psi_{e_1}^* \boldsymbol{\mu_e} \psi_{e_0} \mathrm{d}\tau_e$ is the electronic transition dipole moment $\boldsymbol{\mu}_{e_0 e_1}$. The product of the two terms is the transition dipole moment for the vibronic transition $\boldsymbol{\mu}_{(e_0,v_0),(e_1,v_j')}$.

Concept first introduced by Lorentz for his semiclassical study of the absorption and emission of light, the oscillator strength f can be defined quantum mechanically for a discrete transition between an initial state $|\mathrm{i}\rangle$ and final state $|\mathrm{f}\rangle$ as:[56]

$$f_{\mathrm{i,f}} = \frac{2m_\mathrm{e}}{3q^2\hbar^2} |\boldsymbol{\mu}_{\mathrm{if}}|^2 (E(\mathrm{f}) - \mathrm{E(i)}) \tag{1.15}$$

where $E(\mathrm{f})$ and $E(\mathrm{i})$ are the energies of the initial $|\mathrm{i}\rangle$ and final $|\mathrm{f}\rangle$ states. For the vibronic transition previously studied this translates to:

$$\begin{aligned} f_{(e_0,v_0),(e_1,v_j')} &= \frac{2m_\mathrm{e}}{3q^2\hbar^2} |\boldsymbol{\mu}_{(e_0,v_0),(e_1,v_j')}|^2 \Delta E_{(e_0,v_0),(e_1,v_j')} \\ &= 4.70 \times 10^{29} \nu_{(e_0,v_0),(e_1,v_j')} |\boldsymbol{\mu}_{(e_0,v_0),(e_1,v_j')}|^2 \end{aligned} \tag{1.16}$$

where ν is the transition wavenumber and the rest of the expression has been evaluated numerically.

This expression can be extended to the whole electronic transition e_0 to e_1 given an appropriate definition of an equivalent wavenumber ν_{eq}. The total probability of transitions to all vibronic states of the first electronic level is equal to the probability of transition from the ground electronic level to the first excited electronic level,[56]

consequently:

$$|\boldsymbol{\mu}_{e_0e_1}|^2 = \sum_j |\boldsymbol{\mu}_{(e_0,v_0),(e_1,v'_j)}|^2. \tag{1.17}$$

The total oscillator strength f_{e_0,e_1} for the electronic transition is distributed among the vibronic transitions by the Franck Condon overlap integrals:

$$\begin{aligned} f_{e_0,e_1} &= \sum_j f_{(e_0,v_0),(e_1,v'_j)} \\ &= 4.70 \times 10^{29} \sum_j \nu_{(e_0,v_0),(e_1,v'_j)} |\boldsymbol{\mu}_{(e_0,v_0),(e_1,v'_j)}|^2 \\ &= 4.70 \times 10^{29} |\boldsymbol{\mu}_{e_0e_1}|^2 \sum_j \nu_{(e_0,v_0),(e_1,v'_j)} |F_{(e_0,v_0),(e_1,v'_j)}|^2 \\ &= 4.70 \times 10^{29} |\boldsymbol{\mu}_{e_0e_1}|^2 \nu_{\mathrm{eq}} \end{aligned} \tag{1.18}$$

where

$$\nu_{\mathrm{eq}} = \sum_j |F_{(e_0,v_0),(e_1,v'_j)}|^2 \nu_{(e_0,v_0),(e_1,v'_j)}. \tag{1.19}$$

This notion of oscillator strength can be extended to an ensemble of chromophores in solution or in thin films (where interference effects are in first approximation neglected) and to include the actual lineshapes. To do so, the oscillator strength is linked to Einstein's absorption coefficient:[56]

$$\begin{aligned} B_{e_0e_1} &= \sum_j B_{(e_0,v_0),(e_1,v'_j)} \\ &= \sum_j \frac{8\pi^3}{3h^2} |\boldsymbol{\mu}_{(e_0,v_0),(e_1,v'_j)}|^2, \\ &= \frac{\ln 10 \mathrm{c}}{h n_0 N_A} \int \frac{\epsilon(\nu)}{\nu} \mathrm{d}\nu \end{aligned} \tag{1.20}$$

where N_A is the Avogadro number, n_0 the refractive index of the medium, c the speed of light, $\epsilon(\nu)$ the decadic molar extinction coefficient and the integral is taken over the whole $\epsilon(\nu)$ distribution.

The total oscillator strength f_{e_0,e_1} is then:

$$f_{e_0,e_1} = \frac{40\epsilon_r\epsilon_0 m_\mathrm{e} \ln 10\mathrm{c}}{q^2 N_A h} \int \epsilon(E)\mathrm{d}E, \tag{1.21}$$

where ϵ is expressed in terms of energy.

1.4.5 Excitation and Emission Processes

The expressions derived in the previous section can be used to understand the photophysics of organic molecules. It is clear from Equation 1.14 that the most likely vibrational state in the excited state must be the one that corresponds to the largest value of $|F_{(e_0,v_0),(e_1,v'_j)}|^2$ (Franck Condon factors). This is the Franck-Condon principle which makes it possible to compare the different vibrational transition probabilities for a given electronic transition.

As the most probable transition tend to preserve positions and momenta of the nuclei, it is well represented by a vertical arrow in a diagram such as the one in Figure 1.4 (a) where the transition corresponds to a maximum spatial overlap between two vibrational wavefunctions.

Excitations between higher electronic levels are also possible, however the energy separation between them is usually significantly smaller[56] than between the ground level and first electronic level. This usually lead to internal conversion between the n^{th} and $(n-1)^{\mathrm{th}}$ electronic level (for $n > 1$) as the transition via vibrational relaxation is accessible thanks to the two levels proximity in energy. The internal conversion rate is much faster than a possible direct photon-emission rate resulting in Kasha's rule: "The emitting level of a given multiplicity is the lowest excited level of that multiplicity"[61] stating that the only appreciable yield of photon emission is obtained for a radiation emitted from the first electronic level to the ground level. In other words, most PL is measured from the ground vibrational state of the first electronic

level to any of the vibrational states of the ground electronic level with intensities following the Franck Condon factors, mirroring the absorption spectrum, as illustrated in Figure 1.4 (b).

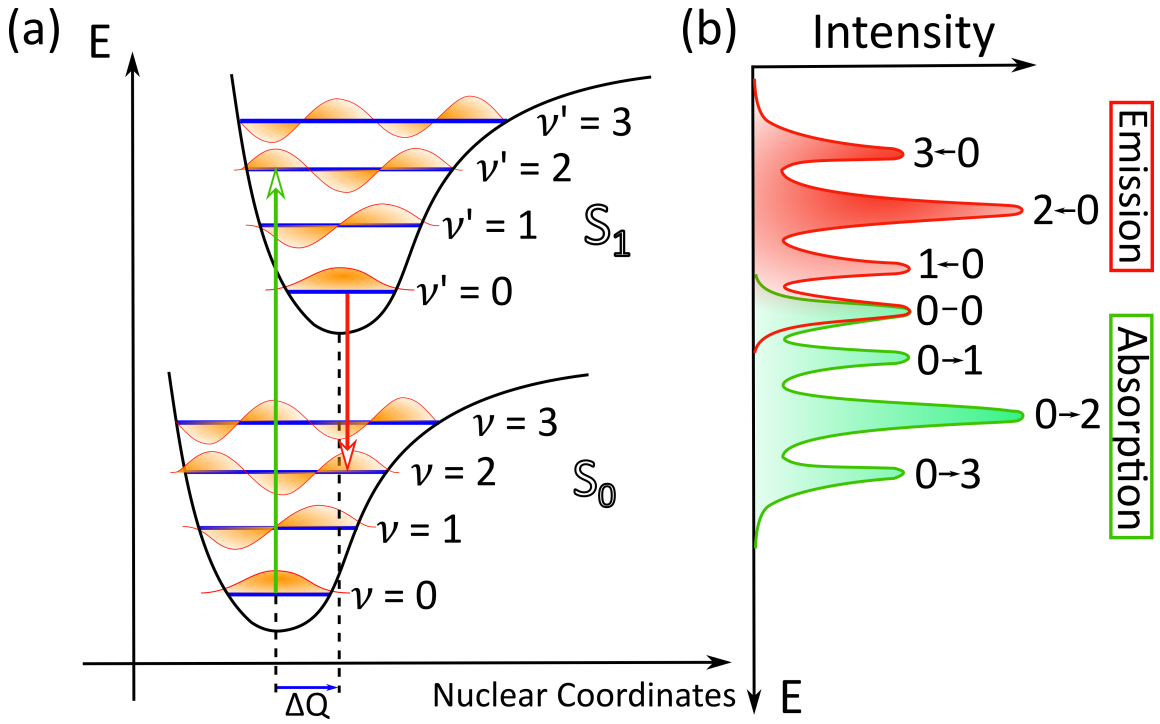


Figure 1.4: (a) Illustration of the Franck-Condon principle in absorption and emission between the ground electronic state S_0 and the first excited electronic state S_1 separated in nuclear coordinates by ΔQ. The maximum vibrational wavefunction overlap between the two electronic states in absorption (green arrow) and emission (red arrow) correspond to the strongest absorption and emission peaks in the corresponding vibronic structure (b).

Actual absorption and emission spectra can however significantly differ from the ones shown in Figure 1.4 (b) as organic molecules form soft materials in which electronic excitation can not only trigger a change in nuclei coordinates but also lead to conformational relaxation before any emission process can take place. This usually results in stabilization of the excited state S_1 and lowers the energy of the $S_{e_1,v_0'}$ from which emission occurs resulting in a shifted 0-0 frequency, the Stokes shift, between absorption and emission.

There also exists properties specific to conjugated polymers. In general, all poly-

mer chains inside a sample do not contain the same number of monomers and as a higher conjugation length results in a higher delocalization, a high polydispersity index (PDI) together with strong degrees of structural disorder usually results in a broad inhomogeneously broadened absorption band as represented in Figure 1.5.[54] Also, singlet excitons in undiluted solid-state samples can typically undergo energy transfer to lower HOMO-LUMO energy sites prior to radiative recombination. While a high PDI plays a significant role in absorption, one can often observe a well resolved vibronic progression in emission as PL occurs only from a self-selected subset of lower energy sites. This subset is accessed through rapid migration of the excitations via non-radiative Förster resonant energy transfer (FRET) taking place for distances between chromophores of less than 10 nm, with the energy being redistributed to lower energy sites before emission.[56] Figure 1.5 shows what can be expected from typical absorption and emission spectra for conjugated polymers.

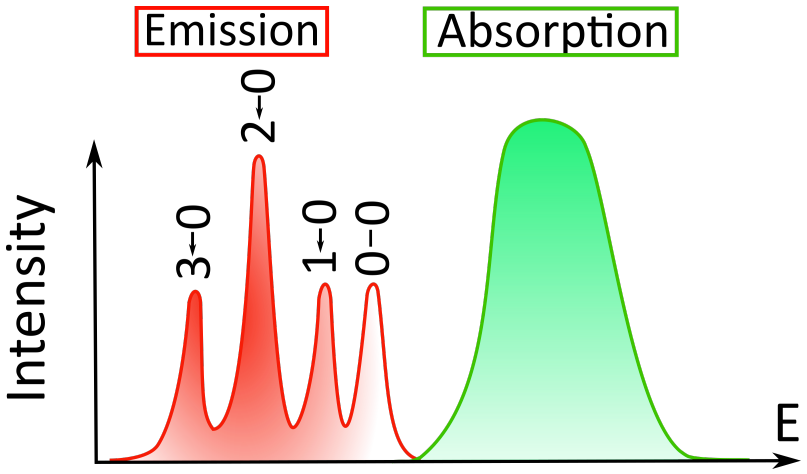


Figure 1.5: Typical absorption (in green) and emission spectra (in red) observed for semiconducting polymers. The inhomogeneously broadened absorption is a result of the large degree of disorder. Conformational relaxation of the excited state followed by rapid migration of the excitations to lower energy sites before emission results in the well resolved vibronic progression in luminescence.

1.5 Structure/Photophysics Relationship

Chain structure (conformation) as well as the immediate environment (packing) inside a polymer film greatly impact its photophysics. The excitons which are formed over a few molecular units can feel the electronic potential from neighbouring chains which can lead to the formation of shared excitations. An example of this are excimers in which two chromophores share electrons in the excited state but not in the ground state giving rise to a broad red-shifted emission.[56]

Also, the diversity of syntheses strategies used in polymer fabrication can lead to different molecular weights (Mw)s, PDIs or even purity. Furthermore, since most polymers are solution processed,[57] the solvent and deposition method (spin-coating, drop casting etc.[54]) used can result in very different structural properties. Finally, post-processing treatments such as thermal or solvent annealing can lead to changes in both the intra- and inter-chain configuration.

These considerations are essential and clearly stated in this thesis in order to ensure reproducibility of the results.

Chapter 2

Exciton-Polaritons in Organic Microcavities

2.1 Introduction

In this chapter we describe how photons can interact strongly with excitons to give rise to new quasi-particles: the polaritons which, while retaining characteristics from their light and matter constituents, exhibit their own unique physical characteristics. We note that this thesis focuses on the collective interaction of an ensemble of excitons with the light field and that while polaritons here refer to exciton-polaritons, these can be formed using a wide range of oscillating polarization fields: surface plasmon polaritons (coupling of surface plasmons to light), vibrational polaritons (coupling of vibrational modes to light), plexcitons (coupling of plasmons with excitons) and magnon polaritons (coupling of a magnetic dipole).
From this chapter and in the rest of this thesis the hat notation for Hamiltonians $\hat{H}$ and operators $\hat{o}$ is dropped for readability.

2.2 Planar Microcavities

2.2.1 Confining Photons in Planar Microcavities

A planar or Fabry-Pérot microcavity is formed when two mirrors separated by a distance L (of sub-μm to μm scale) surround a dielectric medium as shown in Figure 2.1 (a). In its simplest form, the cavity can be filled with air, the cavity refractive index is then simply $n = n_{\text{air}} = 1$ and standing waves satisfying the round trip phase condition $\rho \equiv 0\ (2\pi)$ (where ρ is the phase change experienced during a roundtrip inside the cavity) are the only resonant modes for the electric field. More generally, for a constant refractive index n and if we suppose ideal mirrors then the resonant mode pulse frequencies are:

$$\omega_{\text{cav}_\text{i}} = \frac{\pi \text{c}}{n(i+1)L}, \tag{2.1}$$

where c is the speed of light in vacuum and i an integer such that $i \geqslant 0$. The corresponding cavity photon energy is $E_{\mathrm{cav_i}} = \hbar\omega_{\mathrm{cav_i}}$ and can be measured when probing the microcavity either in reflectivity (Figure 2.1 (b)) or transmissivity by locating the spectral minima (respectively maxima). While planar microcavities are at the centre of this thesis we note that there exists a variety of structures that have been used to experiment and interact with photonic modes such as photonic crystals, micropillars (confining resonant gallery modes), microdisks etc.[62]

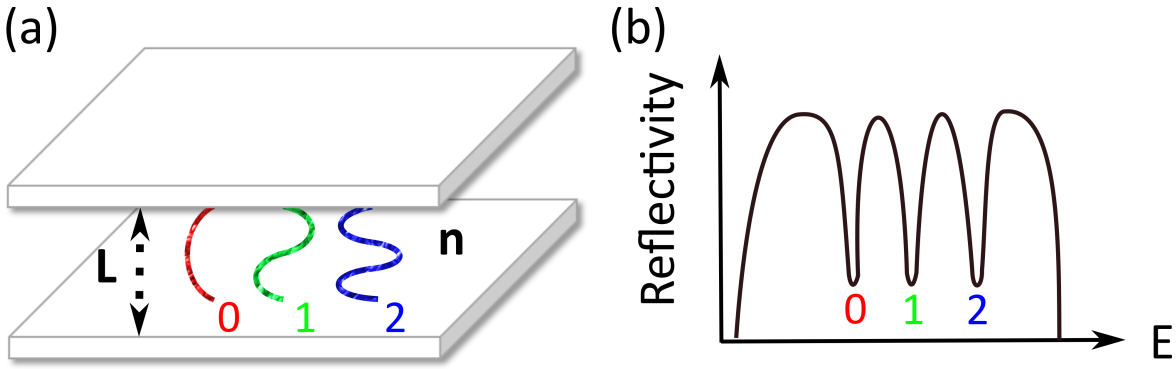


Figure 2.1: (a) Schematic representation of a planar microcavity containing a dielectric with constant refractive index n with two mirrors separated by a distance L. In red, green, and blue, the three first cavity modes characterized in reflectivity (b) by their energies $E_{\mathrm{cav}_{0,1,2}} = \hbar\omega_{\mathrm{cav}_{0,1,2}}$ defined in the text.

2.2.2 Dielectric and Metallic Mirrors

In reality, mirrors are not perfectly reflective (R_{bottom} and $R_{\mathrm{top}} < 1$) with losses due to photons escaping from the cavity. The spectral distribution of each resonant mode is then broadened accordingly by the loss term κ. In first approximation, these losses are well modelled by a Lorentzian broadening term γ_{cav} and the quality factor Q for the cavity mode lying lowest in energy (E_{cav_0})can be defined as:

$$\mathrm{Q} = \frac{\omega_0}{\gamma_{\mathrm{cav}}}, \tag{2.2}$$

where the damping inside the cavity decreases as Q increases. When using two mirrors with identical reflectivities R, a simpler expression for the quality factor is $\mathrm{Q} = \frac{\pi\sqrt{R}}{1-R}$. Two types of mirrors, dielectric and metallic, can be used to fabricate microcavities with different Q values. On the one hand, DBRs are used for applications requiring very high Q factors (from a few hundreds to several thousands) such as exciton-polariton lasing or non-equilibrium BEC, and are fabricated by alternating layers of high (n_H) and low (n_L) refractive indices materials: Ta_2O_5/SiO_2, TiO_2/SiO_2 are examples of commonly used pairs. The thicknesses of the layers is chosen following Bragg's condition: $4n_\mathrm{H}d_\mathrm{H} = 4n_\mathrm{L}d_\mathrm{L} = \lambda$ which forms the reflectivity:[63]

$$R = 1 - 4\frac{n_\mathrm{ext}}{n_\mathrm{c}}\left(\frac{n_\mathrm{L}}{n_\mathrm{H}}\right)^{2\mathrm{N}}, \tag{2.3}$$

where N is the number of mirror pairs, n_c the refractive index of the medium from which the light is incident and n_ext the refractive index of the medium into which the light escapes. The reflectivity can easily be in excess of $\mathrm{R} = 99\%$ for those mirrors and is closely maintained around a central wavelength λ inside a stopband whose width increases with the contrast between the layers refractive indices: $n_\mathrm{H} - n_\mathrm{L}$. Thanks to their very low losses, this kind of mirror is used to extend the lifetime of photons inside the cavity and consequently their possible interactions.

Nevertheless, when used to form a microcavity, DBRs give rise to a non-negligible amount of field penetration through the mirrors:[63]

$$L_\mathrm{depth} = \frac{\lambda n_\mathrm{H} n_\mathrm{L}}{2n_\mathrm{c}(n_\mathrm{H} - n_\mathrm{L})}, \tag{2.4}$$

which lead to typical field penetrations of a few hundred nms.

Metallic mirrors, which present large extinction coefficient k values of their complex refractive index are an altenative to DBRs. The Q factors for the corresponding microcavities are typically much smaller than for their DBR counterparts, a few

tenths to a hundred, due to lower reflectivity with typical values around 90%. The penetration depth L_{depth} is however much shorter than for DBR mirrors which reduces the mode volume V_{m} of the resulting photonic modes and the reflectivity itself is usually preserved over a much larger frequency bandwith.

2.3 Light-Matter Interaction from Linear Dispersion Theory

2.3.1 Weak and Strong Coupling Regimes

A semiconducting medium is now introduced inside the microcavity. We first neglect any disorder inside the material and suppose that all the excitons are correctly described by an isotropic Lorentzian model: they have a well defined transition pulse frequency ω_{ex} whose spectral distribution is only radiatively broadened by γ_{ex} and their transition dipole moment $\boldsymbol{\mu}$ has no preferential orientation in space. Since the materials used in this thesis are not strongly magnetic the magnetic susceptibility μ_{r} can be neglected and the complex refractive index is:

$$\tilde{n}^2 = (n + \mathrm{i}k)^2 = \epsilon(\omega), \tag{2.5}$$

which in the Lorentzian model is given by:[27,64]

$$\begin{aligned} \epsilon(\omega) &= I_3 \epsilon_0 \epsilon_m \times (1 + \chi(\omega)) \\ &= I_3 \epsilon_0 \epsilon_m \times \left(1 + \frac{4g_0^2}{\omega_{\text{ex}}^2 - \omega^2 - \mathrm{i}\gamma_{\text{ex}}\omega}\right). \end{aligned} \tag{2.6}$$

In Equation 2.6, $\chi(\omega)$ is the dielectric susceptibility of the material, γ_{ex} the radiative broadening of the excitons, ϵ_m the background permittivity of the material away from

the excitonic resonance and g_0 is the amplitude of the resonance:[27]

$$g_0 = \sqrt{\frac{f N_{\mathrm{ex}} e^2}{m}}, \tag{2.7}$$

where f is the oscillator strength of the transition, N_{ex} the exciton density, and m (e) the mass (charge) of the electron. Figure 2.2 shows the structure (a) as well as a typical complex refractive index profile for the material considered (b).

Linear dispersion theory allows to determine the resonances of the system as the spectral positions of the maxima (respectively minima) in transmissivity (respectively reflectivity). Let us first examine the case of an empty cavity ($g_0 = 0$ and $n_c = 1$). For ideal mirrors, the phase shift experienced by a photon of energy E after a roundtrip is:

$$\rho(E) = \frac{2 n_{\mathrm{cav}} E L}{\hbar \mathrm{c}}. \tag{2.8}$$

The first solution for $\rho(E) \equiv 0$ (2π) is the lowest energy cavity mode and one extremum is observed.

Let us now consider $g_0 > 0$ for which the cavity medium can interact with the photons. We also assume that the exciton and photon pulse frequencies are at resonance: $\omega_{\mathrm{ex}} = \omega_{\mathrm{cav}_0}$. Solving Equation 2.8 for the real part of the refractive index allows to derive three solutions for $\rho(E) \equiv 0$ (2π)[65] called in order of increasing energy: $E_{\mathrm{LP_{res}}}$, E_{cav_0} and E_{UPres}. For a real microcavity with losses characterized by γ_{cav}, the maxima (respectively minima) in transmissivity (respectively reflectivity) for $\mathrm{E_{LP_{res}}}, \mathrm{E_{UP_{res}}}$ are approximately Lorentzian in shape with a full width at half maximum (FWHM):[65]

$$\mathrm{LP/UP_{FWHM}} \approx \hbar \left(\frac{\gamma_{\mathrm{ex}} + \gamma_{\mathrm{cav}}}{2} \right). \tag{2.9}$$

$\hbar\Omega_0 = E_{\mathrm{UP_{res}}} - E_{\mathrm{LPres}}$ is the Rabi-splitting energy at resonance and can be expressed as:[65,66]

$$\hbar\Omega_0 = 2\hbar\sqrt{g_{\mathrm{res}}^2 - \frac{(\gamma_{\mathrm{ex}} - \gamma_{\mathrm{cav}})^2}{4}}, \tag{2.10}$$

where g_{res} is the coupling strength at resonance and is equal to:[27,67]

$$g_{\mathrm{res}} = \sqrt{N}\frac{\boldsymbol{\mu}.\mathbf{E}}{\hbar}, \tag{2.11}$$

where N is the exciton density, $\boldsymbol{\mu}$ is the transition dipole moment for one exciton and $\mathbf{E}$ is the vacuum-field inside the cavity:[63,67–69]

$$|\mathbf{E}| = \sqrt{\frac{\hbar\omega_{\mathrm{ex}}}{2\epsilon_{\mathrm{eff}}V_{\mathrm{m}}}}, \tag{2.12}$$

where $\epsilon_{\mathrm{eff}} = \epsilon_0\epsilon_{\mathrm{m}}$ is the effective dielectric permittivity of the cavity medium away from the excitonic resonance and V_{m} is the cavity mode volume. For a one dimensional cavity $V_{\mathrm{m}} = L_{\mathrm{eff}}$ with $L_{\mathrm{eff}} = L + 2L_{\mathrm{depth}}$; in the specific case of ideal mirrors, $L_{\mathrm{depth}} = 0$ and $g_{\mathrm{res}} = g_0$.

Equation 2.10 can be used to make the distinction between two different physical regimes whose characteristics in energy are shown in Figure 2.2 (c), (d). For $E_{\mathrm{LP_{res}}}$ and $E_{\mathrm{UP_{res}}}$ to be correctly defined the relation:

$$g_{\mathrm{res}} > \frac{|\gamma_{\mathrm{ex}} - \gamma_{\mathrm{cav}}|}{2} \tag{2.13}$$

must be satisfied. Below this value the system is dominated by damping: the excitons act incoherently as the photons decay too quickly for the interaction to take place. In terms of transmissivity and reflectivity spectra, a central maxima (respectively minima) at $E = E_{\mathrm{cav_0}}$ is observed and the profile of $\rho(E)$ is only slightly curved compared with the empty cavity case, this is the weak coupling regime. Further details on this regime can be found in Appendix A.

When Equation 2.13 is fulfilled, $E_{\mathrm{LP_{res}}}$ and E_{UPres} are defined and their energies are those of the Lower (LP) and Upper (UP) Polaritons at resonance. The different sources of damping have now been overcome by the interaction strength giving way to the strong coupling (SC) regime. The peak at $E = E_{\mathrm{ex}} = E_{\mathrm{cav_0}}$ is no longer visible in transmissivity or reflectivity as the cavity photons are absorbed by the cavity medium but the Rabi-splitting itself is not yet spectrally resolved since the widths of the LP and UP are still too broad:

$$\hbar\left(\frac{\gamma_{\mathrm{ex}} + \gamma_{\mathrm{cav}}}{2}\right) > \hbar\Omega_0. \tag{2.14}$$

Only when

$$\Omega_0 > \frac{\gamma_{\mathrm{ex}} + \gamma_{\mathrm{cav}}}{2} \Leftrightarrow g_{\mathrm{res}} > \frac{\gamma_{\mathrm{ex}}^2 + \gamma_{\mathrm{cav}}^2}{2} \tag{2.15}$$

does the splitting becomes resolved. Equation 2.15 corresponds to the visibility condition of the SC regime in transmissivity and reflectivity.

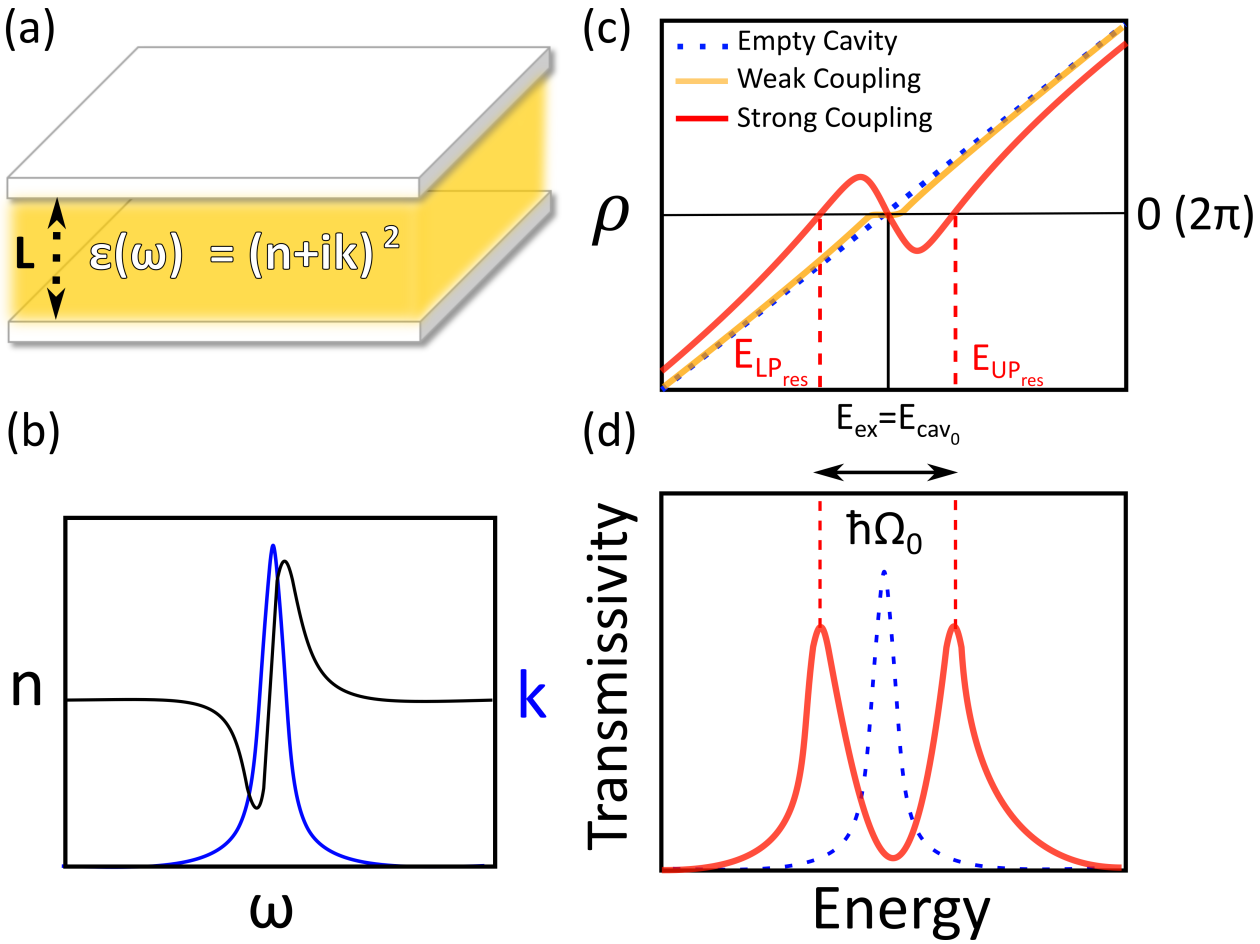


Figure 2.2: (a) Planar microcavity filled with a dielectric medium of permittivity $\epsilon(\omega)$ modelled using a Lorentzian susceptibility, resulting in the complex refractive index $\tilde{n} = n + ik$ shown in (b). (c) Roundtrip phase change ρ vs energy in the weak (orange solid line) and strong (red solid line) coupling regimes (dashed blue lines represent the empty cavity situation). In the SC regime, the two outermosts crossings for $\rho(E) \equiv 0\ (2\pi)$ correspond to the $E_{\mathrm{LP_{res}}}$ and $E_{\mathrm{UP_{res}}}$ while the crossing at $E = E_{\mathrm{ex}} = E_{\mathrm{cav_0}}$ is destroyed by absorption resulting in the LP and UP (solid red) in transmissivity (d) separated by $\hbar\Omega_0$.

2.3.2 Time-Domain Perspective

Time resolved signals are obtained by performing a Fourier transform to the transmissivity and reflectivity. In the SC regime, this results in the Rabi oscillations varying as $\sin(\frac{\Omega_0}{2}t)^2$.[65,70] These Rabi oscillations correspond to coherent exchanges of energy between the exciton and photon modes and are similar to the ones observed for a driven two level system. Their duration is finite, determined by the damping sources

γ_{ex} and γ_{cav}, and can be hindered by the presence of inhomogeneous broadening.[71]

2.4 Strong Light-Matter Interaction from a Quantum Perspective

2.4.1 Quantum Description of Polaritons as the Interaction of the Electromagnetic Field with a Polarization Field

The seminal works by Hopfield and Agranovich[25,27] on the contribution of excitons to the dielectric constants of crystals is presented here and provides us with the main analytical model for SC and USC in the rest of our thesis: the Hopfield-Agranovich (HA) model.[22,28]

Polaritons are formed when an oscillating polarization field $\mathbf{P}$ interacts with the electromagnetic field.[27] Following second quantization of the total Lagrangian density $\mathbf{L}$ in the Coulomb gauge (where the magnetic vector potential $\mathbf{A}$ is taken so that $\boldsymbol{\nabla}.\mathbf{A} = 0$), the total Hamiltonian of the system can be obtained as the sum of three terms:

$$H = H_{\text{pol}} + H_{\text{EM}} + H_{\text{int}}, \tag{2.16}$$

where:

$$H_{\text{EM}} = \hbar \sum_{\mathbf{k}} \left(\omega_{p,\mathbf{k}} \left(a_{\mathbf{k}}^{\dagger} a_{\mathbf{k}} + \frac{1}{2} \right) \right), \tag{2.17}$$

$$H_{\text{pol}} = \hbar \sum_{\mathbf{k}} \left(\omega_0 \left(b_{\mathbf{k}}^{\dagger} b_{\mathbf{k}} + \frac{1}{2} \right) \right), \tag{2.18}$$

and

$$H_{\text{int}} = i\hbar \sum_{\mathbf{k}} \frac{\Omega_{\mathbf{k}}}{2} \left(a_{\mathbf{k}}^{\dagger} b_{\mathbf{k}} - a_{\mathbf{k}} b_{\mathbf{k}}^{\dagger} + a_{\mathbf{k}} b_{-\mathbf{k}} - a_{\mathbf{k}}^{\dagger} b_{-\mathbf{k}}^{\dagger} \right) + \tag{2.19}$$

$$D_{\mathbf{k}} \left(a_{\mathbf{k}} a_{-\mathbf{k}} + a_{\mathbf{k}}^{\dagger} a_{-\mathbf{k}}^{\dagger} + a_{\mathbf{k}}^{\dagger} a_{\mathbf{k}} + a_{\mathbf{k}} a_{\mathbf{k}}^{\dagger} \right). \tag{2.20}$$

In the three Hamiltonians, for a wavector $\mathbf{k}$, the annihilation and creation operators for the electromagnectic field $a_{\mathbf{k}}$ and $a_{\mathbf{k}}^{\dagger}$ respectively annihilate and create a photon at pulse frequency $\omega_{\mathrm{p}_{\mathbf{k}}}$, similarly b and $b^{\dagger}$ annihilate and create an excitation of the polarization field at pulse frequency ω_0.[1] $\hbar\Omega_{\mathbf{k}}$ is the Rabi-splitting energy associated with the wavevector $\mathbf{k}$ and $D_{\mathbf{k}}$ the contribution of the squared magnetic vector potential $\mathbf{A}^2$ which form the diamagnetic terms.

Different sets of hypotheses in the following sections allow to diagonalize H thanks to the introduction of polariton operators.

2.4.2 Coupling of Excitons as a Quantized Set of Polarization Fields

In the fourth part of his work, Hopfield focuses on the interaction of different populations of Frenkel excitons characterized by their pulse frequencies ω_j with the electromagnetic field. Inside a dielectric crystal, he demonstrates that under hypotheses that we recall below, each exciton population forms a quantized polarization field that interacts independently with the electromagnetic field.

Frenkel excitons can be represented as tightly bound excited electronic states of a dielectric crystal in which the energies of the excitons $\hbar\omega_j$ are mapped to the excited atomic states energies. The atoms are considered distant enough from one another so that closest neighbours wavefunctions do not overlap. The annihilation b and creation $b^{\dagger}$ operators for the excitons are then formed, those operators being approximately bosonic for a number of excitons $N_{\mathrm{ex}} = \sum_j N_j$ much smaller than the number of atoms in the crystal N_{at} since the operator $b^{\dagger}$ produces an error in the normalization of the double-excitation wave.

[1] Interestingly Hopfield defined the fundamental excitation of the polarization field as the polariton, referring for example to the exciton as a polariton. The widely accepted definition is now that the polaritons correspond to the eigenvalues of the total Hamiltonian H and are created (respectively annihilated) using the polariton operators that are defined further in the text.

The exciton-photon interaction Hamiltonian can then be written:

$$H = H_{\text{exciton}} + H_{\text{photon}} + H_{\text{exciton-photon}} + H_{\text{exciton-exciton}} \tag{2.21}$$

where constant terms are lumped into the ground state (GS) energy. At this point we specialise the demonstration to the case of a microcavity containing an isotropic dielectric for which the in-plane wavevector $\mathbf{q}$ is a good quantum number since the normal wavevector component k_z is quantized. The cavity photon pulse frequency $\omega_{\text{p}_\mathbf{k}} = \omega_{\text{cav}_\mathbf{q}}$ is fully characterized by $\mathbf{q}$ and we have:

$$H_{\text{exciton}} = \sum_{\mathbf{q}} \hbar \sum_{j} \omega_j b^\dagger_{j,\mathbf{q}} b_{j,\mathbf{q}}, \tag{2.22}$$

and

$$H_{\text{photon}} = \sum_{\mathbf{q}} \hbar \omega_{\text{cav}_\mathbf{q}} a^\dagger_\mathbf{q} a_\mathbf{q}. \tag{2.23}$$

The HA model is only valid for low excitation densities so that interactions between excitons represented by $H_{\text{exciton-exciton}}$ can be neglected. The approximate exciton-photon interaction Hamiltonian of the tightly bound excitons is then:

$$H_{\text{exciton-photon}} = \sum_{\mathbf{q}} D_\mathbf{q} \left((a^\dagger_\mathbf{q} a_\mathbf{q} + a_\mathbf{q} a^\dagger_\mathbf{q}) + (a_\mathbf{q} a_{-\mathbf{q}} + a^\dagger_\mathbf{q} a^\dagger_{-\mathbf{q}}) \right) + \tag{2.24}$$

$$i\hbar \sum_{j} \frac{\Omega_{j,\mathbf{q}}}{2} \left((a^\dagger_\mathbf{q} b_{j,\mathbf{q}} - a_\mathbf{q} b^\dagger_{j,\mathbf{q}}) + (a_\mathbf{q} b_{j,-\mathbf{q}} - a^\dagger_\mathbf{q} b^\dagger_{j,-\mathbf{q}}) \right). \tag{2.25}$$

in which $\hbar\Omega_{j,\mathbf{q}}$ is the Rabi-splitting energy associated with the j^{th} exciton and $D_\mathbf{q} = \sum_j D_{\mathbf{q}_i} = \sum_j \left(\frac{\Omega^2_{j,\mathbf{q}}}{4\omega j} \right)$ is the sum of each diamagnetic contribution corresponding to a renormalization of the field due to the light-matter interaction.[33,72,73] Under these assumptions each exciton population acts as a quantized polarization field interacting separately with the electromagnetic field. We note that the HA model can easily be adapted to any other oscillating polarization fields (surface plasmons, phonons etc.).

2.4.3 Strong Light-Matter Coupling in the Rotating Wave Approximation

We now examine one exciton population of transition pulse frequency ω_{ex} in the SC regime. A useful factor to make physical assumptions at this point is the normalized coupling ratio at resonance:[33,34]

$$\eta = \frac{2g_{\text{res}}}{\omega_{\text{ex}}}. \tag{2.26}$$

In this section $\eta < 0.2$, the coupling strength is small compared with $\hbar\omega_{\text{ex}}$ and we neglect the losses from the cavity ($\gamma_{\text{cav}} = 0$) as well as from the excitons ($\gamma_{\text{ex}} = 0$) so that using Equation 2.10: $\Omega_0 \approx 2g_{\text{res}}$.

For the interaction Hamiltonian in Equation 2.24, $\mathbf{q}$ and $-\mathbf{q}$ are opposite wavevectors and in the interaction picture $-\mathbf{q}$ results in quickly counter rotating (also called anti-resonant) exponential terms, which can be neglected using the rotating wave approximation as long as η is small.[28] Since $\frac{D_0}{\Omega_0} = \frac{\Omega_0}{4\omega_{\text{ex}}} \approx \frac{\eta}{4} \ll 1$ we can also neglect the diamagnetic terms. The total Hamiltonian then reads:

$$\begin{aligned} H &= H_{\text{exciton}} + H_{\text{photon}} + H_{\text{exciton-photon}} \\ &= \sum_{\mathbf{q}} \hbar\omega_{\text{ex}} b^\dagger_{\mathbf{q}} b_{\mathbf{q}} + \hbar\omega_{\text{cav}_{\mathbf{q}}} a^\dagger_{\mathbf{q}} a_{\mathbf{q}} + i\hbar\frac{\Omega_{\mathbf{q}}}{2}(a^\dagger_{\mathbf{q}} b_{\mathbf{q}} - a_{\mathbf{q}} b^\dagger_{\mathbf{q}}). \end{aligned} \tag{2.27}$$

In order to diagonalize this Hamiltonian, the lower and upper polariton annihilation

$$p_{i,\mathbf{q}} = w_{i,\mathbf{q}} a_{\mathbf{q}} + x_{i,\mathbf{q}} b_{\mathbf{q}} \tag{2.28}$$

and creation

$$p^\dagger_{i,\mathbf{q}} = w_{i,\mathbf{q}} a^\dagger_{\mathbf{q}} + x_{i,\mathbf{q}} b^\dagger_{\mathbf{q}} \tag{2.29}$$

operators for $i \in \{\text{LP}, \text{UP}\}$ where w and x respectively label the photon and exciton Hopfield coefficients are introduced. The polariton operators are chosen so that they

fulfill the bosonic commutation rules:

$$[p_{i,\mathbf{q}}, p_{i,\mathbf{q}}^{\dagger}] = 1, \tag{2.30}$$

which in turns imposes the following relation on the Hopfield coefficients:

$$|w_{i,\mathbf{q}}|^2 + |x_{i,\mathbf{q}}|^2 = 1, \tag{2.31}$$

where $|w_{i,\mathbf{q}}|^2$ and $|x_{i,\mathbf{q}}|^2$ respectively represent the photon and exciton fractions. The Hamiltonian can now be diagonalized as: $H = E_G + \sum_{i\in\{\mathrm{LP,UP}\}} \sum_{\mathbf{q}} \hbar\omega_{i,\mathbf{q}} p_{i,\mathbf{q}}^{\dagger} p_{i,\mathbf{q}}$ where E_G is the ground state energy and the LP and UP pulse frequencies are obtained provided that:

$$\mathbf{v}_{i,\mathbf{q}} = (w_{i,\mathbf{q}}, x_{i,\mathbf{q}})^T \tag{2.32}$$

is a solution to the eigenvalue problem:

$$M_{\mathrm{SC}_\mathbf{q}} \mathbf{v}_{i,\mathbf{q}} = \omega_{i,\mathbf{q}} \mathbf{v}_{i,\mathbf{q}}, \tag{2.33}$$

where $M_{\mathrm{SC}_\mathbf{q}}$ reads

$$M_{\mathrm{SC}_\mathbf{q}} = \begin{bmatrix} \omega_{\mathrm{cav},\mathbf{q}} & -i\frac{\Omega_\mathbf{q}}{2} \\ i\frac{\Omega_\mathbf{q}}{2} & \omega_{\mathrm{ex}} \end{bmatrix}. \tag{2.34}$$

This problem is identical to the one of two masses m linked to two walls by two springs of different constants k_{cav} and k_{ex} (yielding two resonant pulse frequencies for the two uncoupled oscillators ω_{cav} and ω_{ex}) themselves joined together by a third spring of constant k_{int}. The two oscillators enter SC once k_{int} is large enough and the eigenvalues of $M_\mathbf{q}$ become the new normal modes pulse frequencies giving Equation 2.44 the name of coupled oscillators model (COM). The corresponding solutions are:

$$\omega_{\mathrm{LP}_\mathbf{q},\mathrm{UP}_\mathbf{q}} = \frac{1}{2}\left(\omega_{\mathrm{cav}_\mathbf{q}} + \omega_{\mathrm{ex}} \pm \sqrt{\Omega_\mathbf{q}^2 + (\omega_{\mathrm{cav}_\mathbf{q}} - \omega_{\mathrm{ex}})^2}\right) \tag{2.35}$$

for which the corresponding photon fraction for the LP is (for the other fractions use: $|x_{\mathrm{UP},\mathbf{q}}|^2 = |w_{\mathrm{LP},\mathbf{q}}|^2, |w_{\mathrm{UP},\mathbf{q}}|^2 = |x_{\mathrm{LP},\mathbf{q}}|^2 = 1 - |w_{\mathrm{LP},\mathbf{q}}|^2$):

$$|w_{\mathrm{LP},\mathbf{q}}|^2 = \frac{1}{1 + \left(\frac{\hbar\Omega_{\mathbf{q}}}{2\hbar(\omega_{\mathrm{LP},\mathbf{q}} - \omega_{\mathrm{cav}_{\mathbf{q}}})}\right)^2} \tag{2.36}$$

At resonance $\omega_{\mathrm{cav}_{\mathbf{q}}} = \omega_{\mathrm{ex}}$ and we have:

$$\omega_{\mathrm{LP_{res}},\mathrm{UP_{res}}} = \omega_{\mathrm{ex}} \pm \frac{\Omega_0}{2} \tag{2.37}$$

In the SC regime at resonance, the LP and UP split symmetrically around $\hbar\omega_{\mathrm{ex}}$ and are separated by the Rabi splitting energy $\hbar\Omega_0$, the photon fractions and exciton fractions are equal to $\frac{1}{2}$ making the polaritons half-light half-matter.

2.4.4 Ultrastrong Coupling, Beyond the Rotating Wave Approximation

When $\eta > 0.2$, $\hbar\Omega_0$ becomes directly comparable to the exciton energy $\hbar\omega_{\mathrm{ex}}$ and the counter rotating terms (which create and annihilate particles with opposite wavevectors $-\mathbf{q}$) as well as the contribution from the diamagnetic terms can no longer be neglected.[22,28] This also holds for n populations of excitons ($n > 1$) for which at least one value of η_j satisfies:

$$\eta_j = \frac{2g_j}{\omega_j} > 0.2, \tag{2.38}$$

for the j^{th} population (characterized by its resonance pulse frequency ω_j). Several excitonic resonances create Middle Polaritons (MP)s spectrally observable between the LP and UP. In order to diagonalize the full Hamiltonian, new forms of the polariton

annihilation

$$p_{i,\mathbf{q}} = w_{i,\mathbf{q}} a_{\mathbf{q}} + \sum_j x_{i,j,\mathbf{q}} b_{j,\mathbf{q}} + y_{i,\mathbf{q}} a^{\dagger}_{-\mathbf{q}} + \sum_j z_{i,j,\mathbf{q}} b^{\dagger}_{j,-\mathbf{q}} \tag{2.39}$$

and creation

$$p_{i,\mathbf{q}} = w_{i,\mathbf{q}} a^{\dagger}_{\mathbf{q}} + \sum_j x_{i,j,\mathbf{q}} b^{\dagger}_{j,\mathbf{q}} + y_{i,\mathbf{q}} a_{-\mathbf{q}} + \sum_j z_{i,j,\mathbf{q}} b_{j,-\mathbf{q}} \tag{2.40}$$

operators are introduced for $i \in \{\mathrm{LP}, \mathrm{MP}_1..\mathrm{MP}_\mathrm{n}, \mathrm{UP}\}$ where w, x, y and z label, respectively, the photon, exciton, anomalous photon and anomalous exciton Hopfield coefficients. The polariton operators are defined to fulfill the bosonic commutation rules:

$$[p_{i,\mathbf{q}}, p^{\dagger}_{i,\mathbf{q}}] = 1, \tag{2.41}$$

which in turns imposes the following relation on the Hopfield coefficients:

$$|w_{i,\mathbf{q}}|^2 + \sum_j |x_{i,j,\mathbf{q}}|^2 - |y_{i,\mathbf{q}}|^2 - \sum_j |z_{i,j,\mathbf{q}}|^2 = 1. \tag{2.42}$$

The Hamiltonian is diagonalized following the same method as in the previous section provided that:

$$\mathbf{v}_{i,\mathbf{q}} = (w_{i,\mathbf{q}}, x_{i,1,\mathbf{q}}, ..., x_{i,n,\mathbf{q}}, y_{i,\mathbf{q}}, z_{i,1,\mathbf{q}}, ..., z_{i,n,\mathbf{q}})^T \tag{2.43}$$

is solution to the eigenvalue problem:

$$M_{\mathrm{USC}_\mathbf{q}} \mathbf{v}_{i,\mathbf{q}} = \omega_{i,\mathbf{q}} \mathbf{v}_{i,\mathbf{q}}, \tag{2.44}$$

where $M_{\mathrm{USC}_\mathbf{q}}$ equals:

$$M_{\mathrm{USC}_\mathbf{q}} = \begin{bmatrix} \omega_{\mathrm{cav},\mathbf{q}} + 2D_\mathbf{q} & -i\frac{\Omega_{1,\mathbf{q}}}{2} & ... & -i\frac{\Omega_{n,\mathbf{q}}}{2} & -2D_\mathbf{q} & -i\frac{\Omega_{1,\mathbf{q}}}{2} & \dots & -i\frac{\Omega_{n,\mathbf{q}}}{2} \\ i\frac{\Omega_{1,\mathbf{q}}}{2} & \omega_1 & 0 & 0 & -i\frac{\Omega_{1,\mathbf{q}}}{2} & 0 & 0 & 0 \\ \vdots & 0 & \ddots & 0 & \vdots & 0 & 0 & 0 \\ i\frac{\Omega_{n,\mathbf{q}}}{2} & 0 & 0 & \omega_n & -i\frac{\Omega_{n,\mathbf{q}}}{2} & 0 & 0 & 0 \\ 2D_\mathbf{q} & -i\frac{\Omega_{1,\mathbf{q}}}{2} & ... & -i\frac{\Omega_{n,\mathbf{q}}}{2} & -\omega_{\mathrm{cav},\mathbf{q}} - 2D_\mathbf{q} & -i\frac{\Omega_{1,\mathbf{q}}}{2} & \dots & -i\frac{\Omega_{n,\mathbf{q}}}{2} \\ -i\frac{\Omega_{1,\mathbf{q}}}{2} & 0 & 0 & 0 & i\frac{\Omega_{1,\mathbf{q}}}{2} & -\omega_1 & 0 & 0 \\ \vdots & 0 & 0 & 0 & \vdots & 0 & \ddots & 0 \\ -i\frac{\Omega_{n,\mathbf{q}}}{2} & 0 & 0 & 0 & i\frac{\Omega_{2,\mathbf{q}}}{2} & 0 & 0 & -\omega_2 \end{bmatrix}. \tag{2.45}$$

There are $2n$ eigenvalues for this matrix, half of them are positive and represent the polariton pulse frequencies while the other half is made of their negative opposites. We detail below the solutions at resonance for 1 population of excitons with transition pulse frequency ω_{ex}. We note that in this thesis we will use at most two populations $j \in \{1, 2\}$ but that the model can readily be extended.[74] For one population of excitons:

$$\omega_{\mathrm{LP_{res}},\mathrm{UP_{res}}} = \frac{1}{2}\left(\sqrt{\Omega_0^2 + 4\omega_{\mathrm{ex}}^2} \pm \Omega_0\right). \tag{2.46}$$

The energy splitting is no longer symmetric around ω_{ex} at resonance and specifically blue shifts the LP with an increased exciton content compared with SC.

The vacuum ground state $|G\rangle$ is defined as the polariton vacuum:

$$p_{i,q}\,|G\rangle = 0, \tag{2.47}$$

and corresponds to the absence of polariton excitations. In the USC regime:

$$\langle G|\, a^\dagger_{\mathbf{q}} a_{\mathbf{q}}\, |G\rangle = |y_{\mathrm{LP},\mathbf{q}}|^2 + |y_{\mathrm{UP},\mathbf{q}}|^2 \text{ and} \tag{2.48}$$

$$\langle G|\, b^\dagger_{\mathbf{q}} b_{\mathbf{q}}\, |G\rangle = |z_{\mathrm{LP},\mathbf{q}}|^2 + |z_{\mathrm{UP},\mathbf{q}}|^2. \tag{2.49}$$

$|G\rangle$ is a squeezed state containing virtual excitations from the different polaritonic modes, this is a notable difference with the SC regime where the ground state corresponds to the exciton and photon vacuum. It has been suggested that these virtual particles could be released if one was able to drive the system non-adiabatically.[28,75] There exists another regime for $\eta > 2$ i.e. when $\hbar\Omega_0 > \hbar\omega_{\mathrm{ex}}$ called the deep strong coupling regime. In this physical regime, the diamagnetic terms of the Hamiltonian become dominant and light-matter decoupling can be observed with for example the breakdown of the Purcell effect.[37,75] This regime is yet to be reported in organic microcavities.

2.4.5 Semi-classical Equivalent

A simple equivalence exists[22] between the solutions of the HA model and those of obtained using a semi-classical model for a microcavity made of ideal mirrors containing a dielectric of Lorenztian permittivity (Equation 2.6) where the broadening γ_{ex} is considered null. We recall the Helmholtz wave equation for the different media:

$$\mathbf{k} \times [(\mu^{-1}) \cdot \mathbf{k} \times \mathbf{E}] + \frac{\omega^2}{c^2} \epsilon \cdot \mathbf{E} = \mathbf{0}, \tag{2.50}$$

the permeability μ can safely be considered to be the identity matrix for all layers. Equation 2.50 can be reformulated using the matrix $\mathbf{M}(\omega)$ such that:

$$\mathbf{M}(\omega)\mathbf{E} = \mathbf{0}. \tag{2.51}$$

A propagating wave solution of Equation 2.50 incident on the microcavity structure takes the form:

$$\mathbf{E}_i(\mathbf{r},t) = \mathbf{E}_{0_i} \mathrm{e}^{-\mathrm{i}[k_x x + k_y y + k_z z - \omega t]}, \tag{2.52}$$

and in Equation 2.51 $\mathbf{M}$ then reads:

$$\mathbf{M}(\omega) = \begin{pmatrix} \epsilon_x \frac{\omega^2}{c^2} - k_y^2 - k_z^2 & k_x k_y & k_x k_z \\ k_y k_x & \epsilon_y \frac{\omega^2}{c^2} - k_z^2 - k_x^2 & k_y kz \\ k_z k_x & k_z k_y & \epsilon_z \frac{\omega^2}{c^2} - k_x^2 - k_y^2 \end{pmatrix}. \tag{2.53}$$

Since ω_{cav} only experiences the permittivity $\epsilon = \epsilon_0 \epsilon_m$ and k_z is quantized inside the cavity, then using the cavity mode lying lowest in energy we have at normal incidence ($\theta = 0°$):

$$k_z^2 = \epsilon_m \frac{\omega_{\mathrm{cav}_0}^2}{c^2}. \tag{2.54}$$

From Equation 2.50:

$$k^2 = \epsilon_m \frac{\omega_{\mathrm{cav}}^2}{c^2}, \tag{2.55}$$

and using Snell law (θ_m being the propagation angle inside the central layer):

$$k^2 \cos^2 \theta_m = k_z^2 \Leftrightarrow \omega_{\mathrm{cav}}^2 = \frac{\omega_{\mathrm{cav}_0}^2}{1 - \frac{\sin^2 \theta}{\epsilon_m}}. \tag{2.56}$$

The rotational symmetry around the z-axis allows us to choose:

$$\mathbf{k} = \begin{pmatrix} k_x \\ 0 \\ k_z \end{pmatrix}, \; k_y = 0. \tag{2.57}$$

For TE polarization:

$$\mathbf{E}_{0_i} = \begin{pmatrix} 0 \\ E_{0_{iy}} \\ 0 \end{pmatrix}, \tag{2.58}$$

while for TM polarization:

$$\mathbf{E}_{0_i} = \begin{pmatrix} E_{0_{ix}} \\ 0 \\ E_{0_{iz}} \end{pmatrix}. \tag{2.59}$$

For both polarizations, Equation 2.51 reduces to:

$$[1 + \chi(\omega)]\epsilon_m \frac{\omega^2}{c^2} - k_z^2 - k_x^2 = 0 \tag{2.60}$$

inside the cavity. We now re-write Equation D.20 using $k_x^2 = k^2 \sin^2\theta_m = \frac{\omega^2}{c^2}\sin^2\theta$, replace $\chi(\omega)$ by its expression and obtain:

$$4g_0^2 = (\omega^2 - \omega_{\text{ex}}^2)(\omega^2 - \omega_{\text{cav}}^2). \tag{2.61}$$

When $\omega_{\text{cav}} = \omega_{\text{ex}}$ the solutions of Equation 2.61 are: $\omega_-^+ = \sqrt{(\omega_{\text{ex}}^2 + g_0)} \pm g_0$ which are identical to the ones obtained with the HA model for: $\hbar\Omega_0 = \hbar\omega_{\text{UP}_{\text{res}}} - \hbar\omega_{\text{LP}_{\text{res}}} = 2\hbar g_0$.

2.4.6 Disorder and Inhomogeneous Broadening

Disorder in semiconductors can lead to the spread of the transition pulse frequencies of an exciton population leading in turn to the dielectric permittivity:[76]

$$\epsilon(\omega) = \epsilon_m\epsilon_0 + \int_0^{+\infty} \epsilon(\omega, \omega_0) r(\omega_0) d\omega_0, \tag{2.62}$$

where $r(\omega_0)$ is the spectral density of oscillators at the pulse frequency ω_0. The model presented so far neglects the impact of disorder as sources of damping are ho-

mogeneous and the result of the uncertainty principle. The effects of inhomogeneous broadening on SC have been previously reported[71,76,77] with important conclusions listed below.

Firstly, the value of $\hbar\Omega_0$ obtained using our previous model is preserved as long as the integrated absorption strength of the exciton is maintained and the inhomogeneous broadening is small compared to $\hbar\Omega_0$. Then, the inhomogeneous broadening rapidly destroys coherent exchanges (Rabi oscillations) expected to take place between the exciton and cavity mode. Finally, the polariton states do not suffer from this broadening and are in fact homogeneously broadened, effect associated with motional narrowing which averages disorder effects thanks to the greater delocalization of the polariton compared with the exciton.

2.4.7 Notes on the Normalized Coupling Ratio

The normalized coupling ratio η defined in Equation 2.26 is subject to different definitions in the research community. Historically, it was first used by Ciuti *et al.* in their work on intersubband polaritons:[28]

$$\eta_{\text{Ciuti}} = \frac{\Omega_0}{2\omega_{\text{ex}}}, \tag{2.63}$$

where the cavity and exciton broadenings γ_{cav} and γ_{ex} were neglected and therefore intrisically met the condition:

$$g_{\text{res}}^2 \gg \frac{(\gamma_{\text{ex}} - \gamma_{\text{cav}})^2}{4}. \tag{2.64}$$

Using Equation 2.10 it was evident that:

$$\Omega_0 \approx 2g_{\text{res}}, \tag{2.65}$$

making Ω_0 and $2g_{\text{res}}$ interchangeable.

This definition is different from Equation 2.26 as the frequency used by Ciuti and coworkers is defined as the frequency of the Rabi oscillations between exciton and photon modes, which is equal to $\Omega_{\text{exch}} = \frac{\Omega_0}{2}$, and the assumption made in Equation 2.65 is not straightforward for our system.

Nowadays, the more commonly accepted definition across physical systems for the normalized coupling ratio is:[33,34]

$$\eta_{\text{cmn}} = \frac{g_{\text{res}}}{\omega_{\text{ex}}} \tag{2.66}$$

which has been used to compare the different experimental realizations of USC.

For ultrastrongly coupled organic microcavities, η has usually been reported in yet another way:[22–24,30]

$$\eta_{\text{org}} = \frac{\Omega_0}{\omega_{\text{ex}}}. \tag{2.67}$$

Apart from the difference in factor 2 with Equation 2.66 explained previously, this formulation which we adopt during the rest of the thesis needs one further clarification to justify its reasonable equivalence with Equation 2.10.

The organic semiconductors presented here have an exciton lifetime $\leqslant 1$ ns[7] which corresponds to an homogeneous broadening of a few μeVs, as such the influence of γ_{ex} can be neglected. We have also seen in the previous section that inhomogeneous broadening will not affect $\hbar\Omega_0$ as long as its value is small compared to the splitting itself. The only real source of deviation is then the broadening of metallic microcavities cavity modes which can easily reach ≈ 100 meV.[22] The lowest value of $\hbar\Omega_0$ that we observe in this thesis where we make a claim of USC is $\hbar\Omega_0 = 0.80$ eV compared with a cavity mode FWHM of ≈ 105 meV, this results in a maximum difference of $\approx 0.4\%$ between η_{org} and $2\eta_{\text{cmn}}$. As this difference is small, from this point and for the rest of the thesis: $\eta = \eta_{\text{org}}$.

2.5 Applicability of the Model to Microcavities Containing Conjugated Polymers

2.5.1 Organic Polariton Dynamics in the Linear Regime

There exists two main dynamics regimes in strongly coupled systems. For low excitation densities, in the linear regime which will be used exclusively during this thesis, the polaritons are well characterized by the HA model as the polariton-polariton interactions are negligible and the dynamics can therefore be understood by examining the dominant relaxation pathways.

The polariton-polariton interactions become dominant at higher excitation densities giving way to non-linear responses[30,78] and stimulated processes which have enabled experimental realizations of exciton-polariton lasing,[14] non-equilibrium BEC[15,16] and superfluidity.[19] While this regime is not at the centre of this thesis, we keep in mind that the techniques presented here are expected to benefit its study.

For organic microcavities operating in the linear regime, specificities arise from the complex energetic structure of the uncoupled semiconductor. Upon non-resonant radiative pumping (above the exciton energy) of a strongly coupled microcavity, PL is almost exclusively emitted from the LP. This kind of pumping scheme generates highly excited states whose exact nature is still the object of discussion, whether they are directly populating the UP or higher weakly coupled excitonic states.[79,80] These excitations however quickly decay ($\approx$ 100 fs) into the exciton reservoir. While the population of the reservoir could in certain cases be thermally excited back into the UP the scattering channels are much more efficient (on the order of 10 fs) and usually prevent the UP from having any notable excitation signature.[81]

From the exciton reservoir, two main mechanisms can occur to populate the LP: radiative pumping or vibronically assisted scattering.[82–84] These processes are relatively slow ($\approx$ 1 ps) compared with the other dynamics and often lead to a large fraction

of the excitations staying in the reservoir.[80,85] The main difference between them is that radiative pumping occurs in favour of species with the largest oscillator strength as they are most efficiently coupled to the cavity photons, while other species coupled to other vibronic levels decay through vibronic transitions.[81,86] Combination of both phenomena can occur in which the radiative transition ends up in one of the excited vibrational levels of the ground state which decays later.[87,88] Once the LP has been reached, decay via the photonic channel of the polaritons happens too fast ($\approx$ 100 fs) for other further relaxation to happen. The main dynamics discussed are represented in Figure 2.3.

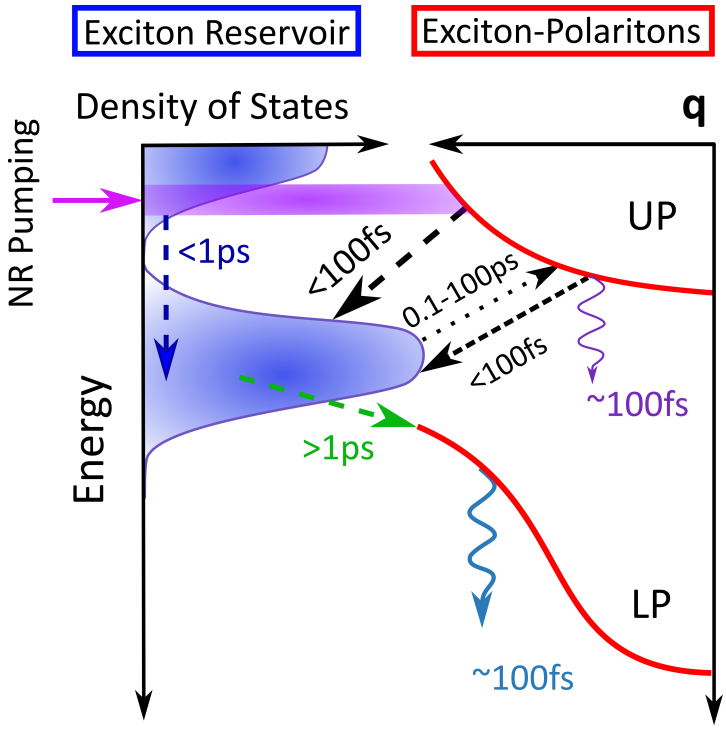


Figure 2.3: Relaxation Pathways in strongly coupled organic microcavities under non-resonant (NR) excitation (represented by the purple band). The straight blue arrow shows relaxation inside the exciton reservoir, the green one represents vibronically assisted scattering in which a phonon is first emitted out of the exciton reservoir with the remaining excitation then populating the LP, the black lines show the different interactions between the UP and the reservoir with a thermal equilibrium in favour of the latter. The different vertical curved arrows represent radiative emission from the polaritons. All time scales are estimate and depend eventually on the characteristic of the system.

2.5.2 The Importance of the Vibronic Structure, the Holstein-Tavis-Cummings Model

In this thesis, the HA model containing at most two exciton populations is used. Until recently, most spectroscopic analysis of strongly coupled molecular microcavities have either placed resolved vibronic peaks on the same footing as individual exciton transitions by adding an equivalent number of oscillators to the Hamiltonian,[14–16,19,20] or tried to account for unresolved-vibronic-level-induced absorption asymmetries using broadening terms.[89] These models, close to that used here, are efficient (mostly because the dielectric permittivity of a semiconductor with several exciton populations resembles the permittivity of an organic semiconductor with a vibronic progression), well-adapted to fitting procedures and explain to reasonable accuracy the time-integrated reflectivity and photoluminescence spectra. It is clear, however, that they emerge in a rather *ad-hoc* way without a precise knowledge of the underlying molecular physics.

The HA model ignores by definition electron-phonon coupling and can fail to describe certain aspects of organic polaritons. In 2002, Hobson *et al.*[21] and Lidzey et. al.[90] measured in distinct experiments luminescence from what was thought to be at the time uncoupled excitons. Further peculiarity was that those states were almost dark in reflectivity or transmissivity. Fifteen years later, Herrera and Spano published a subsequent theory of dark vibronic polaritons[88,91,92] describing those states as dark vibronic polaritons, evidence of admixtures of multiple vibronic transitions coupled to a single photon state close in energy to the exciton resonance. Taking into account the roles and interactions of each emitter and accounting for the vibronic couplings existing in the molecular structure through the Holstein term of the Holstein-Tavis-Cummings (HTC) model, they were further able to propose that the emission from the LP (on pumping the exciton reservoir) is enhanced by direct photon leakage from Y-type dark vibronic polariton states which provided a further explantion to the

standing question that direct LP pumping was rather inefficient in comparison to the non-resonant pumping scheme previously presented in the previous section.[68] The HTC Hamiltonian reads:[91–93]

$$H_{\mathrm{HTC}} = \omega_v \sum_n b_n^\dagger b_n + \sum_n \left[\omega_e + \omega_v \lambda (b_n + b_n^\dagger) \left|e_n\right\rangle \left\langle e_n\right|\right] \tag{2.68}$$

$$+ \frac{\Omega}{2} \sum_n \left(\left|g_n\right\rangle \left\langle e_n\right| a^\dagger + \left|e_n\right\rangle \left\langle g_n\right| a\right) \tag{2.69}$$

where $\omega_e = \omega_{00} + \omega_v \lambda^2$ is the vertical Franck-Condon transition pulse frequency for the vibrational pulse frequency ω_v and λ^2 is the Huang-Rhys factor which characterizes the strength of the vibronic coupling. While this model bears resemblance with the HA model, the operator b_n now annihilates one quantum of vibration on the n^{th} chromophore and the transition between ground and excited state on chromophore n is handled by $\left|e_n\right\rangle \left\langle e_n\right|$.

It is clear that this model takes into account the full organic picture described in Chapter 1. Its computational complexity can however make it difficult to be applied directly into fitting schemes for several populations of excitons in the USC regime, and requires a precise photophysical knowledge of the embedded organic semiconductor. For these reasons we restrain our analysis to the HA model in this thesis whilst retaining that the HTC model is likely to be able to explain unusual dynamics arising inside organic microcavities.

Chapter 3

Sample Fabrication and Characterization

3.1 Sample Fabrication

3.1.1 Materials

The polyfluorenes poly(9,9-dioctylfluorene-co-benzothiadiazole) (F8BT), poly(9,9-dioctylfluorene (PFO) and poly(2,7-(9,9-dihexylfluorene)-co-bithiophene)(F6T2) were used as received and their chemical structures are shown in Figure 3.1. Note that the PFO batches used in Chapter 4 and Chapter 5 are different since a low molecular weight (Mw) was found to be favourable for efficient LC alignment. Also displayed in Figure 3.1 is the chemical structure of the photoalignment molecule SD1 used throughout Chapter 5 and 6.

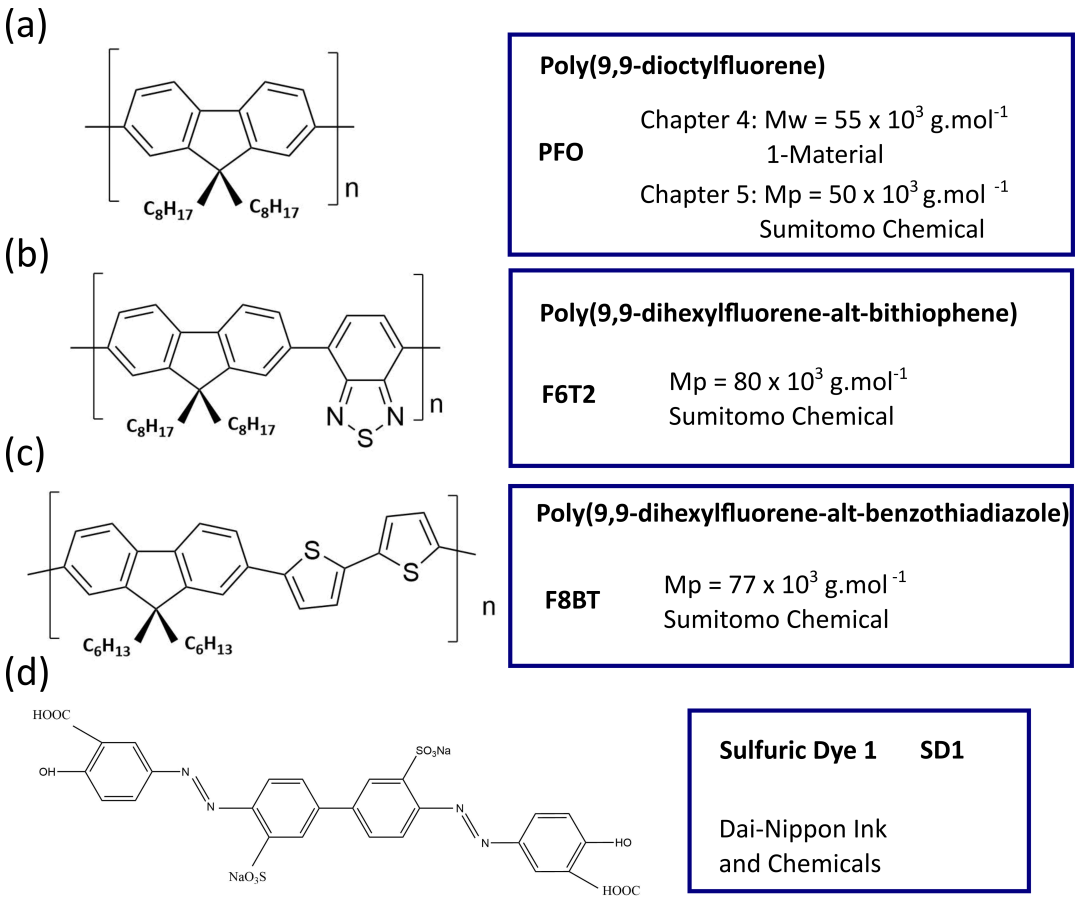


Figure 3.1: Chemical structure and molecular weights of the polymers: (a) PFO, (b) F6T2 and (c) F8BT. (d) Chemical structure of SD1 used as photoalignment layer.

3.1.2 Thin Film Fabrication

All polymers were dissolved in a range of solvents suitable to the production of smooth and homogeneous layers. For the polymers, two solvents with relatively high Hildebrand parameter value δ were used: toluene ($\delta \approx 8.9$, $T_{boiling} = 110°C$[54]) and chloroform ($\delta \approx 9.1$, $T_{boiling} = 65°C$[54]), other solvents were used during the experiments but led to the fabrication of lower quality films. All organic bare films were spin-coated either on a cleaned fused silica substrate or metallic mirrors using speeds ranging from a few hundreds to a few thousands of revolutions per minute (rpm) with speed conditions detailed with each experiment.

3.1.3 The Glassy- and β-phase of PFO

PFO has been employed to good effect in the fabrication of a wide range of devices, including Light-Emitting Diodes (LED)s,[94] transistors,[95] optically-pumped photon and exciton-polariton lasers.[96–99] In the solid state, its soft nature enables the formation of distinct conformational isomers: the glassy, crystalline, and β-phase chain conformations.[100] Information on the crystalline conformation, which is not used in this thesis and can be observed upon slow cooling from the nematic melt, is reported elsewhere.[100–103]

In the glassy-phase, represented in Figure 3.2 (a), the PFO chains adopt a worm-like configuration, with a mean fluorene-fluorene single bond torsion angle $\phi_{tor} \sim 135°$.[102] The β-phase (shown in Figure 3.2 (b)), with linearly-extended, planar chain segments[102,104] and a well-defined value of $\phi_{tor} = 180°$ can then be readily generated in the otherwise glassy film by thermally cycling or solvent vapour annealing,[101,105–109] slow drying,[102,110] and swelling with solvent or solvent/non-solvent mixtures.[111,112] Another approach, used in Chapter 4, consists in adding controlled amounts of 1,8-diiodooctane[113] or paraffin oil[114] to the polymer solution prior to spin-coating, allowing a systematic variation in β-phase fraction without the need for post-deposition

treatment.

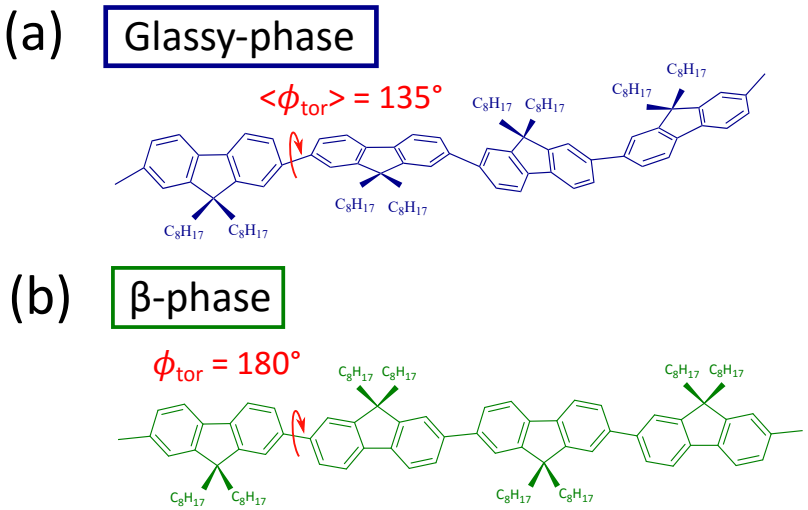


Figure 3.2: The glassy- (a) and β-phase (b) conformations of PFO displayed together with their respective intermonomer torsion angle ϕ_{tor}.

The difference in geometry between the glassy- and β-phase gives rise to two separate populations of excitons X_{g} and X_{β} that can coexist inside a single PFO film. The presence of X_{β} excitons leads to red-shifted, characteristically well-resolved, vibronically-structured absorption and PL emission bands, with a small Stokes shift.[101,102,105–107,110] The associated refractive index and optical gain changes are similarly notable.[108,109,112,115–117] The changes in optical properties with increasing percentages of β-phase segments ($\%_{\beta}$) are experimentally examined at the beginning of Chapter 4.

More generally, conformational tunability allows detailed studies of photophysics, including energy migration processes[118] and dichroism.[107] In addition, it provides a metamaterials structuring approach to patterning the refractive index in order to generate photonic structures.[109,112]

3.1.4 Thermal Evaporation of Aluminium

Aluminium mirrors were fabricated for our microcavity mirrors enabling low mode volumes V_{m} and high reflectivities in the UV and a large part of the visible.

During thermal evaporation, metallic pellets of aluminium (Al 99.999% pure, Kurt J. Lesker[119]) were placed in a tungsten boat which was then resistively heated up to the metal sublimation point. Due to the high reactivity of aluminium, a few rules of thumb were followed[120] to preserve their reflectivity: (i) The vacuum pressure inside the chamber was maintained at P = 10^{-7}-10^{-9} mbar; (ii) The evaporation was performed at relatively high rate $\sim$ 10 A.s^{-1}.

The evaporation rate as well as the target thickness were controlled using a quartz crystal monitor (QCM) located inside the chamber. For both thin films and aluminium mirrors, the final thicknesses were checked using a DekTak[121] profilometer.

3.1.5 Microcavity Fabrication

The microcavities were fabricated following a relatively similar process to the one illustrated in Figure 3.3. Cleaned fused silica substrates were first brought into the evaporation chamber in which a 100 nm thick Al mirror was evaporated, the sample was taken out of the evaporation chamber and the organic layers were spun (with sometimes additional treatments as described in Chapter 4 and 5), finally the samples were brought back into the evaporation chamber where an approximately 20 nm thick Al mirror was evaporated. The Q factor of a so-called empty Al microcavity (filled with a 100 nm thick film of polymethyl methacrylate (PMMA)) was measured: $Q \sim 45$ for a corresponding cavity mode FWHM of 120 meV.

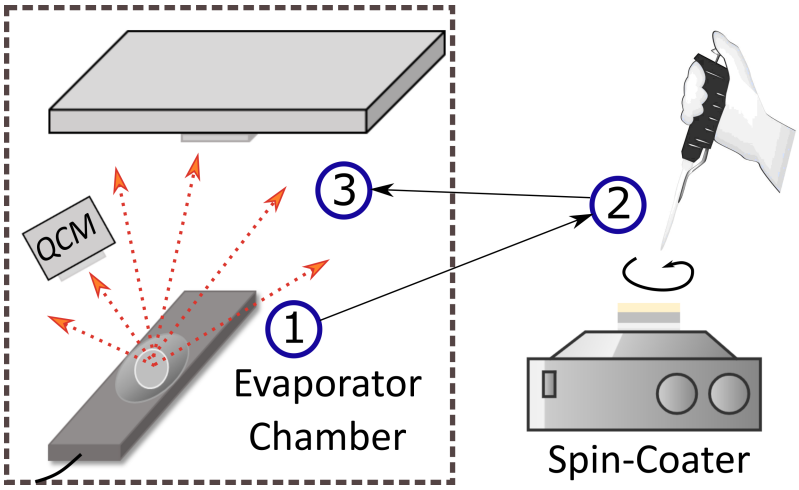


Figure 3.3: Microcavity fabrication process: (1) The Al pellets contained in the tungsten boat are heated up to sublimation through resistive heating, the QCM located above the metal source allowing for evaporation rate and target thickness control for the deposited layers; (2) The samples are taken out of the chamber and the organic layers are spincoated; (3) The samples are brought back into the evaporation chamber where the top mirror is evaporated.

3.2 Optical Characterization: Experimental

3.2.1 UV-Visible Absorption

Thin film absorption spectra were measured using a Perkin-Elmer Lambda 1050 UV/Vis spectrophotometer[122] for which a transmissivity measurement at normal incidence and a specular reflectivity measurement at 6 degrees were performed. The baseline transmissivity and reflectivity from the fused silica substrates were then substracted to the corresponding acquisitions and the resulting signals were summed to yield the absorption spectra. Scattering measurements were not conducted, they could have led to slight deviations in the absorption spectra, the roughness was therefore systematically checked via ellipsometry and did not exceed 5 nm for all samples. Further interference considerations inside the films were considered but found to have negligible effect on the absorption spectra.

3.2.2 Variable Angle Spectroscopic Ellipsometry

Variable Angle Spectroscopic Ellipsometry (VASE) was performed throughout this thesis to extract the thin film optical constants using a J.A. Woollam ESM-300[123] ellipsometer with light incident from 45° to 75°. VASE analyses the changes of polarization of an incident source of light following reflection at different angles upon the surface of a sample. By first measuring the complex reflectivity ratio: $\rho = \frac{r_{TE}}{r_{TM}} = \tan(\psi)e^{i\Delta}$, one can extract the values of ψ and Δ which can then be fitted using models that relate to the physical properties of the film or multilayer structure studied. All the analysis was conducted using the CompleteEASE software.[123]

3.2.3 Angle-Resolved Reflectivity and Photoluminescence

While VASE enables thin film optical constants modelling, polarized angle-resolved reflectivity allows to characterize the different resonant modes of a microcavity. As demonstrated in Section 2.4.5, the cavity mode pulse frequency ω_{cav} can readily be tuned by varying the polar angle θ of the incident light in order to extract $\hbar\Omega_0$ via fitting of the reflectivity minima dispersions using the HA model. During these measurements, the avoided crossing of the exciton energy by the LP and UP is observed and is a characteristic of the SC regime.

In Chapter 4, this kind of measurement is conducted with the J.A. Woollam ESM-300 ellipsometer for angles varying from 45° to 75°. A home-built optical setup, fully automated, is used in Chapter 5 and 6 in order to acquire reflectivity data from a larger range of angles, to allow for rotation around the normal of the sample plane (azimuthal rotation) and to reduce the size of the probed spot down to 1 mm to reduce potential broadening arising from the microcavity surface inhomogeneity. The optical setup is represented in Figure 3.4

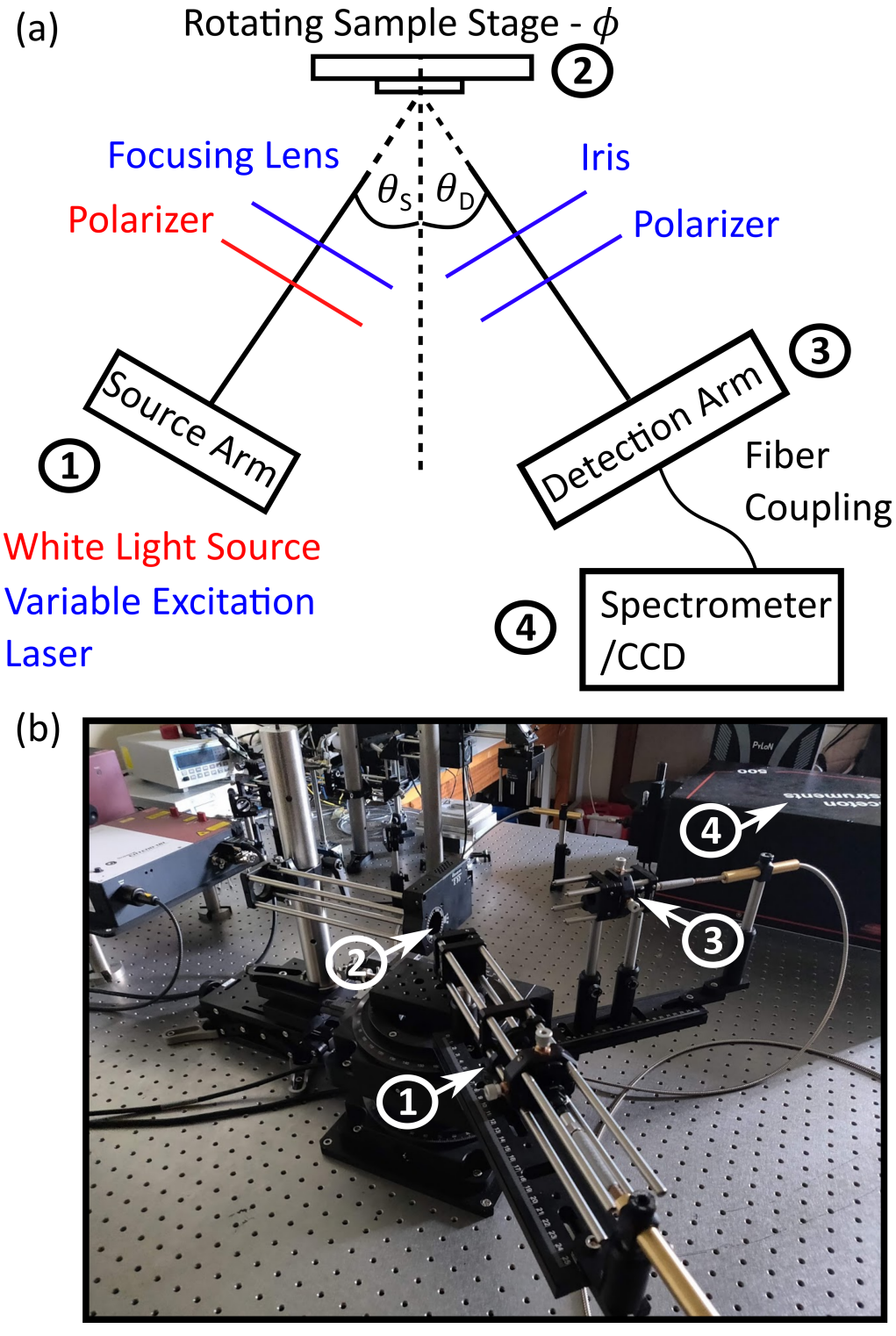


Figure 3.4: (a) Schematic representation of the optical setup built to measure angle-resolved reflectivity (specific parts in red) and PL (specific parts in blue) for different polar (θ) and azimuthal (ϕ) angles. The numbers in (a) match the real components shown in the picture (b) of the actual setup.

In this configuration, the microcavities were placed at the centre of a stage with two independent rotating arms. A deuterium-halogen light source (DH-2000-DUV from Ocean Optics[124]) was coupled into a fiber whose output was collimated onto a broadband polarizer (WP25M-UB from Thorlabs[125]) and onto the sample (final spot size 1 mm). The reflected light was then coupled into a second fiber placed onto the second arm and analyzed using a spectrometer (HRS 500, 150 g/mm grating with blazing wavelength at 300 nm) and CCD (Pylon-2KB) from Princeton Instruments.[126] In all cases, a neat aluminium mirror with known reflectivity was used as a reference. In Chapter 4, time-integrated PL from the bare films and angle-resolved PL were recorded using a Horiba Fluorolog spectrofluorometer[127] with excitation wavelength selected according to the sample. In Chapter 5, both PL measurements were performed on the home-built setup. The fiber coupled to the white light source was disconnected and the first arm was positioned at 75° relative to the sample plane normal. The pulsed laser beam from a supercontinuum white light laser (SuperK Extreme with its UV spectral extension unit Extend-UV, NKT Photonics[128]) was used as excitation source and focused onto the sample (spot size < 1 mm). The excitation energy was tuned according to the optical transitions, the incident power was kept low ($\leq 10\mu$W) with pulse widths of 20 to 30 ps and a repetition rate of 77.87 MHz. The broadband polarizer was placed on the collection arm, at a distance of 10 cm from the sample. Two nearly closed irises (~ 1 cm) at a distance of 5 cm from each other were then placed before the coupling lens of the collection fiber in order to ensure that the collected light was emitted at the desired angle in the horizontal plane. The light was then analysed using the spectrometer and CCD described before using this time a 300 g/mm grating blazed at a wavelength of 500 nm. For the polymer films, the light was collected at normal incidence. For the microcavities the acquisition angle was varied by 1° steps from -40 to 60°.

3.3 Optical Characterization: Simulation

3.3.1 Transfer Matrix Calculations

Transfer Matrix Calculations (TMC) based on the propagation of the electromagnetic field inside a multilayer stack[63] were performed to compute the transmissivity and reflectivity spectra of the microcavities using the optical constants obtained via VASE. An algorithm extending the core capabilities of the *py_matrix* package[129] was developed and optimized for arbitrary dielectric tensors following the formalism used by Mansuripur *et al.*[130]

3.3.2 Fitting Model

The HA model (Section 2.4.4) including up to two excitonic resonances was implemented as a fitting algorithm using both a Python[131] module and Matlab.[132] Once the reflectivity sets were measured, the dispersions of the minima were fitted (in Chapter 4, additional minima from the PL were added to the fitting set) using the Rabi-splitting energies $\hbar\Omega_{0_j}$, the effective refractive index $n_{\mathrm{eff}_{\mathrm{TE,TM}}}$ and the photonic mode energy at normal incidence $E_{\mathrm{cav}}(0)$ as fitting parameters. For the cavity mode, the following expression was used for metallic microcavities:[22]

$$\omega_{\mathrm{cav}_{(\mathrm{TE,TM}),\mathrm{q}}} = \omega_{\mathrm{cav}_{(\mathrm{TE,TM})}}(\theta) \tag{3.1}$$

$$= \omega_{\mathrm{cav}}(0)\left(1 - \frac{\sin^2(\theta)}{n^2_{\mathrm{eff}_{\mathrm{TE,TM}}}}\right)^{-\frac{1}{2}} \tag{3.2}$$

where $n_{\mathrm{eff}_{\mathrm{TE}}}$ $n_{\mathrm{eff}_{\mathrm{TM}}}$ are polarization dependent (see Appendix B Section B.3 for more details). For the Rabi energy of population j at a given wavevector $\mathbf{q}$, the following expression[22,28] was used:

$$\Omega_{\mathbf{q},j} = \Omega_{0j}\sqrt{\frac{\omega_j}{\omega_{\mathrm{cav}}}} \tag{3.3}$$

where ω_j is the pulse resonance frequency of the j^{th} population of excitons and $\hbar\Omega_{0j}$ the Rabi-splitting energy at resonance for $\omega_{\text{cav}} = \omega_j$.

Chapter 4

Conformational Control for Strong Coupling

Copyright notice: The content of this chapter was adapted with permission from: Conformational control of exciton-polariton physics in metal-poly(9,9-dioctylfluorene)-metal cavities - F. Le Roux, D. D. C. Bradley *Physical Review B*, **98**, 195306 (2018)

4.1 Introduction

In this chapter, control is exerted over the exciton-polariton physics in metal-PFO-metal microcavities via conformational changes to the polymer backbone. Using thin-film samples containing increasing fractions of β-phase chain segments, a systematic study is reported for the mode characteristics and resulting light emission properties of cavities containing two distinct exciton sub-populations within the same semiconductor. USC for disordered glassy-phase excitons (X_{g}) is observed from angle-resolved reflectivity measurements, with $\hbar\Omega_0$ in excess of 1.05 eV (more than 30% of the exciton transition energy) for both TE- and TM-polarized light. A splitting of the LP branch is then induced via introduction of β-phase excitons (X_β) and increases with their growing fraction. In all cases, the PL emanates from the lowermost polariton branch, allowing conformational control to be exerted over the emission energy and its angular variation. Dispersion-free cavities with highly saturated blue-violet emission are thus enabled. Experimental results are discussed in terms of the full HA Hamiltonian presented in Chapter 2. The importance of taking account of the molecular characteristics of the semiconductor for an accurate description of its SC behaviour is directly considered, in specific relation to the discussion led in Section 2.5.2.

4.2 PFO Thin Film Optical Properties

4.2.1 Absorption and Photoluminescence Spectra

PFO thin film samples were deposited on pre-cleaned fused silica substrates by spin coating (2300 rpm for one minute). Both the solutions and the substrates were pre-heated at 80°C for 5 minutes immediately prior to deposition. The thicknesses of the resulting films were measured, using a Dektak[121] profilometer, to be 75 - 85 $\pm$

2 nm, with β-phase chain segment fractions tuned from 0 (glassy-phase) to 15.8 $\pm$ 0.5 % by adding 100 μL aliquots of increasing concentration (0 to 35 μL per mL) 1-8 diiodooctane in toluene solutions to 1.9 mL portions of a baseline 13.5 mg per mL PFO in toluene solution; this yields mixtures with 0 to 0.175 vol% 1-8 diiodooctane. Samples were prepared with eight different β-phase fractions, namely 0, 1.1 $\pm$ 0.5, 1.5 $\pm$ 0.5, 3.7 $\pm$ 0.5, 10.0 $\pm$ 0.5, 12.3 $\pm$ 0.5, 13.9 $\pm$ 0.5 and 15.8 $\pm$ 0.5%, determined from the relative strength of the duly weighted (to correct for the known oscillator strength increase), integrated X_β absorption contribution.[133] These fractions are used as reference labels for both films and corresponding microcavities in the rest of this chapter. Thin film absorption spectra were measured and corrected for specular reflectance. Figure 4.1 shows data for four samples, namely those with 0, 3.7 $\pm$ 0.5, 12.3 $\pm$ 0.5 and 15.8 $\pm$ 0.5% β-phase fractions, whilst the corresponding spectra for samples with the other four fractions are presented in Appendix B (Figure B.1). In Figure 4.1 (a) the 0% (glassy-phase) absorption spectrum can be described, for simplicity, as comprising two dominant contributions, namely a lower energy delocalized X_g $S_0 - S_1$ exciton band (peaked at $\sim$ 3.25 eV) and higher energy absorption (shoulder at $\sim$ 5.28 eV, peak at $\sim$ 5.71 eV and higher energy shoulder at $\sim$ 6.25 eV) associated with ring-localized fluorene states;[106] the additional absorption at $\sim$ 4.25 eV is much weaker. A schematic glassy-phase chain segment is shown at the bottom of panel (a), with deviations from the mean fluorene-fluorene single bond torsion angle ($\sim$ 135°) generating multiple conformers that cause inhomogeneous broadening of the X_g $S_0 - S_1$ absorption.[102] The expected vibronic structure is not then resolved, with the FWHM linewidth of the transition $\approx$ 0.6 eV.

Formation of β-phase chain segments (c.f. schematic structure at the bottom of panel (d)) leads to the appearance of a characteristic (0-0) vibronic absorption peak at 2.87 $\pm$ 0.01 eV, superimposed on the red-edge of the X_g band.[101,105,106] This absorption grows in proportion to the film β-phase fraction (c.f. panels (c) and (d)) and is accom-

panied by additional spectral changes associated with the higher vibronics of the X_β $S_0 - S_1$ optical transition, that lie in the vicinity of the X_g absorption peak.[101, 105, 106] PL spectra were measured with excitation wavelength set to 3.31 eV (375 nm). For both glassy- and β-phase samples, the thin-film PL spectra reveal relatively well-resolved vibronic structures; as noted in Section 1.4.5, absorption probes the whole ensemble of chain segment conformations whilst PL occurs only from a self-selected subset of lower energy sites following energy transfer within the ensemble. In the glassy case (c.f. Figure 4.1 (a)), the X_g $S_1 - S_0$ (0-0), (0-1) and (0-2) PL vibronic peaks appear at 2.93 eV (423 nm), 2.77 eV (448 nm) and 2.58 eV (481 nm) whereas following β-phase chain segment formation the PL vibronic peaks red-shift to 2.83 eV (438 nm), 2.66 eV (467 nm) and 2.49 eV (497 nm), also becoming better resolved (c.f. Figure 4.1 (b), (c), (d)). β-phase chain segments have a reduced optical gap on account of their enhanced conjugation and their well-defined nature leads to the observed reduction in inhomogeneous broadening.[106, 118] Efficient and rapid ($\sim$ ps) exciton transfer from glassy- to β-phase chain segments then leads to X_β emission dominating the PL spectrum even at relatively low β-phase fractions;[111, 118] β-phase segments act as a self-dopant to which glassy-phase excitations are funneled.[134]

4.2.2 Optical Constants

The optical constants for all eight β-phase fraction films (0, 1.1, 1.5, 3.7, 10.0, 12.3, 13.9 and 15.8 %), were determined using VASE[1]. Recognizing that PFO chains tend to lie preferentially within the plane of the film[134–136] a uniaxial anisotropic model was used to fit these data and extract the in-plane (ordinary), (n_{xy}, k_{xy}), and out-of-plane (extra-ordinary), (n_z, k_z), spectral components of the complex refractive index $\tilde{n} = n + ik$. Interferometric enhancement of the measurement sensitivity allows a

[1]For each sample, three reflection-geometry measurements were performed with light incident at 45°, 50°, and 55° (angles of incidence are quoted relative to the plane normal), together with a normal incidence (0°) transmittance measurement.

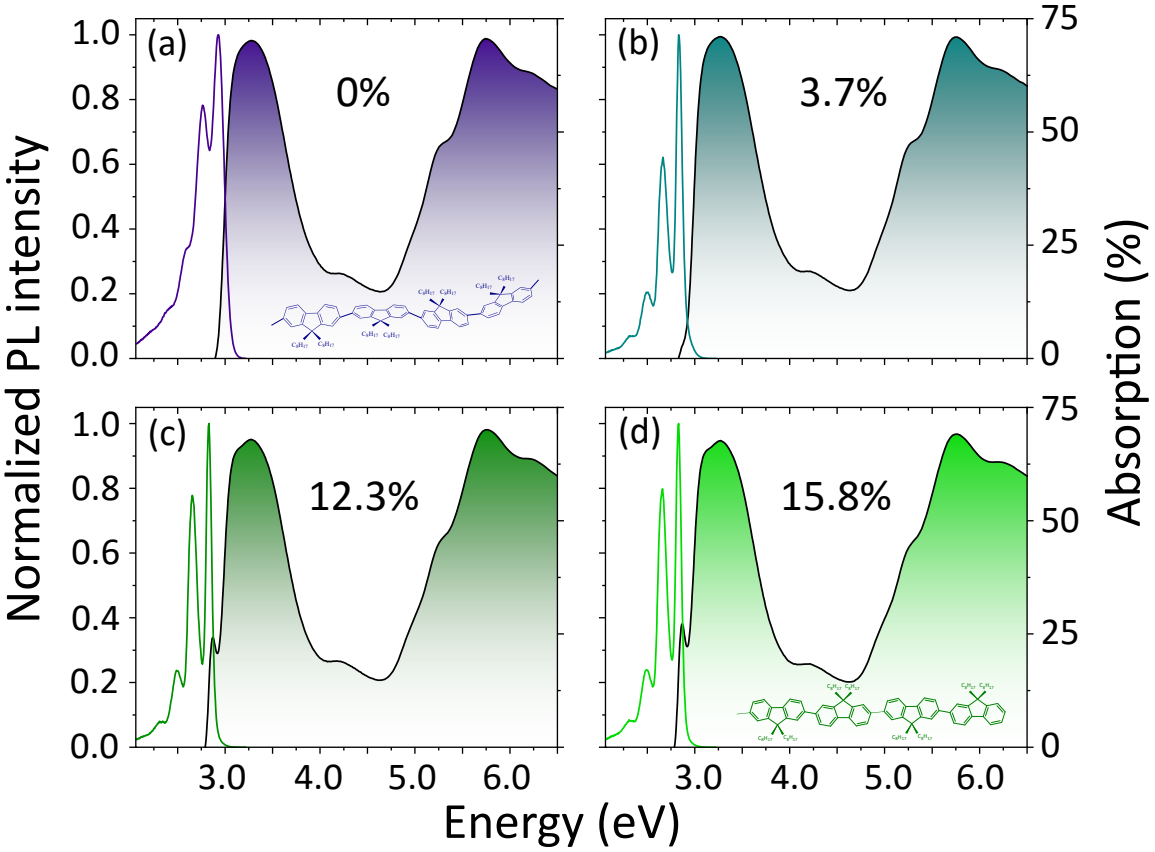


Figure 4.1: Absorption and PL spectra for spin-coated PFO films containing: (a) 0 (glassy-phase), (b) 3.7, (c) 12.3, and (d) 15.8% β-phase chain segments. Note the emergence of a shoulder (b) and then a resolved peak ((c) and (d)) on the red edge of the absorption with increasing β-phase fraction. A schematic glassy-phase chain segment (one conformer of many) is shown in panel (a) and the β-phase chain extended structure in panel (d).

more accurate determination of the refractive index anisotropy[136] but that is not a key concern for the current work. Previous studies have reported ellipsometry-derived values for (n_{xy}, k_{xy}) and (n_z, k_z) for glassy PFO[134,135,137] and have modeled (n_{xy}, k_{xy}) for different β-phase fractions, using a semi-empirical approach based on the separability of X_g and X_β contributions.[109,109,112] Our experiments agree with and extend those earlier results by providing experimental data for a systematic and wide ranging variation in β-phase fraction.

Thin film optical constants determined for four β-phase fractions are shown in Figure 4.2, with data for the other four films presented in Appendix B (Figure B.2).

As expected, emergence of the X_β (0-0) vibronic peak in k leads to a correspondingly significant enhancement in n across the PL spectral range.[108,109] As a direct consequence, spatial patterning of the β-phase fraction, for example using dip pen nanolithography, then allows the fabrication of photonic structures such as laser gratings.[112]

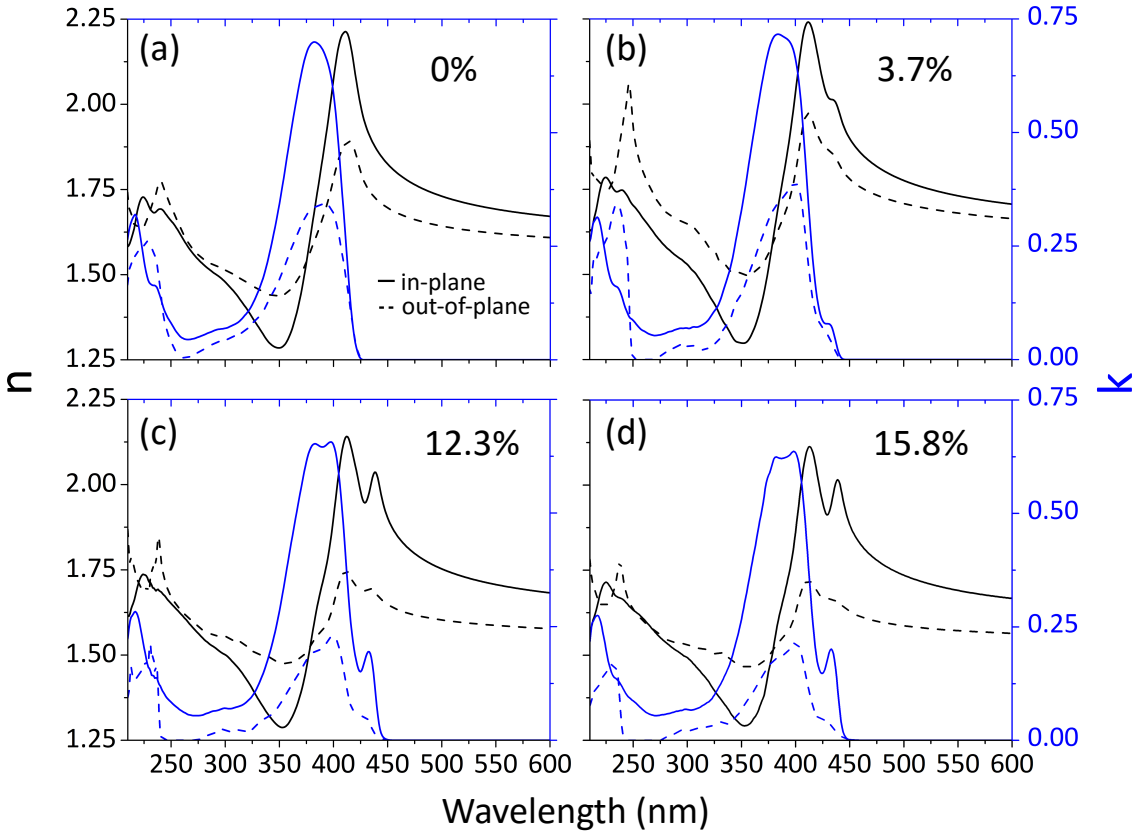


Figure 4.2: Optical constants for spin-coated PFO thin films containing: (a) 0 % (glassy-phase), (b) 3.7, (c) 12.3, and (d) 15.8% β-phase chain segments. The black and blue lines are, respectively, the real (n) and imaginary (k) parts of the complex refractive index, $\tilde{n} = n + ik$. Solid lines give in-plane (n_{xy}, k_{xy}) and dashed lines out-of-plane (n_z, k_z) values.

4.3 Exciton-Polariton Physics: Measurement and Simulation

4.3.1 Microcavity Fabrication

TMC based on the optical constants presented in Figure 4.2 were used to design the Al-PFO-Al microcavity structures and to interpret the observed angle-resolved reflectivity and PL results. Microcavities consisting of films of PFO sandwiched between 100 nm bottom and 23 nm top Al mirrors were fabricated for all eight β-phase fractions. The mirrors were thermally evaporated at a base pressure of $\sim 10^{-7}$ mbar on cleaned fused silica substrates (bottom mirror) and on top of the PFO film (top mirror); the latter was spin-coated onto the bottom mirror from toluene solutions containing varying concentrations (identical to the ones used for the bare films) of 1,8-diiodooctane additive, the resulting polymer film thicknesses were determined by fitting TMC to the reflectivity spectra, yielding 82 to 92 $\pm$ 2 nm.

4.3.2 Angle-Resolved Reflectivity Spectra for Varying β-phase Fractions

Reflectivity spectra (across the energy range 2.5 to 5 eV) were measured for incidence angles between 45 and 75° and plotted as R intensity maps on an energy vs angle plane. Both TE- and TM-polarizations were measured since they show significantly different behaviour.[138] The TE-polarized results for four (0%, 3.7%, 12.3%, and 15.8%) of the eight microcavities are shown in Figure. 4.3, with the other four datasets in Appendix B (Figure B.3). For each map, the reflectivity minima (polariton energy levels) obtained via TMC (white dashed-lines) using the optical constants from Figure. 4.2 are overlaid on the experimental dispersions (presented as colour-coded R intensities). There are two resolved levels (LP and UP) for β-phase fractions

$\leqslant 1.5\%$, and three levels (LP, MP and UP) evident for β-phase fractions $\geqslant 3.7\%$; the use of these labels is discussed in the following sections. For each panel, the inset shows the spectral dispersion of the lowest polariton branches (LP only for (a), LP and MP for (b), (c) and (d)) plotted between 2.80 and 2.98 eV for incidence angles, from bottom to top, of 45, 60 and 75°. In addition, to the right of each panel is the corresponding, colour-rendered, in-plane extinction coefficient spectrum.

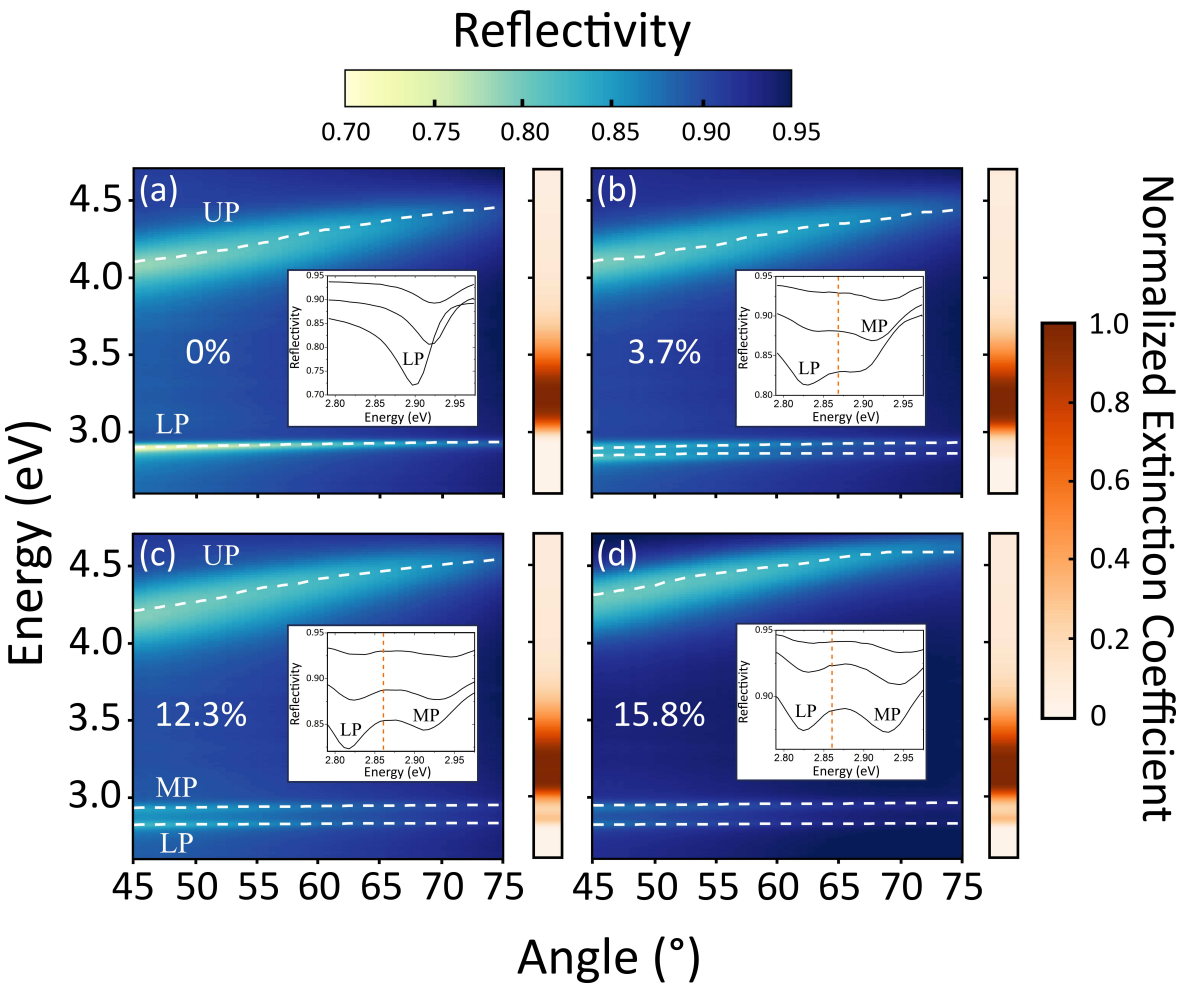


Figure 4.3: Experimental, angle-resolved, TE-polarized reflectivity maps for microcavities containing (a) 0, (b) 3.7, (c) 12.3, and (d) 15.8% β-phase chain segments. The inset to each panel shows the spectral dispersion of the polariton branches between 2.80 and 2.98 eV for incidence angles (bottom to top) 45, 60 and 75°. Note the splitting of the LP into two separate branches (LP and MP) for $\geqslant$ 3.7% β-phase fraction (panels (b), (c) and (d)), spaced either side of the X_β (0-0) vibronic peak at 2.87 eV (3.7%) and 2.86 eV (12.3%, 15.8%) (orange dashed vertical line). The corresponding normalized, in-plane, bare-film, colour-rendered extinction coefficient spectra taken from Figure. 4.2 are shown to the right of each map. Also shown, as overlaid white dashed lines, are the reflectivity minima dispersion curves obtained from TMC.

From Figure 4.3 (a) the energy splitting between the X_g-derived LP and UP branches clearly exceeds 1 eV (analytical derivation of the Rabi energy is perfomed in Section 4.4). The LP also has a much narrower FWHM linewidth (0.05 $\pm$ 0.005 eV at 45°) than does the UP (0.31 $\pm$ 0.05 eV), generally a signature of motional narrowing

effects within the inhomogeneously broadened $S_0 - S_1$ transition as the photon mode energy gets closer to the centre of the excitonic distribution (c.f. extinction coefficient spectrum to right of panel). Quantification of the associated coupling parameters is performed in Section 4.4.

The R-map in Figure 4.3 (b), for the $3.7 \pm 0.5\%$ β-phase fraction film, shows the appearance of an additional polariton branch. The resulting MP branch lies relatively close to the LP branch of the 0% cavity with a new LP branch emerging at lower energy. Analogous behaviour is seen in Figure 4.3 (c) and (d) with an increasing LP to MP energy separation as the β-phase fraction grows; detailed analysis of this behaviour is presented in Section 4.5.2. The panel insets show this splitting in greater detail, presenting energy cross-sections at fixed angles.

For the 12.3% β-phase cavity (Figure 4.3 (c) inset), the LP FWHM at 45° was fitted to be 0.053 ± 0.01 eV, with the error largely arising from the proximity of the MP. The LP R-dip at this angle is significantly deeper than that for the MP but with increasing angle, equivalent to increasing the photon mode energy, the relative intensity of the R-dips reverses and the MP becomes the deeper one. This is entirely as expected for the anti-crossing behaviour observable in SC.

4.3.3 Angle-Resolved Photoluminescence Emission

Angle-resolved PL emission was measured with the excitation energy set to 3.31 eV (375 nm). Spectra were recorded for emission angles between 10 and 65° at 2.5° steps and a polarizer was used to separate TE and TM polarizations. The excitation energy was chosen to optically pump the intense absorption line arising predominantly from glassy-phase X_g $S_0 - S_1$ optical transitions. Figure 4.4 shows normalized PL intensity maps plotted on energy vs angle planes for both TE- ((a) and (b)) and TM-polarized ((c) and (d)) emission from 0% ((a) and (c)) and 12.3% ((b) and (d)) β-phase microcavities. The dashed blue lines are TMC of the LP dispersion as per

Figure 4.3. The colour-rendered free-space unpolarized PL intensity spectra for bare films are plotted to the left and right of their respective PL maps; the panels to the left of (a) and (c) corresponding to 0% and the panels to the right of (b) and (d) to 12.3% β-phase fraction. In all cases the microcavity emission is dominated by a single peak originating from the LP, both in the presence and absence of β-phase chain segments.

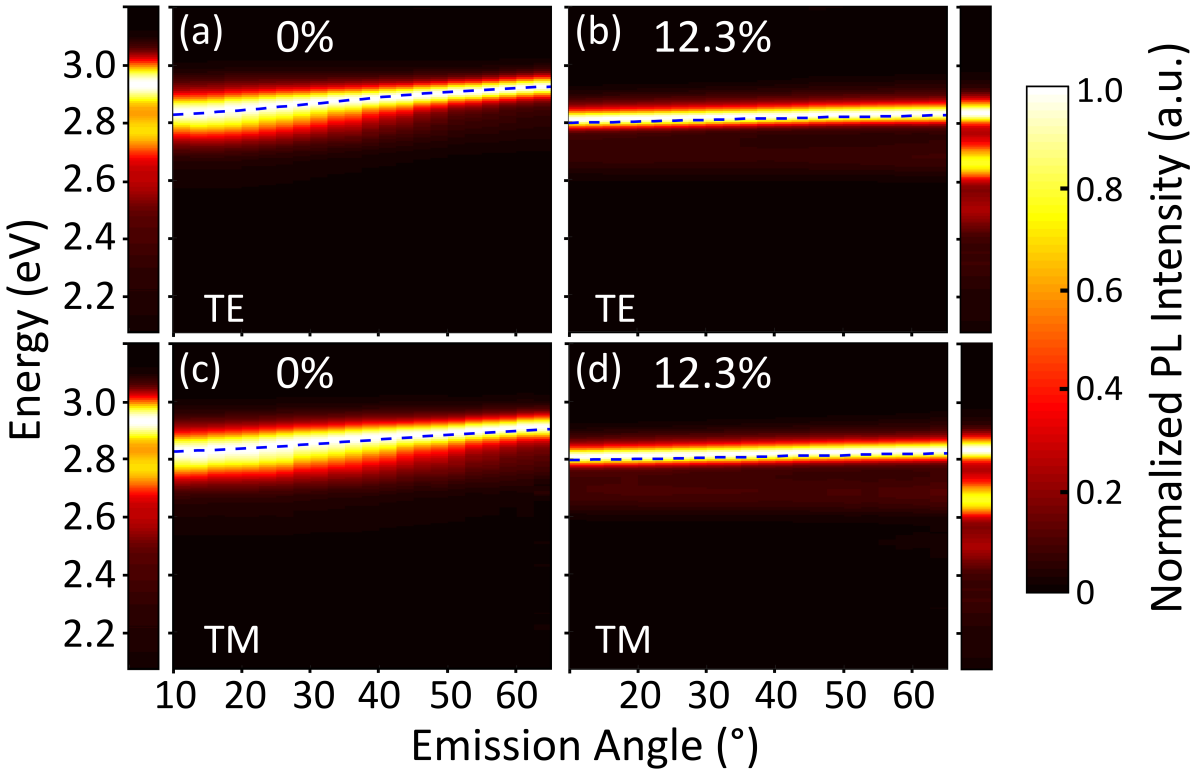


Figure 4.4: Angle-resolved PL spectral intensity maps for microcavities containing 0% ((a) and (c)) and 12.3% ((b) and (d)) β-phase chain segments, with TE ((a) and (b)) and TM ((c) and (d)) polarized spectra plotted separately. The colour-rendered spectra to the left of (a) and (c) and right of (b) and (d) present the PL emission obtained for the corresponding bare films (Figure 4.1 (a) and (c)). The overlaid blue dashed line is the LP angular dispersion obtained from TMC.

At 45°, for 0% β-phase, the TE- and TM-polarized emission FWHM linewidths are both $\Delta E_{\mathrm{FWHM}} = 91 \pm 5$ meV. This is substantially (> six-fold) narrower than for PFO bare film X_{g} PL emission - where $\Delta E_{\mathrm{FWHM}} \approx 600$ meV, determined by the inhomogeneously broadened vibronic progression - and narrower even than the

deconvolved (0-0) vibronic peak for which $\Delta E_{\mathrm{FWHM}} \approx 135$ meV. It is shown further in Section 4.4 that for TE polarization this linewidth is also narrower than the photon mode linewidth (145 meV) of an equivalent cavity with an effective refractive index $n_{\mathrm{eff}} = 1.6$, consistent with results obtained in similar studies elsewhere.[22–24] At the same angle, for 12.3% β-phase fraction cavities, both TE- and TM-polarized $\Delta E_{\mathrm{FWHM}} = 50 \pm 3$ meV, comparable to the width of the LP (53 ± 10 meV) obtained from reflectivity, but narrower than the resolved (0-0) vibronic of the X_β PL emission from bare films ($\Delta E_{\mathrm{FWHM}} = 76 \pm 2$ meV). It is also almost three times narrower than the photon mode width (again 145 meV).

For the 0% cavity, the LP emission gradually blue-shifts from 2.82 eV to 2.92 eV, for both polarizations, as the angle increases from 10 to 65°. This relatively weak dispersion is directly comparable to that seen in other USC studies.[22–24] Introduction of X_β strong coupling further diminishes the LP dispersion and for the 12.3% cavity the LP is essentially dispersionless, with PL emission then becoming angle insensitive. As previously noted,[8] this is of direct interest for the fabrication of high spectral-purity LEDs that would not suffer from the significant angular blue-shift that is typical for weakly-coupled microcavity structures.[139,140] Further details are given in Appendix B Figure B.5 and accompanying text. In addition, although as a consequence of LP lineshape asymmetry there is weak (accounting for $< 10\%$ of the total) lower energy emission from the 12.3% cavity, this would not prevent the achievement of an exceptionally-saturated, deep-blue/violet LED emission. The measured LP PL spectrum corresponds to colour coordinate CIE $(x,y) = (0.161,0.018)$, with dominant wavelength 447 nm and 99% saturation (see Appendix B Figure B.5).

4.4 Theoretical Analysis

The large (> 1 eV) LP to UP splitting of the polariton energy levels relative to the centre of the X_{g} optical transition (3.25 eV) firmly suggests USC, a hypothesis that is confirmed *a posteriori* by determining the corresponding $\hbar\Omega_0$ through comparison to the HA model. In this chapter, two distinct exciton populations (X_{g} and X_β) simultaneously coupled to the cavity are considered. These populations are treated as spectrally localized oscillators (1 and 2) whereas in reality their oscillator strengths are rather more spread in energy, across resolved (X_β) and un-resolved (X_{g}) vibronic progressions that spectrally overlap. The nature of the coupling is, therefore, subject to further consideration in Section 4.5.2 but for now the theoretical analysis proceeds along the simpler (spectrally localized oscillator) path in order to more readily explore the essential features of the governing physics.

Following diagonalization of the full Hamiltonian, the characteristic matrix of the problem $M_{\mathbf{q}}$ is given by Equation2.45:

$$M_{\mathbf{q}} = \begin{bmatrix} \omega_{\mathrm{cav},\mathbf{q}} + 2D_{\mathbf{q}} & -i\frac{\Omega_{1,\mathbf{q}}}{2} & -i\frac{\Omega_{2,\mathbf{q}}}{2} & -2D_{\mathbf{q}} & -i\frac{\Omega_{1,\mathbf{q}}}{2} & -i\frac{\Omega_{2,\mathbf{q}}}{2} \\ i\frac{\Omega_{1,\mathbf{q}}}{2} & \omega_1 & 0 & -i\frac{\Omega_{1,\mathbf{q}}}{2} & 0 & 0 \\ i\frac{\Omega_{2,\mathbf{q}}}{2} & 0 & \omega_2 & -i\frac{\Omega_{2,\mathbf{q}}}{2} & 0 & 0 \\ 2D_{\mathbf{q}} & -i\frac{\Omega_{1,\mathbf{q}}}{2} & -i\frac{\Omega_{2,\mathbf{q}}}{2} & -\omega_{\mathrm{cav},\mathbf{q}} - 2D_{\mathbf{q}} & -i\frac{\Omega_{1,\mathbf{q}}}{2} & -i\frac{\Omega_{2,\mathbf{q}}}{2} \\ -i\frac{\Omega_{1,\mathbf{q}}}{2} & 0 & 0 & i\frac{\Omega_{1,\mathbf{q}}}{2} & -\omega_1 & 0 \\ -i\frac{\Omega_{2,\mathbf{q}}}{2} & 0 & 0 & i\frac{\Omega_{2,\mathbf{q}}}{2} & 0 & -\omega_2 \end{bmatrix}, \tag{4.1}$$

with $\omega_{i,\mathbf{q}} \in \{\omega_{\mathrm{LP},\mathbf{q}}, \omega_{\mathrm{MP},\mathbf{q}}, \omega_{\mathrm{UP},\mathbf{q}}, -\omega_{\mathrm{LP},\mathbf{q}}, -\omega_{\mathrm{MP},\mathbf{q}}, -\omega_{\mathrm{UP},\mathbf{q}}\}$. In the case of a single exciton oscillator, $M_{\mathbf{q}}$ reduces to the 4 x 4 Hopfield-like USC matrix. $\omega_{\mathrm{cav}}(\theta)$ can be approximated using Equation 3.1:

$$\omega_{\mathrm{cav}_{(\mathrm{TE,TM}),\mathbf{q}}} = \omega_{\mathrm{cav}}(0)\left(1 - \frac{\sin^2(\theta)}{n^2_{\mathrm{eff}_{\mathrm{TE,TM}}}}\right)^{-\frac{1}{2}} \tag{4.2}$$

where $n_{\text{eff}_{\text{TE,TM}}}$ is polarization dependent. The eigenvalues of $M_{\mathbf{q}}$ were fitted to the experimental results for each cavity, for both TE- and TM-polarization, using the PL maxima in the 10 - 45° range from Figure 4.4 together with the R-minima in the 45 - 75° range from Figure 4.3. The 4 x 4 HA matrix was used for the 0% microcavity, while the full matrix $M_{\mathbf{q}}$ of Equation 4.1 was used for β-phase fractions $\geqslant 3.7\%$. The 1.1 and 1.5 % β-phase microcavities were left out of the initial analysis as the β-phase content is too small/insufficiently spectrally separated to induce a splitting of the LP branch. They are briefly discussed in the following section in light of the results for the other microcavities.

The value of $\hbar\omega_1$ was set to be at the energy that corresponds to the mid-point of the integral oscillator strength for the X_{g} $S_0 - S_1$ optical transition using:

$$\int_{2.8}^{\hbar\omega_1} \epsilon(\omega)\mathrm{d}\omega = \frac{1}{2}\int_{2.8}^{3.7} \epsilon(\omega)\mathrm{d}\omega, \tag{4.3}$$

where $\epsilon(\omega)$ is the extinction coefficient for X_{g} in the 2.8 to 3.7 eV energy range; this yields $\hbar\omega_1 = 3.25$ eV. Conversely $\hbar\omega_2$ was set to the $S_0 - S_1$ (0-0) vibronic peak energy of the X_β in-plane extinction coefficient, namely 2.87 eV for 3.7 and 10% cavities and, reflecting a slight red-shift with increasing β-phase content, 2.86 eV for 12.3, 13.9 and 15.8% cavities.[101, 105, 106] This choice for $\hbar\omega_2$ is discussed further in the Section 4.5.2 and arises from the dominant contribution that the β-phase (0-0) vibronic transition appears to make when the 0% LP splits into MP and LP. It allows good fits to the data, whereas the equivalent integral to that used for $\hbar\omega_1$ gives inconsistent results.

Table 4.1 collects together pre-set and extracted parameter values for the 0 and $\geq 3.7\%$ cavities. Note that the fitted values for $n_{\text{eff}_{\text{TE}}} \sim 1.7$ are close to the background index of glassy-phase PFO (Figure 4.2 (a)), whereas $n_{\text{eff}_{\text{TM}}} \sim 2.5$ is significantly higher, as a result of the additional coupling of the TM-polarized photon mode to the Metal-Insulator-Metal (MIM) plasmon mode supported by the cavity.[22, 141, 142]

Figure 4.5 further presents (experimental and calculated) exciton, cavity, and polariton angular dispersions for the 0% ((a) and (c)) and 12.3% ((b) and (d)) cavities for both TE- ((a) and (b)) and TM-polarization ((c) and (d)). This shows a satisfactory agreement between the theoretical calculation and experimental measurements.

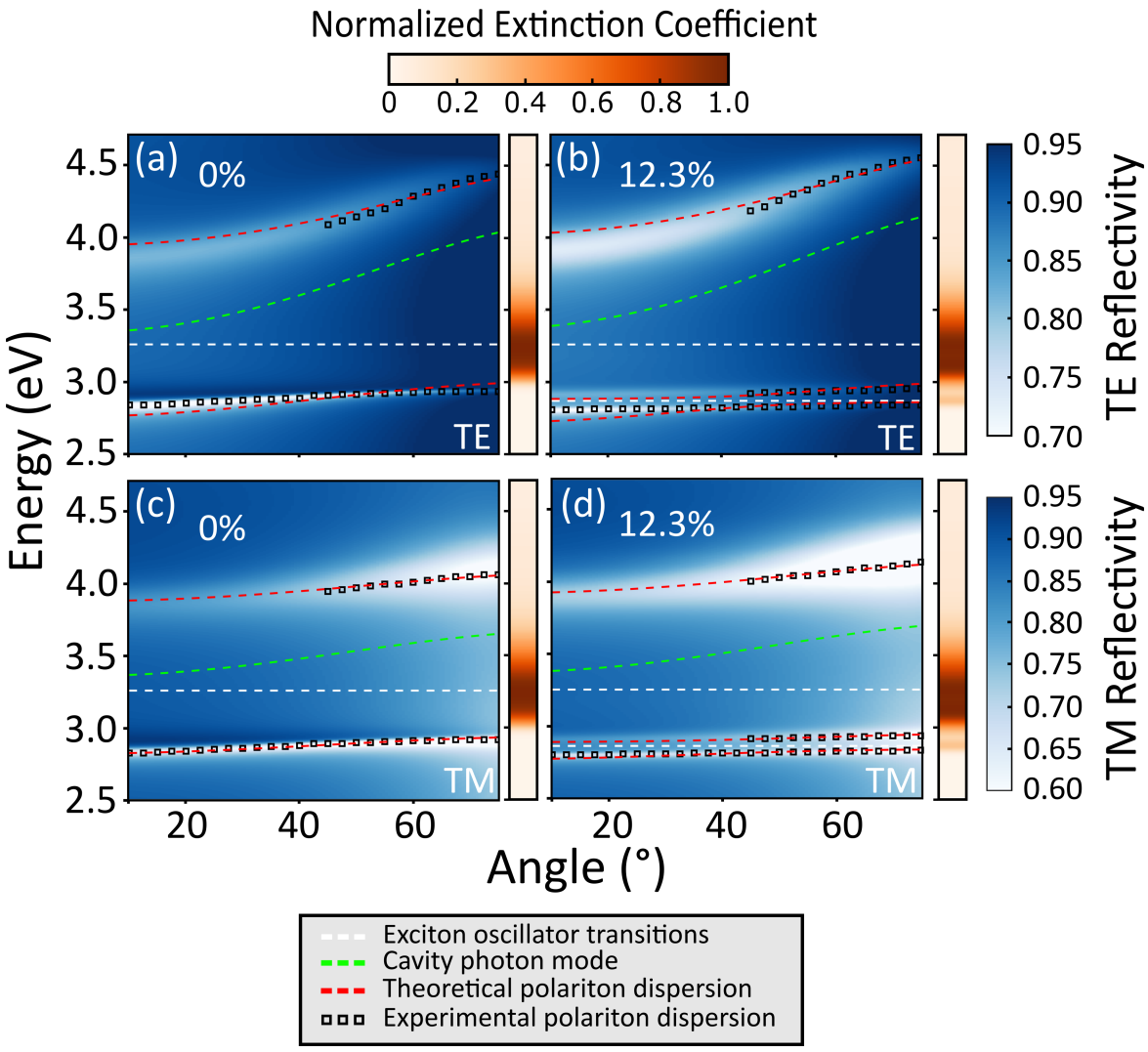


Figure 4.5: Experimental and calculated exciton, cavity, and polariton angular dispersions for the 0% ((a) and (c)) and 12.3% ((b) and (d)) cavities for both TE- ((a) and (b)) and TM-polarization ((c) and (d)). The background to each panel comprises the associated R-map obtained from TMC, on top of which are overlaid exciton oscillator energies (horizontal white dashed lines), experimental (black squares) polariton branch, and calculated coupling-free cavity photon mode (green dashed line) dispersions. The black squares data are LP PL maxima (Figure 4.4) for incidence angles between 15 and 45° and R-minima (Figure 4.3) between 45 and 75°, with $M_{\mathbf{q}}$ polariton eigenvalue fits shown by red dashed lines. The normalized in-plane extinction coefficients (Figure 4.2) for bare films with corresponding β-phase fractions are shown to the right of each panel.

β-phase content: $\%_\beta$ (%)	0	3.7 ± 0.5	10.0 ± 0.5	12.3 ± 0.5	13.9 ± 0.5	15.8 ± 0.5
$\hbar\omega_2$(eV)[1]	-	2.87	2.87	2.86	2.86	2.86
$\hbar\Omega_{01_{\mathrm{TE}}}$(meV)[2]	1180 ± 20	1230 ± 20	1230 ± 20	1270 ± 20	1290 ± 20	1300 ± 20
$\hbar\Omega_{01_{\mathrm{TM}}}$(meV)[3]	1050 ± 20	1020 ± 20	1100 ± 20	1110 ± 20	1120 ± 20	1140 ± 20
$\hbar\Omega_{02_{\mathrm{TE}}}$(meV)[4]	-	85 ± 10	126 ± 15	156 ± 10	168 ± 10	172 ± 10
$\hbar\Omega_{02_{\mathrm{TM}}}$(meV)[5]	-	100 ± 10	123 ± 10	170 ± 10	175 ± 10	171 ± 10
$n_{\mathrm{eff}_{\mathrm{TE}}}$[6]	1.7 ± 0.1	1.6 ± 0.1	1.7 ± 0.1	1.7 ± 0.1	1.7 ± 0.1	1.7 ± 0.1
$n_{\mathrm{eff}_{\mathrm{TM}}}$[7]	2.5 ± 0.1	2.5 ± 0.1	2.6 ± 0.1	2.5 ± 0.1	2.4 ± 0.1	2.3 ± 0.1
$\hbar\omega_{\mathrm{cav}_{\mathrm{TE}}}(0)$(eV)[8]	3.33 ± 0.06	3.28 ± 0.04	3.24 ± 0.06	3.37 ± 0.04	3.42 ± 0.05	3.50 ± 0.1
$\hbar\omega_{\mathrm{cav}_{\mathrm{TM}}}(0)$(eV)[9]	3.35 ± 0.02	3.32 ± 0.04	3.30 ± 0.05	3.37 ± 0.04	3.40 ± 0.05	3.42 ± 0.04

[1] Exciton oscillator 2 transition energy.
[2] TE-polarized Rabi energy associated with exciton 1 for $\omega_{\mathrm{cav}_{\mathrm{TE}}} = \omega_1$ (see definition in the text).
[3] TM-polarized Rabi energy associated with exciton 1 for $\omega_{\mathrm{cav}_{\mathrm{TM}}} = \omega_1$
[4] TE-polarized Rabi energy associated with exciton 2 for $\omega_{\mathrm{cav}_{\mathrm{TE}}} = \omega_2$ (see definition in the text).
[5] TM-polarized Rabi energy associated with exciton 2 for $\omega_{\mathrm{cav}_{\mathrm{TM}}} = \omega_2$
[6] Effective refractive index for TE polarization.
[7] Effective refractive index for TM polarization.
[8] TE-polarized energy of the bare cavity mode at normal incidence.
[9] TM-polarized energy of the bare cavity mode at normal incidence.

Table 4.1: Extracted and pre-set parameter values for microcavities containing various β-phase fractions, as modelled in the text. The values are shown for both TE- and TM-polarization.

Starting with the 0% microcavity (Figure 4.5 (a), TE-polarized), the fitted Rabi energy $\hbar\Omega_{01_{\mathrm{TE}}} = 1.18$ eV is slightly higher but still in good agreement with the value previously reported by Tropf *et al.* (1.09 eV) for a similar PFO cavity.[137] The coupling ratio $\eta_1 = \frac{\Omega_{01_{\mathrm{TE}}}}{\omega_1} = 36\%$ clearly exceeds the $\approx 20\%$ value that delineates USC[22] and thereby justifies use of the HA Hamiltonian. The value of $\hbar\Omega_{01_{\mathrm{TM}}} = 1.05$ eV (Figure 4.5 (b), Table 4.1) is somewhat lower than $\hbar\Omega_{01_{\mathrm{TE}}}$ due to a strong tendency for PFO chains to lie within the film plane,[134–136] reducing the out-of-plane oscillator strength. The exciton $|x_{i,1,\mathbf{q}}|^2$ and photon fractions $|w_{i,\mathbf{q}}|^2$ of the LP and UP for TE-polarization are represented by dashed lines in Figure 4.6 (a) and (c). As expected, the LP branch becomes increasingly exciton-like and the UP increasingly photon-like as the angle, i.e. the in-plane wave vector, is increased. Also presented in Figure 4.6

(d) by the dashed line is the content of virtual photons ($|y_{\mathrm{LP},\mathbf{q}}|^2 + |y_{\mathrm{UP},\mathbf{q}}|^2$) in the GS: as η exceeds 20%, the squeezed vacuum forms where the virtual photon content is expected to be preserved even in the presence of high losses.[75]

The 12.3% cavity (Figure 4.5 (b) and (d)) is representative of the $X_\beta \geqslant 3.7\%$ set and shows the already noted (Figure 4.3 (c)) splitting of the 0% cavity LP into new LP and MP branches. The slight increase (Table 4.1) in the USC $\hbar\Omega_{01_{\mathrm{TE,TM}}}$ for this and the other microcavities in the set, is discussed more fully in Section 4.5.2, with specific X_β contributions considered to more than compensate for the reducing X_g absorption coefficient as the two exciton populations interchange. The simultaneous increase (Table 4.1) in $\hbar\Omega_{02_{\mathrm{TE}}}$ ($\hbar\Omega_{02_{\mathrm{TM}}}$) from 85 ± 10 to 172 ± 10 meV (100 ± 10 to 175 ± 10 meV) on increasing the X_β fraction from 3.7 to 15.8% accompanies an evident increase in X_β extinction coefficient and is also discussed in more detail in Section 4.5.2. The exciton $|x_{i,j,\mathbf{q}}|^2$ and photon $|w_{i,\mathbf{q}}|^2$ fractions are presented (solid lines, TE-polarization) in Figure 4.6 (a), (b) and (c) for the LP, MP and UP branches, respectively, of the 12.3% cavity. A substantial mixing of exciton oscillators 1 and 2 in the LP and MP branches is apparent in Figure 4.6 (a) and (b). In addition, a very small contribution ($\sim 0.2\%$) from exciton oscillator 2 is also present in the UP (Figure 4.6 (c)), highlighting the ability for exciton-polariton physics to create complex energy pathways between polariton levels lying at very different energies. Lastly, as expected from $\hbar\Omega_{02} \ll \hbar\Omega_{01}$, the virtual exciton content in the GS, being the sum of $|z_{\mathrm{LP},1,\mathbf{q}}|^2 + |z_{\mathrm{MP},1,\mathbf{q}}|^2 + |z_{\mathrm{UP},1,\mathbf{q}}|^2$ for oscillator 1 and $|z_{\mathrm{LP},2,\mathbf{q}}|^2 + |z_{\mathrm{MP},2,\mathbf{q}}|^2 + |z_{\mathrm{UP},2,\mathbf{q}}|^2$ for oscillator 2, is dominated by the former (blue solid line).

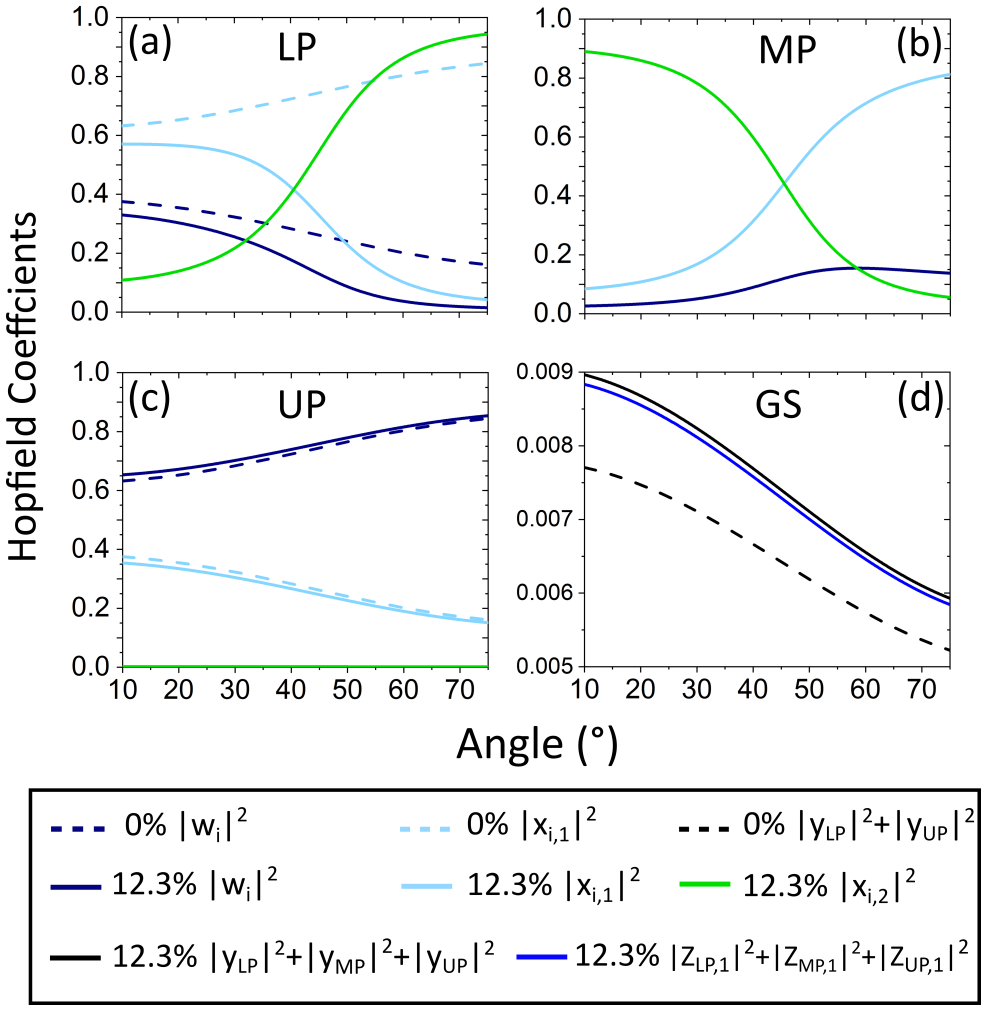


Figure 4.6: TE-polarized Hopfield coefficients for 0% and 12.3% microcavities, obtained using the model presented in Section 4.4. Results are shown for: (a) LP, (b) MP, (c) UP, and (d) GS. Note the efficient mixing of excitons from populations 1 (solid light blue line) and 2 (solid green line) within the LP (a) and MP (b) of the 12.3% microcavity.

4.5 Discussion

4.5.1 Limitations of the Theoretical Model

A maximum difference of order 0.1 eV can be observed between the TE-polarization LP fit and experimental data for the 0% and 12.3% cavities in Figure 4.5 (a) and (b). Equation 3.1, used to determine the photon mode $\omega_{\mathrm{cav}_{\mathrm{TE,TM}}}(\theta)$ dispersion, is expected

to be a good approximation below the light line of the material ($\frac{\sin^2(\theta)}{n_b^2} \ll 1$ where n_b is the background refractive index of the material) and where, as here, the photon energy is far from the metal mirror plasma frequency ($\hbar\omega_p > 12$ eV for Al).[22] Note also that if the full trigonometric equations[141,142] are used instead, then only minor alterations (≈ 0.02 eV) occur in the computed LP and UP branch dispersions (see Appendix B Section B.3 for a full derivation). This indicates that the use of Equation 3.1 is reasonable and that other factors must contribute more to the observed discrepancy.

Previous studies have noted that the presence of higher lying exciton resonances will affect the polariton dispersion.[22,137] Such resonances are clearly visible in Figure 4.1 (a) and Figure 4.2 (a) for energies located above 5 eV. TMC using the optical constants presented in Figure 4.2 (a) show that for any photon mode with high enough energy, these resonances yield multiple anti-crossings for which a straightforward analysis is not possible. To test whether adding just a single composite higher energy exciton oscillator, as done by Tropf *et al.*,[137] can improve the fit to the LP and UP branches (which would then become respectively LP and MP), the eigenvalues of the full matrix $M_{\mathbf{q}}$ were fitted to the 0% microcavity experimental results, with $\hbar\omega_2$ and its Rabi energy $\hbar\Omega_{02}$ allowed to vary respectively in the 4.5 to 6 eV and 0 to 2 eV range. No significant improvement to the fitting residuals was found using this approach, demonstrating that the addition of a single higher energy exciton oscillator does not provide a satisfactory explanation either.

The spectral shape of the exciton extinction coefficient is expected also to be an important consideration[89] which we discuss in the next section following a more detailed consideration of the Rabi splitting energies $\hbar\Omega_{02_{\mathrm{TE,TM}}}$ for the $\geq 3.7\%$ β-phase microcavities.

4.5.2 Rabi Energies and their Dependence on the Oscillator Strengths of the X_{g} and X_{β} Populations

As examined in Chapter 2, when radiative damping is included, the Rabi splitting energy associated with an exciton population is given by Equation 2.10:

$$\hbar\Omega_0 = 2\sqrt{g_{\mathrm{res}}^2 - \frac{(\gamma_{\mathrm{ex}} - \gamma_{\mathrm{cav}})^2}{4}} \tag{4.4}$$

where g_{res} is from Equation 2.11:

$$g_{\mathrm{res}} = \sqrt{N}\frac{\boldsymbol{\mu}.\mathbf{E}}{\hbar}, \tag{4.5}$$

and γ_{cav} and γ_{ex} are respectively the cavity and exciton radiative broadenings.

In this chapter, both glassy- (X_{g}) and β-phase (X_{β}) excitons have radiative lifetimes $\leqslant 1$ ns[7] and from the uncertainty principle, such lifetimes would yield radiative broadening of order a few μeV, γ_{ex} can therefore be neglected in Equation 4.4.

The FWHM of the cavity is ~ 145 meV which is comparable to the values of $\hbar\Omega_{02_{\mathrm{TE}}}$. Besides, inhomogeneous broadening can not directly replace homogeneous broadening as it was shown to affect the Rabi energy when comparable in width with no simple analytical correspondence (Section 2.4.6). Indeed, the values of $\hbar\Omega_{02_{\mathrm{TE}}}$ extracted in Section 4.4 fall in the range 85 to 172 meV and are therefore directly comparable to a lower bound estimate of the inhomogeneous broadening (the (0-0) vibronic peak of the in-plane extinction coefficient, $k_{X_{\beta}}(E)$ for the β-phase in Figure 4.7 (b) has a FWHM of 73 meV).

In addition, another feature of the exciton distributions would be overly simplified using Equation 2.10, namely that they both result from a superposition of underlying vibronic contributions, respectively unresolved and resolved for the glassy- and β-phase samples. As highlighted in Section 2.5.2 the effects of these vibronic pro-

gressions require calculation intensive approaches. It is, however, expected that the energy spread of the vibronic progressions ($\geqslant$ hundreds of meV) will always undermine the validity of using Equation 2.10.

Following these considerations, we have chosen to directly use Equation 4.5 to obtain an approximative Rabi energy $\hbar\Omega_{02}$. This approach is not wholly satisfactory and more accurate derivations, relying on suitable molecule-focused models, will need to be pursued in future research on this topic. We consider, however that it is appropriate in the context of this thesis. We can then derive that for j separable and spectrally distinct exciton oscillators that the Rabi energies should scale as:

$$\hbar\Omega_{0j} \propto \sqrt{N_j f_j}, \tag{4.6}$$

where N_j and f_j are respectively the number of type-j oscillators and their oscillator strength. For simplicity, it is assumed at first, somewhat naïvely, that the type-1 and -2 oscillators correspond strictly to X_g ($j = 1$) and X_β ($j = 2$) and it is noted that the proportionality constant is identical for both. Next, to allow comparison of the corresponding Rabi energies it is further assumed that the average chromophore lengths for X_g and X_β comprise the same number of monomer units[133] such that the total number of excitons in the polymer film, $N_0 = N_\mathrm{g} + N_\beta = \frac{(100-\%_\beta)N_0}{100} + \frac{\%_\beta N_0}{100}$ where $\%_\beta$ is the β-phase fraction. Equation 4.6 is then rewritten for both populations:

$$\hbar\Omega_{01_{\mathrm{TE,TM}}}(100 - \%_\beta) = A_{\mathrm{TE,TM}}\sqrt{f_{\mathrm{g}_{\mathrm{TE,TM}}}}\sqrt{100 - \%_\beta} \tag{4.7}$$

and

$$\hbar\Omega_{02_{\mathrm{TE,TM}}}(\%_\beta) = A_{\mathrm{TE,TM}}\sqrt{f_{\beta_{\mathrm{TE,TM}}}}\sqrt{\%_\beta}, \tag{4.8}$$

with $f_{\mathrm{g}_{\mathrm{TE,TM}}}$ and $f_{\beta_{\mathrm{TE,TM}}}$ the oscillator strengths associated with X_g and X_β, respectively, and $A_{\mathrm{TE,TM}}$ a population-independent constant. Figure 4.7 (a) shows the

resulting fit of Equation 4.8 to the $\hbar\Omega_{02_{\mathrm{TE}}}$ values from Table 4.1 for $\%_\beta \geqslant 3.7\%$; similar results are obtained for the TM-polarization data. The fit gives:

$$\hbar\Omega_{02_{\mathrm{TE}}}(\%_\beta) = (43.4 \pm 0.9)\sqrt{\%_\beta}\ \mathrm{meV} \tag{4.9}$$

However, using time-dependent Density Functional Theory (DFT), with the same assumption concerning equal X_{g} and X_β chromophore length as above, Huang *et al.*[133] calculated that the ratio $r = \sqrt{\frac{f_\beta}{f_{\mathrm{g}}}}$ should be equal to 1.04. For comparison, Equations 4.7, 4.8, 4.9 together with Rabi energy $\hbar\Omega_{01_{\mathrm{TE}}}(0\%) = 1.18$ eV (see Table 4.1) and the assumption $\sqrt{\frac{f_\beta}{f_{\mathrm{g}}}} \approx \sqrt{\frac{f_{\beta_{\mathrm{TE}}}}{f_{\mathrm{g}_{\mathrm{TE}}}}}$, allow derivation of an approximate 'experimental' r-value $\approx \frac{\hbar\Omega_{02_{\mathrm{TE}}}(100\%)}{\hbar\Omega_{01_{\mathrm{TE}}}(0\%)} = \frac{434}{1180} = 0.368$, which is almost three times smaller than the calculated ratio. In addition, if $\hbar\Omega_{01_{\mathrm{TE}}}$ was indeed only determined by contributions from X_{g}, then one would expect this splitting to decrease as the X_β fraction increased. What is observed, however, is that $\hbar\Omega_{01}$ slightly increases (by ~ 0.1 eV) with increasing X_β fraction.

Approaching these inconsistencies from a different direction, the experimental Rabi energies and ratio $r = 0.368$ are used to assess in more detail the contributions of X_{g} and X_β to the exciton-photon coupling. Using the known separability of the X_{g} and X_β optical coefficients[108,109,112] a 0.842 (i.e. $1 - \frac{\%_\beta}{100}$) weighted in-plane $k_{X_{\mathrm{g}}}(E)$ glassy-phase extinction coefficient spectrum (Figure 4.2 (a)) was subtracted from the corresponding 15.8% spectrum (Figure 4.2 (d)) to yield an effective $k_{X_\beta}(E)$ spectrum (Figure 4.7 (b)). As expected,[101,105,106] the spectral distribution of $k_{X_\beta}(E)$ shows a clearly resolved vibronic progression with $S_0 - S_1$ (0-0), (0-1) and (0-2) vibronic peaks. Among these, the (0-1) and (0-2) vibronic peaks overlap fully with $k_{X_{\mathrm{g}}}(E)$ which falls to zero at around 2.91 eV, with only the (0-0) lying at lower energy. As a consequence, one might anticipate that the X_β vibronic peaks play different roles.

Using Equation 1.21 the X_{g} and X_{β} oscillator strengths are given by:

$$f_{\mathrm{g},\beta} \propto \int k_{X_{\mathrm{g}},X_{\beta}}(E)\mathrm{d}E, \tag{4.10}$$

where the proportionality constant does not depend on the conformation. Considering that the MP (located at around 2.90 eV in Figure 4.5 (d)) lies below the low energy cut-off for $k_{X_{\mathrm{g}}}(E)$ one may reasonably assume that the oscillator strength contributing to the splitting between MP and LP derives entirely from X_{β}:

$$N_2 = N_{\beta}. \tag{4.11}$$

The oscillator strength f_{β} is, however, too large (by a factor of 8) to explain the magnitude of $\hbar\Omega_{02_{\mathrm{TE}}}$ obtained from Figure 4.7 (a). Instead, one can define an energy E_l such that the necessary oscillator strength f_2 is the partial integral of $k_{X_{\beta}}(E)$ from 2.7 to E_l eV:

$$f_2 = \frac{\int_{2.7}^{E_l} k_{X_{\beta}}(E)\mathrm{d}E}{\int_{2.7}^{3.4} k_{X_{\beta}}(E)\mathrm{d}E} f_{\beta} = R(E_l) f_{\beta}. \tag{4.12}$$

Conversely, as already noted above, the variation of $\hbar\Omega_{01}$ with X_{β} fraction tells us that

$$N_1 = N_{\mathrm{g}} + N_{\beta} = N_0, \tag{4.13}$$

and that f_1 combines a weighted sum of X_{g} and X_{β} contributions, comprising the whole of f_{g} and a fractional part of f_{β}, namely $f_{\beta} - f_2$ or equivalently the partial integral of $k_{X_{\beta}}(E)$ across the range from E_l to 3.4 eV:

$$f_1 = \frac{N_{\mathrm{g}} f_{\mathrm{g}} + N_{\beta}(1 - R(E_l)) f_{\beta}}{N_0} = \left[\frac{100 - \%_{\beta}}{100r^2} + \frac{\%_{\beta}(1 - R(E_l))}{100}\right] f_{\beta}. \tag{4.14}$$

From Equation 4.6 and Equation 4.11 to Equation 4.14 we obtain:

$$\frac{\hbar\Omega_{02_{\mathrm{TE,TM}}}}{\hbar\Omega_{01_{\mathrm{TE,TM}}}} = \sqrt{\frac{N_2 f_2}{N_1 f_1}} = \sqrt{\frac{\%_\beta f_2}{100 f_1}} = \sqrt{\frac{\%_\beta R(E_l)}{\frac{100-\%_\beta}{r^2} + \%_\beta(1-R(E_l))}}. \tag{4.15}$$

Numerically solving Equation 4.15 for the 15.8% cavity with $\hbar\Omega_{01_{\mathrm{TE}}} = 1.30$ eV and $\hbar\Omega_{02_{\mathrm{TE}}} = 172$ meV (Table 4.1) leads to $E_l \approx 2.85$ eV. This does not provide any particular intuition other than confirming that a relatively small fraction of the overall X_β oscillator strength actually contributes to the MP to LP splitting.

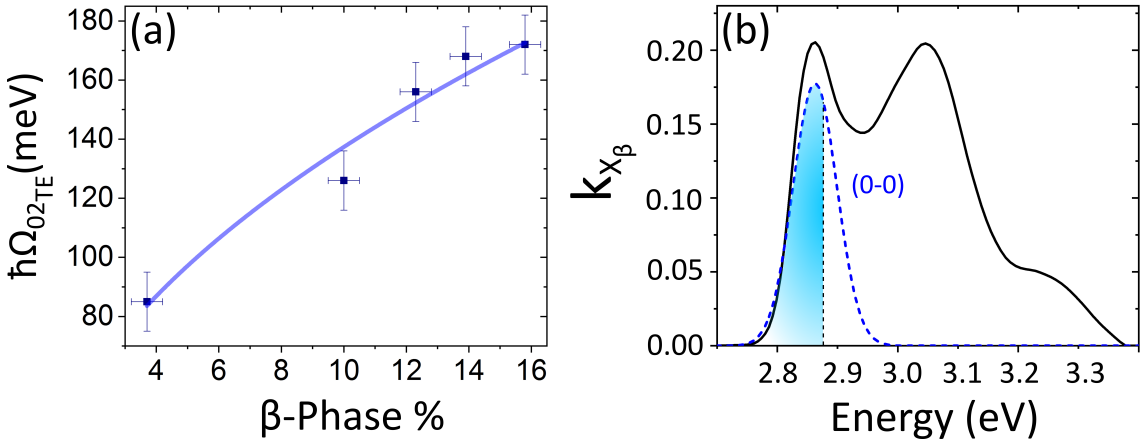


Figure 4.7: (a) Rabi splitting energy ($\hbar\Omega_{02_{\mathrm{TE}}}$, filled blue squares data) as a function of β-phase fraction. The solid blue line is the square-root fit ($\hbar\Omega_{02_{\mathrm{TE}}}$ =(43.4±0.9) $\sqrt{\%_\beta}$ meV) described in the text. (b) In-plane extinction coefficient, k_{X_β}(E), for the β-phase component of a 15.8 % film, extracted from Figure 4.2(d) following the procedure described in Section 4.5.2. The oscillator strength associated with the light-blue highlighted part of the de-convolved (0-0) vibronic transition (dashed blue line) is sufficient to explain the observed Rabi-splitting ($\hbar\Omega_{02_{\mathrm{TE}}}$) between LP and MP. The remainder of the (0-0) together with the (0-1) and (0-2) vibronic transitions can then contribute to the Rabi-splitting ($\hbar\Omega_{01_{\mathrm{TE}}}$) between MP and UP, compensating for the interchange in exciton populations between X_{g} and X_β.

A different and perhaps more physical approach would be to ask: What fraction of the (0-0) vibronic peak is needed? This of course implicitly imposes a dominant role for the (0-0) peak, an action that is supported by the rationale used above to conclude that $N_2 = N_\beta$, namely that only $k_{X_\beta}(E)$ extends in energy below the MP at ≈ 2.90 eV. Here we add the extension that of $k_{X_\beta}(E)$ it is only the (0-0) vibronic that

so extends. The question is then readily addressed by fitting the $k_{X_\beta}(E)$ spectrum to Gaussians representing the three resolved vibronic peaks. The resultant (0-0) peak fit (dashed blue line) and the highlighted light blue region representing the required contribution are shown in Figure 4.7(b). Taking this approach also helps to rationalize the chosen values for $\hbar\omega_2$ in Section 4.4 as they are the corresponding (0-0) vibronic peak energies. The remainder of the (0-0) together with the (0-1) and (0-2) vibronic transitions can then contribute to the Rabi-splitting ($\hbar\Omega_{01_{\mathrm{TE}}}$) between MP and UP, compensating, as already noted, for the interchange in exciton populations between X_{g} and X_β.

Whilst this phenomenological approach gives us a reasonable feel for the factors that lie behind the observed behaviour, the precise nature of their contributions remains somewhat ambiguous, mainly because, as discussed in Section 2.5.2, the HA model is not fully adapted to the physics of strongly coupled molecular microcavities. This is an area in which additional experimental studies can be envisaged, to provide data against which developing theoretical models can then be tested.

The present study provides a complex scenario in which the extinction coefficient comprises spectrally overlapping contributions from the X_{g} and X_β populations with, respectively unresolved and resolved vibronic progressions. In addition, the weighting of the two contributions adjusts as the β-phase percentage varies, making simple asymmetry corrections problematic. The description of the microscopic features presented above is consequently only partially complete. As discussed in Section 2.5.2, the HTC model may provide a framework with which to more fully explore the role of the two exciton populations for all β-phase fractions including the 1.1 and 1.5% microcavities left out of the analysis in Section 4.4. A further aspect of PFO photophysics to note is the fast non-radiative transfer ($\sim$ps)[111,118] between glassy- and β-phase chain segments that might additionally enhance rapid LP occupation and thereby prevent the simultaneous MP emission seen for other systems.[42] Applying

the HTC model to the dual exciton population (X_{g} plus X_{β}) PFO system studied here would then require the incorporation of several non-negligible additions. The reported simulations to date were limited to a single exciton population that was in the strong coupling regime only, already then requiring intensive calculations to represent at most $N_0 \in [10-20]$.[88,91,92] It will be necessary to extend the current version of the model to include the anti-resonant terms characteristic of USC, then take account of the two different exciton populations, and do so with a relevant number of emitters. In the latter case, in order to provide a good representation for a series of different β-phase fractions, $N_0 \sim$ 100 would probably be necessary.

4.6 Conclusion

We have reported in this chapter a detailed study of USC for glassy-phase PFO excitons (X_{g}) within metal-polymer-metal cavities. Control was then exerted over the exciton-polariton physics via the generation of increasing fractions of β-phase chain segments, allowing a systematic study of the dependence of the mode characteristics and resulting light emission properties on the relative X_{g} and X_{β} populations. X_{g} USC showed Rabi splitting energies in excess of 1.05 eV (more than 30% of the exciton transition energy) for both TE- and TM-polarized light. The splitting of the LP, induced by X_{β} SC, increased with growing X_{β} fraction as expected. However, only a fraction of the oscillator strength of the X_{β} (0-0) vibronic peak appeared to dominate this splitting, with the remainder and higher vibronics (that overlap spectrally with X_{g} absorption) contributing instead to maintenance and indeed partial enhancement of USC, thereby compensating for the reducing X_{g} population (c.f. $\hbar\Omega_{01}$ values in Table 4.1). In all cases, PL emanated from the LP, allowing conformational control to be exerted over the emission spectrum and angular dispersion. For a cavity with 12.3% β-phase the PL was dispersionless within its $\sim$ 50 meV FWHM linewidth, high-

lighting the possibility to use such structures for high purity, angle-insensitive LEDs. An equivalent LED emission spectrum to that measured for PL would yield colour coordinates CIE (x, y) = (0.161, 0.018), with dominant wavelength 447 nm and 99% saturation. Experimental results were discussed in terms of the full HA Hamiltonian for the case of two exciton populations (X_{g} and X_{β}) simultaneously present within a single semiconductor (PFO). The additional importance of taking account of the molecular characteristics of the semiconductor for an accurate description of its strong coupling behaviour was directly evidenced. Consideration of the variation in Rabi energies as X_{g} and X_{β} populations interchange led to a better understanding of how these populations are at play behind the couplings. This first pass at investigating the role of microscopic features has generated the realization that a full understanding of conformational control for exciton-polariton physics will require further significant theoretical input. Models that properly take account of vibronic coupling, such as the one presented in Section 2.5.2,[88,91,92] are important in this regard. Achieving such understanding is necessary in order to fully exploit the potential of conformational control, both as a versatile test bed for SC theory and as a path towards novel light sources.

Chapter 5

Enhanced and Polarization Dependent Coupling for Photoaligned Liquid Crystalline Conjugated Polymer Microcavities

Copyright notice: The content of this chapter was adapted with permission from: Enhanced and Polarization-Dependent Coupling for Photoaligned Liquid Crystalline Conjugated Polymer Microcavities - F. Le Roux, R. A. Taylor, D. D. C. Bradley *ACS Photonics*, 7, 3, 746–758 (2020)

5.1 Introduction

In this chapter, the fabrication and optical characterization of organic microcavities containing the LCCPs: F8BT, PFO and F6T2 (see Section 3.1.1 for their details) aligned on top of a thin transparent SD1 photoalignment layer are reported. We extract the optical constants of the aligned films using VASE and fabricate metallic microcavities in which the USC regime is manifest both for the aligned and non-aligned LCCPs. Transition dipole moment alignment enables a systematic increase in the interaction strength, with unprecedented solid-state Rabi splittings of up to 1.80 eV, the first to reach energies comparable to those in the visible spectrum. With an optical gap of 2.79 eV for F6T2 this gives the highest-to-date organic microcavity coupling ratio, $\eta = 65\%$. We also demonstrate that the coupling strength is polarization-dependent with bright polariton photoluminescence for TE polarization parallel to the polymer chains and either no emission or weakly coupled emission from the corresponding TM polarization.

The large oscillator strengths of organic semiconductors combined with the small mode volumes V_{m} of metallic microcavities[143] have enabled $\hbar\Omega_0 \geq 1$ eV,[22–24,144] with values up to $\hbar\Omega_0 = 1.12$ eV.[78,145] We examine $\hbar\Omega_0$ as in Chapter 4 using Equation 2.10:

$$\hbar\Omega_0 = 2\sqrt{g_{\mathrm{res}}^2 - \frac{(\gamma_{\mathrm{ex}} - \gamma_{\mathrm{cav}})^2}{4}} \tag{5.1}$$

where g_{res} is given by Equation 2.11:

$$g_{\mathrm{res}} = \sqrt{N}\frac{\boldsymbol{\mu}.\mathbf{E}}{\hbar}, \tag{5.2}$$

and γ_{cav} and γ_{ex} are respectively the cavity and exciton radiative broadenings.

In this chapter, the exciton populations are well spectrally separated and the radiative broadenings are of the order a few μeV, γ_{ex} is neglected. The values of $\hbar\Omega_0$ derived here are all in excess of 0.8 eV allowing to neglect the influence of inhomoge-

neous broadening as examined in Section 2.4.6. The cavity broadening $\hbar\gamma_{\mathrm{cav}}$ reaches values of ∼100 meV (for a corresponding Q factor of around 25) which as stated in Section 2.4.7 enables: $\hbar\Omega_0 \approx 2g_{\mathrm{res}}$. Consequently:

$$\hbar\Omega_0 \approx 2\sqrt{N}\boldsymbol{\mu}.\mathbf{E} = 2\frac{\boldsymbol{\mu}.\mathbf{E}}{|\mathbf{E}|}\sqrt{\frac{N\hbar\omega_{\mathrm{ex}}}{2\epsilon_{\mathrm{eff}}V_{\mathrm{m}}}}. \tag{5.3}$$

One way to increase the value of the coupling ratio is to work with lower energy excitons, as done by Barachati *et al.*,[30] resulting in a then record $\eta = 62\%$. This approach is inherently accompanied by a reduction of $\hbar\Omega_0$ compared with the use of excitons lying at higher energies with equivalent oscillator strengths. The alternative is to look to increase $\hbar\Omega_0$; The most direct routes to achieve this include (i) increasing N, which although generally not straightforward can be done, for example, by reducing the bulkiness of conjugated polymer solubilizing groups[146] (ii) increasing $\boldsymbol{\mu}$ through conformational control (Chapter 4) or a photo-switchable configuration change,[143] and/or (iii) increasing $\boldsymbol{\mu}.\boldsymbol{E}$, a phenomenom observed along the preferential axes of organic crystals[13] or for oriented J-aggregates.[43] In the latter case, uniaxial orientation has been shown to enhance conjugated polymer thin film refractive index (and correspondingly transition dipole moment) in the direction parallel to the chain orientation axis[147,148] yielding an enhanced dot product for a suitable polarization of $\boldsymbol{E}$. This offers a clear route to enhancing $\hbar\Omega_0$ that is demonstrated below, using a photoalignment process to achieve thermotropic LCCP chain orientation. Two recent reports on the coupling of LC vibrational modes[46] and carbon nanotube Wannier excitons[44] have particularly shown that $\boldsymbol{\mu}.\boldsymbol{E}$ can be maximized in this way and that polarization-dependence, which has previously been theoretically investigated,[149,150] allows for applications discussed at the end of this chapter.

5.2 LCCP Orientation

Previous approaches to LCCP orientation typically used a traditional rubbed polyimide (PI) alignment layer onto which the polymer was spin coated prior to thermal treatment.[151] The clearing temperatures of LCCPs are relatively high (∼200-300°C),[151,152] leading to the requirement for a high temperature stable PI, for which there are limited commercial options. Precursor route poly(p-phenylenevinylene) has also been used as an alternative rubbed alignment layer, having the advantage of temperature stability and an electronic structure that more readily permits charge injection from the underlying electrode to the LCCP.[153] Other approaches to orientation include stretching and rubbing the conjugated polymer,[154] Langmuir-Blodgett deposition,[155] use of an aligned host matrix[156] or nanoimpriting.[157] Successful fabrication of polarized light emitting diodes[153,158,158–161] and polarized photoluminescence structures[147] has resulted, together with intrachain mobility enhanced transistors.[162] For a variety of practical reasons, oriented LCCPs have, however, not been used before in strongly or ultrastrongly-coupled microcavities. The results described within this chapter present a new and detailed study of microcavity structures containing films of oriented PFO, F8BT and F6T2. In addition, instead of using a rubbed PI alignment layer we use here a photoalignment film. Non-contact photoalignment of liquid crystal mesophases has emerged[163] as a promising alternative to rubbing-induced alignment. Among photoalignment layer materials, the azobenzene-containing SD1, has shown high temperature stability and remarkable quality for the alignment of low molecular weight LCs.[164,165] The orientation of F8BT using SD1 has also been recently observed.[166] Potential advantages of using SD1 photoalignment for photonics and polaritonics are threefold, namely that the SD1 layer can be very thin (≤ 5 nm), that it is almost transparent in the visible (peak absorption at ~ 3.25 eV) and that it is a patternable process which allows a straightforward way to fabricate novel photonic structures.[165,167]

5.3 Thin Film Fabrication and Optical Properties

5.3.1 Oriented LCCP Thin Film Fabrication

The bare films (used for ellipsometry and PL) of SD1, PFO, F8BT, F6T2 were spin-coated from solutions in 2-methoxyethanol (SD1 at 1 mg.mL^{-1}), toluene (PFO at 18 mg.mL^{-1} and F8BT at 18 mg.mL^{-1}) and chloroform (F6T2 at 13 mg.mL^{-1})[1]. All solutions were prepared in an inert environment, left to stir overnight at a temperature of 55°C except for F6T2 in chloroform which was left stirring at room temperature. All solutions were then filtered using a 0.45 μm PTFE filter. All samples were spin-coated on top of fused silica substrates. The non-aligned polymer films were spun for 1 min at a speed of 2000 rpm with an acceleration of 1200 rpm.s^{-1}. For the aligned polymer films, the SD1 layer was first spincoated by spinning 5 s at 500 rpm (acceleration 500 rpm.s^{-1}) and 25 s at 2000 rpm (acceleration 1200 rpm.s^{-1}). The film was then annealed for 6 minutes at a temperature of 150°C to drive any traces of solvent away. The alignment of the SD1 layer was performed in air by exposing the sample to 5 mW of polarized UV light (emitted by a M365LP1 LED in front of a broadband WP25M-UB polarizer from Thorlabs[125]) for 10 minutes; The SD1 chains aligning perpendicular to the direction of the polarized light.[164,165] The samples were then put back in an inert environment where the polymer layer was spincoated by spinning for 1 min at a speed of 2000 rpm with an acceleration of 1500 rpm.s^{-1}. Each polymer was then thermally annealed into their respective nematic phases (160°C for PFO, 220°C for F6T2, 250°C for F8BT) using a Linkam THMS600[169] heating stage with a heating rate of 30°C.min^{-1}. This temperature was held for 10 minutes and subsequent quenching to room temperature was realized by quickly placing the sample on the metallic floor of the glovebox while applying a gentle flow of nitrogen.

[1] anhydrous chloroform (≥99%) and anhydrous 2-methoxyethanol(≥99.8%) were purchased from Sigma-Aldrich.[168] Solvents were used as received.

5.3.2 Optical Properties of Oriented LCCP Thin Films

The optical constants for thin films of PFO, F8BT, F6T2 (see Appendix C Section C.1 for an additional description of the fabrication and characterization of the orientation of the β-phase of PFO) were extracted using VASE[2]. Similarly to Chapter 4, the optical constants are well fitted[137,170] using an in-plane/out-of plane anisotropic model yielding the components $n_{\text{ord}}, k_{\text{ord}}, n_{\text{ex}}, k_{\text{ex}}$ of the complex refractive index $\tilde{n} = n + ik$. Figure 5.1 shows (in green) the in-plane optical constants ($n_{\text{ord}}, k_{\text{ord}}$) for F8BT (b), PFO (c) and F6T2 (d) (The complete sets of optical components extracted are shown in Appendix C Section C.2). All spectra comprise either one or several inhomogeneously broadened distributions of chain-delocalised exciton transitions ($E_{\text{X}_{\text{PFO}}}$ peaked at around 3.23 eV, $E_{\text{X}_{\text{F8BT}_1}}$ and $E_{\text{X}_{\text{F8BT}_2}}$ peaked at respectively 3.82 eV and 2.70 eV and $E_{X_{\text{F6T2}}}$ at 2.79 eV), with higher lying features above 5 eV associated to ring-localized fluorene states.[117]

Following photoalignment of an SD1 spincoated film in the in-plane y direction, the optical components $n_x, n_y, n_z, k_x, k_y, k_z$ were extracted using a biaxial anisotropic model[171] and are shown in Figure 5.1 (a). As expected, the alignment brings about intense n_y, k_y optical components compared to their perpendicular counterparts n_x, k_x. Polymer layers of F8BT, PFO and F6T2 were then spincoated on top of the photoaligned SD1, thermally annealed into their respective nematic phases and subsequently quenched to room-temperature. Homogeneous (in-plane) uniaxial alignment was thereby generated along the y direction, with quenching freezing the order within a nematic glass state. The corresponding optical components of the obtained films were fitted and are shown in Figure 5.1 (b),(c),(d) with n_y, k_y substantially larger than n_x, k_x. The x axis matches the direction of the polarizer used during the pho-

[2]For each sample, 8 reflection-geometry measurements were performed with light incident from 45° to 61° (angles of incidence are quoted relative to the plane normal) together with a normal incidence (0°) transmission measurement, for the aligned films the measurement was performed at $\Phi = 0°$)

toalignment of SD1 which confirms that the polymer chains align parallel to SD1, orthogonal to the electric field direction x to which the SD1 film was exposed.[164, 165] The use of the (x, y) coordinate system is further validated in Appendix C Section C.3 by measuring the TE- and TM-polarized transmissivities at normal incidence while rotating a thin film of oriented PFO.

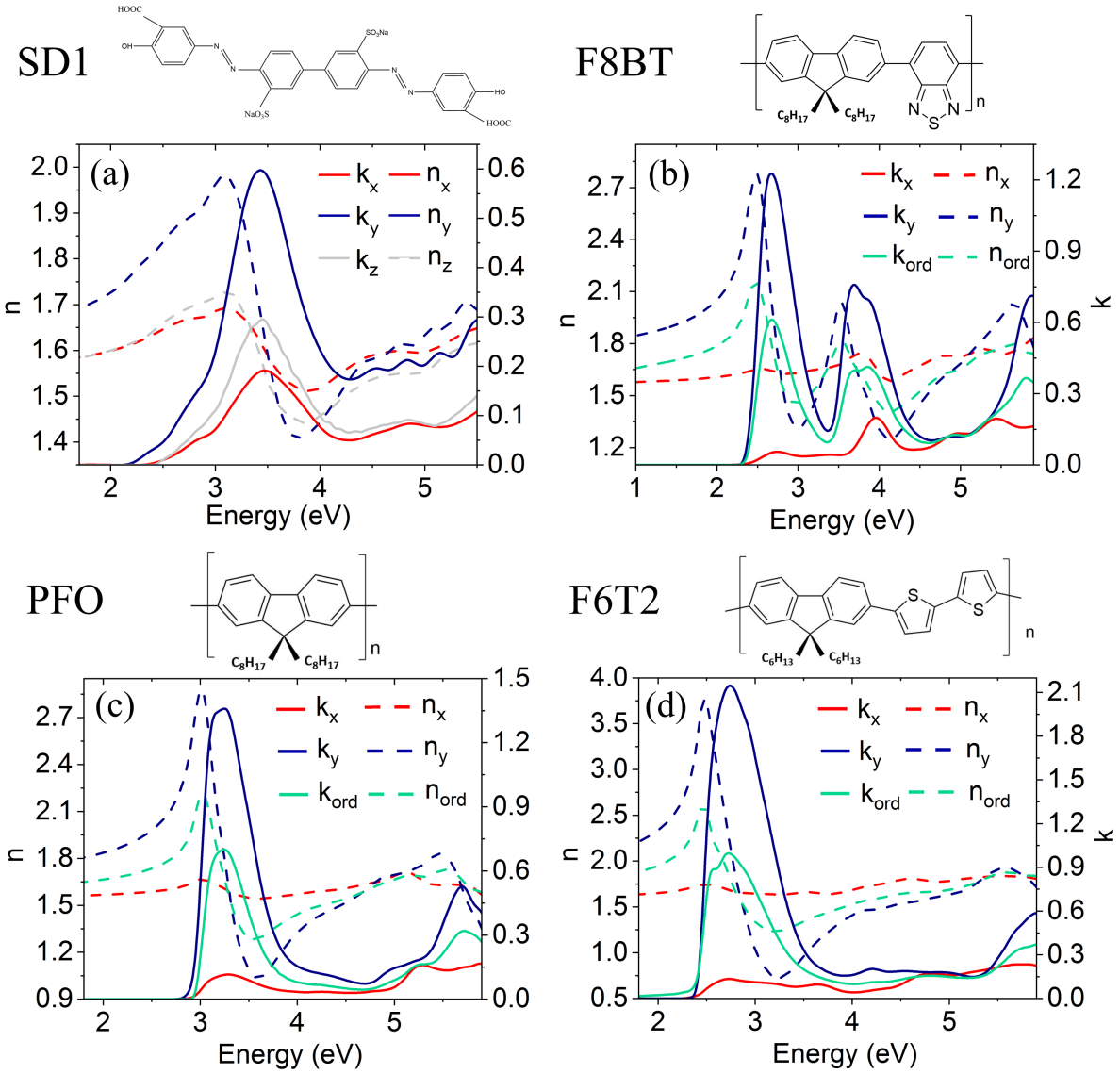


Figure 5.1: (a) Optical components n_x n_y, n_z, k_x, k_y, k_z for a thin film of SD1 aligned along the y direction. (b),(c),(d) In green: In-plane n_{ord}, k_{ord} optical components for spincoated F8BT (b), PFO (c) and F6T2 (d). The in-plane optical components of the films following alignment are shown in blue for n_y, k_y (parallel to the alignment direction) and in red for n_x, k_x (perpendicular to the alignment direction) for SD1 (a), F8BT (b), PFO (c) and F6T2 (d). Dashed lines give the real component of the complex refractive index $\tilde{n} = n + ik$, solid lines the imaginary component.

Time-integrated PL spectra were recorded at normal incidence for the three polymers and are shown in Figure 5.2. The spectra were measured at normal incidence with the collection polarizer both in vertical (blue) and horizontal (red) positions; for the aligned films, the vertical direction matched the direction of the alignment.

In each case, we calculate the integrated ratio $R_{\mathrm{VH}} = \int \frac{I_{\mathrm{V}}(E)}{I_{\mathrm{H}}(E)} \mathrm{d}E$ which reveals the presence of in-plane uniaxial alignment in the film. For F8BT, the spectrum of the non-aligned film (Figure 5.2 (a)) reveals an inhomogeneously broadened distribution with $S_1 - S_0$ (0-0), (0-1) vibronic peaks located at 2.29 eV (541 nm) and 2.15 eV (577 nm). We calculate $R_{\mathrm{VH}} = 1.08$, with the deviation from unity being fully accounted for by the degree of polarization of the excitation laser beam; as expected the polymer chains have no preferential in-plane orientation. For the aligned F8BT (Figure 5.2 (b)), the same spectral positions for the vibronic peaks are recorded but with a difference in relative heights due to thickness variations between the aligned and non-aligned films. The integrated ratio $R_{\mathrm{VH}} = 8.3$ confirms a significant in-plane preferential alignment of polymer chains within the emitting layer (in-depth studies relating the polarized emission to the microscopic parameters of aligned F8BT can be found in Ref[159]). For non-aligned PFO (Figure 5.2 (c)), the $S_1 - S_0$ well resolved (0-0), (0-1) and (0-2) PL vibronic peaks appear at 2.88 eV (430 nm), 2.71 eV (457 nm) and 2.58 eV (481 nm) with an integrated ratio R_{VH} that increases from 1.09 to 6.9 from non-aligned to aligned film (Figure 5.2 (d)). As the vibronic structure is well resolved in this case, we calculate the peak ratios $R_{\mathrm{pVH}}(E) = \frac{I_{\mathrm{V}}(E)}{I_{\mathrm{H}}(E)}$ for $R_{\mathrm{pVH}}(2.88)$, $R_{\mathrm{pVH}}(2.71)$ and $R_{\mathrm{pVH}}(2.58)$, yielding ratios 11.2, 9.5 and 8.2, respectively. These results are comparable to those obtained previously using rubbed PI layers.[158] For non-aligned F6T2 (Figure 5.2 (e)), the PL vibronic peaks appear at 2.28 eV (544 nm), 2.12 eV (585 nm) and 1.95 eV (636 nm) and R_{VH} increases from a value of 1.16 to 3.50 (Figure 5.2 (f)), albeit for a ratio that is harder to accurately determine than for F8BT and PFO, due to weaker light emission and an enhanced noise floor that needed to be removed using a fast Fourier transform algorithm.

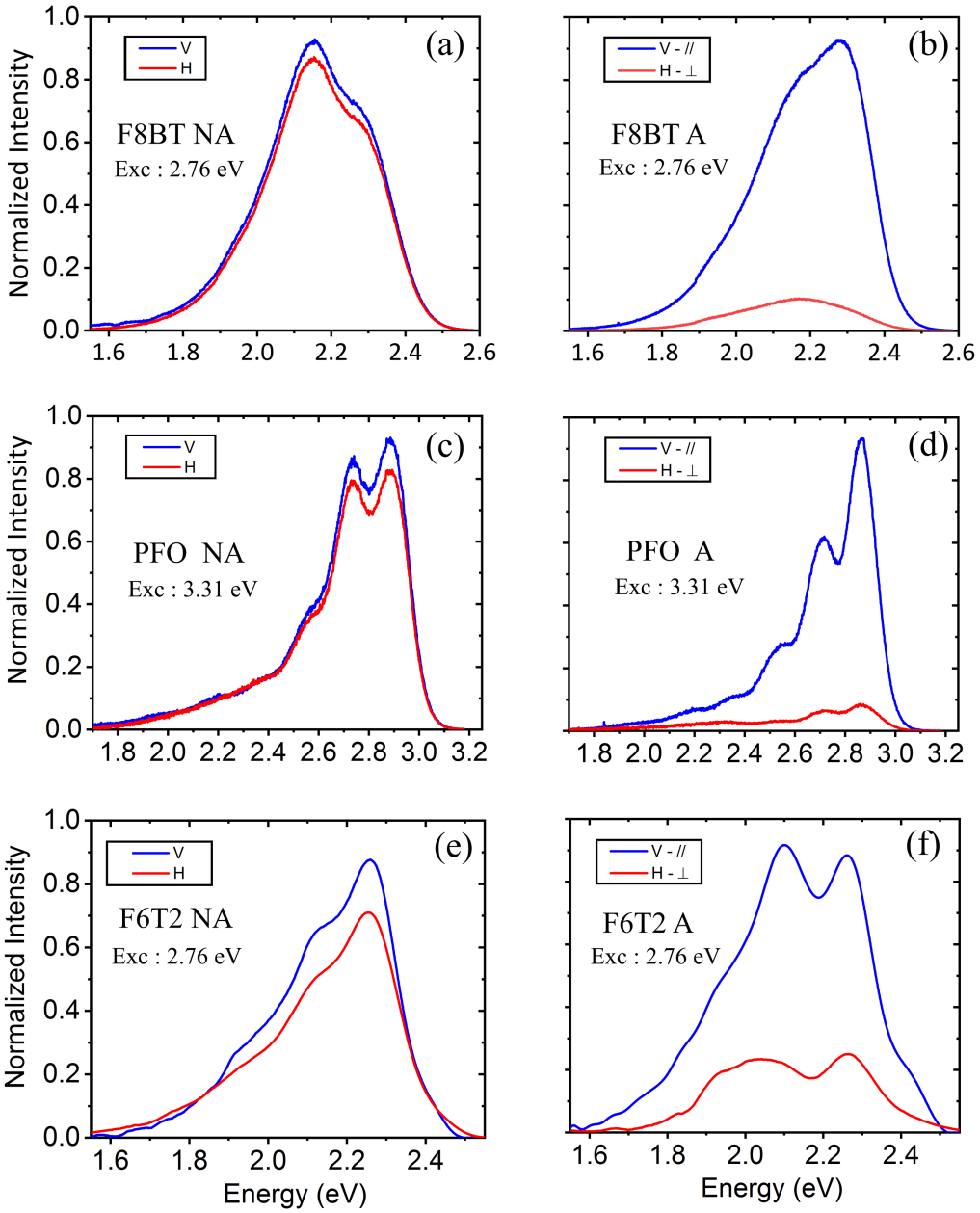


Figure 5.2: PL spectra for non-aligned ((a), (c) and (e)) and aligned ((b), (d) and (f)) F8BT ((a) and (b)), PFO ((c) and (d)) and F6T2 ((e) and (f)) thin films. For a given polymer in a given alignment state, the parallel and perpendicular spectra were plotted on the same scaled intensity axis range to allow for their comparisons. Solid blue lines show the PL collected using a polarizer in the vertical direction and red lines in the horizontal direction. In panels (b), (d) and (f): // and $\perp$ indicate that the collection polarizer direction respectively matches or is perpendicular to the orientation direction of the polymer chains in the film. A fast Fourier transform algorithm was used for F6T2 ((e) and (f)) to reduce noise in the recorded signal.

5.4 Microcavities Containing Oriented LCCP: Fabrication, Measurement and Analysis

5.4.1 Microcavity Fabrication

Al-Polymer-Al microcavities were fabricated using both non-aligned and aligned F8BT, PFO and F6T2 polymer films with chain orientation achieved via SD1 photoalignment. For each microcavity, a 100 nm thick bottom and approximately 20 nm thick upper mirror were evaporated at a rate of 10 A.s^{-1} at a pressure of 10^{-9} mbar. For the non-aligned cavities, the spincoating conditions used on top of the bottom mirror were identical to the ones described for the bare films. For the aligned cavities, the SD1 layer was spincoated on top of the bottom mirror. The structures fabricated had low Q factors ~ 25. The concentration of the SD1 solution in 2-methoxyethanol was increased to 3 mg.mL^{-1} as spincoating SD1 on a metallic surface results in lower thicknesses than on fused silica. A slightly thicker layer also acts as a protection layer to prevent the aluminium from reacting with the polymer upon annealing at high temperatures (using 1 mg.mL^{-1} SD1 solution resulted in samples unfit for measurement). The sample was then annealed 6 minutes at a temperature of 150°C to drive any traces of solvent away and the rest of the alignment procedure was similar to the one used for the bare films. For the spincoating of the polymer layers, the solution concentrations were in some cases adjusted so as to adjust the thicknesses and therefore the cavity mode energy. The concentrations used in the non-aligned microcavities were: PFO at 19 mg.mL^{-1}, F8BT at 20 mg.mL^{-1} and F6T2 at 15 mg.mL^{-1}. The concentrations for the aligned microcavities were: PFO at 18 mg.mL^{-1}, F8BT at 18 mg.mL^{-1}, F6T2 at 13 mg.mL^{-1}.

5.4.2 Angle-Resolved Reflectivity and Analysis

Angle-resolved polarized reflectivity maps were recorded for each microcavity by varying the angle θ formed between the vector normal to the microcavity plane and the incident light direction. For the oriented polymer cavities, the measurement was performed at an angle Φ (formed between TE polarization and the polymer chain direction) equal to 0°. All results were analysed using the HA Hamiltonian including either one (PFO, F6T2) or two (F8BT) separate excitons, with all fitting results displayed in Table 5.1. For each microcavity, the experimental results are supported by TMC whose outputs are shown in Appendix C Section C.5. The reference results obtained for the non-aligned PFO and F8BT cavities are also shown in Appendix C Section C.4 and confirm a previous report[137] for F8BT and the results of Chapter 4 (obtained using a different PFO as specified in Chapter 3).

Measured and fitted results for the non-aligned F6T2 cavity for TE polarization are shown in Figure 5.3 (a) where we observe the LP and UP branches split about the exciton energy ($E_{\mathrm{X_{F6T2}}} = 2.72$ eV), with a separation of more than 1 eV that provides clear evidence of USC. Even though the layer is non-aligned, the measured Rabi splitting energy $\hbar\Omega_{0_{\mathrm{TE}}} = 1.38 \pm 0.01$ eV, corresponding to a coupling ratio $\eta = 49\%$, is the largest splitting reported to-date. As expected, the results for TM polarization (Figure 5.4 (a)) display a flatter angular dispersion for the polaritons as the effective refractive index $n_{\mathrm{eff_{TM}}}$ of the microcavity increases due to polarization-dependent penetration through the metallic mirrors.[22,141,142] For this polarization, the in-plane/out-of-plane anisotropy of the active layer slightly reduces the Rabi energy down to $\hbar\Omega_{0_{\mathrm{TM}}} = 1.27 \pm 0.01$ eV, as the contribution of the weaker out-of plane (k_{ex}) component to the overall interaction increases along with θ.[22]

Results for the aligned PFO, F6T2 and F8BT cavities are shown, respectively, in Figure 5.3 (b), (c) and (d) for TE polarization at $\Phi = 0°$. In each case, USC is clearly observed with fitting results revealing a systematic increase for $\hbar\Omega_{0_{\mathrm{TE},\Phi=0°}}$ of

$\sim$ 40% compared to the non-aligned cavities. As the transition dipole moment $\boldsymbol{\mu}$ rotates together with the polymer chains in the y direction, the relative increase in coupling strength can be calculated using the term $\boldsymbol{\mu.E}$ in Equation 5.3 to be: $\frac{\cos(0)}{\cos(\frac{\pi}{4})} - 1 = (\sqrt{2} - 1) \sim 41\%$ for TE polarization.

All the $\hbar\Omega_{0_{\mathrm{TE},\Phi=0^\circ}}$ values derived here, apart from that just reported for non-aligned F6T2, exceed previous reports: the aligned F8BT cavity exhibits $\hbar\Omega_{01_{\mathrm{TE},\Phi=0^\circ}} = 1.18 \pm 0.01$ eV and $\hbar\Omega_{02_{\mathrm{TE},\Phi=0^\circ}} = 1.25 \pm 0.01$ eV, the aligned PFO cavity $\hbar\Omega_{0_{\mathrm{TE},\Phi=0^\circ}} = 1.47 \pm 0.01$ eV and the aligned F6T2 cavity reaches an unprecedented value of $\hbar\Omega_{0_{\mathrm{TE},\Phi=0^\circ}} = 1.80 \pm 0.01$ eV. To our knowledge, this last value is the first Rabi splitting for a solid-state system to reach a value comparable to photons in the visible spectrum ($\sim$ 689 nm), exceeding by more than 60% the previous record.[78,145] The corresponding coupling ratio $g \sim 65\%$ is also slightly higher than those previously reported,[30] a notable result given that the η-value reported here was obtained for an exciton lying some ~ 1.6 eV higher in energy.

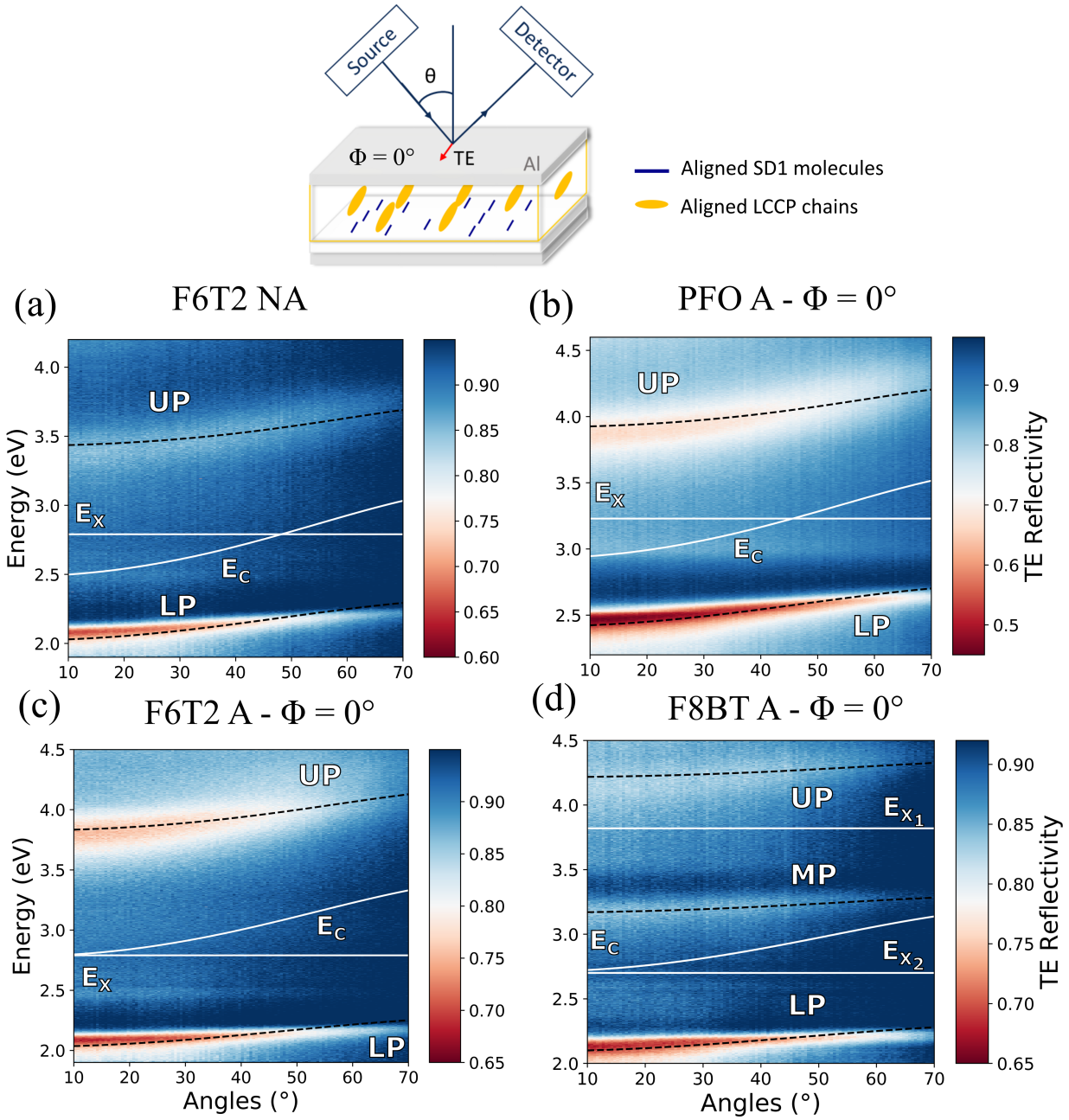


Figure 5.3: Experimental, angle-resolved, TE-polarized reflectivity maps for microcavities containing: (a) non-aligned F6T2, (b) aligned PFO, (c) aligned F6T2 and (d) aligned F8BT. For (b), (c) and (d), the measurements were performed at $\Phi = 0°$ (see text and schematic experimental geometry shown above the maps). The overlaid solid white lines show the exciton E_X and cavity mode E_C dispersions and the black dashed lines the polariton branch dispersions derived from the analytical model. Note the Fano-like asymmetry around the LP for (a), (b) and (c) similar to that observed in a previous report[22] and the reduced LP linewidth relative to the UP as a consequence of motional narrowing.[76,172]

The results for TM polarization for the aligned polymer cavities are shown in Figure 5.4 (b), (c) and (d). In those measurements, the weak coupling regime is clearly observed for F6T2 (c) and F8BT (d) as the LP and UP are no longer visible and are replaced by a single photonic mode. For PFO (b), the reflectivity observed does not show proper anti-crossing around the exciton ($E_{\mathrm{X_{PFO}}} = 3.23$ eV), with PL measurements in the next section further showing a lack of evidence for SC. These results offer exciting new opportunities that are further examined in the discussion section below.

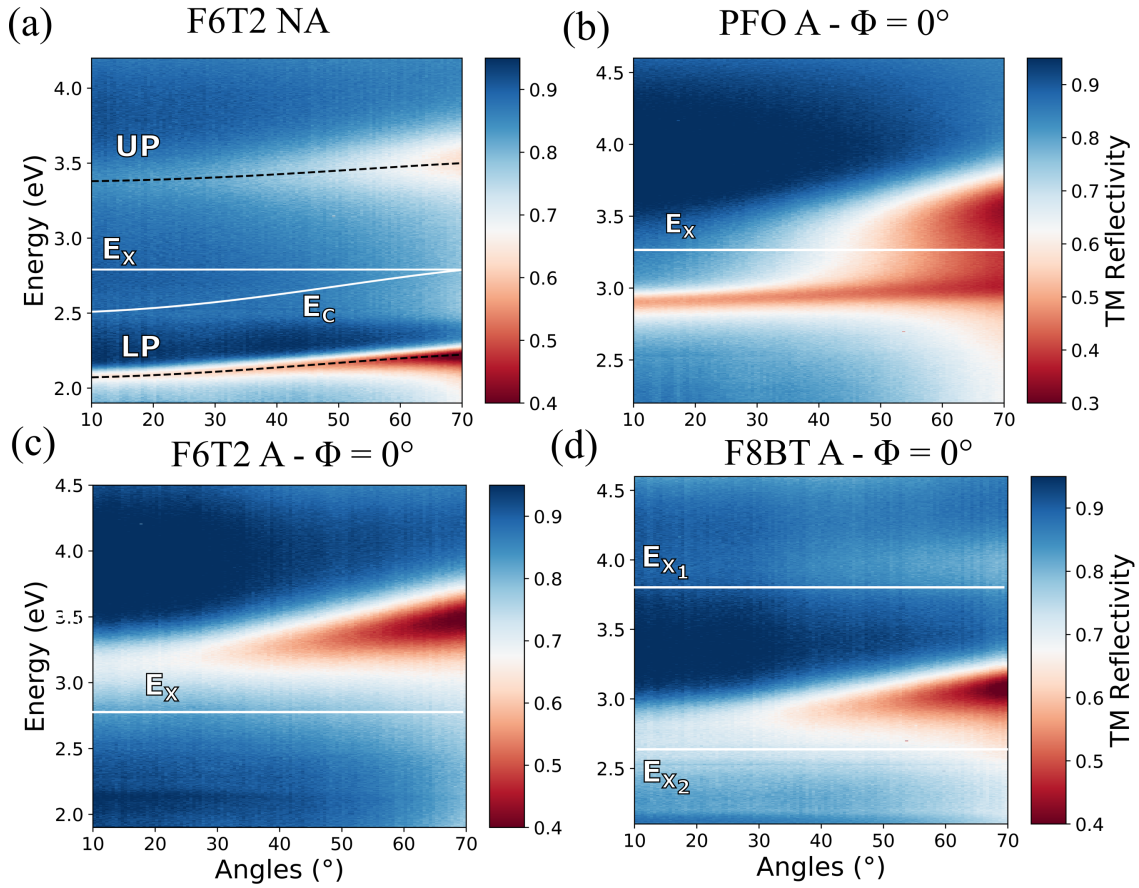


Figure 5.4: Experimental, angle-resolved, TM-polarized reflectivity maps for micro-cavities containing (a) non-aligned F6T2, (b) aligned PFO, (c) aligned F6T2 and (d) aligned F8BT. For (b), (c) and (d), the measurements were performed at $\Phi = 0°$ (see text for definition) and the overlaid solid white lines show the respective exciton energies, E_{X}. In (a) in addition to E_{X}, the second white line presents the cavity mode dispersion, E_{C}. The black dashed lines show the polariton branch dispersions derived from the analytical model.

Polymer:	PFO NA	PFO A	F8BT NA	F8BT A	F6T2 NA	F6T2 A
$\hbar\omega_1$(eV)[1]	3.23	3.23	3.82	3.82	2.79	2.79
$\hbar\omega_2$(eV)[2]	-	-	2.70	2.70	-	-
$\hbar\Omega_{01_{\mathrm{TE}}}$(eV)[3]	1.02 ± 0.01	1.47 ± 0.01	0.84 ± 0.01	1.18 ± 0.01	1.38 ± 0.01	1.80 ± 0.01
$\eta_{1_{\mathrm{TE}}}\%$[4]	32	46	22	31	49	65
$\hbar\Omega_{01_{\mathrm{TM}}}$(eV)[5]	0.97 ± 0.01	-	0.80 ± 0.01	-	1.27 ± 0.01	-
$\eta_{1_{\mathrm{TM}}}\%$[6]	30	-	21	-	46	-
$\hbar\Omega_{02_{\mathrm{TE}}}$(eV)[7]	-	-	0.84 ± 0.01	1.25 ± 0.01	-	-
$\eta_{2_{\mathrm{TE}}}\%$[8]	-	-	31	46	-	-
$\hbar\Omega_{02_{\mathrm{TM}}}$(meV)[9]	-	-	0.80 ± 0.01	-	-	-
$\eta_{2_{\mathrm{TM}}}\%$[10]	-	-	30	-	-	-
$n_{\mathrm{eff}_{\mathrm{TE}}}$[11]	1.68 ± 0.01	1.70 ± 0.01	1.70 ± 0.01	1.87 ± 0.01	1.64 ± 0.01	1.71 ± 0.01
$n_{\mathrm{eff}_{\mathrm{TM}}}$[12]	2.33 ± 0.01	-	2.37 ± 0.01	-	2.12 ± 0.01	-
$E_{\mathrm{c}_{\mathrm{TE}}}(0)$(eV)[13]	3.13 ± 0.02	2.92 ± 0.02	2.54 ± 0.02	2.71 ± 0.02	2.48 ± 0.02	2.78 ± 0.02
$E_{\mathrm{c}_{\mathrm{TM}}}(0)$(eV)[14]	3.15 ± 0.02	-	2.59 ± 0.02	-	2.50 ± 0.02	-

[1] Exciton oscillator 1 transition energy.
[2] Exciton oscillator 2 transition energy.
[3] TE-polarized Rabi energy associated with exciton 1 for $\omega_{\mathrm{cav}_{\mathrm{TE}}} = \omega_1$ (see definition in the text).
[4] TE-polarized normalized coupling ratio energy associated with exciton 1 (see definition in the text).
[5] TM-polarized Rabi energy associated with exciton 1 for $\omega_{\mathrm{cav}_{\mathrm{TM}}} = \omega_1$ (see definition in the text).
[6] TM-polarized normalized coupling ratio energy associated with exciton 1 (see definition in the text).
[7] TE-polarized Rabi energy associated with exciton 2 for $\omega_{\mathrm{cav}_{\mathrm{TE}}} = \omega_2$ (see definition in the text).
[8] TE-polarized normalized coupling ratio energy associated with exciton 2 (see definition in the text).
[9] TM-polarized Rabi energy associated with exciton 2 for $\omega_{\mathrm{cav}_{\mathrm{TM}}} = \omega_2$ (see definition in the text).
[10] TM-polarized normalized coupling ratio energy associated with exciton 2 (see definition in the text).
[11] Effective refractive index for TE polarization.
[12] Effective refractive index for TM polarization.
[13] TE-polarized energy of the bare cavity mode at normal incidence.
[14] TM-polarized energy of the bare cavity mode at normal incidence.

Table 5.1: Extracted and pre-set parameter values for microcavities containing non-aligned and aligned polymers, modelled using the HA Hamiltonian. Values are shown for both TE- and TM-polarization, at $\Phi = 0°$ (see definition in the text) for the aligned cavities. The initials A and NA respectively designate aligned and non-aligned polymer layers.

5.4.3 Angle-Resolved Photoluminescence

Angle-resolved PL was recorded for each microcavity using the same laser source and excitation geometry as used for the thin film PL measurements; the laser beam was focused onto the sample at a fixed angle of incidence of 75°. For each microcavity, the average laser power was kept low ($\leq 10\ \mu$W) and the photon energy was chosen to optically pump one of the intense absorptions arising from the optical transitions of the underlying polymer. For the aligned cavities, the measurement was performed at $\Phi = 0°$.

Figure 5.5 shows PL intensity maps plotted on an energy vs emission angle for both TE- ((a), (c) and (e))) and TM-polarized ((b), (d) and (f)) light emission from the non-aligned F8BT ((a) and (b)), PFO ((c) and (d)) and F6T2 ((e) and (f)) microcavities. In each case the emission is dominated by a narrow single peak originating from the LP which is relatively insensitive to angular-dispersion, a recognizable feature of USC.[22–24] Table 5.2 reports the peak positions and FWHM values at normal incidence, together with the angular dispersion from 0 to 60°. The results for PFO agree with Chapter 4 and the range of polymers used here allows for emissions across a large part of the visible spectrum; in the blue at $\sim$ 452 nm for PFO, green at $\sim$ 537 nm for F8BT and yellow/orange at $\sim$ 588 nm for F6T2.

Corresponding PL intensity maps for the aligned cavities are shown in Figure 5.6. TE-polarized emission ((a), (c) and (f)) resembles that observed from non-aligned microcavities with a single LP peak. There is however an energy shift for F8BT and PFO between non-aligned and aligned cavities: the peak emission is recorded at 2.13 eV at normal incidence for aligned F8BT compared to 2.31 eV when non-aligned, and at 2.59 eV for aligned PFO compared to 2.74 eV when non-aligned. These red-shifts are not the result of different thicknesses between the cavities as TMC show that for each pair, the polymer layer thicknesses are comparable (the aligned F8BT is 110 nm-thick compared to 118 nm when non-aligned, the aligned PFO 97 nm-thick

compared to 96 nm when non-aligned). They are, rather, direct evidence of the increased interaction strength which repels the UP and LP to respectively higher and lower energies. The emission for aligned and non-aligned F6T2 is closer in energy at normal incidence (2.11 eV aligned compared with 2.10 eV non-aligned) and is this time the result of a much larger thickness for the non-aligned F6T2 layer; the aligned F6T2 is 94 nm-thick compared to 123 nm non-aligned film. This results in lower cavity mode and LP energies in the non-aligned case, as observed in Figure 5.3, which compensates for the difference in interaction strength between the two microcavities. TM-polarized measurements ((b), (d) and (f)) show no distinguishable emission for F8BT (b) and F6T2 (g) as the only photonic mode in both those cavities lies too high in energy to allow any emission from the underlying polymer. The cavity modes are at $\sim$ 3 eV for F6T2 and $\sim$ 2.9 eV for F8BT whereas PL emission is located at energies lower than 2.6 eV for both F6T2 and F8BT (Figure 5.2 (b) and (f)). For the microcavity containing aligned PFO (d), a 5-times weaker, broad, angle-independent TM-polarized emission was detected, with two maxima at 2.88 and 2.71 eV coinciding with the PL peaks from the bare film (Figure 5.2 (d)). This confirms that the microcavity no longer operates under USC for this polarization. The emission emerges via the photonic mode at $\sim$ 2.88 eV (see Figure 5.2 (b)) and even though this photonic mode overlaps with the most intense part of the bare film PL, the resulting signal is much weaker in TM than TE polarization as the emission in the direction perpendicular to the chain orientation direction is much weaker.

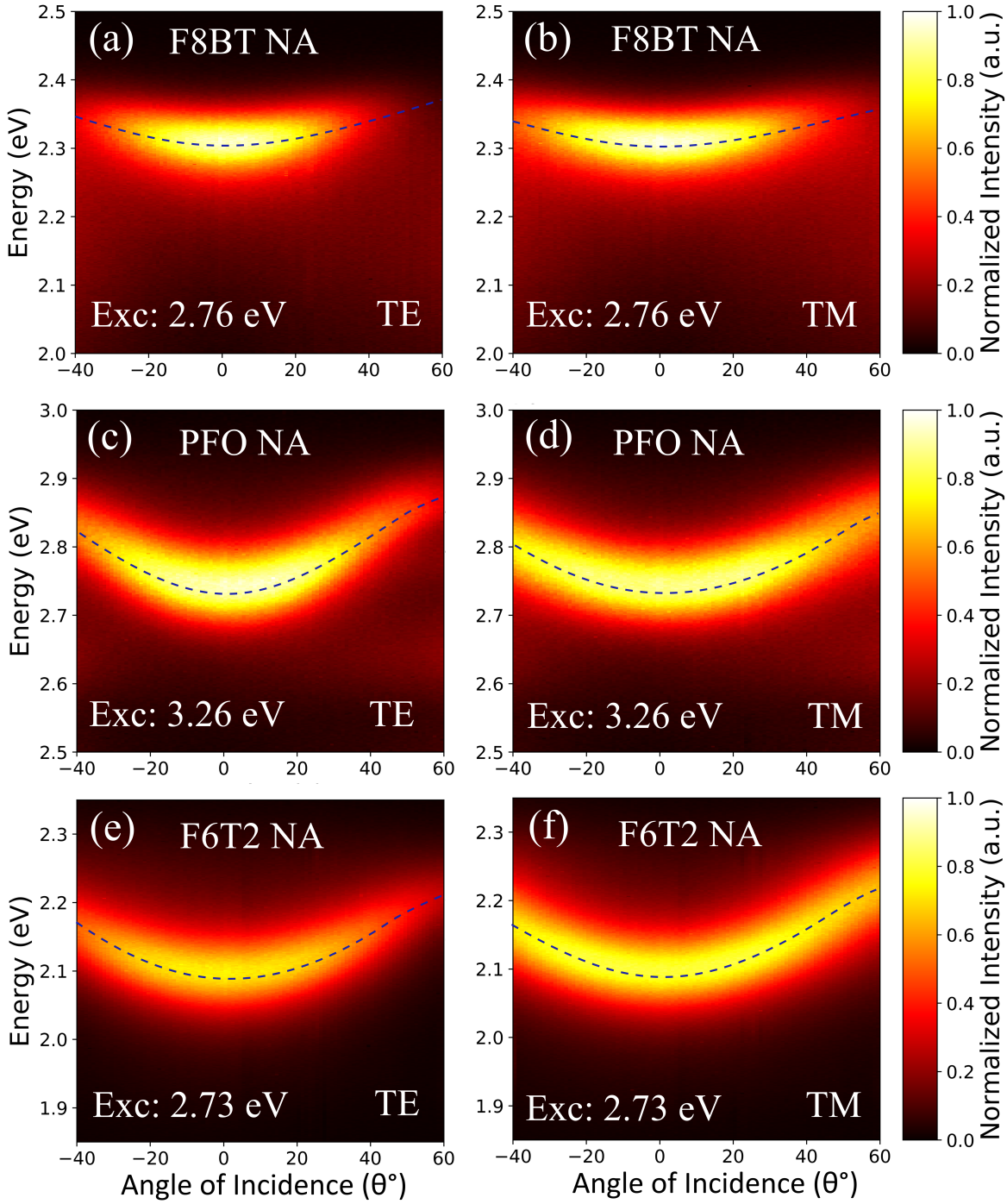


Figure 5.5: Angle-resolved PL spectral intensity maps for microcavities containing non-aligned F8BT ((a) and (b)), PFO ((c) and (d)) and F6T2 ((e) and (f)), with TE ((a), (c), (e)) and TM ((b), (d), (f)) polarized spectra plotted separately. Overlaid dashed blue lines correspond to the lower polariton modes fitted previously using the analytical model. The excitation energy, Exc, is given for each measurement. Each polarization pair ((a) and (b)), ((c) and (d)), ((e) and (f)) was plotted on the same scaled intensity axis range.

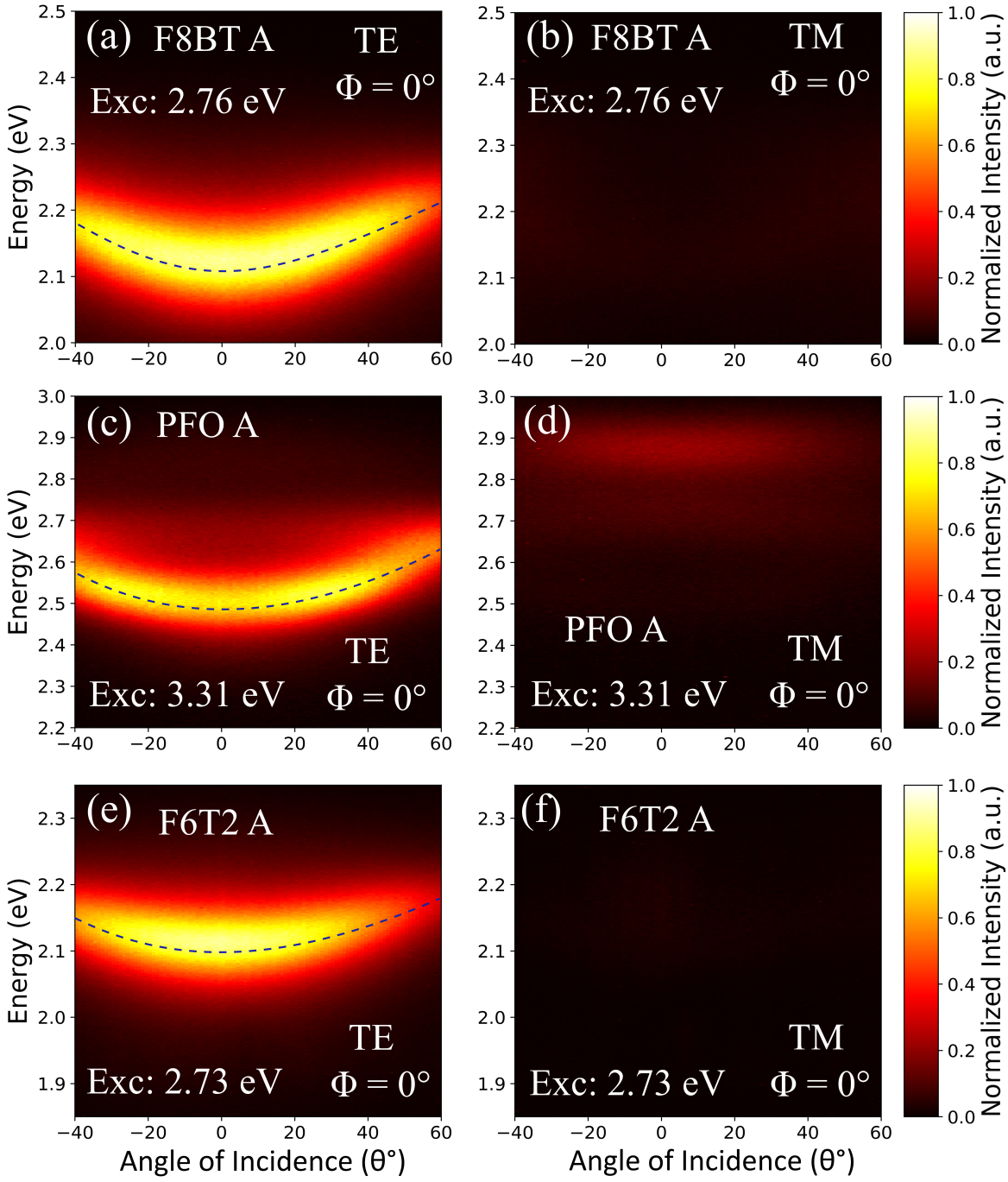


Figure 5.6: Angle-resolved PL spectral intensity maps for microcavities containing aligned F8BT ((a) and (b)), PFO ((c) and (d)) and F6T2 ((e) and (f)), with TE ((a), (c), (e)) and TM ((b), (d), (f)) polarized spectra plotted separately. Overlaid dashed blue lines correspond to the lower polariton modes fitted previously using the analytical model. The measurements were performed at $\Phi = 0°$ (see text for definition) . Each polarization pair ((a) and (b)), ((c) and (d)), ((e) and (f)) was plotted on the same scaled intensity axis range.

Polymer:	PFO NA	PFO A	F8BT NA	F8BT A	F6T2 NA	F6T2 A
Peak position (eV)	2.74	2.59	2.31	2.13	2.10	2.11
FWHM_{TE} (meV)	99 ± 1	140 ± 5	89 ± 5	127 ± 1	109 ± 1	109 ± 1
FWHM_{TM} (meV)	99 ± 1	-	82 ± 5	-	109 ± 1	-
TE dispersion (meV)	130	50	30	80	110	60
TM dispersion (meV)	110	-	20	-	110	-

Table 5.2: Peak positions and FWHM values at normal incidence ($\theta = 0°$) for the TE- and TM-polarized emissions displayed in Figures 5.5 and 5.6. The angular dispersion of the emission for both polarizations from $\theta = 0$ to 60° is also reported. The initials A and NA respectively designate aligned and non-aligned polymer layers.

5.5 Conclusion

We have fabricated organic microcavities containing the LCCPs: PFO, F8BT and F6T2, aligned using thin SD1 photoalignment layers. Microcavities with non-aligned films yield USC with $\hbar\Omega_{0_{F6T2}} = 1.34$ eV for F6T2, a value that exceeds all previous reports. Alignment subsequently allowed a systematic increase in coupling strength for light polarised parallel to the polymer chain direction, with $\hbar\Omega_0$ reaching as high as 1.80 eV, again for F6T2; an unprecedented value comparable to photon energies in the red part of the visible spectrum. This value further leads to the highest coupling ratio $\eta = 65\%$, reported to date for a solid-state system.[33,34] TE-polarized, angle-resolved PL, with excitation **E**-vector parallel to the chain orientation direction, revealed LP emission red-shifted relative to that from the non-aligned cavities, a clear signature of the increased interaction strength. In this geometry, the absence of polariton branches from the TM-polarized reflectivity together with weak or absent PL emission confirmed polarization dependent coupling strengths. Finally, by demonstrating this behaviour for three different polymers, we confirmed its generality for LCCPs. The opportunity to reach coupling ratios at resonance closer to 90% exists if such alignment can be achieved for LCCPs with excitons at lower energies.

Chapter 6

Transmissivity and Reflectivity of a TE-polarized Wave Incident on a Microcavity Containing Strongly Coupled Excitons with In-plane Uniaxially Oriented Transition Dipole Moments

Copyright notice: The content of this chapter was adapted with permission from: Transmissivity and Reflectivity of a TE-polarized Wave Incident on a Microcavity Containing Strongly Coupled Excitons with In-plane Uniaxially Oriented Transition Dipole Moments - F. Le Roux, R. A. Taylor, D. D. C. Bradley *Physica Status Solidi B*, doi: 10.1002/pssb.202000235 (2020)

6.1 Introduction

In this chapter we report on the reflectivity and transmissivity of a TE-polarized wave incident on a microcavity containing strongly coupled excitons with in-plane uniaxially oriented transition dipole moments and present a different interpretation to a previous report.[44] We first discuss the propagation of the electric field inside the cavity and make the distinction between two different physical cases: the first previously observed[44] and the second which enables the interpretation of our own measurements on a microcavity containing an oriented layer of liquid-crystalline PFO. We confirm that in all cases, the reflected and transmitted electric fields derive from photons leaking parallel and perpendicular to the transition dipole moment orientation. Recent experimental demonstrations of SC using oriented J-aggregates,[43] nanotubes (made of carbon[44] or tungsten disulfide[45]), LCs[46] and LCCPs (Chapter 5) have been reported and study the influence of orienting $\boldsymbol{\mu}$ on the resulting polaritons. Fitting the energy dispersions of the minima (maxima) of the reflected (transmitted) intensity spectra obtained by varying the polar angle θ (shown in Figure 6.1) is usually sufficient to characterize the strength of the interaction taking place inside a microcavity as described in Section 3.2.3. For microcavities containing in-plane anisotropies however, the transmissivity and reflectivity further depends on the azimuthal angle ϕ (represented in Figure 6.1) as revealed by the theoretical analysis conducted by Litinskaya *et al.*[149] and Balagurov *et al.*[150]

In the following sections we examine the specific case of a TE-polarized wave incident on a microcavity containing strongly coupled excitons with $\boldsymbol{\mu}$ oriented along y (see Figure 6.1). We focus on the effect of rotating the electric field E with respect to ϕ and show that in the presence of cavity damping broad enough compared with $\hbar\Omega_{0y}$ (the Rabi-splitting energy induced by the excitons in the y direction) the measured quantities are made of two extrema which get closer in energy as ϕ is increased. While this result resembles the one obtained when increasing θ in strongly coupled micro-

cavities where $\boldsymbol{\mu}$ has no preferential in-plane orientation, we show that the extrema are in fact the superposition of separate intensities originating from the propagation of two waves dephased by experiencing either the permittivity brought about by the excitons along y (yielding the LP and UP extrema) or the background permittivity along x (yielding a photonic mode extremum). We underline that this measurement has previously led to a different interpretation.[44]

When $\hbar\Omega_{0y}$ is much larger than the cavity damping, we recover signals in which the three extrema become clearly resolved and do not experience any spectral shift upon increase of ϕ. We support our results by fabricating and measuring the TE-reflectivity from a metallic microcavity containing an oriented layer of liquid-crystalline PFO.

6.2 TE-polarized Wave Propagation

We first examine the propagation of an incident TE-polarized wave inside a microcavity containing excitons with $\boldsymbol{\mu}$ oriented along y. The geometry is shown in Figure 6.1.

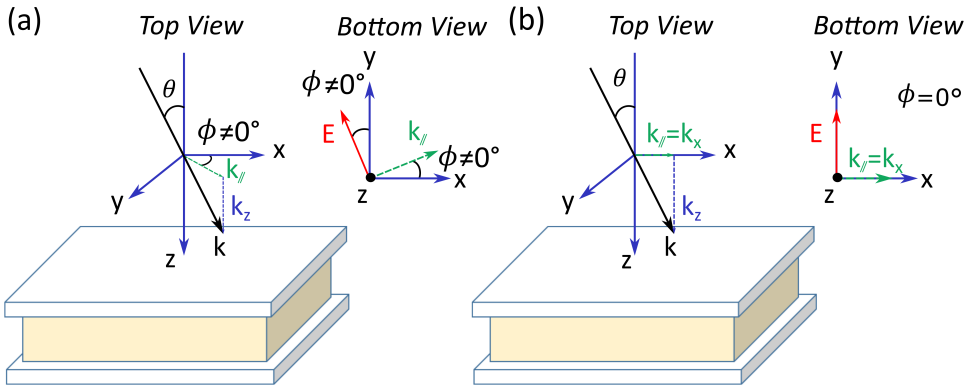


Figure 6.1: Geometry and angles used in this chapter, θ is the polar angle formed between $\mathbf{k}$ and the z-axis, for a TE-polarized wave ϕ is the azimuthal angle formed between E and the y-axis, and $\mathbf{k}_{/\!/}$ is the in-plane component of the wavevector $\mathbf{k}$. In (a) $\phi \neq 0°$, in (b) $\phi = 0°$: E is parallel to the transition dipole moment $\boldsymbol{\mu}$ of the excitons and the wave propagates experiencing ϵ_y, a similar situation arises for $\phi = 90°$, where E becomes parallel to the x-axis and the wave experiences ϵ_x.

In the linear approximation, the dielectric permittivity tensor of the cavity layer

takes the form:

$$\epsilon(\omega) = \epsilon_0 \begin{pmatrix} \epsilon_x & 0 & 0 \\ 0 & \epsilon_y & 0 \\ 0 & 0 & \epsilon_z \end{pmatrix}. \tag{6.1}$$

As per Equation 2.52, in the outside medium, a TE-polarized plane wave incident on the microcavity can be written:

$$\mathbf{E}_i(\mathbf{r}, t) = \mathbf{E}_{0_i} \mathrm{e}^{-\mathrm{i}[k_x x + k_y y + k_z z - \omega t]}, \tag{6.2}$$

where: $\mathbf{E}_{0_i} = E_{0_i x}\mathbf{i} + E_{0_i y}\mathbf{j}$. The propagation of TE-polarized waves in birefringent media is well documented:[173–175] if $\mathbf{E}_{0_i}$ is parallel to either the x-axis or the y-axis then the wave propagates experiencing the corresponding axis permittivity (see Figure 6.1 (b)), otherwise the x and y components propagate separately and are dephased according to the in-plane anisotropy of the medium.

We now focus on angle-resolved transmissivity and reflectivity which commonly allow characterization of the SC regime. We take below the example of reflectivity but note that the reasoning and therefore results, are qualitatively similar for transmissivity. We use a Lorentzian model to represent the electric susceptibility of the excitons inside the cavity layer as per Equation 2.6:

$$\chi(\omega) = \frac{4g_0^2}{\omega_{\mathrm{ex}}^2 - \omega^2 - \mathrm{i}\gamma_{\mathrm{ex}}\omega}, \tag{6.3}$$

and the dielectric permittivity then reads:

$$\epsilon(\omega) = \epsilon_0 \begin{pmatrix} \epsilon_{\mathrm{m}} & 0 & 0 \\ 0 & \epsilon_{\mathrm{m}}(1 + \chi(\omega)) & 0 \\ 0 & 0 & \epsilon_{\mathrm{m}} \end{pmatrix}, \tag{6.4}$$

where ϵ_{m} is the background permittivity of the dielectric layer. We decompose the

incoming wave along the x-axis and y-axis:

$$\mathbf{E_{0_i}} = |\mathbf{E_{0_i}}| \begin{pmatrix} -\sin\phi \\ \cos\phi \\ 0 \end{pmatrix} \tag{6.5}$$

Similarly to what was noted by Balagurov *et al.*,[150] the x-axis component experiences the permittivity $\epsilon_x = \epsilon_0\epsilon_\mathrm{m}$ and the resulting wave is weakly coupled to the structure while the y-axis component experiences the permittivity ϵ_y and the physics falls back to that of SC inside an hypothetical medium where $\epsilon_x = \epsilon_y = \epsilon_\mathrm{ord}$ where ϵ_ord is the ordinary (in-plane) component of the permittivity, yielding the LP and UP (see Appendix D Sections D.1 and D.2). The overall reflected electric field can then be written under the form:

$$\mathbf{E_r} = |\mathbf{E_{0_i}}| \begin{pmatrix} -r_x(\theta,\omega)\sin\phi \\ r_y(\theta,\omega)\cos\phi \\ 0 \end{pmatrix}, \tag{6.6}$$

where $r_x(\theta,\omega)$ and $r_y(\theta,\omega)$ can be fully determined using TMC. Since $r_x(\theta,\omega)$ and $r_y(\theta,\omega)$ are calculated using ϵ_x and ϵ_y, they do not yield in-phase reflected waves except in very specific cases where the dimensions of the cavity allow matching of the phase-changes experienced in the two directions. Following averaging, the total reflected intensity becomes the sum of the weighted contributions along the x and y directions:

$$\mathbf{R_r}(\phi,\theta,\omega) = |r_x(\theta,\omega)|^2 \sin^2\phi + |r_y(\theta,\omega)|^2 \cos^2\phi \tag{6.7}$$

which, as we will see in the next section, can lead to the existence of one to three minima (maxima for transmissivity) that require careful interpretation.

6.3 Simulations

We can identify two cases using Equation 6.7 and the coupling considerations made in the previous section: (i) The photonic mode broadening along the x-axis is comparable to $\hbar\Omega_{0y}$ and the LP and UP extrema in reflectivity/transmissivity observed along the y-axis mix with the photonic mode extremum along the x-axis to form two peaks for $\phi \in]0°, 90°[$ that converge towards the photonic mode energy as ϕ is increased; (ii) $\hbar\Omega_{0y}$ is intense enough so that the LP and UP along the y-axis are distant enough spectrally to not mix with the central photonic mode extremum along the x-axis resulting in three peaks for $\phi \in]0°, 90°[$.

Figure 6.2 (b) shows the simulated transmissivity at normal incidence ($\theta = 0°$) for an aluminium microcavity (Al thickness 100 nm at the bottom, 30 nm at the top) containing a 94.5 nm thick layer of material M1 whose susceptibility parameters are: $\epsilon_{\mathrm{m}} = 2.56$, $\hbar\omega_{\mathrm{ex}} = 3.25$ eV, $g_0 = 4 \times 10^{12}$ rad s^{-1} and $\gamma_{\mathrm{ex}} = 10^{12}$ rad s^{-1} (corresponding to a FWHM: $\hbar\gamma_{\mathrm{ex}} \sim 0.7$ meV). The cavity mode at normal incidence is slightly detuned $\hbar\Delta = \hbar(\omega_{\mathrm{ex}} - \omega_{\mathrm{cav}}) = 9.5$ meV and its broadening is: $\hbar\kappa = 110$ meV. The linewidths of the polaritons in the y direction are measured : $\mathrm{FWHM}_{\mathrm{UP/LP}} \sim 55$ meV which is correctly predicted by: $\mathrm{FWHM}_{\mathrm{UP/LP}} = \hbar\frac{\kappa+\gamma_{\mathrm{ex}}}{2}$.[65] (see Appendix D Section D.3), we derive: $\hbar\Omega_{0y} = 58$ meV which is resolved as $\hbar\Omega_{0y} > \hbar\frac{\kappa+\gamma_{\mathrm{ex}}}{2}$.

For $\phi \in]0°, 90°[$, since $\hbar\Omega_{0y} + \mathrm{FWHM}_{\mathrm{UP/LP}} < \hbar\kappa$, the transmissivity is composed of two peaks with each peak being the sum of one polariton and the overlapping photonic mode transmissivities mixed together thanks to the large value of $\hbar\kappa$: this situation corresponds to the first physical case previously identified. As ϕ is increased, the relative transmissivity of the photonic mode along the x-axis increases while the transmissivities of the polaritons along the y-axis decrease (following Equation 6.7) bringing the peaks closer until they give way to the cavity mode at 3.2405 eV for $\phi = 90°$.

The extrema dispersions are represented in Figure 6.2 (c), for $\phi \in]0°, 90°[$, we fur-

ther note that each transmissivity maximum derives from orthogonal contributions along the x-axis and the y-axis and as such does not characterize an eigenmode of the structure. This first transmissivity analysis offers an explanation to a previous experimental observation.[44]

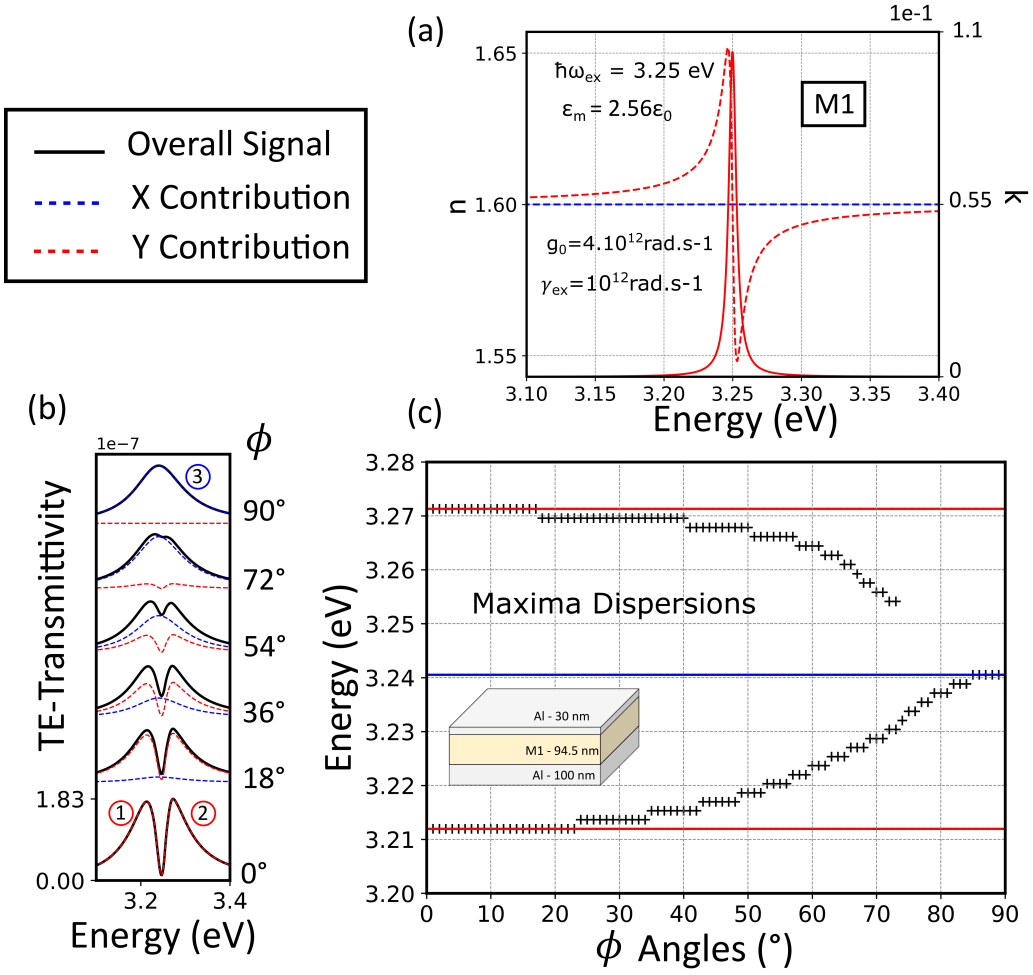


Figure 6.2: (a) In red and blue respectively (n_y, k_y) and (n_x, k_x) optical components for a simulated material M1 with susceptibility $\chi(\omega)$ using the physical parameters in the inset. Dashed lines give the real component of the complex refractive index $\tilde{n} = n + \mathrm{i}k$, solid lines the imaginary component. (b) Simulated TE-transmissivity at $\theta = 0°$ for $\phi = 0°, 18°, 36°, 54°, 72°, 90°$ of the microcavity displayed in the inset of (c), the black curves represents the total transmissivity which is a superposition of the transmissivities originating from the y direction (in dashed red) and x direction (in dashed blue). Peaks 1 and 2 (in dashed red) are the result of strong light matter coupling in the y direction, peak 3 is the photonic mode (in dashed blue) resulting from the uncoupled x direction. Note the increasing amplitude of peak 3 and decreasing amplitude of peaks 1 and 2 as ϕ is increased. (c) Dispersions of the TE-transmissivity maxima for ϕ varying by steps of 1°: the black crosses indicate the positions of the maxima for the two peaks in the main signal up until $\phi = 73°$, angle from which the two maxima are no longer resolved and replaced by a single maximum, in red the angle-independent positions of the two peaks induced by SC along the y-axis, in blue the angle-independent position of the photonic mode along the x-axis. Note that the maxima from the overall signal converge towards the photonic mode energy with increasing ϕ.

Figure 6.3 (b) shows the simulated transmissivity at normal incidence ($\theta = 0°$)

for an aluminium microcavity (Al thickness 100 nm at the bottom, 30 nm at the top) containing a 94.5 nm thick layer of material M2 whose susceptibility parameters are: $\epsilon_{\mathrm{m}} = 2.56$, $\hbar\omega_{\mathrm{ex}} = 3.25\,\mathrm{eV}$, $g_0 = 10^{14}\,\mathrm{rad.s^{-1}}$ and $\gamma_{\mathrm{ex}} = 4\times10^{13}$ $\mathrm{rad.s^{-1}}$ (corresponding to a FWHM $= \hbar\gamma_{\mathrm{ex}} \sim 26\,\mathrm{meV}$). For this structure, $\hbar\Omega_{0y}$ is fitted: $\hbar\Omega_{0y} = 1.38\,\mathrm{eV}$. This splitting represents $\sim 42\%$ of the exciton energy $\hbar\omega_{\mathrm{ex}} = 3.25\,\mathrm{eV}$ bringing the system into USC along the y-axis. $\hbar\kappa$ is this time more than one order of magnitude smaller than $\hbar\Omega_{0y}$ and $\hbar\Omega_{0y} + \mathrm{FWHM_{UP/LP}} \gg \hbar\kappa$, the transmissivity now resolves three peaks for $\phi \in]0°, 90°[$ which are the two polaritons and the photonic mode transmissivities weighted by ϕ (Equation 6.7). As ϕ is increased, the relative transmissivity of the photonic mode along the x-axis increases while the transmissivities of the polaritons along the y-axis decrease changing the relative heights of the peaks without spectrally shifting them corresponding to the second physical case previously identified. The extrema positions are represented in Figure 6.3 (c).

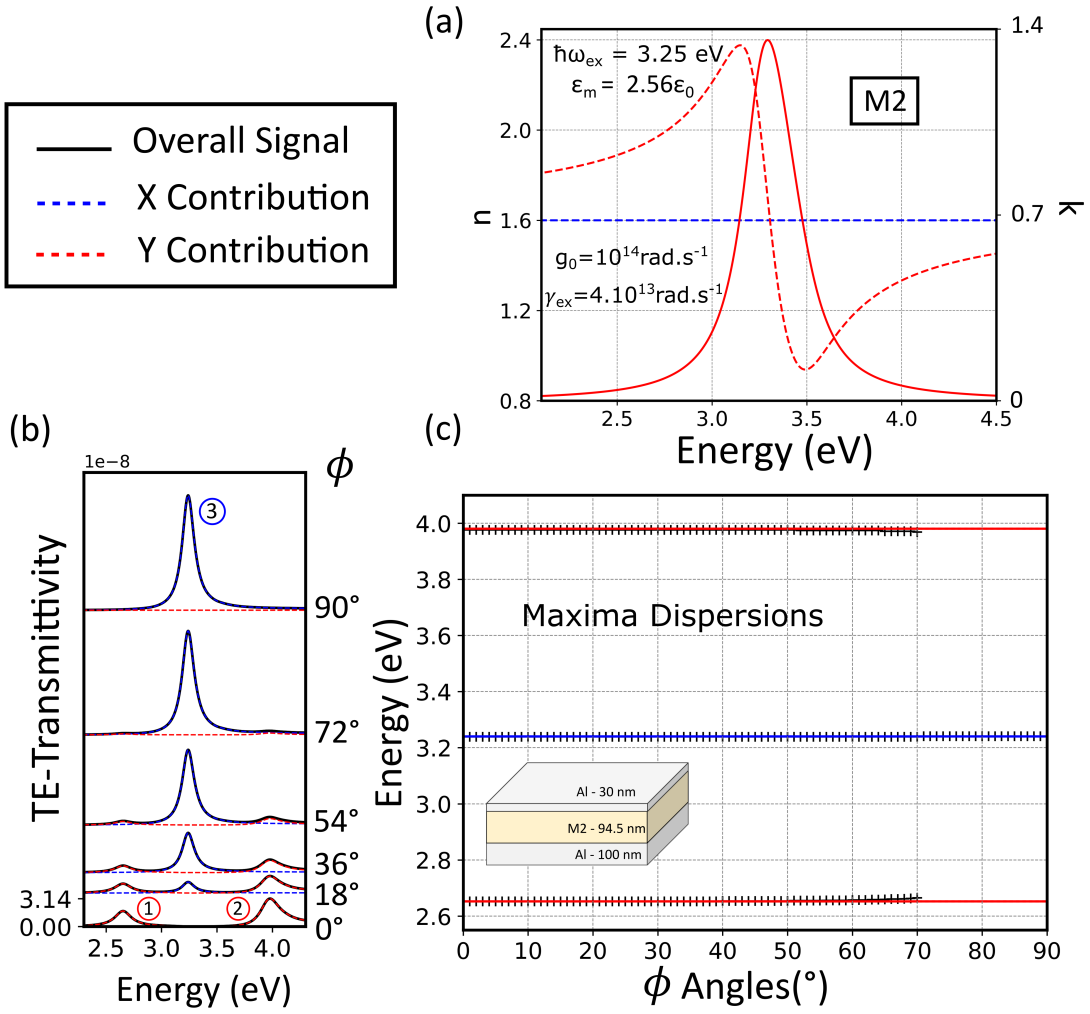


Figure 6.3: (a) In red and blue respectively $(n_y,\ k_y)$ and $(n_x,\ k_x)$ optical components for a simulated material M2 with susceptibility $\chi(\omega)$ using the physical parameters in the inset. Dashed lines give the real component of the complex refractive index $\tilde{n} = n + \mathrm{i}k$, solid lines the imaginary component. (b) Simulated TE-transmissivity at $\theta = 0°$ for $\phi = 0°, 18°, 36°, 54°, 72°, 90°$ of the microcavity displayed in the inset of (c), the black curves represents the total transmissivity which is a superposition of the transmissivities originating from the y direction (in dashed red) and x direction (in dashed blue). Peaks 1 and 2 (in dashed red) are the result of USC in the y direction, peak 3 is the photonic mode (in dashed blue) resulting from the uncoupled x direction. Note the increasing amplitude of peak 3 and decreasing amplitude of peaks 1 and 2 as ϕ is increased. (c) Dispersions of the TE-transmissivity maxima for ϕ varying by steps of 1°: the black crosses indicate the angle-independent positions of the maxima for the well resolved three peaks in the main signal up until $\phi = 70°$, angle from which the two maxima from the y direction are no longer visible, in red the angle-independent positions of the two peaks induced by SC along the y-axis, in blue the angle-independent position of the photonic mode along the x-axis. Note that the positions of the maxima in the main signal matches the positions of peak 1, 2 and 3.

We note that the TE-transmissivity values obtained in Figure 6.2 (b) and Figure 6.3 (b) are too low to be actually measured. Figure 6.4 (a) and (b) represent simulated TE-reflectivities for similar structures differing in a 99.5 nm thick cavity layer and the measurement being performed at $\theta = 30°$ to keep the detuning at $\Delta = 10$ meV. The origin of the minima observed are analog to the maxima in transmissivity and the interpretation is identical to the one previously made. We then proceed in the following section to fabricate and measure a microcavity with similar characteristics to the one showed in Figure 6.3 (c), corresponding to the second physical case previously identified.

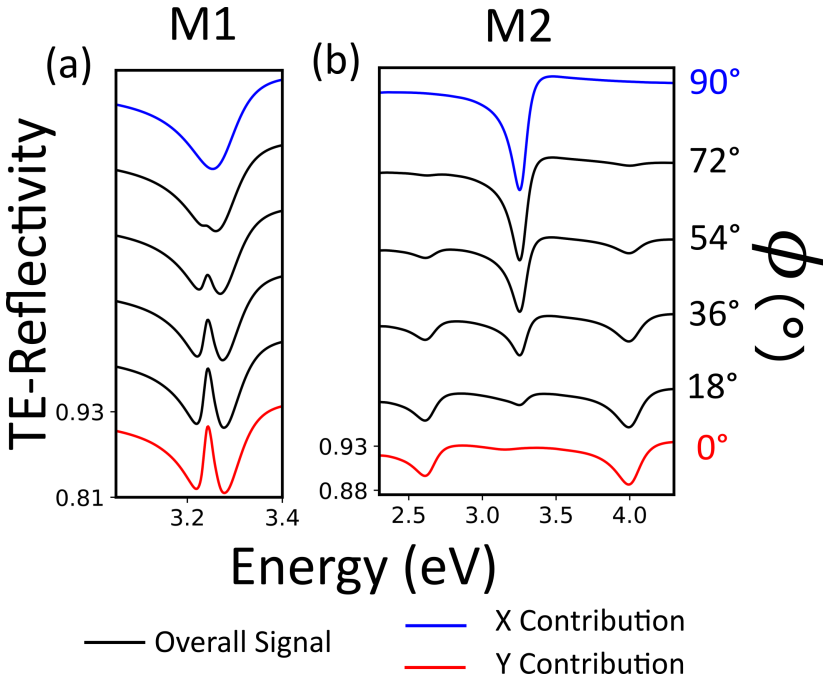


Figure 6.4: Simulated TE-reflectivity at $\theta = 30°$ for $\phi = 0°, 18°, 36°, 54°, 72°, 90°$ of the microcavities displayed in the inset of Figure 6.2 (c) for (a) and Figure 6.3 (c) for (b) with a 99.5 nm material layer thickness. In both cases the simulated values at $\phi = 0°$ (in solid red) correspond to the reflectivity contributions from the LP and UP in the y direction, the simulated values at $\phi = 90°$ (in solid blue) correspond to the reflectivity contribution from the photonic mode in the x direction. For other values of ϕ, two main minima are visible in (a) and get closer in energy with increasing values of ϕ as the relative reflectivity contribution along the y-axis decreases and the one along the x-axis increases until only one peak corresponding to the photonic mode along the x-axis is visible. In (b) three main minima are visible but do not shift in energy with increasing values of ϕ as the relative reflectivity contribution along y decreases and the one along x increases.

6.4 Experimental Comparison with a Microcavity Containing an Oriented LCCP

We fabricated a microcavity containing a layer of PFO whose chains were oriented along y using the fabrication protocol described in Chapter 5, the structure and orientation are shown in Figure 6.5 (a) and (b) and the TE-reflectivity was measured for different values of ϕ and θ. The coupling strength for E parallel to the y-axis is almost identical to the one in Chapter 5 (see Appendix D Section D.4 for derivation), TMC confirm the dimensions of the structure and from both simulations and experiments, zero detuning between cavity mode and exciton (centered at 3.25 eV) is reached for $\theta = 46°$.

A few differences exist between this system and the simulations presented in the previous section: (i) The permittivity of the embedded layer is not strictly identical to the one used in Equation 6.4 as there exists remaining optical activity along the x-axis, however much less intense than along the y-axis; (ii) The exciton spectral distribution is inhomogeneously broadened (as a result of deviations from the mean fluorene-fluorene single bond torsion angle ($\sim 135°$)[102]) but this broadening does not alter the value of $\hbar\Omega_{0y}$.[76,77]

Figure 6.5 (c) shows the simulated TE-transmissivity for $\theta = 46°$ for increasing values of $\phi = 0°, 18°, 36°, 54°, 72°, 90°$. At $\phi = 0°$, E is parallel to y and we observe two intense maxima (1 and 3) that correspond to the LP and UP. Interestingly, we also observe the formation of another peak (2) close to the LP at ~ 2.95 eV which corresponds to a further LP brought about by SC of the second-order longitudinal mode supported by the cavity with the excitons (this coupling is made possible thanks to the intense absorption in the y direction), this shoulder peak is shown in more detail in the inset of Figure 6.5 (c).

For $\phi \in]0°, 90°[$, we observe the formation of four maxima. The two most outer ones

in energy correspond to the LP and UP transmissivities identified as peaks 1 and 3 created by SC of the lowest lying cavity mode to the excitons. Given the large value of $\hbar\Omega_{0y} = 1.47$ eV compared with the cavity mode broadening $\hbar\kappa = 220$ meV those maxima are similar in nature to those in Figure 6.3 (b) and consequently do not shift in energy as ϕ is increased.

The two remaining maxima are better understood by examining $\phi = 90°$. For this angle, E is perpendicular to the y-axis and the remaining optical activity along the x-axis causes the photonic mode to split around the exciton at 3.25 eV (peak 4 at 3.0 eV and peak 5 at 3.67 eV). Maxima 4 and 5 are not clearly resolved since the oscillator strength along the x-axis is not intense enough following orientations of the PFO chains, it was demonstrated in Ref 22 that the broad and unstructured emission from this structure confirmed weak coupling along the x-axis.

For $\phi \in]0°, 90°[$, the second lowest maximum in energy is the superposition of peaks 2 and 4, 0.05 eV apart in energy, whose respective broadenings allow for their mixing, with the overall maximum seemingly shifting to lower energies as ϕ is increased. Finally, the third lowest maximum in energy corresponds to peak 5 and does not shift with increasing ϕ. Figure 6.5 (d) shows the experimental measurement of the TE-reflectivity at $\theta = 46°$. All the minima are similar to the maxima identified using the simulated TE-transmissivity in Figure 6.5 (c) and their spectral positions is confirmed by simulating the TE-reflectivity in Figure 6.5 (e).

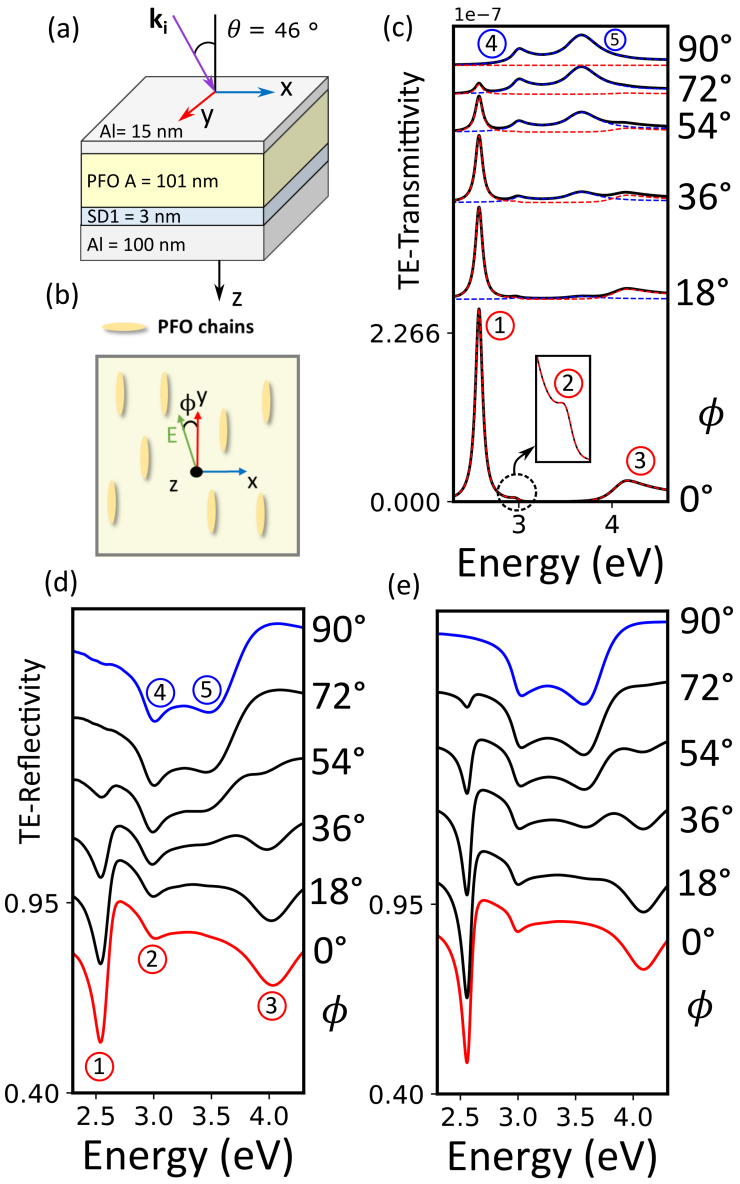


Figure 6.5: (a) Schematic of the microcavity structure fabricated. The PFO chains were oriented (A) using the protocol presented in Chapter 5. The TE-reflectivity is measured at $\theta = 46°$. (b) Bottom view of the orientation of the PFO chains along the y-axis, the measurement is performed by rotating the sample relative to the electric field E (in green), forming the azimuthal angle ϕ. (c) Simulated TE-transmissivity at $\theta = 46°$ for $\phi = 0°, 18°, 36°, 54°, 72°, 90°$, the black curves represent the total transmissivity which is a superposition of the transmissivities originating from the y direction (in dashed red) and x direction (in dashed blue). Peaks 1, 2 and 3 (in dashed red) are the result of USC along y for the lowest lying energy cavity mode (1 and 3) and the second lowest lying energy cavity mode (2). Peak 4 and 5 are the result of a splitting of the photonic mode in the x direction due to remaining optical activity. Further explanations can be found in text. (d) Measured TE-reflectivity at $\theta = 46°$ for $\phi = 0°, 18°, 36°, 54°, 72°, 90°$, the numbered minima correspond to the ones simulated in transmissivity. (e) Simulated TE-Reflectivity at $\theta = 46°$ for $\phi = 0°, 18°, 36°, 54°, 72°, 90°$ confirming the experimental observations.

6.5 Conclusion

We have carefully examined the effects of rotating the electric field with respect to ϕ for an incident TE-polarized wave on the measured reflectivity and transmissivity of a microcavity containing strongly coupled excitons with in-plane uniaxially oriented transition dipole moments. We have demonstrated that when the cavity damping $\hbar\kappa$ is broad enough compared to $\hbar\Omega_{0y}$, TE-transmissivity and reflectivity present two extrema for $\phi \in]0°, 90°[$ which get closer in energy as ϕ is increased. While this resembles the result obtained upon increase of the polar angle θ when the transition dipole moment has no preferential in-plane orientation, these extrema are the superposition of separate intensities originating from the propagation of two waves experiencing either SC along the y-axis or weak coupling along the x-axis but mixed thanks to the losses $\hbar\kappa$. This experimental observation was reported for oriented carbon nanotubes[44] and this work offers a physical interpretation. In the case where $\hbar\Omega_{0y}$ is much larger than the cavity damping, we showed that the measured reflectivity and transmissivity present three extrema for $\phi \in]0°, 90°[$ which are the separate contributions from the different directions, as such they do not experience any spectral shifting with increasing ϕ. We supported our analytical model by fabricating and measuring the TE-reflectivity from a metallic microcavity containing an oriented layer of liquid-crystalline PFO and interpreted the different extrema observed by considering separately the contributions from the x and y directions.

Chapter 7

Summary And Outlook

In Chapter 4 and 5, acting solely on the intra- (respectively inter-) chain geometry of semiconducting polymers we have introduced novel and compatible experimental techniques which enable enhancement, tuning and polarization sensitivity over light-matter interaction.

In Chapter 4, control was exerted over the exciton-polariton physics via the generation of increasing fractions of β-phase chain segments in an otherwise glassy-phase PFO cavity, allowing a systematic study of the dependence of the mode characteristics and resulting light emission properties on the relative exciton populations. The emission characteristics were engineered to refine the already attractive USC effects, yielding, for example, essentially dispersion-free LP emission for both polarizations at modest fractions (e.g. 12.3 %) of β-phase chain segments.

As other studies have shown,[22,24,29–31] the metal-polymer-metal microcavity structure employed provides a format suited to the electrical injection of carriers, thereby offering the prospect of efficient, angle-insensitive, high colour saturation, wholly-polarized LEDs with emission coming from the dispersion-free LP branch.[8] Since the splitting between the LP and MP is governed by varying the intensity of the resolved β-phase (0-0) vibronic peak, modifying the energy landscape to study vibronically assisted

scattering mechanisms towards efficient exciton-polariton lasing (demonstrated for the glassy-phase of PFO[99]) and non-equilibrium BEC[87] may be possible. The study of PFO and its β-phase in a high-Q microcavity might also allow quantitative understanding of population mechanisms for the LP ground state in organic condensates.

In Chapter 5, we have fabricated organic microcavities containing the LCCPs: PFO, F8BT and F6T2, aligned using thin SD1 photoalignment layers. Transition dipole alignment allowed a systematic increase in coupling strength for light polarised parallel to the polymer chain direction, with $\hbar\Omega_{\mathrm{R}}$ reaching as high as 1.80 eV for F6T2, the largest Rabi-splitting value comparable to photon energies in the red part of the visible spectrum. This value further led to the highest coupling ratio $\eta = 65\%$, reported to date for a solid-state system.[33,34] TE-polarized, angle-resolved PL, with excitation $\boldsymbol{E}$-vector parallel to the chain orientation direction, revealed increased interaction strengths while the absence of polariton branches from the TM-polarized reflectivity together with weak or absent PL emission confirmed polarization dependent coupling strengths.

In Chapter 6, we theoretically and experimentally investigated the reflectivity and transmissivity of an incident TE-polarized wave on a microcavity containing excitons with in-plane uniaxially oriented transition dipole moments. We demonstrated that when the cavity damping $\hbar\kappa$ is broad enough compared to $\hbar\Omega_y$, the Rabi-splitting energy in the direction of the alignment, TE-transmissivity and reflectivity present two extrema for $\phi \in]0°, 90°[$ which get closer in energy as ϕ is increased but highlighted that those extrema are the results of intensities originating from two orthogonal waves and that a careful interpretation of those measurements is essential to preserve physical meaning.

For microcavities containing oriented LCCPs, the opportunity to reach coupling ratios closer to 90% exists if the alignment can be achieved with excitons at lower energies. Besides, several unique research alleys exist for anisotropic polaritons: chain orien-

tation could enable table-top observation of topologically protected edge modes in plexcitonic systems[176] and the possibility to align SD1 at mesoscopic scales[165–167] allows for a local orientation of the polymer chains that could lead to fabrication of the missing NOT gate in polaritonic optical logic thanks to a spontaneous splitting between TE and TM polarizations.[2,177,178]

The combination of the techniques presented in this thesis should also enable the fabrication of complex energy landscapes, for example by generating local segments of controlled fractions of oriented β-phase in PFO,[112] which could help address challenges in quantum simulation.[179] We further expect that a wide range of polarization sensitive devices (photodiodes,[180] transistors[17]) and phenomena, including non-equilibrium BEC and exciton-polariton lasing (recently demonstrated with pentafluorene[181] and PFO[99]) will take advantage of both energy and polarization control. The spontaneous polarization observed during lasing and condensation could for instance be manipulated using molecular orientation and the threshold could be reduced by increasing the number of participating chromophores through chain orientation in lower dimensionality structures.[179]

Appendices

Appendix A

Weak Coupling and the Purcell Effect

The weak coupling regime has been identified in Section 2.3.1 for:

$$g_{\mathrm{res}} < \frac{|\gamma_{\mathrm{ex}} - \gamma_{\mathrm{cav}}|}{2}. \tag{A.1}$$

Since the losses of the system are the dominating process, a perturbative approach correctly describes the transition rates inside the microcavity with Fermi's golden rule,[182] which expresses the transition rate Γ of an excited state as a function of the density of states in the final state $D_{\mathrm{f}}(E)$ resulting in:

$$\Gamma = h|\boldsymbol{\mu}_{\mathrm{e,f}}|^2 D_{\mathrm{f}}(E). \tag{A.2}$$

The difference with spontaneous emission in free space is that D_{f} is now shaped by the cavity and can effectively increase (resp. decrease) the density of states available at resonance (resp. away from resonance), this is the Purcell effect.[183] The transition rate increase at resonance is proportional to the Purcell factor F_{P}:[183]

$$\frac{\Gamma_{\mathrm{cav}}}{\Gamma_0} \propto F_{\mathrm{p}} = \frac{3}{4\pi^2}\left(\frac{\lambda_c}{n_c}\right)^3 \frac{Q}{V}. \tag{A.3}$$

The ability to control the decay rates thanks to the Purcell effect has been extensively used.[184,185]

Appendix B

Supporting Information: Chapter 4

B.1 PFO Thin Film Optical Properties

B.1.1 Absorption and Photoluminescence Spectra

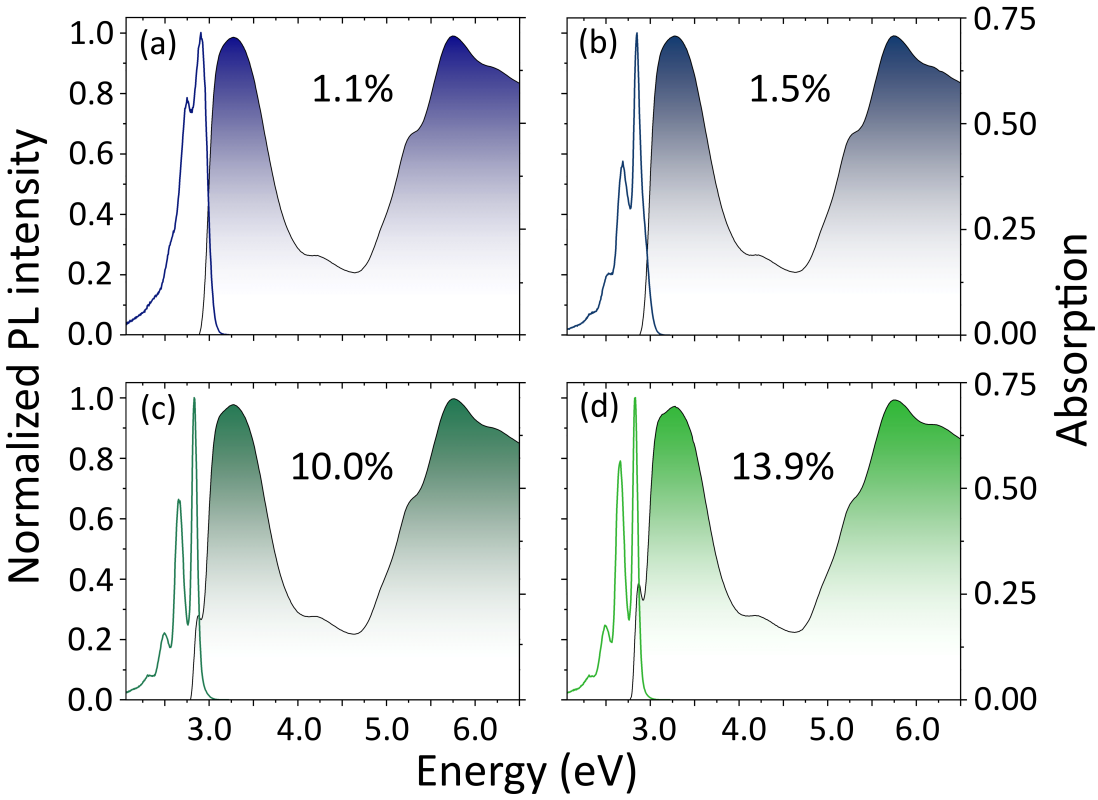


Figure B.1: Absorption and PL spectra for spin-coated PFO films containing: (a) 1.1, (b) 1.5, (c) 10, and (d) 13.9% β-phase chain segments.

B.1.2 Optical Constants

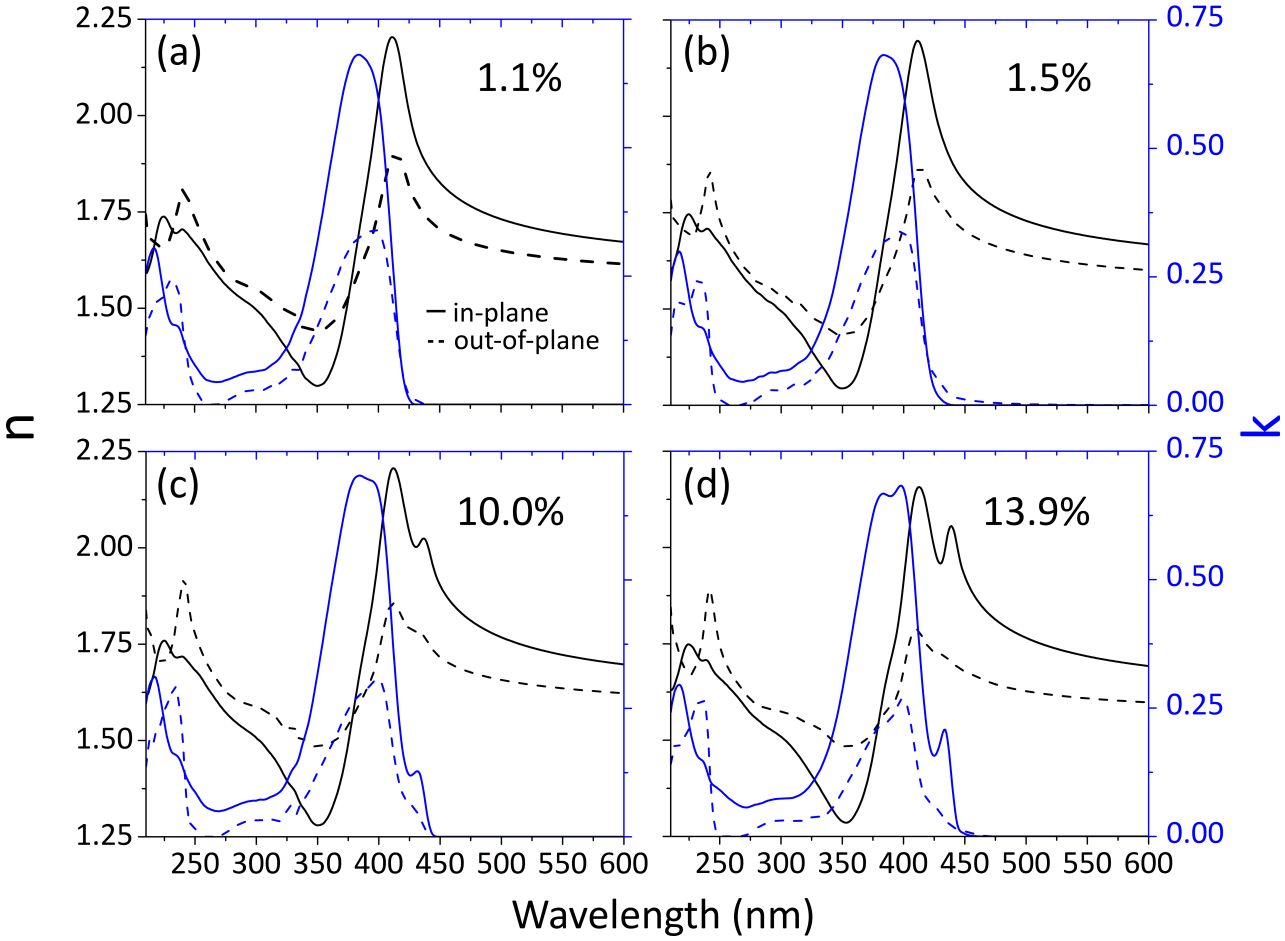


Figure B.2: Optical constants for spin-coated PFO thin films containing: (a) 1.1, (b) 1.5, (c) 10, and (d) 13.9% β-phase chain segments. The black and blue lines are, respectively, the real (n) and imaginary (k) parts of the complex refractive index, $\tilde{n} = n + ik$. Solid lines give in-plane (n_{xy}, k_{xy}) and dashed lines out-of-plane (n_z, k_z) values.

B.2 Metal-PFO-Metal Exciton-Polariton Physics: Measurement and Simulation

B.2.1 Angle-resolved TE-polarized Reflectivity Maps

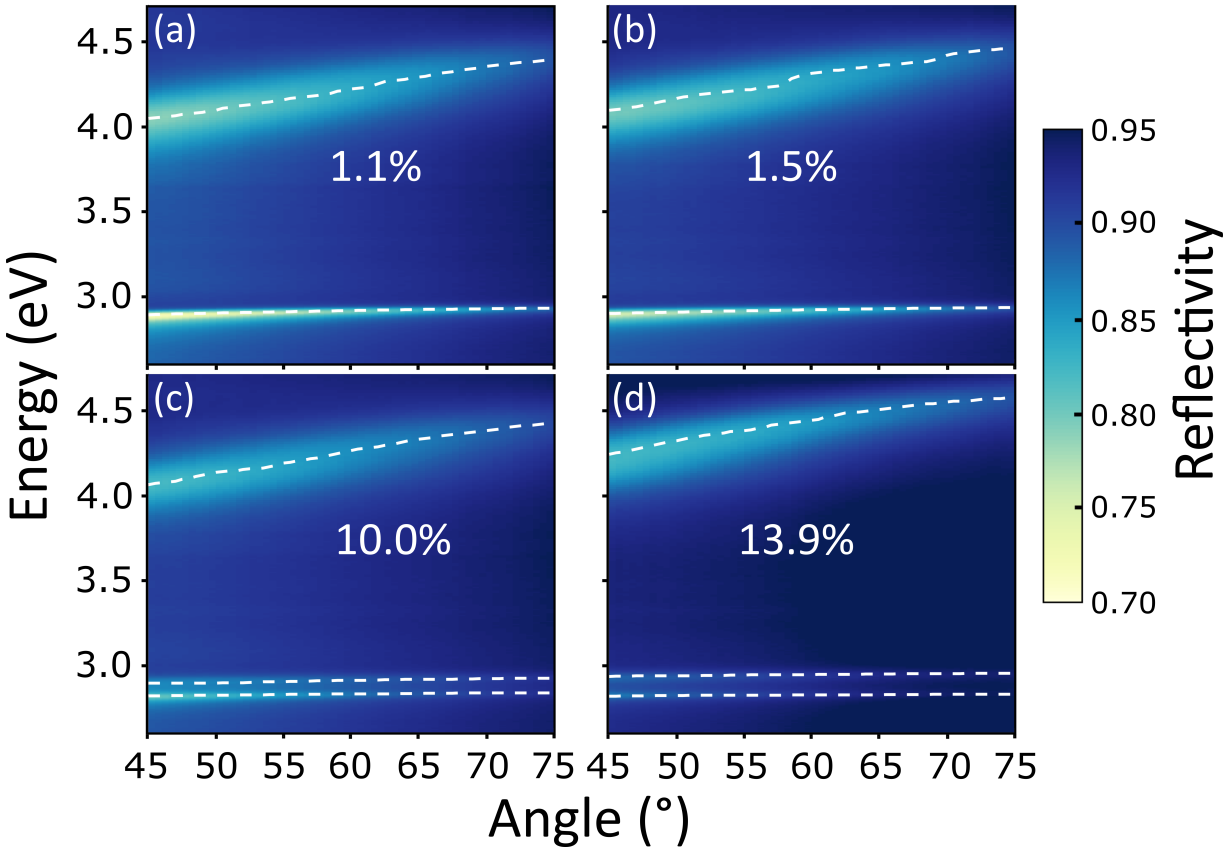


Figure B.3: Experimental, angle-resolved, TE-polarized reflectivity maps for microcavities containing (a) 1.1, (b) 1.5, (c) 10, and (d) 13.9% β-phase chain segments. The overlaid, white dashed lines are the reflectivity minima dispersion curves obtained from TMC.

B.2.2 Angle-resolved TM-polarized Reflectivity Maps

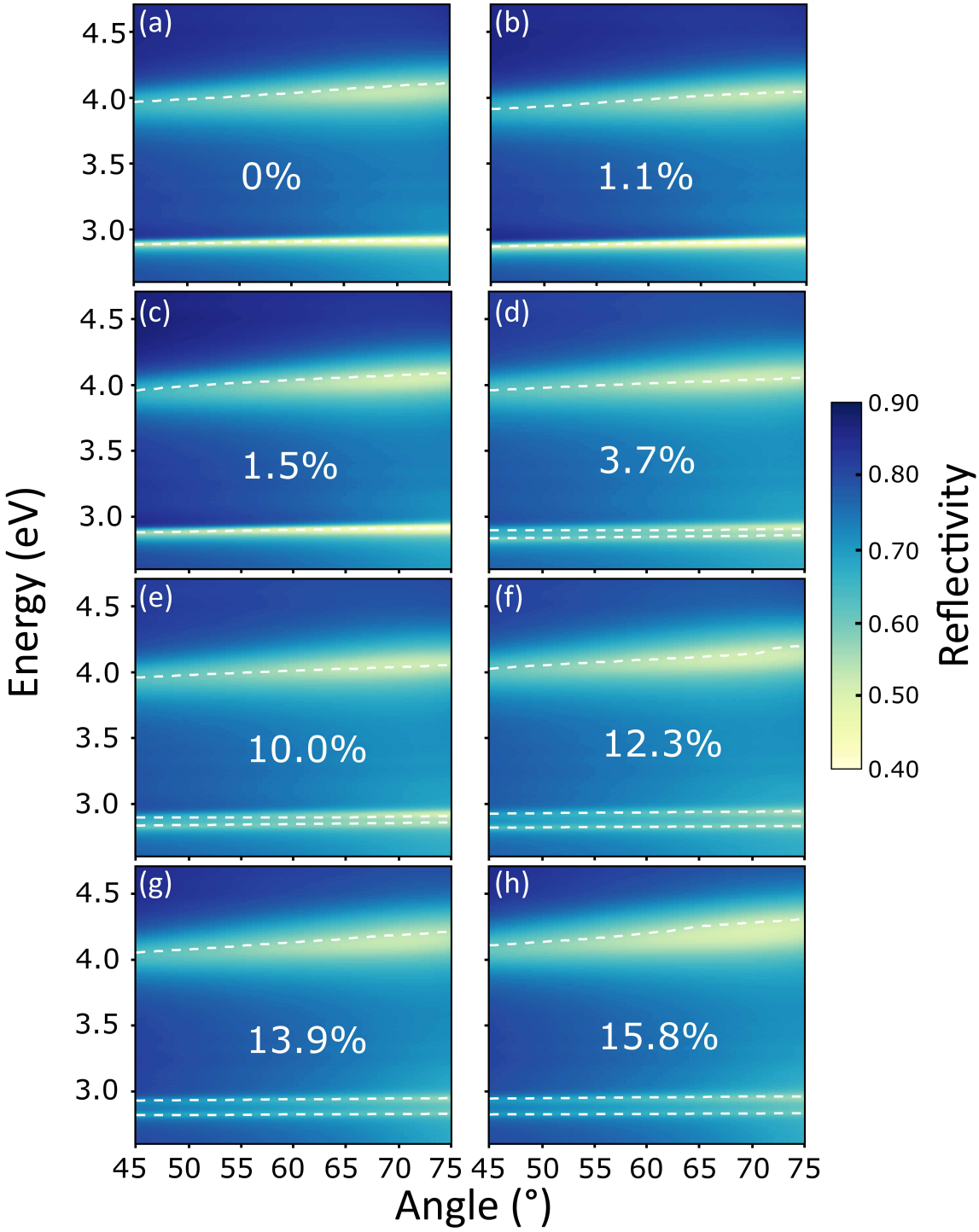


Figure B.4: Experimental, angle-resolved, TM-polarized reflectivity maps for microcavities containing (a) 0, (b) 1.1, (c) 1.5, (d) 3.7, (e) 10.0, (f) 12.3, (g) 13.9 and (h) 15.8% β-phase chain segments. The overlaid, white dashed lines are the reflectivity minima dispersion curves obtained from TMC.

B.2.3 Photoluminescence Spectral Characteristics

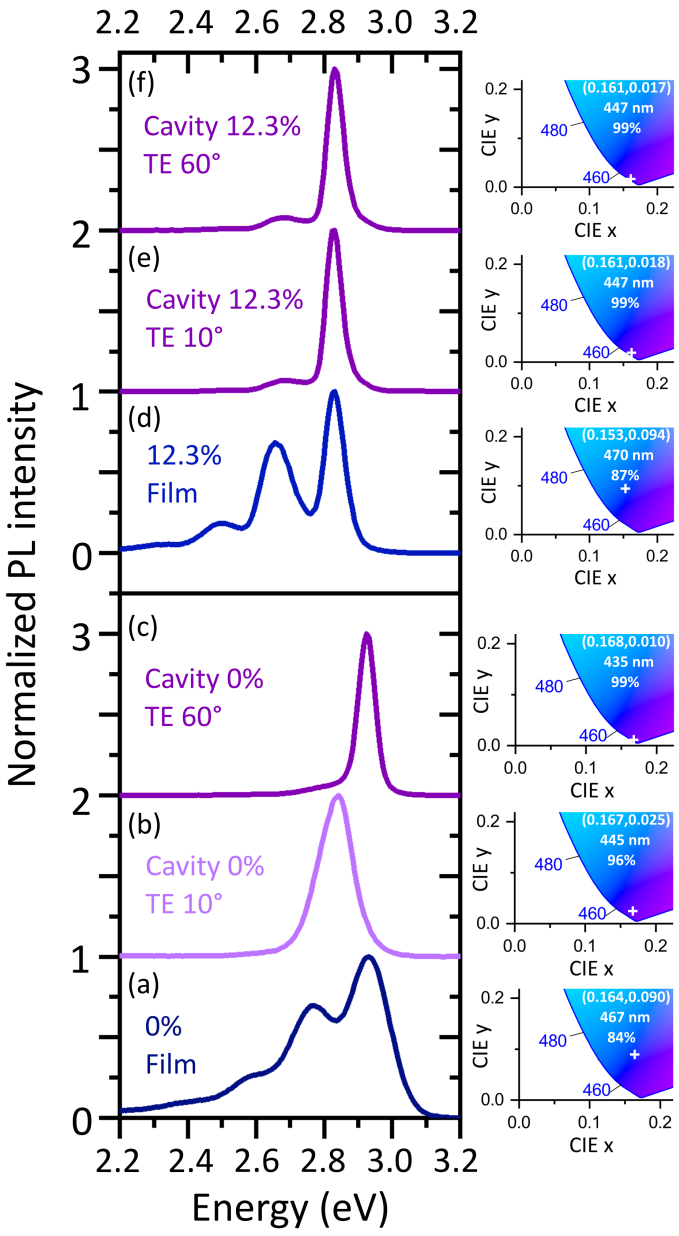


Figure B.5: Thin film PL spectra for (a) 0% and (d) 12.3% film samples, and TE-polarized lower polariton PL spectra for (b) and (c) 0% and (e) and (f) 12.3% cavities. The LP emission from cavities is shown for both 10° ((b) and (e)) and 60° ((c) and (f)) to illustrate the spectral dispersion as a function of angle, which is weak for the 0% cavity and absent for the 12.3% cavity. To the right of each spectrum is a CIE (x,y) plot with the corresponding coordinates marked by a cross. The numerical values are also reported together with the dominant wavelength (nm) and saturation (%).

B.3 Photon-mode Dispersion

In our study, at 75° incidence relative to the plane normal for the TE-polarization, $\frac{\sin^2(\theta)}{n_b^2} \sim 0.36$. Being close to 1, this could create a noticeable error on the photon dispersions and in turn on the computed dispersions for the polaritons. In order to study the error arising from this approximation we refer to the original derivation[141] of the cavity mode in a Metal-Insulator-Metal (MIM) structure and a more recent analysis dedicated to exciton-polariton physics.[142] The exact trigonometric equations governing the TE and TM photon modes are:[142]

$$\text{TE} : \cot\left(\frac{k_d L}{2}\right) = \frac{k_d}{\kappa_p} \tag{B.1}$$

$$\text{TM} : \cot\left(\frac{k_d L}{2}\right) = -\frac{\kappa_p \epsilon_d}{k_d \epsilon_p} \tag{B.2}$$

Where κ_p and k_d, respectively the z-components of the wavevector inside the metal and inside the dielectric are defined by:

$$\kappa_p(\omega, k) = \sqrt{k^2 - \frac{\omega^2}{c^2}\epsilon_p(\omega)} \tag{B.3}$$

$$k_d(\omega, k) = \sqrt{\frac{\omega^2}{c^2}\epsilon_d(\omega) - k^2} \tag{B.4}$$

Where ϵ_p is the permittivity of Al[186] and ϵ_d is the background permittivity of the dielectric film. The deviations observed in our study are notable only for TE-polarization, on which we therefore focus. In order to compare the results obtained with and without the approximation we performed the fitting procedure for our microcavities using Equation B.1. We numerically solved Equation B.1 at each angle for film thicknesses in the range 80 to 100 nm (0.1 nm step) and for ϵ_d values in the range 2 to 3.5 (0.01 step). We then used these datasets in the fitting procedure, leading to a variation (see Figure B.6 for the 0% microcavity) of at most 0.02 eV that is too

small to explain the observed deviations ~ 0.1 eV.

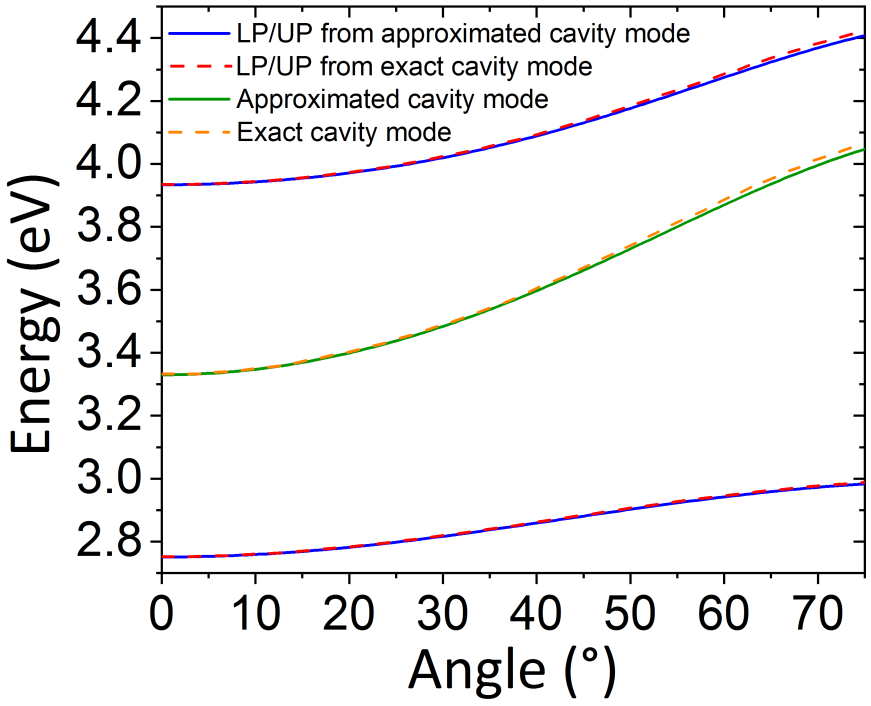


Figure B.6: Exact and approximated TE-polarized cavity mode fittings for the 0% microcavity. The fitted thickness obtained using the exact cavity mode (Equation B.1) is 84.5 ± 1 nm in good agreement with $\hbar\omega_{\mathrm{cav}}(0) = 3.32$ eV (corresponding to a thickness of 84 nm for $n_{\mathrm{eff}_{\mathrm{TE}}} = 1.7$ using TMC) for the approximated cavity mode. The fitted background permittivity is found to be $\epsilon_{\mathrm{d}} = 2.89$ using both exact and approximated cavity modes. The small differences between the two methods at higher angles (towards 70° for the UP and cavity modes is at most 0.02 eV and therefore not enough to explain the deviations ($\sim$0.1 eV) between our experimental and analytical results.

Appendix C

Supporting Information: Chapter 5

C.1 Fabrication of Aligned PFO in its β-phase

We present in what follows a fabrication protocol for the alignment of the β-phase of PFO. The protocol is first identical to the one described in Section 5.3.1. Following orientation of PFO in its glassy phase the sample is exposed to saturated toluene vapor at 50° for 24 hours with the resulting optical constants presented in the next section.

C.2 Optical constants of non-aligned (NA) and aligned (A) LCCP films

Figure C.1 displays the optical constants for the LCCP films used in Chapter 5. Figure C.2 shows the optical constants for a film of oriented β-phase PFO, the optical constants reveal the formation of a shoulder on the red edge of the absorption and as expected, its pronounced alignment in the y direction.

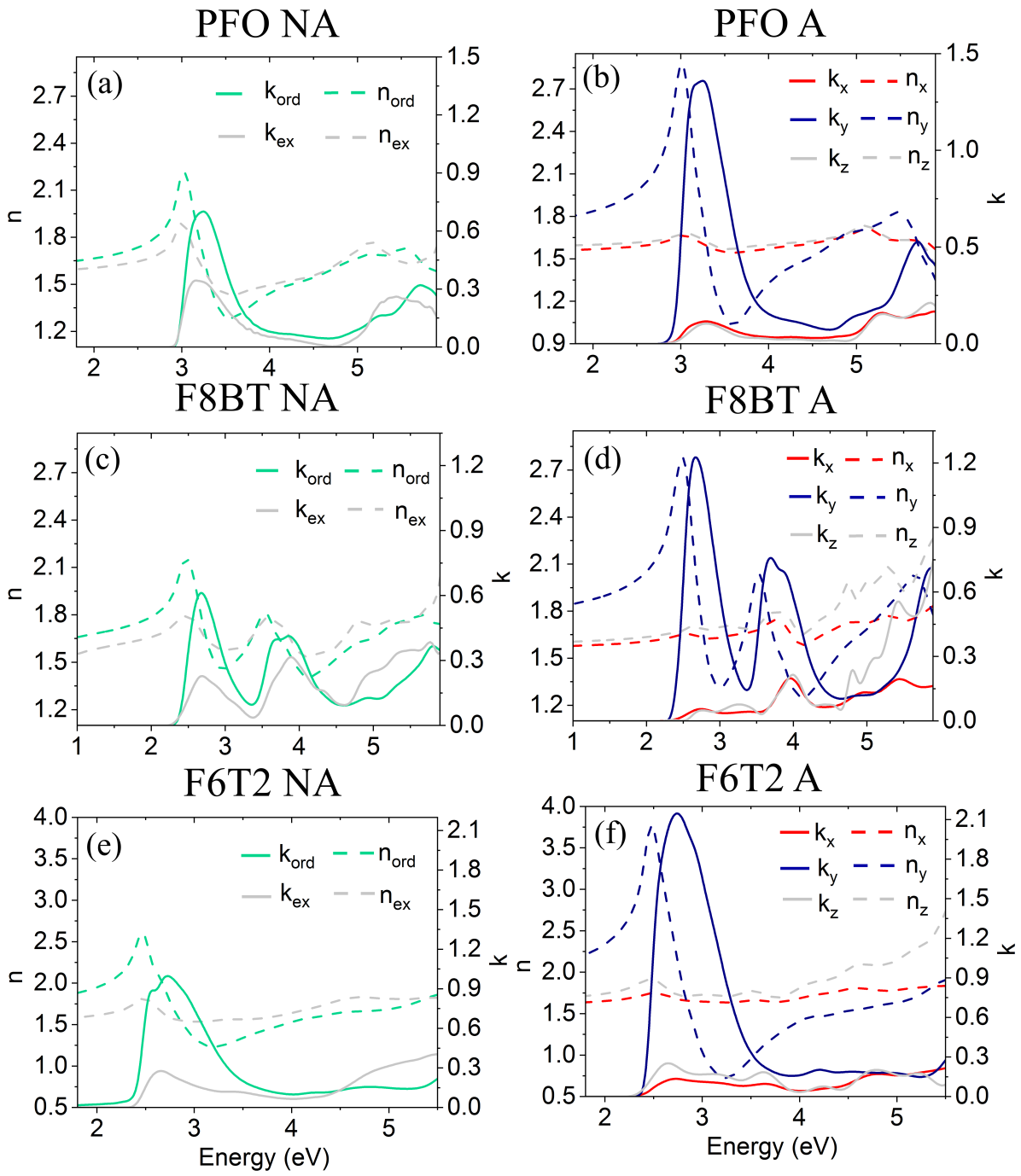


Figure C.1: In green and grey respectively in-plane (n_{ord}, k_{ord}) and out-of-plane (n_{ex}, k_{ex}) optical components for non-aligned PFO (a), F8BT (c), F6T2 (e) thin films. In blue, red and grey respectively in-plane in the aligned polymer chains direction (n_y, k_y), in-plane in the direction perpendicular to the chains (n_x, k_x) and out-of plane (n_z, k_z) optical components for aligned PFO (b), F6T2 (c), F8BT (d). Dashed lines give the real component of the complex refractive index $\tilde{n} = n + ik$, solid lines the imaginary component.

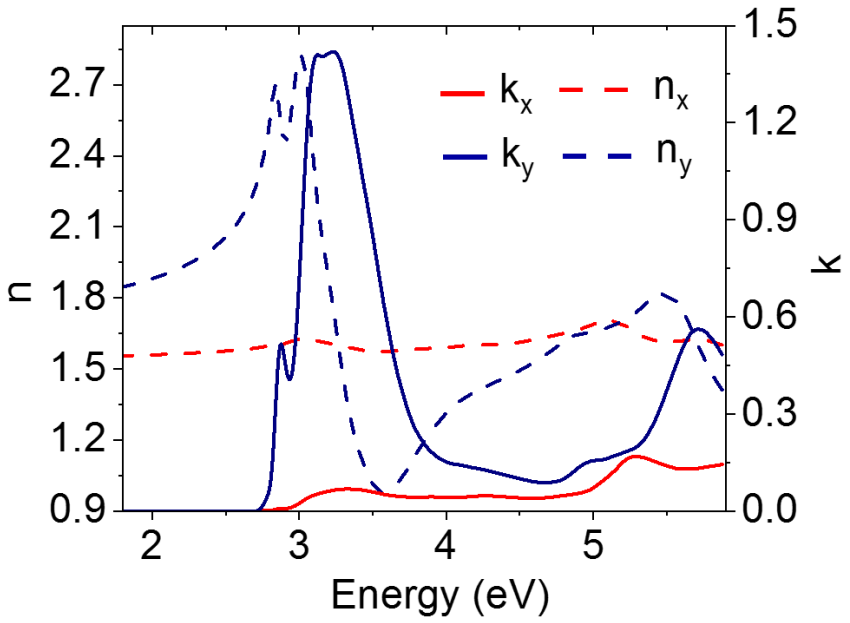


Figure C.2: In-plane optical components of a PFO film following alignment and exposition to toluene vapour for 24 hours are shown in blue for n_y, k_y (parallel to the alignment direction) and in red for n_x, k_x (perpendicular to the alignment direction). Dashed lines give the real component of the complex refractive index $\tilde{n} = n + ik$, solid lines the imaginary component. Note the pronounced peak in absorption at ~2.87 eV once the β-phase has been formed in the alignment direction.

C.3 Angular variation of TE- and TM-polarized transmissivities at normal incidence for a thin film of aligned PFO

We measure the TE- and TM-polarized transmissivities of a thin film of aligned PFO at normal incidence while rotating the sample. The sample angle is defined as the angle formed between the direction x (which is the direction of the polarizer that was

used during the alignment of SD1) and the p polarization. We define the ratio:

$$R_{\mathrm{T}} = \begin{cases} \frac{\int_{E_{\min}}^{E_{\max}} T_{\mathrm{ref}} - T_{\mathrm{s}} \mathrm{d}E}{\int_{E_{\min}}^{E_{\max}} T_{\mathrm{ref}} - T_{\mathrm{p}} \mathrm{d}E} \text{ if } T_{\mathrm{s}} > T_{\mathrm{p}}, \\ \frac{\int_{E_{\min}}^{E_{\max}} T_{\mathrm{ref}} - T_{\mathrm{p}} \mathrm{d}E}{\int_{E_{\min}}^{E_{\max}} T_{\mathrm{ref}} - T_{\mathrm{s}} \mathrm{d}E} \text{ if } T_{\mathrm{s}} \leqslant T_{\mathrm{p}} \end{cases} \tag{C.1}$$

where T_{ref} is the transmittance obtained for a quartz substrate, $E_{\min}$ and $E_{\max}$ the energies around the exciton distribution (for PFO: $E_{\min} = 2.10$ eV and $E_{\max} = 3.80$ eV). Figure C.3 shows the values of R_{T} for sample angles ranging from $-15°$ to $105°$. Two minimas of around 0.2 are clearly observable at $0°$ and $90°$ while unity is reached precisely at $45°$. These values confirm the alignment of the average transition dipole moment along the y direction (direction perpendicular to the polarizer direction used for the alignment of SD1) and justify the use of x and y as principal coordinates.

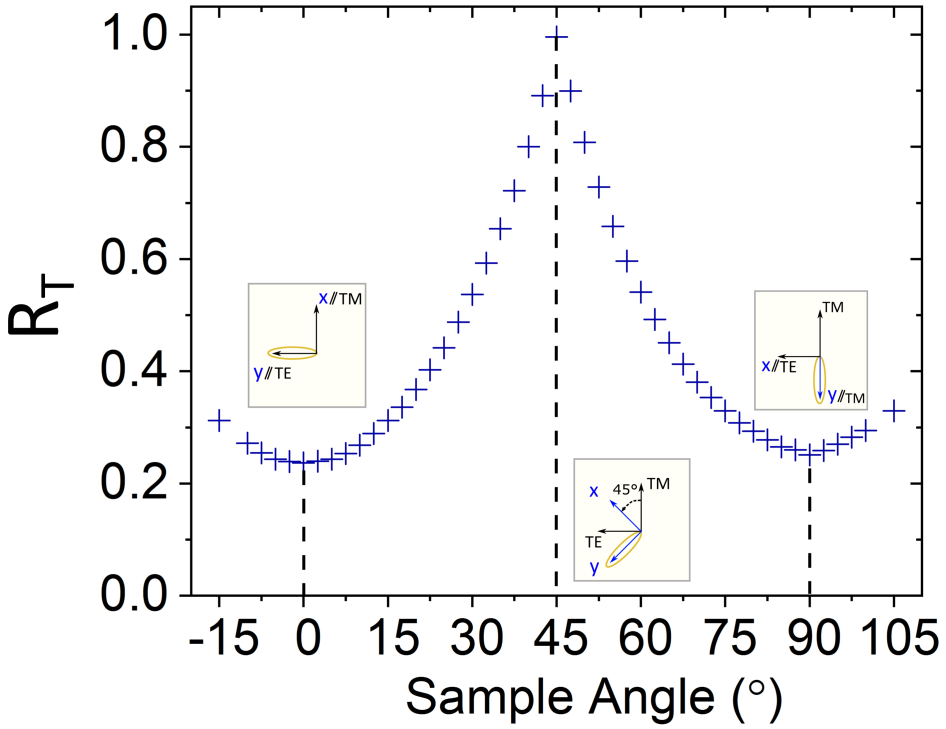


Figure C.3: R_{T} vs sample angle as defined in text. Two minimas are clearly observed at $0°$ and $90°$ while a maximum is observed at $45°$. These three specific geometries correspond to the represented experiment schematics.

C.4 Experimental and Analytical Results for Non-aligned F8BT and PFO Microcavities

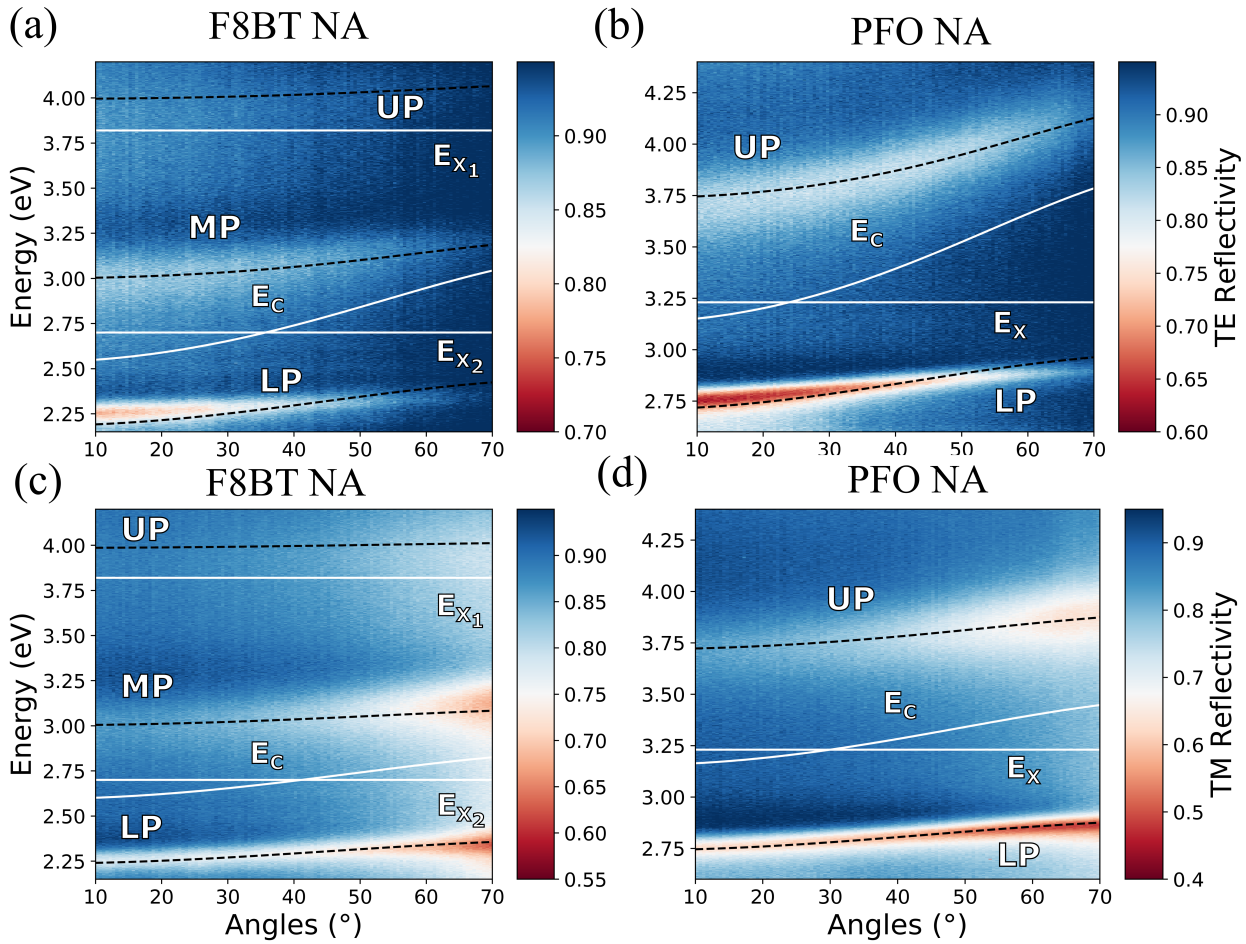


Figure C.4: Experimental, angle-resolved, TE-polarized reflectivity maps for microcavities containing non-aligned F8BT (a,c) and PFO (b,d) for the TE (a,b) and TM (c,d) polarizations. Overlaid are the fitting curves obtained using the analytical model presented in Methods, the fitting values are shown in Table 1. Overlaid solid white lines are the Excitons E_{X_j} and cavity E_C modes, black dashed lines are the polaritons obtained from fitting using the analytical model.

C.5 TMC Results

Figure C.5, C.6, C.7 show the results obtained from TMC using the optical constants obtained in Figure C.4 for F8BT (Figure C.5), PFO (Figure C.6) and F6T2

(Figure C.7) against the corresponding experimental reflectivity measurements for all microcavities presented in this work. The thicknesses indicated are the simulated layer thicknesses for the corresponding polymer or SD1 layer. For the aligned cavities Φ is the azimuthal angle formed between the incident TE-polarization direction and the polymer chain direction.

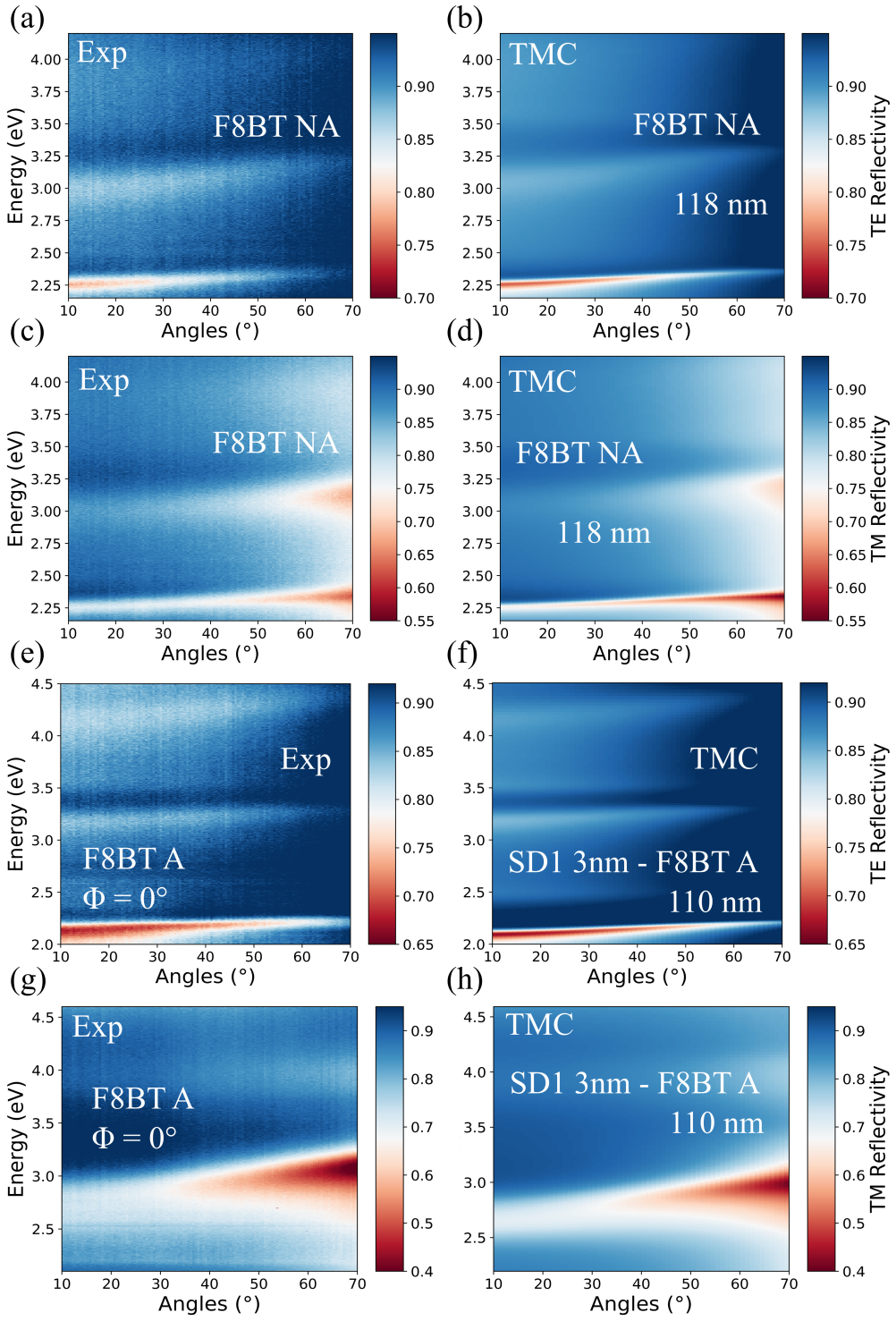


Figure C.5: On the left, Experimental, angle-resolved, TE-(a,e) and TM-(c,g) polarized reflectivity maps for microcavities containing non-aligned (a,c) and aligned (e,g) F8BT. On the right, TMC results showing angle-resolved, TE-(b,f) and TM-(d,h) polarized reflectivity maps for microcavities containing non-aligned (b,c) and aligned (e,g) F8BT. For the aligned cavities, the measurements and calculations were performed for $\Phi = 0°$. The thicknesses displayed in white correspond to the SD1 and polymer layer thicknesses used in the TMC.

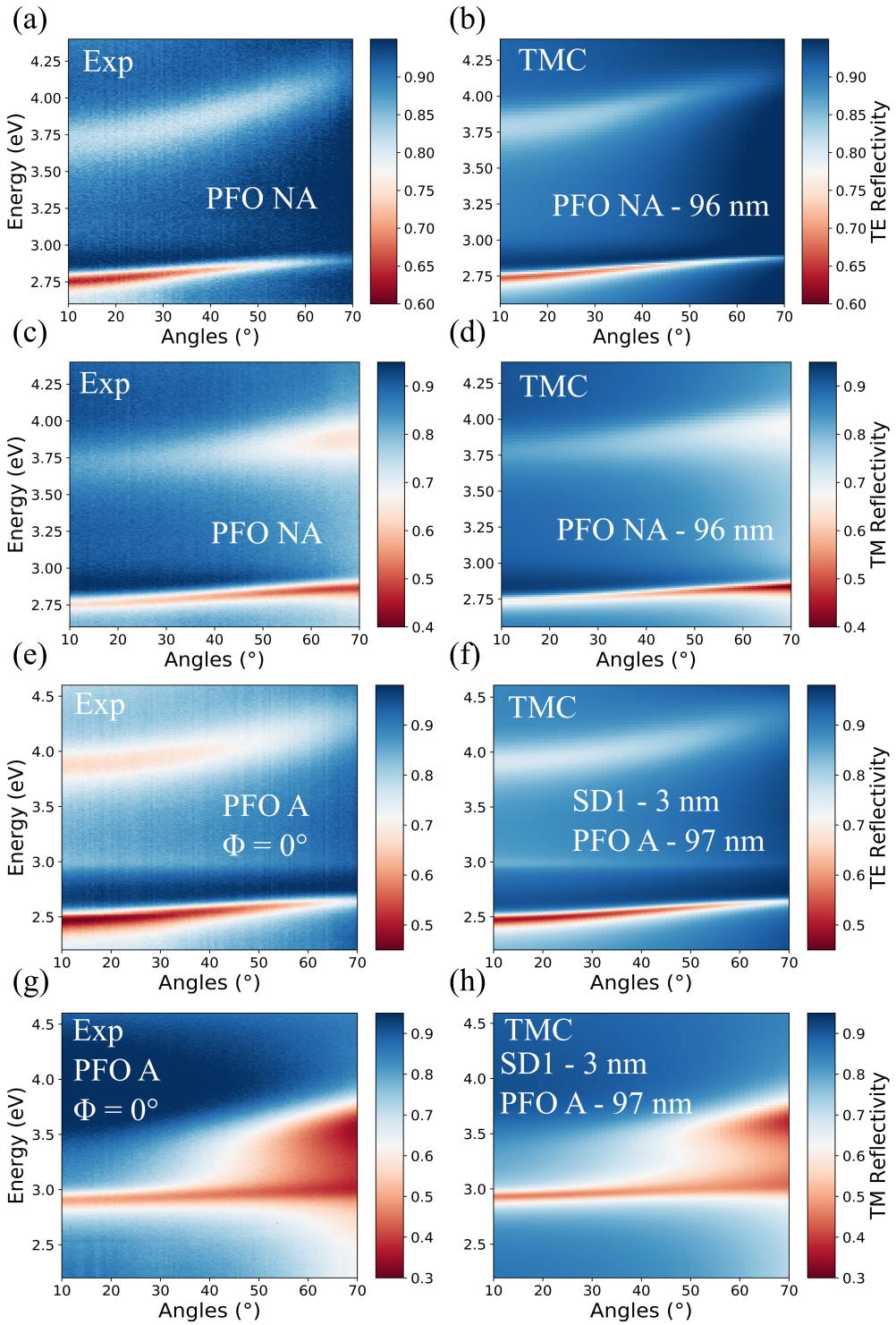


Figure C.6: On the left, Experimental, angle-resolved, TE-(a,e) and TM-(c,g) polarized reflectivity maps for microcavities containing non-aligned (a,c) and aligned (e,g) PFO. On the right, TMC results showing angle-resolved, TE-(b,f) and TM-(d,h) polarized reflectivity maps for microcavities containing non-aligned (b,c) and aligned (e,g) PFO. For the aligned cavities, the measurements and calculations were performed for $\Phi = 0°$. The thicknesses displayed in white correspond to the SD1 and polymer layer thicknesses used in the TMC.

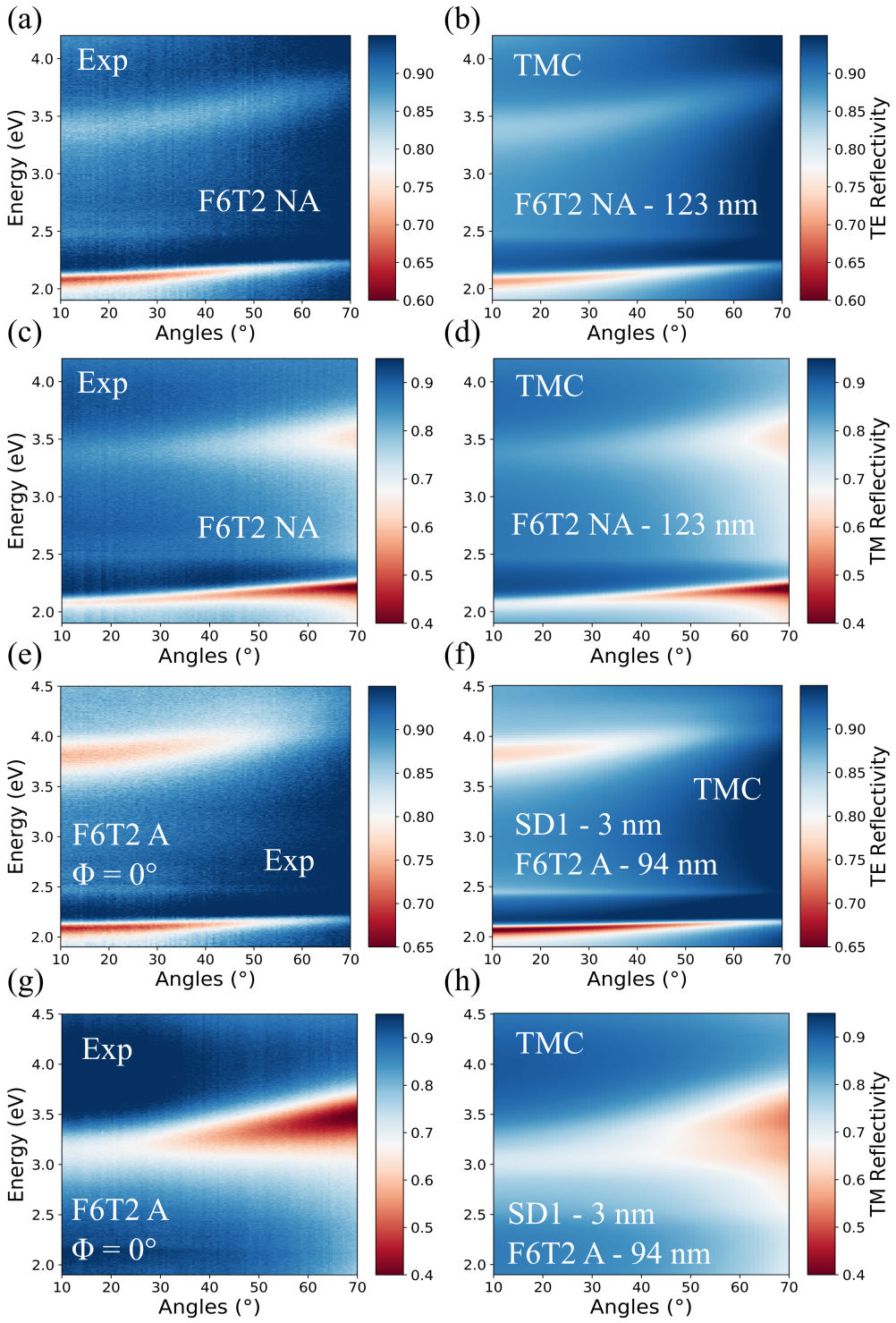


Figure C.7: On the left, Experimental, angle-resolved, TE-(a,e) and TM-(c,g) polarized reflectivity maps for microcavities containing non-aligned (a,c) and aligned (e,g) F6T2. On the right, TMC results showing angle-resolved, TE-(b,f) and TM-(d,h) polarized reflectivity maps for microcavities containing non-aligned (b,c) and aligned (e,g) F6T2. For the aligned cavities, the measurements and calculations were performed for $\Phi = 0°$. The thicknesses displayed in white correspond to the SD1 and polymer layer thicknesses used in the TMC.

Appendix D

Supporting Information: Chapter 6

D.1 TE-polarized Wave Propagation in an In-plane/Out-of-plane Anisotropic Medium

In this section we examine the validity of Snell law and the norm of the wavevector $\mathbf{k}$ for a TE-polarized wave propagating in a dielectric medium whose dielectric permittivity tensor is diagonal but not proportional to the identity tensor. We focus on the case of an in-plane/out-of-plane anisotropy i.e. $\epsilon_x = \epsilon_y = \epsilon_{\text{ord}}$ and $\epsilon_z = \epsilon_{\text{ex}}$ where ϵ_{ord} and ϵ_{ex} are respectively the ordinary (in-plane) and extraordinary (out-of-plane) components. The Helmholtz wave equation for the different media in its matrix form is given by Equation 2.51:

$$\mathbf{M}(\omega)\mathbf{E} = \mathbf{0}, \tag{D.1}$$

A propagating wave solution of Equation D.1 incident on the microcavity structure takes the form:

$$\mathbf{E}_i(\mathbf{r}, t) = \mathbf{E}_{0_i} \mathrm{e}^{-\mathrm{i}[k_x x + k_y y + k_z z - \omega t]}. \tag{D.2}$$

In Equation D.1 $\mathbf{M}$ reads:

$$\mathbf{M}(\omega) = \begin{pmatrix} \epsilon_x \frac{\omega^2}{c^2} - k_y^2 - k_z^2 & k_x k_y & k_x k_z \\ k_y k_x & \epsilon_y \frac{\omega^2}{c^2} - k_z^2 - k_x^2 & k_y kz \\ k_z k_x & k_z k_y & \epsilon_z \frac{\omega^2}{c^2} - k_x^2 - k_y^2 \end{pmatrix}. \tag{D.3}$$

We recall Maxwell-Faraday law for the electric and magnetic fields:

$$\mathbf{k} \times \mathbf{E} = \frac{\omega}{c} \mathbf{B}, \tag{D.4}$$

and focus on the case of TE-polarized light: $\mathbf{E}_{0_i} = E_{0_i x}\mathbf{i} + E_{0_i y}\mathbf{j}$.

D.1.1 In-plane/Out-of-plane Anisotropy

The dielectric permittivity takes the form:

$$\epsilon(\omega) = \epsilon_0 \begin{pmatrix} \epsilon_{\text{ord}} & 0 & 0 \\ 0 & \epsilon_{\text{ord}} & 0 \\ 0 & 0 & \epsilon_{\text{ex}} \end{pmatrix}, \tag{D.5}$$

The rotational symmetry around the z-axis allows us to choose:

$$\mathbf{k} = \begin{pmatrix} k_x \\ 0 \\ k_z \end{pmatrix}, \; k_y = 0, \tag{D.6}$$

and

$$\mathbf{E}_{0_i} = \begin{pmatrix} 0 \\ E_{0_{iy}} \\ 0 \end{pmatrix} \text{ with } E_{0_{iy}} \neq 0 \tag{D.7}$$

which matches the schematic in Figure 6.1 (b) without loss of generality. Equation D.1 then reduces to:

$$\epsilon_{\text{ord}} \frac{\omega^2}{c^2} - k_z^2 - k_x^2 = 0. \tag{D.8}$$

As $\mathbf{k^2} = k_x^2 + k_z^2$, we have:

$$\mathbf{k^2} = \epsilon_{\text{ord}} \frac{\omega^2}{c^2}. \tag{D.9}$$

Using the continuity of the normal component of $\mathbf{B}$: B_z and the tangential components of $\mathbf{E}$: E_x, Ey at the dielectric interfaces and Maxwell-Faraday law (Equation D.4) we retrieve:

$$B_{z_{n-1}} = B_{z_n} \Leftrightarrow k_{x_{n-1}} E_{y_{n-1}} = k_{x_n} E_{y_n} \Leftrightarrow k_{x_{n-1}} = k_{x_n}. \tag{D.10}$$

We propagate this equation from the vacuum in which the incident wave propagates with an angle θ to the uniaxial layer in which it propagates with an angle θ_m and retrieve Snell's law:

$$k_{x_0} = k_{x_n} \Rightarrow |k| \sin\theta = |k_n| \sin\theta_m \Leftrightarrow \sin\theta = n_{\text{ord}} \sin\theta_m. \tag{D.11}$$

D.1.2 Biaxial Anisotropy

We study the case where the permittivity tensor has different diagonal elements for all three coordinates (x, y, z):

$$\epsilon(\omega) = \epsilon_0 \begin{pmatrix} \epsilon_x & 0 & 0 \\ 0 & \epsilon_y & 0 \\ 0 & 0 & \epsilon_z \end{pmatrix}, \tag{D.12}$$

In particular we justify the claim made in Chapter 6, that a TE-polarized plane wave can not propagate as a single wave through the cavity medium except if the incoming $\mathbf{E}_i$ is parallel to one of the principal axes x or y. Equation D.1 yields:

$$\begin{cases} (\epsilon_x \frac{\omega^2}{c^2} - k_y^2 - k_z^2)E_x + k_x k_y E_y = 0 \\ (\epsilon_y \frac{\omega^2}{c^2} - k_z^2 - k_x^2)E_y + k_y k_x E_x = 0 \\ \qquad k_z k_x E_x + k_z k_y E_y = 0 \end{cases} \tag{D.13}$$

We first examine the case where $\mathbf{E}_{0_i}$ is not parallel to the x-axis or y-axis and suppose that the incident wave can propagate through the structure, we have:

$$\begin{cases} E_x \neq 0 \,\text{and}\, E_y \neq 0 \\ k_x \neq 0 \,\text{and}\, k_y \neq 0 \\ \qquad k_z \neq 0 \end{cases} \tag{D.14}$$

As $k^2 = k_x^2 + k_y^2 + k_z^2$, we use the third equation in System D.13 and obtain: $k_x E_x = -k_y E_y$ which we re-introduce in System D.14 to derive the equivalent system:

$$\begin{cases} \epsilon_x \frac{\omega^2}{c^2} - k^2 = 0 \\ \epsilon_y \frac{\omega^2}{c^2} - k^2 = 0 \\ k_z k_x E_x + k_z k_y E_y = 0 \end{cases} \tag{D.15}$$

Substracting the second equation to the first equation in System D.15 leads to a contradiction:

$$\epsilon_x - \epsilon_y = 0. \tag{D.16}$$

Therefore an incident TE-polarized wave can not propagate in the dielectric as a single wave if $\mathbf{E}_i$ is not parallel to either the y-axis or the x-axis.

D.2 Strong Coupling in a Microcavity Containing an In-plane/Out-of-plane Anisotropic Central Layer

In this section, we recall a semi-classical demonstration of strong exciton photon coupling for a microcavity containing an in-plane/out-of-plane anisotropic layer sandwiched between two mirrors, physically possible since any incident TE-polarized wave can propagate through the structure, this demonstration is an extension of the semi-classical model presented in Section 2.4.5. The excitons inside the semiconductor layer are modelled using a Lorentzian model for the electric susceptibility as per Equation 2.6:

$$\chi(\omega) = \frac{4g_0^2}{\omega_{\text{ex}}^2 - \omega^2 - \mathrm{i}\gamma_{\text{ex}}\omega}, \tag{D.17}$$

For simplicity, we first neglect the losses due to jγ_{ex} which can be readily included.[22] The permittivity tensor then reads:

$$\epsilon(\omega) = \epsilon_0 \begin{pmatrix} \epsilon_m(1+\chi(\omega)) & 0 & 0 \\ 0 & \epsilon_m(1+\chi(\omega)) & 0 \\ 0 & 0 & \epsilon_m \end{pmatrix}, \tag{D.18}$$

where ϵ_m is the background permittivity of the dielectric layer. From Equation D.1, $\mathbf{M}$ now takes the form:

$$\mathbf{M}(\omega) = \begin{pmatrix} [1+\chi(\omega)]\epsilon_m \frac{\omega^2}{c^2} - k_y^2 - k_z^2 & k_x k_y & k_x k_z \\ k_y k_x & [1+\chi(\omega)]\epsilon_m \frac{\omega^2}{c^2} - k_z^2 - k_x^2 & k_y kz \\ k_z k_x & k_z k_y & \epsilon_m \frac{\omega^2}{c^2} - k_x^2 - k_y^2 \end{pmatrix}. \tag{D.19}$$

We focus on the case of TE-polarized light: $\mathbf{E}_{0_i} = E_{0_i x}\mathbf{i} + E_{0_i y}\mathbf{j}$ (the TM-polarized light case can be found in the literature[22]). As for the first section, thanks to the rotational symmetry around the z-axis, $\mathbf{k}$ takes the same form as in Equation D.6 and $\mathbf{E}_i$ the one in Equation D.7. Equation D.1 then reduces to:

$$[1+\chi(\omega)]\epsilon_m \frac{\omega^2}{c^2} - k_z^2 - k_x^2 = 0 \tag{D.20}$$

inside the cavity layer. k_z is quantized, using the lowest cavity mode at normal incidence ($\theta = 0°$) we have:

$$k_z^2 = \epsilon_m \frac{\omega_{\text{cav}_0}^2}{c^2}, \tag{D.21}$$

and, using Equation D.9:

$$k^2 = \epsilon_m \frac{\omega_{\text{cav}}^2}{c^2}. \tag{D.22}$$

As Snell law is valid, by defining θ_m as the propagation angle inside the central layer we obtain:

$$k^2 \cos^2 \theta_m = k_z^2 \Leftrightarrow \omega_{cav}^2 = \frac{\omega_{\mathrm{cav}_0}^2}{1 - \frac{\sin^2 \theta}{\epsilon_m}}. \tag{D.23}$$

We re-write Equation D.20 using $k_x^2 = k^2 \sin^2 \theta_m = \frac{\omega^2}{c^2} \sin^2 \theta$ and replace $\chi(\omega)$ by its expression, we obtain:

$$4g_0^2 = (\omega^2 - \omega_{\mathrm{ex}}^2)(\omega^2 - \omega_{\mathrm{cav}}^2). \tag{D.24}$$

When $\omega_{\mathrm{cav}} = \omega_{\mathrm{ex}}$ we solve Equation D.24 to find: $\omega_{\mathrm{LP_{res}}}^{\mathrm{UP_{res}}} = \sqrt{(\omega_{\mathrm{ex}}^2 + g_0)} \pm g_0$ which is identical to the solution found in Section 2.4.5 for the isotropic case.

D.3 Fitting of the Rabi-splitting Energies

All the Rabi-splitting energies $\hbar\Omega_0$ mentioned in Chapter 6 have been derived using the HA model. The fitting results for the structure presented in Figure 6.2 (c) and Figure 6.3 (c) of the are respectively shown in Figure D.1 and Figure D.2. The obtained $\hbar\Omega_0$ values are respectively $\hbar\Omega_{\mathrm{R_{M1}}} = 58$ meV and $\hbar\Omega_{\mathrm{R_{M2}}} = 1.38$ eV.

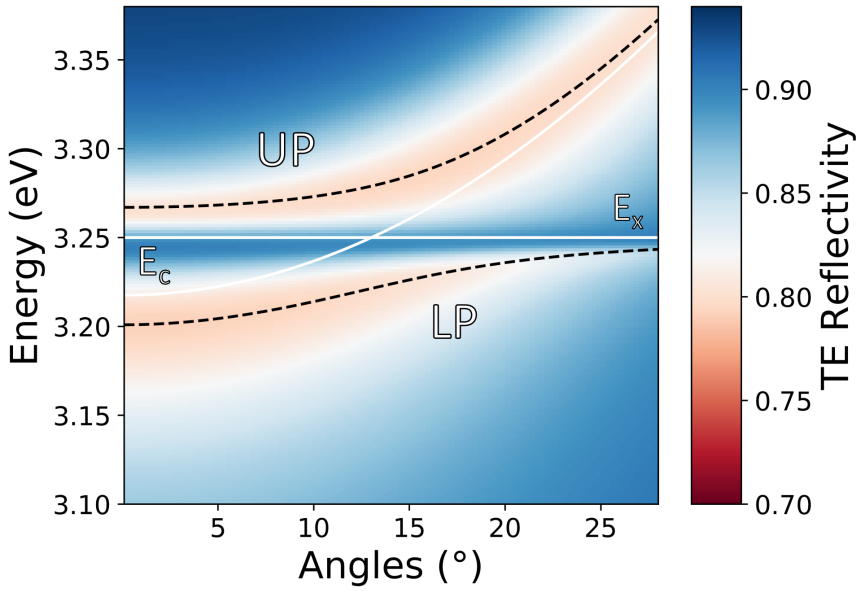


Figure D.1: Simulated, angle-resolved, TE-polarized reflectivity map for a microcavity containing the material M1 as described in the main text. Overlaid are the fitting curves obtained using the HA model. Overlaid solid white lines are the Excitons E_X and cavity E_C modes, black dashed lines are the polaritons (LP/UP) obtained from fitting using the analytical model.

D.4 Experimental Analysis

The fitting results for the structure presented in Figure 6.5 (a) of Chapter 6 are respectively shown in Figure D.3 (using the experimental values) and Figure D.4 (using simulated values and the complex refractive index obtained in Chapter 5). The obtained $\hbar\Omega_0$ values are respectively $\hbar\Omega_{0_{\mathrm{PFO_{exp}}}} = 1.48$ eV and $\hbar\Omega_{0_{\mathrm{PFO_{exp}}}} = 1.50$ eV.

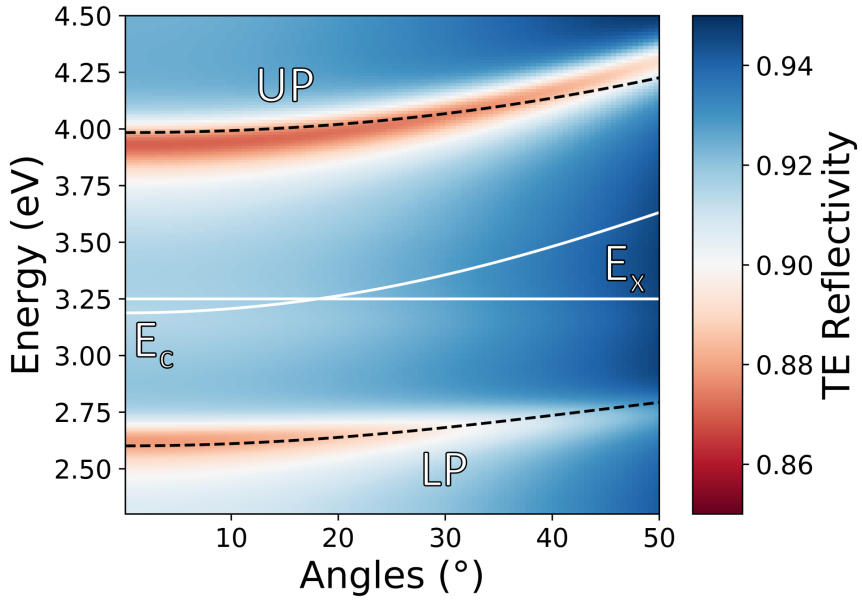


Figure D.2: Simulated, angle-resolved, TE-polarized reflectivity map for a microcavity containing the material M2 as described in the main text. Overlaid are the fitting curves obtained using the HA model. Overlaid solid white lines are the Excitons E_X and cavity E_C modes, black dashed lines are the polaritons (LP/UP) obtained from fitting using the analytical model.

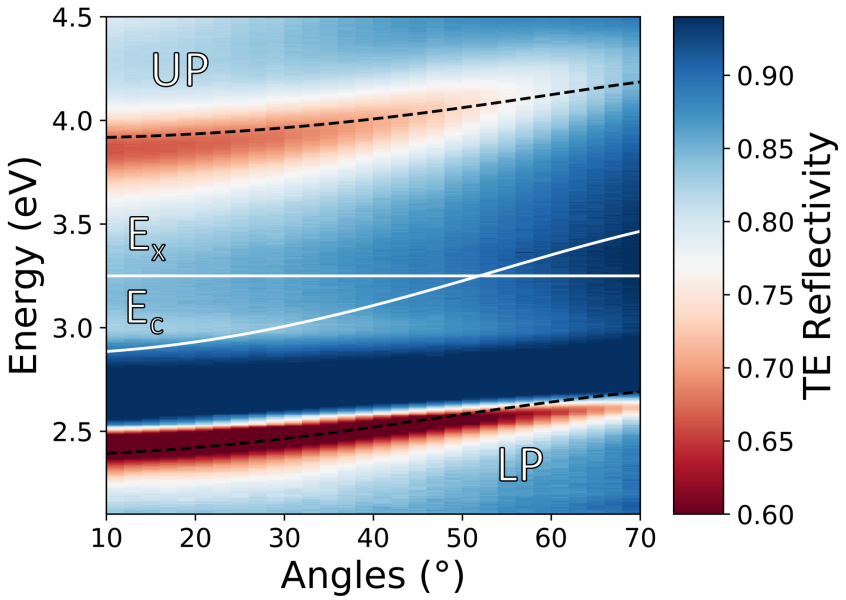


Figure D.3: Experimental, angle-resolved, TE-polarized reflectivity map for a microcavity containing aligned PFO as described in the main text. Overlaid are the fitting curves obtained using the HA model. Overlaid solid white lines are the Excitons E_X and cavity E_C modes, black dashed lines are the polaritons (LP/UP) obtained from fitting using the analytical model.

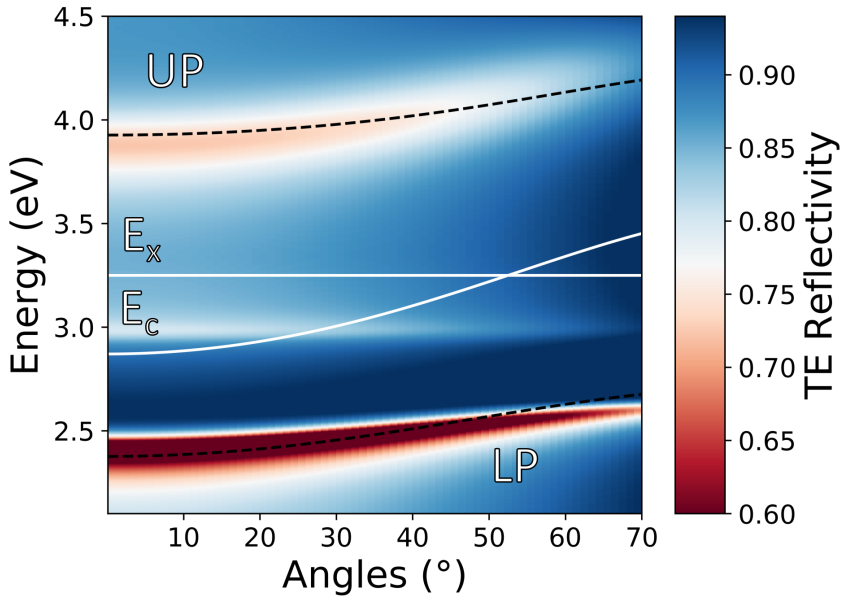


Figure D.4: Simulated, angle-resolved, TE-polarized reflectivity map for a microcavity containing aligned PFO as described in the main text. Overlaid are the fitting curves obtained using the HA model. Overlaid solid white lines are the Excitons E_{X} and cavity E_{C} modes, black dashed lines are the polaritons (LP/UP) obtained from fitting using the analytical model.

Bibliography

[1] C. Weisbuch, M. Nishioka, A. Ishikawa, and Y. Arakawa. Observation of the coupled exciton-photon mode splitting in a semiconductor quantum microcavity. *Physical Review Letters*, 69(23):3314–3317, dec 1992.

[2] Daniele Sanvitto and Stéphane Kéna-Cohen. The road towards polaritonic devices. *Nature Materials*, 15(10):1061–1073, oct 2016.

[3] D. G. Lidzey, D. D. C. Bradley, M. S. Skolnick, T. Virgili, S. Walker, and D. M. Whittaker. Strong exciton–photon coupling in an organic semiconductor microcavity. *Nature*, 395(6697):53–55, sep 1998.

[4] D. G. Lidzey, D. D.C. Bradley, T. Virgili, A. Armitage, M. S. Skolnick, and S. Walker. Room temperature polariton emission from strongly coupled organic semiconductor microcavities. *Physical Review Letters*, 82(16):3316–3319, apr 1999.

[5] David G. Lidzey, Donal D.C. Bradley, Adam Armitage, Steve Walker, and Maurice S. Skolnick. Photon-mediated hybridization of Frenkel excitons in organic semiconductor microcavities. *Science*, 288(5471):1620–1623, jun 2000.

[6] P. Schouwink, H. Von Berlepsch, L. Dähne, and R. F. Mahrt. Observation of strong exciton-photon coupling in an organic microcavity in transmission and photoluminescence. *Journal of Luminescence*, 94-95:821–826, dec 2001.

[7] P. Schouwink, H. Berlepsch, L. Dahne, and R. F. Mahrt. Dependence of Rabi-splitting on the spatial position of the optically active layer in organic microcavities in the strong coupling regime. *Chemical Physics*, 285(1):113–120, dec 2002.

[8] Noriyuki Takada, Toshihide Kamata, and Donal D.C. Bradley. Polariton emission from polysilane-based organic microcavities. *Applied Physics Letters*, 82(12):1812–1814, mar 2003.

[9] R F Oulton, N Takada, J Koe, P N Stavrinou, and D D C Bradley. Strong coupling in organic semiconductor microcavities. *Semiconductor Science and Technology*, 18(10):S419, sep 2003.

[10] R. J. Holmes and S. R. Forrest. Exciton-photon coupling in organic materials with large intersystem crossing rates and strong excited-state molecular relaxation. *Physical Review B - Condensed Matter and Materials Physics*, 71(23):235203, jun 2005.

[11] R N Marks, J J M Halls, D D C Bradley, R H Friend, and A B Holmes. The photovoltaic response in poly(p-phenylene vinylene) thin-film devices. *Journal of Physics: Condensed Matter*, 6(7):1379–1394, feb 1994.

[12] S. Alvarado, P. Seidler, D. G. Lidzey, and D. D. C. Bradley. Direct Determination of the Exciton Binding Energy of Conjugated Polymers Using a Scanning Tunneling Microscope. *Physical Review Letters*, 81(5):1082–1085, aug 1998.

[13] S. Kéna-Cohen, M. Davanço, and S. R. Forrest. Strong exciton-photon coupling in an organic single crystal microcavity. *Physical Review Letters*, 101(11), sep 2008.

[14] S. Kéna-Cohen and S. R. Forrest. Room-temperature polariton lasing in an organic single-crystal microcavity. *Nature Photonics*, 4(6):371–375, jun 2010.

[15] Johannes D. Plumhof, Thilo Stöferle, Lijian Mai, Ullrich Scherf, and Rainer F. Mahrt. Room-temperature Bose–Einstein condensation of cavity exciton–polaritons in a polymer. *Nature Materials*, 13(3):247–252, mar 2014.

[16] K. S. Daskalakis, S. A. Maier, R. Murray, and S. Kéna-Cohen. Nonlinear interactions in an organic polariton condensate. *Nature Materials*, 13(3):271–278, mar 2014.

[17] Anton V. Zasedatelev, Anton V. Baranikov, Darius Urbonas, Fabio Scafirimuto, Ullrich Scherf, Thilo Stöferle, Rainer F. Mahrt, and Pavlos G. Lagoudakis. A room-temperature organic polariton transistor. *Nature Photonics*, 13(6):378–383, jun 2019.

[18] Giovanni Lerario, Antonio Fieramosca, Fábio Barachati, Dario Ballarini, Konstantinos S. Daskalakis, Lorenzo Dominici, Milena De Giorgi, Stefan A. Maier, Giuseppe Gigli, Stéphane Kéna-Cohen, and Daniele Sanvitto. Room-temperature superfluidity in a polariton condensate. *Nature Physics*, 13(9):837–841, sep 2017.

[19] Giovanni Lerario, Dario Ballarini, Antonio Fieramosca, Alessandro Cannavale, Armando Genco, Federica Mangione, Salvatore Gambino, Lorenzo Dominici, Milena De Giorgi, Giuseppe Gigli, and Daniele Sanvitto. High-speed flow of interacting organic polaritons. *Light: Science & Applications*, 6(2):e16212–e16212, feb 2017.

[20] Nataliya Bobrovska, Michał Matuszewski, Konstantinos S. Daskalakis, Stefan A. Maier, and Stéphane Kéna-Cohen. Dynamical Instability of a Nonequilibrium Exciton-Polariton Condensate. *ACS Photonics*, 5(1):111–118, jan 2018.

[21] P. A. Hobson, W. L. Barnes, D. G. Lidzey, G. A. Gehring, D. M. Whittaker, M. S. Skolnick, and S. Walker. Strong exciton-photon coupling in a low-Q all-metal mirror microcavity. *Applied Physics Letters*, 81(19):3519–3521, nov 2002.

[22] Stéphane Kéna-Cohen, Stefan A. Maier, and Donal D. C. Bradley. Ultrastrongly Coupled Exciton-Polaritons in Metal-Clad Organic Semiconductor Microcavities. *Advanced Optical Materials*, 1(11):827–833, nov 2013.

[23] Salvatore Gambino, Marco Mazzeo, Armando Genco, Omar Di Stefano, Salvatore Savasta, Salvatore Patanè, Dario Ballarini, Federica Mangione, Giovanni Lerario, Daniele Sanvitto, and Giuseppe Gigli. Exploring Light–Matter Interaction Phenomena under Ultrastrong Coupling Regime. *ACS Photonics*, 1(10):1042–1048, oct 2014.

[24] M. Mazzeo, A. Genco, S. Gambino, D. Ballarini, F. Mangione, O. Di Stefano, S. Patanè, S. Savasta, D. Sanvitto, and G. Gigli. Ultrastrong light-matter coupling in electrically doped microcavity organic light emitting diodes. *Applied Physics Letters*, 104(23):233303, jun 2014.

[25] V. M. Agranovich. *Opt Spektrosk.*, 2(738), 1957.

[26] V. M. Agranovich. *J. Exptl. Theoret. Phys.*, 37(2):430–441, 1959.

[27] J. J. Hopfield. Theory of the Contribution of Excitons to the Complex Dielectric Constant of Crystals. *Physical Review*, 112(5):1555–1567, dec 1958.

[28] Cristiano Ciuti, Gérald Bastard, and Iacopo Carusotto. Quantum vacuum properties of the intersubband cavity polariton field. *Physical Review B*, 72(11):115303, sep 2005.

[29] Armando Genco, Alessandro Ridolfo, Salvatore Savasta, Salvatore Patanè, Giuseppe Gigli, and Marco Mazzeo. Bright Polariton Coumarin-Based OLEDs Operating in the Ultrastrong Coupling Regime. *Advanced Optical Materials*, 6(17):1800364, sep 2018.

[30] Fábio Barachati, Janos Simon, Yulia A. Getmanenko, Stephen Barlow, Seth R. Marder, and Stéphane Kéna-Cohen. Tunable Third-Harmonic Generation from Polaritons in the Ultrastrong Coupling Regime. *ACS Photonics*, 5(1):119–125, jan 2018.

[31] Martin Held, Arko Graf, Yuriy Zakharko, Pengning Chao, Laura Tropf, Malte C. Gather, and Jana Zaumseil. Ultrastrong Coupling of Electrically Pumped Near-Infrared Exciton-Polaritons in High Mobility Polymers. *Advanced Optical Materials*, 6(3):1700962, feb 2018.

[32] Luigi Garziano, Alessandro Ridolfo, Simone De Liberato, and Salvatore Savasta. Cavity QED in the Ultrastrong Coupling Regime: Photon Bunching from the Emission of Individual Dressed Qubits. *ACS Photonics*, 4(9):2345–2351, sep 2017.

[33] Anton Frisk Kockum, Adam Miranowicz, Simone De Liberato, Salvatore Savasta, and Franco Nori. Ultrastrong coupling between light and matter. *Nature Reviews Physics*, 1(1):19–40, jan 2019.

[34] P. Forn-Díaz, L. Lamata, E. Rico, J. Kono, and E. Solano. Ultrastrong coupling regimes of light-matter interaction. *Reviews of Modern Physics*, 91(2):025005, jun 2019.

[35] Benjamin Askenazi, Angela Vasanelli, Yanko Todorov, Emilie Sakat, Jean-Jacques Greffet, Grégoire Beaudoin, Isabelle Sagnes, and Carlo Sirtori. Midinfrared Ultrastrong Light–Matter Coupling for THz Thermal Emission. *ACS Photonics*, 4(10):2550–2555, oct 2017.

[36] F. Yoshihara, T. Fuse, Z. Ao, S. Ashhab, K. Kakuyanagi, S. Saito, T. Aoki, K. Koshino, and K. Semba. Inversion of Qubit Energy Levels in Qubit-Oscillator Circuits in the Deep-Strong-Coupling Regime. *Physical Review Letters*, 120(18):183601, may 2018.

[37] Andreas Bayer, Marcel Pozimski, Simon Schambeck, Dieter Schuh, Rupert Huber, Dominique Bougeard, and Christoph Lange. Terahertz Light–Matter Interaction beyond Unity Coupling Strength. *Nano Letters*, 17(10):6340–6344, oct 2017.

[38] Felix Benz, Mikolaj K Schmidt, Alexander Dreismann, Rohit Chikkaraddy, Yao Zhang, Angela Demetriadou, Cloudy Carnegie, Hamid Ohadi, Bart de Nijs, Ruben Esteban, Javier Aizpurua, and Jeremy J Baumberg. Single-molecule optomechanics in "picocavities". *Science (New York, N.Y.)*, 354(6313):726–729, nov 2016.

[39] Lucas C. Flatten, David M. Coles, Zhengyu He, David G. Lidzey, Robert A. Taylor, Jamie H. Warner, and Jason M. Smith. Electrically tunable organic-inorganic hybrid polaritons with monolayer WS2. *Nature Communications*, 8(1):1–5, jan 2017.

[40] Gianluca Accorsi, Sonia Carallo, Marco Mazzeo, Armando Genco, Salvatore Gambino, and Giuseppe Gigli. A colour tunable microcavity by weak-to-strong coupling regime transition through a light-switchable material. *Chemical Communications*, 50(9):1122–1124, feb 2014.

[41] Lucas C. Flatten, Sotirios Christodoulou, Robin K. Patel, Alexander Buccheri, David M. Coles, Benjamin P.L. Reid, Robert A. Taylor, Iwan Moreels, and Jason M. Smith. Strong Exciton-Photon Coupling with Colloidal Nanoplatelets in an Open Microcavity. *Nano Letters*, 16(11):7137–7141, nov 2016.

[42] David M. Coles, Qiang Chen, Lucas C. Flatten, Jason M. Smith, Klaus Müllen, Akimitsu Narita, and David G. Lidzey. Strong Exciton-Photon Coupling in a Nanographene Filled Microcavity. *Nano Letters*, 17(9):5521–5525, sep 2017.

[43] D. N. Krizhanovskii, R. Butté, L. G. Connolly, A. I. Tartakovskii, D. G. Lidzey, M. S. Skolnick, and S. Walker. Photoluminescence emission and Raman scattering

polarization in birefringent organic microcavities in the strong coupling regime. *Journal of Applied Physics*, 93(9):5003–5007, may 2003.

[44] Weilu Gao, Xinwei Li, Motoaki Bamba, and Junichiro Kono. Continuous transition between weak and ultrastrong coupling through exceptional points in carbon nanotube microcavity exciton–polaritons. *Nature Photonics*, 12(6):362–367, jun 2018.

[45] Lena Yadgarov, Bojana Višić, Tsafrir Abir, Ron Tenne, Alexander Yu. Polyakov, Roi Levi, Tatyana V. Dolgova, Varvara V. Zubyuk, Andrey A. Fedyanin, Eugene A. Goodilin, Tal Ellenbogen, Reshef Tenne, and Dan Oron. Strong light–matter interaction in tungsten disulfide nanotubes. *Physical Chemistry Chemical Physics*, 20(32):20812–20820, aug 2018.

[46] Manuel Hertzog, Per Rudquist, James A. Hutchison, Jino George, Thomas W. Ebbesen, and Karl Börjesson. Voltage-Controlled Switching of Strong Light-Matter Interactions using Liquid Crystals. *Chemistry - A European Journal*, 23(72):18166–18170, dec 2017.

[47] Peter W. Atkins and Ronald S. Friedman. *Molecular Quantum Mechanics - Fifth Edition*. Oxford University Press, 2010.

[48] M. Born and R. Oppenheimer. Zur Quantentheorie der Molekeln. *Annalen der Physik*, 389(20):457–484, jan 1927.

[49] D. R. Hartree. The Wave Mechanics of an Atom with a Non-Coulomb Central Field Part II Some Results and Discussion. *Mathematical Proceedings of the Cambridge Philosophical Society*, 24(1):111–132, 1928.

[50] W. Pauli. Über den Zusammenhang des Abschlusses der Elektronengruppen im Atom mit der Komplexstruktur der Spektren. *Zeitschrift für Physik*, 31(1):765–783, feb 1925.

[51] V. Fock. Näherungsmethode zur Lösung des quantenmechanischen Mehrkörperproblems. *Zeitschrift für Physik*, 61(1-2):126–148, jan 1930.

[52] J. C. Slater. Note on hartree's method [5]. *Physical Review*, 35(2):210–211, jan 1930.

[53] Thomas Engel and Philip Reid. *Physical Chemistry - Third Edition.* Pearson, 2014.

[54] J. Brandrup, Edmund H. Immergut, and E. A. Grulke. *Polymer Handbook - Fourth Edition.* Wiley, 2003.

[55] C. K. Chiang, C. R. Fincher, Y. W. Park, A. J. Heeger, H. Shirakawa, E. J. Louis, S. C. Gau, and Alan G. MacDiarmid. Electrical conductivity in doped polyacetylene. *Physical Review Letters*, 39(17):1098–1101, oct 1977.

[56] Pope Martin and Swenberg Charles E. *Electronic Processes in Organic Crystals and Polymers - Second Edition.* Oxford University Press, 1999.

[57] John R. Reynolds, Barry C. Thompson, and Terje A. Skotheim. Conjugated Polymers: Properties, Processing, and Applications - Fourth Edition. 2019.

[58] M. A. Baldo, D. F. O'Brien, Y. You, A. Shoustikov, S. Sibley, M. E. Thompson, and S. R. Forrest. Highly efficient phosphorescent emission from organic electroluminescent devices. *Nature*, 395(6698):151–154, sep 1998.

[59] Alexandre S. Davydov. *Quantum Mechanics: International Series in Natural Philosophy.* Pergamon Press, 1965.

[60] J. Franck. Elementary processes of photochemical reactions. *Transactions of the Faraday Society*, 21(FEBRUARY):536–542, jan 1926.

[61] Michael Kasha. Characterization of electronic transitions in complex molecules. *Discussions of the Faraday Society*, 9(0):14–19, jan 1950.

[62] D. S. Dovzhenko, S. V. Ryabchuk, Yu P. Rakovich, and I. R. Nabiev. Light-matter interaction in the strong coupling regime: Configurations, conditions, and applications. 10(8):3589–3605, feb 2018.

[63] Alexey V. Kavokin, Jeremy J. Baumberg, Guillaume Malpuech, and Fabrice P. Laussy. *Microcavities - Second Edition*. Oxford University Press, 2017.

[64] V. M. Agranovich, M. Litinskaia, and D. G. Lidzey. Cavity polaritons in microcavities containing disordered organic semiconductors. *Physical Review B - Condensed Matter and Materials Physics*, 67(8):085311, feb 2003.

[65] Yifu Zhu, Daniel J. Gauthier, S. E. Morin, Qilin Wu, H. J. Carmichael, and T. W. Mossberg. Vacuum Rabi splitting as a feature of linear-dispersion theory: Analysis and experimental observations. *Physical Review Letters*, 64(21):2499–2502, may 1990.

[66] Stéphane Kéna-Cohen. *Strong exciton-photon coupling in organic semiconductor microcavities - Doctoral Thesis*. 2010.

[67] G. Khitrova, H. M. Gibbs, M. Kira, S. W. Koch, and A. Scherer. Vacuum Rabi splitting in semiconductors. 2(2):81–90, feb 2006.

[68] Jino George, Shaojun Wang, Thibault Chervy, Antoine Canaguier-Durand, Gael Schaeffer, Jean-Marie Lehn, James A. Hutchison, Cyriaque Genet, and Thomas W. Ebbesen. Ultra-strong coupling of molecular materials: spectroscopy and dynamics. *Faraday Discussions*, 178(0):281–294, may 2015.

[69] Serge Haroche and Daniel Kleppner. Cavity Quantum Electrodynamics. *Physics Today*, 42(1):24–30, jan 1989.

[70] S. K. Rajendran, W. Wang, D. Brida, A. De Sio, E. Sommer, R. Vogelgesang, D. Coles, D. G. Lidzey, G. Cerullo, C. Lienau, and T. Virgili. Direct evidence

of Rabi oscillations and antiresonance in a strongly coupled organic microcavity. *Physical Review B - Condensed Matter and Materials Physics*, 91(20):201305, may 2015.

[71] Hailin Wang, Young-tak Chough, S. E. Palmer, and Howard Carmichael. Normal mode oscillation in the presence of inhomogeneous broadening. *Optics Express*, 1(12):370, dec 1997.

[72] S. M. Neamtan. The Cerenkov effect and the dielectric constant. *Physical Review*, 92(6):1362–1367, dec 1953.

[73] S. M. Neamtan. A quantum-mechanical definition of refractive index. *Physical Review*, 94(2):327, apr 1954.

[74] Shaocong Hou, Yue Qu, Xiao Liu, and Stephen R. Forrest. Ultrastrong coupling of vibrationally dressed organic Frenkel excitons with Bloch surface waves in a one-sided all-dielectric structure. *Physical Review B*, 100(4):045410, jul 2019.

[75] Simone De Liberato. Virtual photons in the ground state of a dissipative system. *Nature Communications*, 8(1):1–6, dec 2017.

[76] R. Houdré, R. P. Stanley, and M. Ilegems. Vacuum-field Rabi splitting in the presence of inhomogeneous broadening: Resolution of a homogeneous linewidth in an inhomogeneously broadened system. *Physical Review A - Atomic, Molecular, and Optical Physics*, 53(4):2711–2715, 1996.

[77] V. Savona and C. Weisbuch. Theory of time-resolved light emission from polaritons in a semiconductor microcavity under resonant excitation. *Physical Review B - Condensed Matter and Materials Physics*, 54(15):10835–10840, oct 1996.

[78] Bin Liu, Michael Crescimanno, Robert J. Twieg, and Kenneth D. Singer. Dispersion of Third-Harmonic Generation in Organic Cavity Polaritons. *Advanced Optical Materials*, 7(18):1801682, sep 2019.

[79] Michetti P., Mazza L., and La Rocca G. Organic nanophotonics. Nano-optics and nanophotonics (editor Zhao Y). Berlin: Springer,. *Advanced Optical Materials*, pages 39–68, 2015.

[80] T. Virgili, D. Coles, A. M. Adawi, C. Clark, P. Michetti, S. K. Rajendran, D. Brida, D. Polli, G. Cerullo, and D. G. Lidzey. Ultrafast polariton relaxation dynamics in an organic semiconductor microcavity. *Physical Review B - Condensed Matter and Materials Physics*, 83(24):245309, jun 2011.

[81] David M. Coles, Paolo Michetti, Caspar Clark, Ali M. Adawi, and David G. Lidzey. Temperature dependence of the upper-branch polariton population in an organic semiconductor microcavity. *Physical Review B - Condensed Matter and Materials Physics*, 84(20):205214, nov 2011.

[82] J. Chovan, I. E. Perakis, S. Ceccarelli, and D. G. Lidzey. Controlling the interactions between polaritons and molecular vibrations in strongly coupled organic semiconductor microcavities. *Physical Review B - Condensed Matter and Materials Physics*, 78(4):045320, jul 2008.

[83] Richard T. Grant, Paolo Michetti, Andrew J. Musser, Pascal Gregoire, Tersilla Virgili, Eleonora Vella, Marco Cavazzini, Kyriacos Georgiou, Francesco Galeotti, Caspar Clark, Jenny Clark, Carlos Silva, and David G. Lidzey. Polaritons: Efficient Radiative Pumping of Polaritons in a Strongly Coupled Microcavity by a Fluorescent Molecular Dye. *Advanced Optical Materials*, 4(10):1614–1614, oct 2016.

[84] David M. Coles, Paolo Michetti, Caspar Clark, Wing Chung Tsoi, Ali M. Adawi, Ji Seon Kim, and David G. Lidzey. Vibrationally assisted polariton-relaxation processes in strongly coupled organic-semiconductor microcavities. *Advanced Functional Materials*, 21(19):3691–3696, oct 2011.

[85] P. Michetti and G. C. La Rocca. Polariton states in disordered organic microcavities. *Physical Review B - Condensed Matter and Materials Physics*, 71(11):115320, mar 2005.

[86] Dario Ballarini, Milena De Giorgi, Salvatore Gambino, Giovanni Lerario, Marco Mazzeo, Armando Genco, Gianluca Accorsi, Carlo Giansante, Silvia Colella, Stefania D'Agostino, Paolo Cazzato, Daniele Sanvitto, and Giuseppe Gigli. Polariton-Induced Enhanced Emission from an Organic Dye under the Strong Coupling Regime. *Advanced Optical Materials*, 2(11):1076–1081, nov 2014.

[87] L. Mazza, S. Kéna-Cohen, P. Michetti, and G. C. La Rocca. Microscopic theory of polariton lasing via vibronically assisted scattering. *Physical Review B - Condensed Matter and Materials Physics*, 88(7):075321, aug 2013.

[88] Felipe Herrera and Frank C. Spano. Theory of Nanoscale Organic Cavities: The Essential Role of Vibration-Photon Dressed States. *ACS Photonics*, 5(1):65–79, jan 2018.

[89] A. Armitage, D. G. Lidzey, D. D.C. Bradley, T. Virgili, M. S. Skolnick, and S. Walker. Modelling of asymmetric excitons in organic microcavities. *Synthetic Metals*, 111:377–379, jun 2000.

[90] D. G. Lidzey, A. M. Fox, M. D. Rahn, M. S. Skolnick, V. M. Agranovich, and S. Walker. Experimental study of light emission from strongly coupled organic semiconductor microcavities following nonresonant laser excitation. *Physical Re-*

view B - Condensed Matter and Materials Physics, 65(19):1953121–19531210, may 2002.

[91] Felipe Herrera and Frank C. Spano. Absorption and photoluminescence in organic cavity QED. *Physical Review A*, 95(5):053867, may 2017.

[92] Felipe Herrera and Frank C. Spano. Dark Vibronic Polaritons and the Spectroscopy of Organic Microcavities. *Physical Review Letters*, 118(22):223601, may 2017.

[93] M. Ahsan Zeb, Peter G. Kirton, and Jonathan Keeling. Exact States and Spectra of Vibrationally Dressed Polaritons. *ACS Photonics*, 5(1):249–257, jan 2018.

[94] A. W. Grice, D. D.C. Bradley, M. T. Bernius, M. Inbasekaran, W. W. Wu, and E. P. Woo. High brightness and efficiency blue light-emitting polymer diodes. *Applied Physics Letters*, 73(5):629–631, aug 1998.

[95] Lay Lay Chua, Jana Zaumseil, Jui Fen Chang, Eric C.W. Ou, Peter K.H. Ho, Henning Sirringhaus, and Richard H. Friend. General observation of n-type field-effect behaviour in organic semiconductors. *Nature*, 434(7030):194–199, mar 2005.

[96] Ruidong Xia, George Heliotis, Yanbing Hou, and Donal D.C. Bradley. Fluorene-based conjugated polymer optical gain media. *Organic Electronics*, 4(2-3):165–177, sep 2003.

[97] G. Heliotis, R. Xia, D. D.C. Bradley, G. A. Turnbull, I. D.W. Samuel, P. Andrew, and W. L. Barnes. Blue, surface-emitting, distributed feedback polyfluorene lasers. *Applied Physics Letters*, 83(11):2118–2120, sep 2003.

[98] Boon Kar Yap, Ruidong Xia, Mariano Campoy-Quiles, Paul N. Stavrinou, and Donal D.C. Bradley. Simultaneous optimization of charge-carrier mobility and optical gain in semiconducting polymer films. *Nature Materials*, 7(5):376–380, apr 2008.

[99] Mengjie Wei, Sai Kiran Rajendran, Hamid Ohadi, Laura Tropf, Malte C. Gather, Graham A. Turnbull, and Ifor D. W. Samuel. Low-threshold polariton lasing in a highly disordered conjugated polymer. *Optica*, 6(9):1124, sep 2019.

[100] Aleksandr Perevedentsev. *Chain conformation and the photophysics of polyfluorenes - Doctoral Thesis*. 2015.

[101] M. Grell, D. D.C. Bradley, G. Ungar, J. Hill, and K. S. Whitehead. Interplay of physical structure and photophysics for a liquid crystalline polyfluorene. *Macromolecules*, 32(18):5810–5817, 1999.

[102] W. Chunwaschirasiri, B. Tanto, D. L. Huber, and M. J. Winokur. Chain conformations and photoluminescence of poly(di-n-octylfluorene). *Physical Review Letters*, 94(10):107402, mar 2005.

[103] S. H. Chen, A. G. Su, C. H. Su, and S. A. Chen. Crystalline forms and emission behavior of poly(9,9-di-n-octyl-2,7-fluorene). *Macromolecules*, 38(2):379–385, jan 2005.

[104] M. J. Winokur, J. Slinker, and D. L. Huber. Structure, photophysics, and the order-disorder transition to the β phase in poly(9,9-(di-n, n-octyl)fluorene). *Physical Review B - Condensed Matter and Materials Physics*, 67(18):184106, may 2003.

[105] Donal D. C. Bradley, Martin Grell, Xiao Long, Helen Mellor, Alan W. Grice, Michael Inbasekaran, and Edmund P. Woo. Influence of aggregation on the optical properties of a polyfluorene. In Z. Valy Vardeny and Lewis J. Rothberg, editors, *Optical Probes of Conjugated Polymers*, volume 3145, page 254. SPIE, dec 1997.

[106] A. J. Cadby, P. A. Lane, H. Mellor, S. J. Martin, M. Grell, C. Giebeler, D. D.C. Bradley, M. Wohlgenannt, C. An, and Z. V. Vardeny. Film morphology and pho-

tophysics of polyfluorene. *Physical Review B - Condensed Matter and Materials Physics*, 62(23):15604–15609, dec 2000.

[107] M. Grell, D.D.C. Bradley, X. Long, T. Chamberlain, M. Inbasekaran, E.P. Woo, and M. Soliman. Chain geometry, solution aggregation and enhanced dichroism in the liquidcrystalline conjugated polymer poly(9,9-dioctylfluorene). *Acta Polymerica*, 49(8):439–444, aug 1998.

[108] P. Stavrinou, G. Ryu, M Campoy-Quiles, and D. D. C. Bradley. The change in refractive index of poly(9,9-dioctylfluorene) due to the adoption of the β-phase chain conformation. *Journal of Physics: Condensed Matter*, 19, 2007.

[109] Gihan Ryu, Paul N. Stavrinou, and Donal D.C. Bradley. Spatial patterning of the β-phase in poly(9,9-dioctylfluorene): A metamaterials-inspired molecular conformation approach to the fabrication of polymer semiconductor optical structures. *Advanced Functional Materials*, 19(20):3237–3242, oct 2009.

[110] Amena L.T. Khan, Paiboon Sreearunothai, Laura M. Herz, Michael J. Banach, and Anna Köhler. Morphology-dependent energy transfer within polyfluorene thin films. *Physical Review B - Condensed Matter and Materials Physics*, 69(8):085201, feb 2004.

[111] Aleksandr Perevedentsev, Nathan Chander, Ji-Seon Kim, and Donal D. C. Bradley. Spectroscopic properties of poly(9,9-dioctylfluorene) thin films possessing varied fractions of β-phase chain segments: enhanced photoluminescence efficiency via conformation structuring. *Journal of Polymer Science Part B: Polymer Physics*, 54(19):1995–2006, oct 2016.

[112] Aleksandr Perevedentsev, Yannick Sonnefraud, Colin R. Belton, Sanjiv Sharma, Anthony E. G. Cass, Stefan A. Maier, Ji-Seon Kim, Paul N. Stavrinou, and Donal

D. C. Bradley. Dip-pen patterning of poly(9,9-dioctylfluorene) chain-conformation-based nano-photonic elements. *Nature Communications*, 6(1):5977, may 2015.

[113] Jeffrey Peet, Erin Brocker, Yunhua Xu, and Guillermo C. Bazan. Controlled β-phase formation in poly(9,9-di-n-octylfluorene) by processing with alkyl additives. *Advanced Materials*, 20(10):1882–1885, may 2008.

[114] Qi Zhang, Lang Chi, Gang Hai, Yueting Fang, Xiangchun Li, Ruidong Xia, Wei Huang, and Erdan Gu. An Easy Approach to Control β-Phase Formation in PFO Films for Optimized Emission Properties. *Molecules*, 22(2):315, feb 2017.

[115] Tersilla Virgili, Daniele Marinotto, Guglielmo Lanzani, and Donal D.C. Bradley. Ultrafast resonant optical switching in isolated polyfluorenes chains. *Applied Physics Letters*, 86(9):1–3, feb 2005.

[116] G Ryu, R Xia, and D D C Bradley. Optical gain characteristics of β-phase poly(9,9-dioctylfluorene). *Journal of Physics: Condensed Matter*, 19(5):056205, feb 2007.

[117] C. Rothe, F. Galbrecht, U. Scherf, and A. Monkman. The β-Phase of Poly(9,9-dioctylfluorene) as a Potential System for Electrically Pumped Organic Lasing. *Advanced Materials*, 18(16):2137–2140, aug 2006.

[118] M. Ariu, M. Sims, M. D. Rahn, J. Hill, A. M. Fox, D. G. Lidzey, M. Oda, J. Cabanillas-Gonzalez, and D. D.C. Bradley. Exciton migration in β-phase poly(9,9-dioctylfluorene). *Physical Review B - Condensed Matter and Materials Physics*, 67(19):195333, may 2003.

[119] Kurt J. Lesker - https://www.lesker.com/.

[120] Kevin M. McPeak, Sriharsha V. Jayanti, Stephan J.P. Kress, Stefan Meyer, Stelio Iotti, Aurelio Rossinelli, and David J. Norris. Plasmonic films can easily be better: Rules and recipes. *ACS Photonics*, 2(3):326–333, mar 2015.

[121] Bruker Dektak Profilometer - https://www.bruker.com/products/surface-and-dimensional-analysis/stylus-profilometers.html.

[122] Perkin Elmer - https://www.perkinelmer.com/uk/.

[123] J.A. Woolam - https://www.jawoollam.com/.

[124] Ocean Insight - https://www.oceaninsight.com.

[125] Thorlabs - https://www.thorlabs.com.

[126] Princeton Instruments - https://www.princetoninstruments.com.

[127] Horiba Instruments - https://www.horiba.com.

[128] NKT Photonics - https://www.nktphotonics.com/.

[129] GitHub - gevero/py_matrix: A python implementation of the transfer matrix method for multilayer structures with arbitrary dielectric tensors - https://github.com/gevero/py_matrix.

[130] M. Mansuripur. Analysis of multilayer thin-film structures containing magneto-optic and anisotropic media at oblique incidence using 2x2 matrices. *Journal of Applied Physics*, 67(10):6466–6475, may 1990.

[131] Python - https://www.python.org/.

[132] Matlab - https://www.mathworks.com/products/matlab.html.

[133] Long Huang, Xinan Huang, Guannan Sun, Cheng Gu, Dan Lu, and Yuguang Ma. Study of β phase and chains aggregation degrees in poly(9,9-dioctylfluorene) (PFO) solution. *Journal of Physical Chemistry C*, 116(14):7993–7999, apr 2012.

[134] M Ariu, D G Lidzey, M Sims, A J Cadby, P A Lane, and D D C Bradley. The effect of morphology on the temperature-dependent photoluminescence quantum

efficiency of the conjugated polymer poly(9, 9-dioctylfluorene). *Journal of Physics: Condensed Matter*, 14(42):9975–9986, oct 2002.

[135] Mariano Campoy-Quiles, M. Isabel Alonso, Donal D. C. Bradley, and Lee J. Richter. Advanced Ellipsometric Characterization of Conjugated Polymer Films. *Advanced Functional Materials*, 24(15):2116–2134, apr 2014.

[136] M. Campoy-Quiles, P. G. Etchegoin, and D. D. C. Bradley. On the optical anisotropy of conjugated polymer thin films. *Physical Review B*, 72(4):045209, jul 2005.

[137] Laura Tropf, Christof P. Dietrich, Stefanie Herbst, Alexander L. Kanibolotsky, Peter J. Skabara, Frank Würthner, Ifor D. W. Samuel, Malte C. Gather, and Sven Höfling. Influence of optical material properties on strong coupling in organic semiconductor based microcavities. *Applied Physics Letters*, 110(15):153302, apr 2017.

[138] Giovanna Panzarini, Lucio Claudio Andreani, A. Armitage, D. Baxter, M. S. Skolnick, V. N. Astratov, J. S. Roberts, A. Kavokin, M. Vladimirova, and M. A. Kaliteevski. Exciton-light coupling in single and coupled semiconductor microcavities: Polariton dispersion and polarization splitting. *Physical Review B - Condensed Matter and Materials Physics*, 59(7):5082–5089, feb 1999.

[139] T. A. Fisher, D. G. Lidzey, M. A. Pate, M. S. Weaver, D. M. Whittaker, M. S. Skolnick, and D. D.C. Bradley. Electroluminescence from a conjugated polymer microcavity structure. *Applied Physics Letters*, 67(10):1355, sep 1995.

[140] David G. Lidzey, Donal D.C. Bradley, Simon J. Martin, and Malcom A. Pate. Pixelated multicolor microcavity displays. *IEEE Journal on Selected Topics in Quantum Electronics*, 4(1):113–118, jan 1998.

[141] E. N. Economou. Surface Plasmons in Thin Films. *Physical Review*, 182(2):539–554, jun 1969.

[142] M Litinskaya and V M Agranovich. Polariton trap in microcavities with metallic mirrors. *Journal of Physics: Condensed Matter*, 24(1):015302, jan 2012.

[143] T. Schwartz, J. A. Hutchison, C. Genet, and T. W. Ebbesen. Reversible Switching of Ultrastrong Light-Molecule Coupling. *Physical Review Letters*, 106(19):196405, may 2011.

[144] Makoto Suzuki, Kouichi Nishiyama, Nobutaka Kani, Xinping Yu, Keiji Uzumi, Masahiro Funahashi, Fusao Shimokawa, Shunsuke Nakanishi, and Noriaki Tsurumachi. Observation of ultrastrong-coupling regime in the Fabry–Pérot microcavities made of metal mirrors containing Lemke dye. *Applied Physics Letters*, 114(19):191108, may 2019.

[145] Bin Liu, Prabin Rai, John Grezmak, Robert J. Twieg, and Kenneth D. Singer. Coupling of exciton-polaritons in low - Q coupled microcavities beyond the rotating wave approximation. *Physical Review B*, 92(15):155301, oct 2015.

[146] Mariano Campoy-Quiles, Toby Ferenczi, Tiziano Agostinelli, Pablo G. Etchegoin, Youngkyoo Kim, Thomas D. Anthopoulos, Paul N. Stavrinou, Donal D. C. Bradley, and Jenny Nelson. Morphology evolution via self-organization and lateral and vertical diffusion in polymer:fullerene solar cell blends. *Nature Materials*, 7(2):158–164, feb 2008.

[147] T. Virgili, D.G. Lidzey, M. Grell, S. Walker, A. Asimakis, and D.D.C. Bradley. Completely polarized photoluminescence emission from a microcavity containing an aligned conjugated polymer. *Chemical Physics Letters*, 341(3-4):219–224, jun 2001.

[148] M. Campoy-Quiles, P. G. Etchegoin, and D. D. C. Bradley. On the optical anisotropy of conjugated polymer thin films. *Physical Review B*, 72(4):045209, jul 2005.

[149] M. Litinskaya, P. Reineker, and V. M. Agranovich. Exciton-polaritons in a crystalline anisotropic organic microcavity. *physica status solidi (a)*, 201(4):646–654, mar 2004.

[150] D. B. Balagurov and G. C. La Rocca. Organic microcavities with anisotropic optically active materials. *physica status solidi (c)*, 1(3):518–521, feb 2004.

[151] Martin Grell, Donal D. C. Bradley, Mike Inbasekaran, and E. P. Woo. A glass-forming conjugated main-chain liquid crystal polymer for polarized electroluminescence applications. *Advanced Materials*, 9(10):798–802, jan 1997.

[152] M. Grell, M. Redecker, K. S. Whitehead, D. D. C. Bradley, M. Inbasekaran, and E. P. Woo. Monodomain alignment of thermotropic fluorene copolymers. *Liquid Crystals*, 26(9):1403–1407, sep 1999.

[153] K. S. Whitehead, M. Grell, D. D. C. Bradley, M. Jandke, and P. Strohriegl. Highly polarized blue electroluminescence from homogeneously aligned films of poly(9,9-dioctylfluorene). *Applied Physics Letters*, 76(20):2946–2948, may 2000.

[154] Peter Dyreklev, Magnus Berggren, Olle Inganäs, Mats R. Andersson, Olof Wennerström, and Thomas Hjertberg. Polarized electroluminescence from an oriented substituted polythiophene in a light emitting diode. *Advanced Materials*, 7(1):43–45, jan 1995.

[155] Vera Cimrová, Marcus Remmers, Dieter Neher, and Gerhard Wegner. Polarized light emission from LEDs prepared by the Langmuir-Blodgett technique. *Advanced Materials*, 8(2):146–149, feb 1996.

[156] T. W. Hagler, K. Pakbaz, K. F. Voss, and A. J. Heeger. Enhanced order and electronic delocalization in conjugated polymers oriented by gel processing in polyethylene. *Physical Review B*, 44(16):8652–8666, oct 1991.

[157] Z. Zheng, K. Yim, M. Saifullah, M. E. Welland, R. H. Friend, J-S Kim, and Huck W. T. S. Uniaxial Alignment of Liquid-Crystalline Conjugated Polymers by Nanoconfinement. 2007.

[158] K.S Whitehead, M Grell, D.D.C Bradley, M Inbasekaran, and E.P Woo. Polarized emission from liquid crystal polymers. *Synthetic Metals*, 111-112:181–185, jun 2000.

[159] S. A. Schmid, K. H. Yim, M. H. Chang, Z. Zheng, W. T. S. Huck, R. H. Friend, J. S. Kim, and L. M. Herz. Polarization anisotropy dynamics for thin films of a conjugated polymer aligned by nanoimprinting. *Physical Review B*, 77(11):115338, mar 2008.

[160] Dong-Myoung Lee, You-Jin Lee, Jae-Hoon Kim, and Chang-Jae Yu. Birefringence-dependent linearly-polarized emission in a liquid crystalline organic light emitting polymer. *Optics Express*, 25(4):3737, feb 2017.

[161] Masahiro Misaki, Masayuki Chikamatsu, Yuji Yoshida, Reiko Azumi, Nobutaka Tanigaki, Kiyoshi Yase, Shuichi Nagamatsu, and Yasukiyo Ueda. Highly efficient polarized polymer light-emitting diodes utilizing oriented films of β-phase poly(9,9-dioctylfluorene). *Applied Physics Letters*, 93(2):023304, jul 2008.

[162] H. Sirringhaus, R. J. Wilson, R. H. Friend, M. Inbasekaran, W. Wu, E. P. Woo, M. Grell, and D. D. C. Bradley. Mobility enhancement in conjugated polymer field-effect transistors through chain alignment in a liquid-crystalline phase. *Applied Physics Letters*, 77(3):406–408, jul 2000.

[163] Takahiro Seki. New strategies and implications for the photoalignment of liquid crystalline polymers. *Polymer Journal*, 46(11):751–768, nov 2014.

[164] Xihua Li, Vladimir M. Kozenkov, Fion Sze-Yan Yeung, Peizhi Xu, Vladimir G. Chigrinov, and Hoi-Sing Kwok. Liquid-Crystal Photoalignment by Super Thin Azo Dye Layer. *Japanese Journal of Applied Physics*, 45(1A):203–205, jan 2006.

[165] Ling-Ling Ma, Sen-Sen Li, Wen-Song Li, Wei Ji, Bin Luo, Zhi-Gang Zheng, Zhi-Ping Cai, Vladimir Chigrinov, Yan-Qing Lu, Wei Hu, and Lu-Jian Chen. Rationally Designed Dynamic Superstructures Enabled by Photoaligning Cholesteric Liquid Crystals. *Advanced Optical Materials*, 3(12):1691–1696, dec 2015.

[166] Haoran Zhang, Lingling Ma, Qian Zhang, Yuping Shi, Yueting Fang, Ruidong Xia, Wei Hu, and Donal D. C. Bradley. Azobenzene Sulphonic Dye Photoalignment as a Means to Fabricate Liquid Crystalline Conjugated Polymer Chain-Orientation-Based Optical Structures. *Advanced Optical Materials*, page 1901958, feb 2020.

[167] Ling-Ling Ma, Ming-Jie Tang, Wei Hu, Ze-Qun Cui, Shi-Jun Ge, Peng Chen, Lu-Jian Chen, Hao Qian, Li-Feng Chi, and Yan-Qing Lu. Smectic Layer Origami via Preprogrammed Photoalignment. *Advanced Materials*, 29(15):1606671, apr 2017.

[168] Sigma-Aldrich - https://www.sigmaaldrich.com.

[169] Linkam Scientific - http://www.linkam.co.uk/.

[170] F. Le Roux and D. D. C. Bradley. Conformational control of exciton-polariton physics in metal-poly(9,9-dioctylfluorene)-metal cavities. *Physical Review B*, 98(19):195306, nov 2018.

[171] Iryna Valyukh, Hans Arwin, Vladimir Chigrinov, and Sergiy Valyukh. UV-induced in-plane anisotropy in layers of mixture of the azo-dyes SD-1/SDA-2 characterized by spectroscopic ellipsometry. *physica status solidi (c)*, 5(5):1274–1277, may 2008.

[172] Alexey V. Kavokin. Motional narrowing of inhomogeneously broadened excitons in a semiconductor microcavity: Semiclassical treatment. *Physical Review B - Condensed Matter and Materials Physics*, 57(7):3757–3760, 1998.

[173] Toralf Scharf. *Polarized Light in Liquid Crystals and Polymers*. John Wiley & Sons, Inc., Hoboken, NJ, USA, dec 2006.

[174] S. J. Orfanidis. Electromagnetic Waves and Antennas, Chapter 4: Propagation in Birefringent Media. *http://eceweb1.rutgers.edu/orfanidi/ewa/*.

[175] Pochi Yeh. Electromagnetic propagation in birefringent layered media. *Journal of the Optical Society of America*, 69(5):742, may 1979.

[176] Joel Yuen-Zhou, Semion K. Saikin, Tony Zhu, Mehmet C. Onbasli, Caroline A. Ross, Vladimir Bulovic, and Marc A. Baldo. Plexciton Dirac points and topological modes. *Nature Communications*, 7, jun 2016.

[177] T. Espinosa-Ortega and T. C. H. Liew. Complete architecture of integrated photonic circuits based on and and not logic gates of exciton polaritons in semiconductor microcavities. *Physical Review B*, 87(19):195305, may 2013.

[178] D.D. Solnyshkov, O. Bleu, and G. Malpuech. All optical controlled-NOT gate based on an exciton–polariton circuit. *Superlattices and Microstructures*, 83:466–475, jul 2015.

[179] Fabio Scafirimuto, Darius Urbonas, Ullrich Scherf, Rainer F. Mahrt, and Thilo Stöferle. Room-Temperature Exciton-Polariton Condensation in a Tunable Zero-Dimensional Microcavity. *ACS Photonics*, 5(1):85–89, jan 2018.

[180] Elad Eizner, Julien Brodeur, Fábio Barachati, Aravindan Sridharan, and Stéphane Kéna-Cohen. Organic Photodiodes with an Extended Responsivity Using Ultrastrong Light–Matter Coupling. *ACS Photonics*, 5(7):2921–2927, jul 2018.

[181] Sai Kiran Rajendran, Mengjie Wei, Hamid Ohadi, Arvydas Ruseckas, Graham A. Turnbull, and Ifor D. W. Samuel. Low Threshold Polariton Lasing from a Solution-Processed Organic Semiconductor in a Planar Microcavity. *Advanced Optical Materials*, 7(12):1801791, jun 2019.

[182] P. A. M. Dirac. The quantum theory of the emission and absorption of radiation. *Proceedings of the Royal Society of London. Series A, Containing Papers of a Mathematical and Physical Character*, 114(767):243–265, 1927.

[183] E. M. Purcell. Spontaneous emission probabilities at radio frequencies. *Physical Review*, 69(681).

[184] Dirk Englund, David Fattal, Edo Waks, Glenn Solomon, Bingyang Zhang, Toshihiro Nakaoka, Yasuhiko Arakawa, Yoshihisa Yamamoto, and Jelena Vučkovićc. Controlling the spontaneous emission rate of single quantum dots in a two-dimensional photonic crystal. *Physical Review Letters*, 95(1):013904, jul 2005.

[185] Dieter Bimberg, Erik Stock, Anatol Lochmann, Andrei Schliwa, Waldemar Unrau, Michael Münnix, Sven Rodt, Askhat Bakarov, Jan A. Töfflinger, Vladimir A. Haisler, Aleksandr I. Toropov, and Aleksandr K. Kalagin. Quantum dots for single- and entangled-photon emitters. *IEEE Photonics Journal*, 1(1):58–68, jun 2009.

[186] Palik E. *Handbook of Optical Constants of Solids*. Academic Press, 1997.